Progress on the application of the NS-alpha model to wall-bounded flows

by

Katharine Andrea Scott

A thesis
presented to the University of Waterloo
in fulfillment of the
thesis requirement for the degree of
Doctor of Philosophy
in
Mechanical Engineering

Waterloo, Ontario, Canada, 2008

I hereby declare that I am the sole author of this thesis. This is a true copy of the thesis, including any required final revisions, as accepted by my examiners.

I understand that my thesis may be made electronically available to the public.

Abstract

In this thesis we study the NS-α model of flow turbulence. In this model the closure arises through a modified nonlinearity. For the NS-α model currently used in published numerical studies, the parameter representing turbulent fluctuations, α^2, is a scalar and is assumed to be a constant. This corresponds to homogeneous, isotropic fluctuations. In this thesis we investigate the NS-α model for the more practical situation where fluctuations may be inhomogeneous and anisotropic. We begin by reviewing the derivation of the governing equations using Hamilton's principle. This is followed by the formulation of a subgrid model, where the dependent variable is the smoothed velocity. The isotropic and anisotropic subgrid models are then tested on a recirculating cavity flow and a fully turbulent channel flow. Initial tests used a simple definition of the model parameter based on the grid size. Two specific problems with the model in these test cases were isolated and addressed. For the cavity flow we found abrupt changes in the model parameter at the solid boundary led to numerical oscillations. To overcome this problem an alternative definition was proposed and found to produce improved turbulence statistics. For the channel flow, interaction between the model and the velocity streaks near the wall led to high skin friction. A damping factor through the streak-affected region removed this problem.

Acknowledgements

I would like to thank my supervisor, Fue-Sang Lien, and co-supervisors, Kevin Lamb and Meng-Sing Liou, for their guidance, encouragement and enthusiasm. A special thanks to Fue-Sang Lien for keeping me in the realm of engineering, to Kevin Lamb for introducing me to geophysical flows, and to Gordon Stubley and Cécile Devaud for the discussions on academics and teaching philosophies. I would also like to thank all the members of the fluid mechanics group within the Applied Mathematics department for making me welcome at their seminars, where I learned not only interesting aspects of geophysical flows, but also gained insight into how mathematicians and engineers can work together.

There are a number of great students within our research group that have made the last five years much more enjoyable and interesting. In particular, Johan Larsson (who patiently replied to all of my channel flow e-mails), Andrew Keats, Cecilia Lam and Cam McCartney, I hope we can continue our discussions in the years to come. I was lucky to have an excellent office-mate, Amir Baserinia, who provided good conversation breaks, and served as an excellent technical springboard with his clarity.

Over the last five years my mom, my sister and all of my in-laws have been patiently cheering me on, and I grateful for their support. A special thanks to my mom, for teaching me to follow my own path, and to my sister, for her incredible willingness to lend an ear at any time of day or night.

These last five years were made easier and richer thanks to the daily support of my husband Bryan, who was with me every step of the way, through each setback and each accomplishment. Thanks for the impromptu camping trips, the wine nights, and for believing in me.

Contents

List of Tables

List of Figures

Chapter 1

Introduction

Turbulent flows can be readily observed in the world around us. The motion of leaves on a windy day and a billowing smokestack are common examples. These flows exhibit a range of eddy sizes, and while they appear random and intermittent, careful observation may reveal a pattern. It is this dual nature of turbulent flows, random yet containing organized, coherent structures, that makes them difficult to characterize and to study. In combination with the sophisticated numerical, analytical and experimental techniques available today, this has led to widely different, and typically very specialized approaches to model turbulent flows. In light of this, it is good to remember that our basic understanding of turbulent flows is still heavily based on early thought experiments, where careful observation and reasoning were the key tools.

Historically, the academic study of turbulent flows is often traced back to experiments carried out by Osborne Reynolds in 1876. Upon injecting dye into a pipe flow he found that above certain speeds the dye was no longer arranged in layers, but exhibited bursts. This illustrates one of the key properties of turbulent flows that distinguishes them from laminar ones, their ability to transport and mix fluid. This property makes turbulence desirable in some situations, and problematic in others. For example, it is a benefit when increased heat transfer is the goal in combustion devices, but not when the increased momentum transfer leads to higher drag and hence greater fuel consumption for automobiles and aircraft. Turbulence also provides an effective means through which pollutants in the atmosphere and ocean are dispersed. Clearly the study of turbulent flows is of fundamental importance for a wide range of industrial and environmental problems.

In this thesis we will be concerned with the turbulent motion of a three-dimensional incompressible, constant density fluid in Cartesian geometries. The fluid motion is governed by the Navier-Stokes equations, written in non-dimensional form as

$$\frac{\partial u_i}{\partial x_i} = 0, \tag{1.1a}$$

$$\frac{\partial u_i}{\partial t} + u_j \frac{\partial u_i}{\partial x_j} = -\frac{\partial p}{\partial x_i} + \frac{1}{Re}\frac{\partial^2 u_i}{\partial x_k^2}. \tag{1.1b}$$

The parameter that arises through the non-dimensionalization is known as the Reynolds number

$$Re = \frac{ul}{\nu}, \tag{1.2}$$

where u and L are characteristic velocity and length scales of the flow, and ν is the kinematic viscosity. For example, in pipe flow L could be the pipe diameter and u the bulk flow velocity. The Reynolds number is a measure of the relative strength of inertia to viscous forces. This can be seen more directly by writing the Reynolds number as

$$Re = \frac{u \cdot \nabla u}{\nu \nabla^2 u} = O\left(\frac{u^2/l}{\nu u/l^2}\right) = O\left(\frac{ul}{\nu}\right). \tag{1.3}$$

The primary obstacle in solving the Navier-Stokes equations is the wide range of scales that arise in a turbulent flow. The largest scales are on the order of the flow geometry (eg. pipe diameter in a pipe flow), while the smallest scales are those that have just enough inertia to withstand dissipation by viscous forces. This range of scales is a result of the nonlinear term in the Navier-Stokes equation, which transfers energy between different scales. This is seen most easily by writing the nonlinear term in Fourier space (c.f. Pope, pg. 214 [110])

$$F.T.\left(u_j \frac{\partial u_i}{\partial x_j}\right) = ik_j \int_{\boldsymbol{k}=\boldsymbol{p}+\boldsymbol{q}} \hat{u}_i(\boldsymbol{p})\hat{u}_j(\boldsymbol{q}) d\boldsymbol{p}. \tag{1.4}$$

The nonlinear term is now a convolution and describes the interaction between two velocity components, $\hat{\boldsymbol{u}}(\boldsymbol{p})$ and $\hat{\boldsymbol{u}}(\boldsymbol{q})$ where $\boldsymbol{q} = \boldsymbol{k} - \boldsymbol{p}$ and $\boldsymbol{k}, \boldsymbol{p}, \boldsymbol{q}$ are wavenumbers. Taking the dot product of (1.4) with $\hat{\boldsymbol{u}}(\boldsymbol{k})$ would then give the contribution of the nonlinear term to the energy equation for a mode with wavenumber $\boldsymbol{k}$, indicating an energy transfer to or from $\boldsymbol{k}$, mediated by two other scales $\boldsymbol{p}$ and $\boldsymbol{q}$.

The classic picture of the energy transfer in three-dimensional turbulence was put forth by Richardson [115] who conceptualized a turbulent flow as consisting of a cascade wherein large scales transfer energy downscale to smaller ones. Credit for

the energy cascade is, however, typically given to Kolmogorov [61] because he was the first to establish firm ground for this concept by developing a statistical theory amenable to verification by experiment. Kolmogorov considered the relative motion that ensues when a fluid is set into motion by a stirring force. He reasoned that the large scale stirring would lead to 'pulsations' in scales of the next smallest order, which in turn would excite those of the next smallest order, and so on. This cascade of energy would continue until the excitation reached scales small enough to be affected by molecular viscosity, at which point the motion would be damped and the energy transfered into heat. Such a picture of energy transfer provides a plausible means through which the small scales of the flow would have 'forgotten' where they came from, which is central to the hypothesis that a high Reynolds number flow should be locally isotropic in a region far from boundaries and singularities. To assist experimentalists in identifying such regions Kolmogorov put forward two hypotheses that could be tested. Since relative motion can be described by the velocity structure functions

$$\langle |\Delta u|^p(r) \rangle = \langle |u(x+r) - u(x)|^p \rangle, \tag{1.5}$$

where $\langle \cdot \rangle$ denotes an ensemble average, Kolmogorov developed his scaling laws in terms of the distribution laws of the structure functions. The first hypothesis of similarity refers to the small scales that are directly affected by viscosity and states:

- For locally isotropic turbulence the distribution laws of $\langle |\Delta u|^p \rangle$ should be uniquely determined by the kinematic viscosity ν and the energy dissipation rate ϵ.

From this one can use dimensional analysis to obtain the scaling of the p^{th} order structure function to be

$$\langle |\Delta u|^p \rangle \sim u^p F(r/\eta) \tag{1.6}$$

where η is the Kolmogorov length scale , $\eta = (\nu^3/\epsilon)^{1/4}$.

In the study of turbulence models we are generally more concerned with the second hypothesis of similarity because it pertains to larger scales that are capable of being resolved numerically. This is the intermediate range of scales that are affected neither by large-scale stirring, nor by dissipation. The second hypothesis states:

- If the length scale of interest, r, is large compared to the dissipation scale, the distribution laws for $\langle |\Delta u|^p \rangle$ will be uniquely determined by ϵ and do not depend on ν.

In this inertial range dimensional analysis yields,

$$\langle |\Delta u|^p \rangle \sim (\epsilon r)^{p/3}. \tag{1.7}$$

For $p = 2$ this is the 2/3 law for the second-order structure function

$$\langle |\Delta u|^2 \rangle \sim (\epsilon r)^{2/3}. \tag{1.8}$$

Kolmogorov's picture of the energy cascade is usually visualized by looking at the energy spectrum, $E(k)$, rather than the structure functions, because $E(k)$ is easier to measure in practice. The energy spectrum tells us how the kinetic energy is distributed over the wavenumbers

$$\int_V \frac{u_i u_i}{2}\, dV = \int_0^\infty E(k)\, dk. \tag{1.9}$$

Following the same reasoning as above for the inertial range scaling, but working now with $E(k)$ and ϵ yields

$$E(k) \sim \epsilon^{2/3} k^{-5/3}. \tag{1.10}$$

This can also be determined directly from (1.8) using the relationships between the spectral density function and the two-point correlation tensor (see Davidson [14] pg. 229). A sketch of the energy spectrum is shown in Figure 1.1. The flow of energy is denoted by the arrows and shows the energy input at the large scales being transfered through the inertial subrange and dissipated at the small scales. A very good example of an energy spectrum measured in the field can be found in Grant [38]. This was one of the first measurements that verified the $-5/3$ scaling, taken in a tidal channel off the coast of British Columbia using a towed hot film anemometer. The Reynolds number was very high at 4×10^7 and hence thieir spectrum demonstrates a wide inertial subrange. Prior to this measurement most energy spectra were obtained in the laboratory and the Reynolds numbers were not high enough to show a clear inertial subrange.

Kolmogorov's theory also gives a heuristic estimate of the degrees of freedom active in a turbulent flow. By equating the rate at which energy is input at the large scales, u^3/L, to the dissipation rate, ϵ, one can obtain the ratio of the largest to smallest active scales as

$$\frac{L}{\eta} = (Re)^{3/4}. \tag{1.11}$$

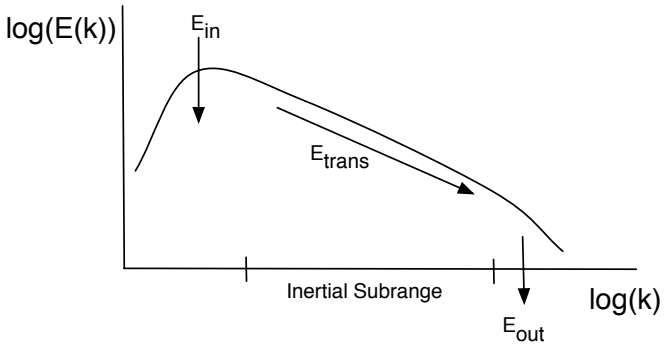

Figure 1.1: Schematic of the energy spectrum for three-dimensional turbulence. They second hypothesis yields the $-5/3$ scaling of the energy spectrum in the inertial subrange.

This means that as the Reynolds number increases we can expect a wider range of active scales. This presents the main difficulty in numerically solving the Navier-Stokes equations. When we solve the discretized equations on a finite computational domain, the smallest flow structure which can be resolved is proportional to the grid spacing, while the largest is proportional to domain size. Clearly then, if the Reynolds number is very high a large grid with a fine mesh will be required. For this reason direct numerical simulations (DNS) of turbulent flows are still limited to fairly low Reynolds numbers. At moderate to high Reynolds numbers a turbulence model must be introduced to account for the scales that cannot be resolved

Large-Eddy Simulation (LES)

The picture of the energy cascade and the hypothesis of local isotropy at the small scales are the central tenets of a turbulence modeling approach known as large eddy simulation (LES). The idea behind LES is to capture the large scales directly and confine modeling to the small scales. Because of the small-scale isotropy this is expected to result in models that are fairly universal, meaning they can be applied to a wide variety of flows without tuning. To remove the small scales a low-pass filter is applied to the Navier-Stokes equations. Denoting the low-pass filtering operation by $\tilde{\cdot}$ the filtered Navier-Stokes equations are

$$\frac{\partial \tilde{u}_i}{\partial x_i} = 0, \tag{1.12a}$$

$$\frac{\partial \tilde{u}_i}{\partial t} + \tilde{u}_j \frac{\partial \tilde{u}_i}{\partial x_j} = -\frac{\partial \tilde{p}}{\partial x_i} + \frac{1}{Re}\frac{\partial^2 \tilde{u}_i}{\partial x_k^2} - \frac{\partial \tau_{ij}}{\partial x_j}, \tag{1.12b}$$

where τ_{ij} is the subgrid stress

$$\tau_{ij} = \widetilde{u_i u_j} - \tilde{u}_i \tilde{u}_j. \tag{1.13}$$

In filtering the Navier-Stokes equations to obtain (1.12a)-(1.12b) it is assumed that the filter operator commutes with differentiation, which means we can write

$$\widetilde{\frac{\partial u_i}{\partial x_i}} = \frac{\partial \tilde{u}_i}{\partial x_i} \qquad \widetilde{\frac{\partial u}{\partial t}} = \frac{\partial \tilde{u}_i}{\partial t}.$$

This is only true when the filter width is not a function of space or time, or for special classes of filters [120, 141]. When nonuniform filters are used additional terms arise in the filtered Navier-Stokes equations, and neglecting these terms leads to the so-called commutator errors. Here we will follow the convention that these terms can be neglected. This subject has received attention only recently, and a thorough treatment can be found in van der Bos [137] and references therein.

In practice, large eddy simulation does not normally involve the application of an explicit filtering operation. Instead, the finite support of the computational grid is normally relied on to provide the filtering [82, 81]. In this context the unclosed term, equation (1.13) is usually referred to as the subgrid stress, and represents those scales that cannot be captured on the computational grid. This term cannot be determined from the filtered velocity field because it contains a product of unfiltered velocity components, $\widetilde{u_i u_j}$. This represents the closure problem in large eddy simulation and the need for subgrid models.

Now consider the filtered Navier-Stokes equation (1.12b) with the grid acting as an implicit filter and with τ_{ij}=0. If this equation is solved numerically on a sufficiently fine grid it is simply a DNS for $\tilde{u}_i$. Attempts to resolve this equation on a coarse grid, as is usually the case, will result in a build-up of energy near the wavenumber corresponding to the grid cut-off, due to nonlinear interactions between the resolved scales[1]. Since the small scales are not resolved the physical dissipation mechanism that would, in reality, drain this energy is missing. An appropriate choice of τ_{ij} will serve to dissipate this energy as it is generated, leading to a stable simulation and good overall prediction of energy dissipation. This is the primary reason for the

[1]Numerically, one can also look at this as aliasing [34]

development of numerous eddy-viscosity models popular in large eddy simulations. In the eddy-viscosity approach the subgrid stress is related to the filtered rate of strain through the constitutive relationship [120]

$$\tau_{ij} - \frac{\delta_{ij}}{3}\tau_{kk} = -2\nu_T \tilde{S}_{ij} \tag{1.14}$$

where ν_T is the eddy viscosity. For LES the most popular choice of eddy viscosity is composed of a mixing length $C_s\Delta$, where Δ is the filter width, and a time scale based on the resolved rate of strain $\tilde{S}_{ij}$

$$\nu_T = (C_s\Delta)^2(2\tilde{S}_{ij}\tilde{S}_{ij})^{1/2}. \tag{1.15}$$

This is known as the Smagorinsky model, and the coefficient C_s is called the Smagorinsky coefficient. It was first proposed by Smagorinsky [127] for numerical weather prediction. Later work by Lilly [77] showed that the coefficient can be determined analytically for isotropic turbulence by equating the energy dissipation rate to the rate at which energy is transferred from the resolved to subgrid scales. For a spectral cut-off filter this yields $C_s = 0.18$. The Smagorinsky model has been found to work well in isotropic turbulence and in free shear flows such as jets and mixing layers. As discussed by Jimenez [55] the success of this model relies largely on its robustness, and not in the fact that it provides a correct model for the flow physics. For example, if the constant C_s is too low then there will be a buildup of energy in the resolved scales, leading to an increase in $\tilde{S}_{ij}$, and thus increased dissipation, bringing the energy drain back to the appropriate level. This can probably account for why selecting a value of C_s substantially lower than that predicted analytically has been fairly successful for simple flows. However, the shortcomings of the Smagorinsky approach in predicting more complex flows are well known. From (1.15) we can see that the simple constitutive relationship assumes alignment between the subgrid stress and the strain rate. It has been found both in analysis of DNS data and in experimental studies that this is far from the truth. For example Tao et al. [131] find the most probable angle between the most extensive eigenvector of the subgrid stress and the most compressive eigenvector of $\tilde{S}_{ij}$ to be 34^o. The alignment is important because it is related to the energy transfer between the resolved and subgrid scales, which is $\tau_{ij}\tilde{S}_{ij}$ when the subgrid stress is symmetric. The Smagorinsky model is also strictly dissipative for positive viscosities, and unstable for negative ones. This means it cannot capture the reverse energy transfer from small to large scales, known as backscatter. Although energy transfer is on average from large to small scales in three-dimensional turbulence, there are a number

of flows where local backscatter effects are important. Examples from shear flows include, the later stages of boundary layer transition [108], hairpin vortices in the near-wall region [109, 42] and vortex pairing in mixing layers [126]. One popular method to incorporate backscatter is by adding a stochastic forcing term [85] to the Smagorinsky model. The rationale behind this is that while a dissipative model can capture the 'in the mean' forward transfer, the subgrid stress exhibits significant fluctuations about this mean, and it is these fluctuations that are responsible for the backscatter. In practice though, backscatter tends to be strongly correlated with coherent structures, leading some to hypothesize that a deterministic model may be more appropriate [109]. Finally, the Smagorinsky model is too dissipative to be used for transitional flows, damping out the small perturbations in the linear instability stage and causing relaminarization of the flow [106, 144].

A remarkable improvement to Smagorinsky's model is the dynamic procedure, proposed by Germano [29], and modified by Lilly [78]. In this approach C_s is determined as a function of the local flow dynamics, which alleviates somewhat the problems encountered with the standard Smagorinksy model in transitional flows and near solid walls. The dynamic model is based on Germano's identity, which relates the subgrid stress determined at a test filtering level to that at the primary filtering level, where the test filter is wider than the primary filter. The only unknown emerging from this identity is C_s. The dynamic model thus allows this parameter to be determined at every grid point, instead of specifying one constant over the entire flow. However, in practice spatial averaging must be included in evaluation of C_s for numerical stability. This can be done either by averaging over homogeneous directions (as is done for example in a channel flow) or by employing a Lagrangian averaging procedure where the average is taken along a streamline [89]. While the dynamic approach has been very successful [106, 113, 103], there are still shortcomings, most notably the computational overhead associated with the test filtering operation, and the assumptions inherent in the eddy viscosity ansatz.

A different approach is represented by the scale-similarity family of models, which are based on the idea that the relevant contribution to the subgrid stress will be from those scales near the filter cut-off, and in this region it is then assumed that

$u \sim \tilde{u}$ [1]. In this case the model for the subgrid stress is[2]

$$\tau_{ij} = \widetilde{\tilde{u}_i \tilde{u}_j} - \tilde{\tilde{u}}_i \tilde{\tilde{u}}_j. \tag{1.17}$$

Unlike the Smagorinsky model, the scale similarity model is known to produce good correlation between the modeled τ_{ij} and that obtained from both filtered DNS [1] and experimental data [79] and is capable of capturing backscatter [90, 109]. However, while it produces good results in *a priori* tests, in practice the model is not dissipative enough [1]. This has led to the development of mixed models, in which the scale similarity term is supplemented with a dissipation term [1, 151]. The dissipation term is usually evaluated dynamically, and the resulting combination of a mixed model with a dynamic procedure is expensive, estimated at adding $\sim 20\%$ to the total computation time as compared to $\sim 7\%$ for the Smagorinsky model for a plane channel flow [106]. It should be noted that cost estimates for the dynamic procedure alone vary widely. For plane channel flow where the coefficient is averaged over homogeneous directions, Piomelli [106] estimates that it adds only 15% to the total computation time. However, for the flow past a square cylinder, where there are no homogeneous directions and either clipping or a Lagrangian averaging procedure are used to stabilize the coefficient, the model has been found to increase the computation time by $200 - 400\%$ [97].

The Smagorinsky and scale-similarity models are only two examples of the vast array of approaches to subgrid modeling that have been proposed and tested. A thorough review can be found in the text by Sagaut [120]. One consistent trend has been the use of models which are either strictly dissipative, or contain a dissipative component. This concept is well-founded, since the role of the model is to mimic the energy drain provided by the smallest scales in the Navier-Stokes equation, that were removed by the filtering operation. As we have discussed above, in some cases it may be necessary to add a backscatter model.

[2]Note that $\tilde{\tilde{u}} \neq \tilde{u}$ unless the filter is a projector (c.f. Sagaut [120], pg. 24), which is one for which $G^n = G$. For example a spectral filter with transfer function

$$G(k) = \begin{cases} 1 & \text{if} \quad k < k_c \\ 0 & \text{otherwise} \end{cases} \tag{1.16}$$

is a projector.

NS-α model

Now, let's say that *instead* of using a model that contains a dissipative term for forward energy transfer and a model for backscatter, we take a step back and ask what our governing equation would look like if we had a system that stopped transferring energy *to* small scales when a certain wavenumber, say k_α, is exceeded, but did not stop the backscatter. In other words, we no longer have to model the forward transfer *to* the small scales because these transfers are not part of the system, nor do we need to model the *missing* backscatter because it has not been removed. This is in essence the idea behind the NS-α model [3].

How does the NS-α model do this? Since we know the energy transfer between different scales comes from the nonlinear term, it is logical that this term should be modified in some way. If we think harder about how energy is transferred in a turbulent flow, this gives us another clue. Physically, the energy transfer from large to small eddies is attributed to a mechanism known as vortex stretching (c.f. Tennekes and Lumley [133]). To understand this phenomena we must derive an equation for the vorticity, defined as $\boldsymbol{\omega} = \nabla \times \mathbf{u}$. This is easily done by first writing the Navier-Stokes equation in velocity-vorticity form

$$\frac{\partial u_i}{\partial t} - \boldsymbol{u} \times \boldsymbol{\omega} = -\frac{\partial}{\partial x_i}\left(p + \frac{1}{2}u_k u_k\right) + \frac{1}{Re}\frac{\partial^2 u_i}{\partial x_k^2}, \tag{1.18}$$

and then taking the curl to obtain

$$\frac{\partial \omega_i}{\partial t} + u_j \frac{\partial \omega_i}{\partial x_j} = \omega_j \frac{\partial u_i}{\partial x_j} + \frac{1}{Re}\frac{\partial^2 \omega_i}{\partial x_k^2}. \tag{1.19}$$

The first term on the right hand side is called the vortex stretching term, although technically it is responsible for stretching, compression and tilting of vortex lines. It is known that on average stretching dominates over compression in turbulent flows, leading to smaller, more intense vortices, in the limit of an inviscid flow [136]. In practice a turbulent flow is populated with a variety of vortical structures, usually categorized as being either sheet-like or tube-like (see Davidson pg. 246 for a discussion). These structures are constantly undergoing deformation by the background strain field [35]. If we think about smoothing this background flow so that the characteristic length scale of the strain field is large relative to the

[3] This is in fact one interpretation of the NS-α equations as a turbulence model. However it should be kept in mind that these equations were not originally developed for the purpose of turbulence modeling. See Holm [46] for a history on the origins of the NS-α equations.

size of the vortices, we would expect the velocity gradients to become less effective at stretching and tilting the vortices. In turn this would prevent the creation of smaller and smaller scales, and hence eliminate the need to model the effects of these scales when we carry out a coarse grid numerical simulation. Because the smoothed background flow is also advecting the vorticity, such a picture leads us to the following vorticity equation

$$\frac{\partial \omega_i}{\partial t} + \tilde{u}_j \frac{\partial \omega_i}{\partial x_j} = \omega_j \frac{\partial \tilde{u}_i}{\partial x_j}. \tag{1.20}$$

The corresponding momentum equation is given by

$$\frac{\partial u_i}{\partial t} + \tilde{u}_j \frac{\partial u_i}{\partial x_j} + u_j \frac{\partial \tilde{u}_j}{\partial x_i} = -\frac{\partial p^\alpha}{\partial x_i}, \tag{1.21}$$

where $p^\alpha = p + u_m \tilde{u}_m/2$. To obtain (1.21) we have enforced continuity on the smoothed velocity, which is logical because this is the advecting velocity in (1.20).

At this point we have not specified how the smoothed and unsmoothed velocities are related. For the NS-α model this is not arbitrary and we will see in Chapter 3 that they are related through a Helmholtz equation (given here for the case where α^2 is constant),

$$u_i = \tilde{u}_i - \alpha^2 \frac{\partial^2 \tilde{u}_i}{\partial x_k^2}. \tag{1.22}$$

In Fourier space

$$\hat{\tilde{u}}_i(\boldsymbol{k}) = \frac{\hat{u}_i(\boldsymbol{k})}{1 + \alpha^2 |\boldsymbol{k}|^2}, \tag{1.23}$$

from which it is clear that the smoothed velocity is low-pass filtered since the high-wavenumber components are attenuated. From this relationship we can see there is a new parameter, α, that can be interpreted as a filter width.

The above equation (1.21) is inviscid and is known as the Euler-α model [50]. The viscous version

$$\frac{\partial u_i}{\partial t} + \tilde{u}_j \frac{\partial u_i}{\partial x_j} + u_j \frac{\partial \tilde{u}_j}{\partial x_i} = -\frac{\partial p^\alpha}{\partial x_i} + \nu \frac{\partial^2 u_i}{\partial x_k^2} \tag{1.24}$$

will be referred to in this thesis as the Navier-Stokes-α or NS-α model (see also [25, 32]). It is also known as the LANS-α model (where LANS is an abbreviation for Lagrangian-Averaged Navier-Stokes) [92, 37] and is closely related to the Viscous Camassa-Holm equation (VCHE). A discussion of the history of the model

and the origin of the different names is given in Holm [50].

The NS-α model is part of a broader class of methods that are based on regularization of the nonlinear terms in the Navier-Stokes equations [32]. The simplest model in this group is the Leray model, which consists of replacing the advecting velocity in the Navier-Stokes equations by a smoothed velocity. The governing equations for the Leray model are

$$\frac{\partial u_i}{\partial x_i} = 0, \tag{1.25a}$$

$$\frac{\partial u_i}{\partial t} + \tilde{u}_j \frac{\partial u_i}{\partial x_j} = -\frac{\partial p}{\partial x_i} + \frac{1}{Re} \frac{\partial^2 u_i}{\partial x_k^2}. \tag{1.25b}$$

Note that in (1.25a) it is the unsmoothed velocity that satisfies the continuity equation. This means the contribution of the nonlinear term to the energy equation cannot be written in a purely redistributive form, and effectively creates an additional source/sink term [140]. Most subgrid models create such an additional term in the energy equation, which is a source/sink term representing energy exchange between the resolved and subgrid scales. However, for the Leray model it has been shown that this additional term can lead to significant problems in wall-bounded flows [140]. For an unbounded mixing-layer the Leray model led to reduced small-scale variability as compared to both the DNS and the NS-α model, but was found to be more robust on coarse meshes than the NS-α model [32], both of which are probably related to the fact that the Leray model has been hypothesized to have an even more compact energy spectrum than the NS-α model [32].

While the development of the NS-α model from a modified vorticity equation (see also Montgomery and Poquet [95]) and the interpretation of α as a smoothing scale or filter width are perfectly valid, in this thesis we will go into greater detail to describe the origin of the NS-α equations and the parameter α. We will see that before α became interpreted as a filter width it had a different definition, either as a measure of the displacement of a particle from a mean trajectory, or as a mixing length. By understanding more clearly the derivation of the NS-α equation (Chapter 3) we will see that the equation used most often in the literature (1.24), and the subgrid model based on this equation [51, 32], assume isotropic and homogeneous fluctuations, meaning the turbulence parameter, α^2, is a scalar and is constant. In this thesis we will consider wall-bounded flows, which are both inhomogeneous and anisotropic. It is very tempting to proceed in these cases by solving the same equa-

tion (1.24) for the more complex flow situation. For the strongly sheared flows in the present thesis early numerical tests following this approach found that the simulations diverged if α^2 was kept constant, and produced erroneous results if anisotropy was incorporated in an ad-hoc manner. Thus it was necessary to develop a more general subgrid model, which was done by starting with the anisotropic, variable-α equations presented in Holm [47].

The outline of the thesis is as follows. In Chapter 2 we will review the literature on the NS-α model and discuss the relationship between the model and turbulence theory. We will see that this model is on solid footing with regards to the theory and has been found capable of capturing both forward energy transfer and backscatter. In theory, the model only seeks to modify the nonlinearity in such a way that the cascade of energy to small scales is attenuated, which is in agreement with the central problem of the Navier-Stokes equation. In Chapter 3 we will present a derivation of the governing equation from Hamilton's principle. This derivation is not new in that it is comprised of principles seen before [5, 47, 3] but it is hoped the presentation is easier for the non-mathematician to understand than that commonly encountered in the literature. In Chapter 4 we will formulate our governing equation into the LES template so that it can be easily implemented in a finite volume code, which will be described in Chapter 5. Benefits and shortcomings to using the model will then be illustrated using two test cases, a lid-driven cavity flow, and a turbulent channel flow, discussed in Chapters 6 and 7 respectively. This will be followed by conclusions and recommendations for future work.

Objectives of the thesis

The majority of existing literature on the NS-α model is theoretical in nature, with most numerical simulations directed towards verifying the underlying theory. For this purpose, studies of isotropic box turbulence are the preferred numerical experiment. The primary goal of this thesis was to investigate the NS-α model in a more general setting. To this end the following objectives were defined:

- Review the derivation of the NS-α equations for the general case of anisotropic and inhomogeneous fluctuations.
- Investigate isotropic and anisotropic versions of the models using an LES methodology. This means developing an equation with the smoothed velocity

as the dependent variable and with the subgrid model written as the divergence of a tensor. Implement this model in a standard finite-volume code used for engineering applications.

- Investigate this subgrid model first basing α^2 on the grid scale, the standard choice for the smoothing scale in the LES community. Determine if this is a good choice for the NS-α model. If not, identify shortcomings and suggest a new definition of α^2.

- Gain insight into how the model changes the resolved flow. If it is not dissipative, then what does it do in physical space? Is it useful?

Chapter 2

Review of Literature on the NS-α model

2.1 Motivation to use the NS-α equations as a turbulence model

2.1.1 Scaling of the Energy Spectrum

In LES we are often concerned with how the model changes the scaling of the energy spectrum on the premise that this will tell us what kind of computational savings we can expect from using the model. For the NS-α model scaling arguments can be deduced in the same manner as is done for the Navier-Stokes equations. Here we discuss arguments for the energy spectrum scaling law that are commonly encountered in the literature. At times the concepts in this section are phenomenological, thus vector notation is dropped as are any constants of order unity.

2.1.1.1 Conserved Energy

Before reviewing scaling arguments for the NS-α equations we need to understand an important difference between the NS-α equations and other models for turbulence. Instead of draining energy from the system, the NS-α equations change the energy conservation properties by conserving a different quadratic form. The conserved energy for the (inviscid) NS-α equations (1.21) is [25]

$$E_\alpha = \frac{1}{V}\int_V \frac{1}{2} u_i \tilde{u}_i \, dV. \tag{2.1}$$

Recalling that the smoothed $\tilde{\boldsymbol{u}}$ and unsmoothed $\boldsymbol{u}$ velocities are related through the Helmholtz operator $\boldsymbol{u} = \tilde{\boldsymbol{u}} - \alpha^2 \nabla^2 \tilde{\boldsymbol{u}}$ we can rewrite this in terms of the smoothed velocity as

$$E_\alpha = \frac{1}{V} \int_V \frac{1}{2} \left(\tilde{u}_i \tilde{u}_i + \alpha^2 |\nabla \tilde{u}_i|^2 \right) \, dV \tag{2.2}$$

where we have integrated by parts and used either periodic boundary conditions or $\tilde{u}_i = 0$ on the boundary. It can be seen in (2.2) that there are two components to the conserved energy, the kinetic energy $\tilde{u}_i \tilde{u}_i / 2$ and a velocity gradient term. The second term is generally considered to impose an energy penalty [17] in the sense that as smaller and smaller scales are generated and the velocity gradients increase this will come at the expense of reduced kinetic energy, $\tilde{u}_i \tilde{u}_i$. If we were to draw only the energy spectrum of $\tilde{u}_i \tilde{u}_i / 2$ we would expect to see the small-scale portion of this spectrum being attenuated with increasing α^2, or with the mean-squared velocity gradient term increasing. The form of the conserved energy also provides another way to look at the effect the model has on vortex stretching. In order to maintain a certain level of kinetic energy in the system the velocity gradients can only become so steep. Because these gradients are related to vorticity $\boldsymbol{\omega} = \nabla \times \boldsymbol{u}$ and the stretching/tilting term $\boldsymbol{\omega} \cdot \nabla \tilde{\boldsymbol{u}}$, the vorticity filaments will be limited in how small they can become.

2.1.1.2 Eddy turnover time arguments

The most common scaling arguments given in the literature for the NS-α model are based on the model put forth by Kraichnan [65]. In this model the interscale transfer rate in the inertial subrange is given by the rate at which an eddy of size $1/k$ transfers its energy to a smaller eddy of size $1/2k$[1]. For this purpose the energy equation in Fourier space is considered. Following Foias et al. [25] we denote $\hat{u}_k$ as the velocity for Fourier modes in the range $[k, 2k)$ and the energy by $e = \hat{u}_k \hat{u}_k / 2$. The energy equation in Fourier space can be written (for the transfer between modes k and $2k$)

$$\frac{\partial e}{\partial t} = T_k - T_{2k} + \nu k^2 e. \tag{2.3}$$

[1]The choice of $2k$ for the second eddy comes from the view that eddies transfer energy most effectively to those which are approximately half their size. Physically this was hypothesized since an eddy can be most effectively stretched by a shear which is approximately of the same order of magnitude. This can be easily visualized by considering stirring the fluid in a coffee cup. A large spoon (but not as large as the domain size, which is the cup) will be a more effective stirring mechanism than a very tiny stir stick. More concrete evidence that energy is transferred mostly to scales separated in wavenumber space by a factor of two is given in the study by Meneveau and Lund [88].

Here T_k denotes the energy transfer from modes with wavenumbers less than k, to those greater than k and T_{2k} is the transfer from modes with wavenumbers less than $2k$ to those greater than $2k$. Kolmogorov's picture of the energy cascade can then be visualized as follows. If we assume there is a large scale forcing, F_k, and that there is a sufficient separation of scales such that the dissipation is only relevant at the very small scales, then the energy injected by the forcing will be approximately balanced by the transfer out of the forcing wavenumber range by nonlinear interactions

$$F_k \sim T_k. \tag{2.4}$$

Similarly, when we get to the dissipation range the energy entering this range should be balanced by viscous dissipation, denoted by ϵ,

$$T_{2^n k} \sim \epsilon, \tag{2.5}$$

where n indicates the number of eddy turnover times. In the inertial range we are by definition far from any forcing or dissipation and energy is only transferred from one eddy to another through nonlinear interactions

$$T_{2^n k} \sim T_{2^{n+1} k}. \tag{2.6}$$

Thus the dissipation rate, ϵ, is also equal to the interscale transfer rate which is the rate at which an eddy of size k transfers its energy to one of size $2k$. Following Kraichnan [65] this is given by the energy in the wavenumber range $[k, 2k)$, divided by the eddy turnover time (τ)

$$\epsilon = \frac{1}{\tau} \int_k^{2k} E(k) dk. \tag{2.7}$$

The eddy turnover time is the time it takes an eddy to turnover, and is based on the eddy size and average eddy velocity

$$\tau = \frac{1}{k U_k}. \tag{2.8}$$

The average eddy velocity can be estimated from the kinetic energy

$$U_k = \left(\int_k^{2k} E(k) dk \right)^{1/2} \sim (k E(k))^{1/2}. \tag{2.9}$$

When we substitute these into the equation for ϵ (equation (2.7)) we find

$$\epsilon = k(kE(k))^{1/2} \int_k^{2k} E(k)dk \sim k^{5/2} E(k)^{3/2}, \tag{2.10}$$

from which the well known inertial-range scaling emerges

$$E(k) \sim \epsilon^{2/3} k^{-5/3}. \tag{2.11}$$

While the above derivation was for the Navier-Stokes equations, the same arguments are followed to develop a scaling law for the NS-α equations (for full details see Foias et al. [25]). We begin with the energy based on the smoothed and unsmoothed velocities

$$e_a \equiv \int_V \frac{\hat{\bar{u}}_i \hat{u}_i}{2}\, dV = \int_0^\infty E_\alpha(k)\, dk, \tag{2.12}$$

and interscale transfer rate

$$\epsilon_\alpha = \frac{1}{\tau} \int_k^{2k} E_\alpha(k)dk. \tag{2.13}$$

Once again the eddy turnover time is given by

$$\tau = \frac{1}{kU_k}. \tag{2.14}$$

What is not clear is how to specify the average eddy velocity. There are three possibilities,

$$U_k = \left(\hat{\bar{u}}_k \hat{\bar{u}}_k\right)^{1/2} = (kE_\alpha(k))^{1/2} (1+\alpha^2 k^2)^{-1/2} \tag{2.15}$$

$$U_k = \left(\hat{u}_k \hat{\bar{u}}_k\right)^{1/2} = (kE_\alpha(k))^{1/2} \tag{2.16}$$

$$U_k = (\hat{u}_k \hat{u}_k)^{1/2} = (kE_\alpha(k))^{1/2} (1+\alpha^2 k^2)^{1/2} \tag{2.17}$$

or,

$$U_k = (kE_\alpha(k))^{1/2} (1+\alpha^2 k^2)^{\frac{n-1}{2}} \qquad \text{for n=0,1,2.} \tag{2.18}$$

Following the same steps as for the Navier-Stokes equations we arrive at the expression for the energy spectral density

$$E_\alpha(k) \sim \frac{\epsilon_\alpha^{2/3} k^{-5/3}}{(1+\alpha^2 k^2)^{\frac{n-1}{3}}}. \tag{2.19}$$

Thus when $(\alpha\, k)^2 \ll 1$ the scaling is the same as for Navier-Stokes turbulence, while for $(\alpha\, k)^2 \gg 1$ it is,

$$n = 0 \qquad k^{-1} \tag{2.20}$$

$$n = 1 \qquad k^{-5/3} \tag{2.21}$$

$$n = 2 \qquad k^{-7/3}. \tag{2.22}$$

Early numerical simulations of the NS-α equations [10, 92] showed an energy spectrum, E_α that had a steeper roll-off than $k^{-5/3}$, which would suggest the average kinetic energy should be based on the product of the unsmoothed velocities ($n = 2$). The fact that the slope is steeper than that of Navier-Stokes turbulence was one of the main reasons why the equations were promoted in the literature as a turbulence model.

2.1.1.3 The Kármán-Howarth equation

We have seen in the previous section that, depending on how we define the eddy turnover time, we arrive at different scalings for the energy spectrum. To further refine the scaling arguments Holm developed the Kármán-Howarth equation for the NS-α equations [48]. This equation relates the third order structure function to the energy dissipation rate. It is the physical space representation of the evolution equation for the spectral tensor $\hat{\phi}_{ij}(k)$, the trace of which is the well-known equation for the energy spectral density $E(k)$ when integrated over spherical shells in wavenumber space. In physical space the trace of the two-point correlation tensor gives the detailed energy balance for the Navier-Stokes equation, where 'detailed energy balance' refers to the energy transfer between different scales in the flow. To develop the Kármán-Howarth equation one first writes the momentum equation for the velocity at a field point x, $u = u(x)$, and then writes a second momentum equation for the velocity at a field point x', $u' = u(x')$, where $x' = x + r$. Multiplying the first equation by u' and the second by u and averaging the results then gives an equation for the two-point correlation tensor $Q_{ij} = \langle u_i u'_j \rangle$ [14]

$$\frac{\partial Q_{ij}}{\partial t} = \frac{\partial}{\partial r_k}\left(S_{ikj} + S_{jki}\right) + \nu \nabla_r^2 Q_{ij}, \tag{2.23}$$

where S_{ikj} is the third-order correlation tensor

$$S_{ikj} = \langle u_i(x) u_k(x) u_j(x + r) \rangle.$$

When you integrate (2.23) over a volume of fluid with periodic boundary conditions the divergence term is zero and we have the familiar result that the rate of change of energy is equal to the viscous dissipation in the absence of forcing.

The Kármán-Howarth equation provides another means to obtain the $-5/3$ law that, unlike the previous methods, comes directly from the Navier-Stokes equation. First of all consider that if we are in an inertial range (where viscous dissipation can be neglected), equation (2.23) tells us

$$\epsilon \sim \frac{u^3}{l},$$

where l is a characteristic eddy length scale. If we keep in mind that $kE(k) \sim u^2$ we obtain,

$$\epsilon \sim \frac{(kE(k))^{3/2}}{l}, \tag{2.24}$$

or

$$E(k) \sim \epsilon^{2/3} k^{-5/3}. \tag{2.25}$$

Thus the scaling law is derived which is free from any assumptions other than isotropy and the existence of an inertial range.

If you follow similar steps as for the Navier-Stokes equation you can arrive at a Kármán-Howarth equation for the NS-α equation [48]. To do this you start with the NS-α equation written in terms of the unsmoothed velocity at a field point x, $u(x)$, and then the equation for the smoothed velocity at a second field point x', $\tilde{u}(x')$. Cross-multiplying, averaging and rewriting in symmetric form, one obtains an equation for the two-point correlation tensor, $Q_{ij}^{\alpha} = \langle u_i \tilde{u}'_j + \tilde{u}_j u'_i \rangle$. It is this tensor that is of interest when developing scaling arguments for the energy e_α. The symmetric form of the Kármán-Howarth equation for the NS-α model is [48]

$$\frac{\partial Q_{ij}^{\alpha}}{\partial t} = \frac{\partial}{\partial r_k}\left(\tau_{ijk} - \alpha^2 \tilde{S}_{ijk}^{\alpha}\right) + 2\nu \nabla_r^2 Q_{ij}^{\alpha}. \tag{2.26}$$

The tensor τ_{ijk} denotes the triple correlation

$$\tau_{ijk} = \langle \left(u_i \tilde{u}'_j + u_j \tilde{u}'_i + u'_i \tilde{u}_j + u'_j \tilde{u}_i\right) \tilde{u}_k \rangle, \tag{2.27}$$

and the last term, $\alpha^2 \tilde{S}_{ijk}^{\alpha}$, is the subgrid term and is a function of only the smoothed velocity and the filter function (see Holm [48] for details). The important thing to

know here is that the subgrid term scales as $\alpha^2\tilde{u}^3/l^2$. From dimensional scaling arguments we then have

$$\epsilon_\alpha = \frac{1}{l}\left(u\tilde{u}^2 - \frac{\alpha^2}{l^2}\tilde{u}^3\right). \tag{2.28}$$

When $(\alpha/l)^2 \sim 0$ the smoothed and unsmoothed velocities are equal, $\tilde{u} \sim u$, which gives the usual Navier-Stokes scaling, $\epsilon \sim u^3/l$. On the other hand when $(\alpha/l)^2 \gg 1$ the scaling is,

$$\tilde{u}^3 \sim \epsilon_\alpha \alpha^{-2} l^3 \tag{2.29}$$

from which you can obtain (using $\tilde{u}u \sim kE_\alpha(k)$ and $u \sim \tilde{u}\alpha^2/l^2$),

$$E_\alpha(k) \sim \epsilon_\alpha^{2/3}\alpha^{2/3}k^{-1} \tag{2.30}$$

This supports the k^{-1} scaling given from the eddy turnover time arguments when the eddy velocity is based on the kinetic energy from the smoothed velocities alone. While this slope is shallower than that of the Navier-Stokes equations, it translates to a slope of k^{-3} for the energy spectrum based on the smoothed velocity alone (using $E_{\tilde{u}}(k) \sim E_\alpha(k)/(1+\alpha^2k^2)$. Thus if we follow an LES methodology and use $\tilde{u}_i$ as the dependent variable we would still expect an energy spectrum with a steeper slope than that of the Navier-Stokes equations, and the equations can still be considered a good candidate for investigation as a subgrid model.

2.1.2 Reduction in Degrees of Freedom

The steeper slope of the energy spectrum for the NS-α equations implies a larger Kolmogorov scale and an overall reduction in the degrees of freedom as compared to the Navier-Stokes equation. An estimate of the Kolmogorov scale for the NS-α equations can be obtained by integrating the energy spectrum,

$$\epsilon_\alpha \sim \int_0^{k_{\eta\alpha}} \nu k^2 E_\alpha \, dk. \tag{2.31}$$

Substituting in the energy spectrum from (2.30) you arrive at

$$k_{\eta\alpha} = \frac{\epsilon_\alpha^{1/6}}{\nu^{1/2}\alpha^{1/3}}, \tag{2.32}$$

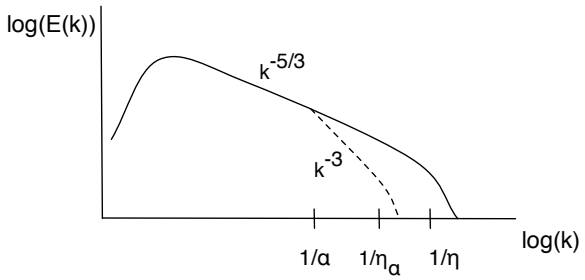

Figure 2.1: Energy spectrum, $E_{\tilde{u}}(k)$, for the NS-α model (based on discussion in Foias [25]). The dotted line shows where the slope is steeeper than the Navier-Stokes spectrum at wavenumbers higher then $1/\alpha$.

where $k_{\eta\alpha}$ is the Kolmogorov scale for the NS-α equation. From this the degrees of freedom can then be estimated [25]

$$DOF_{NS\alpha} = (k_{\eta\alpha} l)^3 \sim \frac{Re^{3/2}}{(\alpha/l)}, \tag{2.33}$$

where l is the characteristic length scale of the energy containing eddies. It was anticipated in early studies that for high Reynolds numbers $\alpha/l \sim const$ and the degrees of freedom would be $DOF_{NS\alpha} \sim Re^{3/2}$, a significant reduction from that of the Navier-Stokes equations, $DOS_{NS} \sim Re^{9/4}$. More recent results suggest $\alpha \sim \eta$ with a much more modest reduction in the degrees of freedom [37]. Foias estimates the Kolmogorov scale for the NS-α equation to be related to that of the NS-α equation according to

$$k_{\eta\alpha} = k_{\eta NS}^{2/3} k_{\alpha}^{1/3} \tag{2.34}$$

where $k_\alpha \sim 1/\alpha$. Given that k_α is generally taken to be in the inertial subrange, this implies $k_{\eta\alpha} < k_{\eta NS}$. A schematic of the proposed energy spectrum [25, 17] is shown in Figure 2.1, where the Kolmogorov scales are marked as η and η_α for the Navier-Stokes and NS-α equations respectively.

2.1.3 Attenuation of nonlinear interactions

Based on the picture given in the introduction that the NS-α model alters the vortex stretching term, and hence the cascade of energy to the small scales, we would expect that the interscale energy transfer for the NS-α equations will be different than that of the Navier-Stokes equations. Further understanding as to how the NS-α equations change the interscale transfer can come from looking at the triad interactions in Fourier space. Recall that the nonlinear term in the Navier-

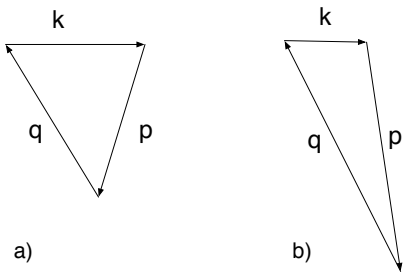

Figure 2.2: Schematic of local (a) and nonlocal (b) triads, c.f. Sagaut [120]

Stokes equation can be written in Fourier space as,

$$F.T.\left(u_j\frac{\partial u_i}{\partial x_j}\right) = ik_j\int_{\boldsymbol{p}+\boldsymbol{q}=\boldsymbol{k}}\hat{u}_j(\boldsymbol{p})\hat{u}_m(\boldsymbol{q})d\boldsymbol{p}. \tag{2.35}$$

The three wavenumbers in (2.35), $\boldsymbol{k},\boldsymbol{p},\boldsymbol{q}$ form a triad, such that $\boldsymbol{k}=\boldsymbol{p}+\boldsymbol{q}$. If all three wavenumbers are of the same order of magnitude, the triad is considered local, and the energy transfer will also be local, as shown in Figure 2.2 (a). On the other hand if one of the legs of the triad differs from the other two in magnitude by a factor of two or more the triad is considered non-local. For the example shown in Figure 2.2 (b) the triad can have both local and nonlocal energy transfer. A study of the triad interactions for 3D Navier-Stokes turbulence was carried out by Waleffe [146] using helical wave decomposition (HWD)[2]. This is similar to a decomposition into Fourier modes, except that each Fourier mode is further decomposed into '+' modes and '-' modes, where the '+/-' refers to the direction in which the velocity vector rotates about the $\boldsymbol{k}$ axis. The velocity field is expressed as

$$\begin{aligned}\boldsymbol{u}(\boldsymbol{x}) &= \sum_k \hat{\boldsymbol{u}}(\boldsymbol{k})e^{i\boldsymbol{k}\cdot\boldsymbol{x}}\\ &= \sum_k \left(a^+(\boldsymbol{k})\boldsymbol{h}_+ + a^-(\boldsymbol{k})\boldsymbol{h}_-\right)e^{i\boldsymbol{k}\cdot\boldsymbol{x}},\end{aligned} \tag{2.36}$$

where a^- and a^+ are helical wave coefficients and $\boldsymbol{h}_+$ and $\boldsymbol{h}_-$ are the new basis vectors. The basis is formed by constructing a plane perpendicular to $\boldsymbol{k}$ and representing the velocity in terms of three components, one of which is in the $\boldsymbol{k}$ direction, and two other components which are orthogonal to each other and to $\boldsymbol{k}$. One can then set the amplitude of the component in the $\boldsymbol{k}$ direction to zero, since $\boldsymbol{k}\cdot\hat{\boldsymbol{u}}=0$ by continuity. The two basis vectors are then chosen to be complex-valued such

[2]This is especially appealing approach for the NS-α model because the nonlinear terms can be written compactly in velocity-vorticity form $\tilde{\boldsymbol{u}}\times\boldsymbol{\omega}$.

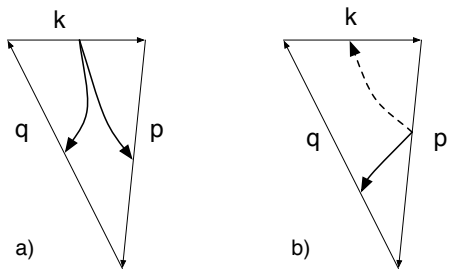

Figure 2.3: Schematic of F triads (a) and R triads (b) after Waleffe [146]. Solid lines indicate forward transfers, while the dashed line is backscatter.

that one rotates clockwise and one counter-clockwise. Using this decomposition each triad discretely conserves energy and helicity.

From this decomposition amplitude equations can be derived for each component $(a_k^{+/-}, a_p^{+/-}, a_q^{+/-})$ of a triad. Analysis of these equations then tells you which modes are stable and which are unstable. Waleffe [146] classified the unstable triads into two groups based on whether the two largest wavevectors have the same spin or opposite spins. In the former case it is shown that the middle wavenumber is unstable and loses energy to the other two, one of which is larger and one of which is smaller. It can be shown that most of the energy is transferred to the smaller wavenumber, which is a reverse transfer, and hence these are called R triads. For the F triads the two largest wavenumbers have opposite spins and it is the smallest wavenumber which is unstable, thus the energy transfer is from large to small scales, or in the forward direction. A sketch of these two types of triads is shown in Figure 2.3. By looking at the vorticity equation Waleffe shows that the stretching term corresponds to an interaction involving HWD coefficients of opposite spin (a^+ and a^-) giving further evidence to the hypothesis that forward transfers are due to vortex stretching. On the other hand, advection of small scales by large ones corresponds to interactions between coefficients with the same spin, and thus this is the physical interpretation of the R triads.

Instead of looking at the full nonlinear term $\boldsymbol{u} \times \boldsymbol{\omega}$, Domaradzki and Holm [17] considered the Fourier transform of the advection term in the NS-α equations

$$F.T.(\tilde{u}_j \frac{\partial u_l}{\partial x_j}) = \frac{i}{2}\left(k_m P_{lj} \int \frac{\hat{u}_j(\boldsymbol{p})\hat{u}_m(\boldsymbol{q})}{1+\alpha^2|\boldsymbol{q}|^2} d\boldsymbol{p} + k_j P_{lm} \int \frac{\hat{u}_m(\boldsymbol{q})\hat{u}_j(\boldsymbol{p})}{1+\alpha^2|\boldsymbol{p}|^2} d\boldsymbol{p}\right) \quad (2.37)$$

where P_{lj} and P_{lm} are the projection tensors that arise when we take the divergence of the momentum equation and project the nonlinear term into a plane perpendicular to $\boldsymbol{k}$ [110]. For example

$$P_{lj} = \delta_{lj} - \frac{k_l k_j}{|\boldsymbol{k}|^2}. \tag{2.38}$$

Based on the nonlinear term (2.37) we can consider the following scenarios

- Consider a local triad where all three scales are large, $|\boldsymbol{k}|\alpha, |\boldsymbol{p}|\alpha|, |\boldsymbol{q}|\alpha \ll 1$. The attenuation factors will be close to unity, $1 + \alpha^2|\boldsymbol{q}|^2 \sim 1 + \alpha^2|\boldsymbol{p}|^2 \sim 1$, and the dynamics of the large scales will be unchanged by the model.

- Consider a local triad where all three scales are small, $|\boldsymbol{k}|\alpha, |\boldsymbol{p}|\alpha, |\boldsymbol{q}|\alpha \gg 1$. The attenuation factors will be very large, $1 + \alpha^2|\boldsymbol{q}|^2 \sim 1 + \alpha^2|\boldsymbol{q}|^2 \gg 1$. In this case the nonlinear transfer term will be close to zero. Thus the dynamics leading to local energy transfer between the small scales are essentially removed.

- Consider a nonlocal triad with $|\boldsymbol{k}|\alpha < 1$ and $|\boldsymbol{p}|\alpha, |\boldsymbol{q}|\alpha$ both $\gg 1$. In this case $\boldsymbol{k}$ is the smallest wavenumber and can lose energy to the other two. These are forward-transfers due to the non-local interaction that occurs between a large scale and two small scales. The attenuation factors will be large and the non-linear term will again be close to zero, indicating that these transfers have been removed.

- Consider a nonlocal triad where $\boldsymbol{k}$ is an intermediate scale, for example $|\boldsymbol{p}| < |\boldsymbol{k}| < |\boldsymbol{q}|$. In this case $\boldsymbol{k}$ is the intermediate wavenumber and can lose energy to the other two [146]. If we let $|\boldsymbol{p}|\alpha \ll 1$, $|\boldsymbol{k}|\alpha \approx 1$ and $|\boldsymbol{q}|\alpha > 1$, the second component of the non-linear term in equation (2.37) will not be changed by the presence of α. Physically, this is the advection of a small scale component $|\boldsymbol{q}|$ by a large scale component $|\boldsymbol{p}|$, and corresponds to the 'non-local sweeping' referred to in the literature [17]. Note that it is the partial smoothing of the nonlinear term that gives rise to this interaction being preserved. If both velocity components were smoothed, the denominator of the non-linear term would contain a product of the two factors, $1 + \alpha^2|\boldsymbol{p}|^2$ and $1 + \alpha^2|\boldsymbol{q}|^2$, and would be damped regardless of which velocity was the advection velocity.

The removal of the small scale interactions can also be seen by decomposing the non-linear term (in physical space) as

$$u_i\tilde{u}_j = \tilde{u}_i\tilde{u}_j + \tilde{u}_j u_i^{sgs} \tag{2.39}$$

where the decomposition into a smoothed and subgrid component is used $u_i = \tilde{u}_i + u_i^{sgs}$ is used [120]. This can be contrasted to the usual nonlinear term

$$u_i u_j = \tilde{u}_i \tilde{u}_j + \tilde{u}_i u_j^{sgs} + \tilde{u}_j u_i^{sgs} + u_i^{sgs} u_j^{sgs}. \tag{2.40}$$

The small-scale triad interactions are represented by the last term $u_i^{sgs} u_j^{sgs}$ [110], and are usually modeled by an eddy viscosity term [11, 28]. In the NS-α equations these dynamics are not generated, and hence an eddy viscosity term is not needed to dissipate them. On a similar note the backscatter from the unresolved scales is not missing in the NS-α model since the triads leading to non-local sweeping are not attenuated. Therefore, a backscatter model is also not needed.

2.2 Results from numerical simulations

In the previous section we have seen that the NS-α equations can be interpreted as a model for turbulence in the sense that they possess fewer degrees of freedom than the Navier-Stokes equations, and in theory attenuate vortex stretching and the cascade of energy to the small scales. Some of these properties have been explored in numerical simulations of box turbulence at modest Reynolds numbers of $Re_\lambda \sim 130$ [10] and $Re_\lambda \sim 90$ [92], where Re_λ is the Reynolds number based on the Taylor microscale and the velocity scale $u = 2\int_0^\infty E(k)dk$. These experiments found an energy spectrum steeper than $k^{-5/3}$, vortex structures that were shorter and fatter than in 3D Navier-Stokes turbulence [10], and that, unlike the Smagorinksy model, the model can predict the correct alignment between the eigenvectors of the strain rate tensor and subgrid stress [92]. None of these simulations were of sufficiently high resolution to confirm the k^{-1} scaling for $E_\alpha(k)$ predicted by the Kármán-Howarth equation (equation (2.30)), and it is only recently that a numerical study addressing this question has been published [37]. Recall that based on the results from the Kármán-Howarth equation, if we were to measure the third order structure function in the NS-α fluid we would expect to find the scaling $\langle |\delta\tilde{u}|^3 \rangle \sim l^3$ from (2.29), while if we were to measure the energy spectrum we would expect to see $E_\alpha(k) \sim k^{-1}$ from (2.30). It therefore came as some surprise to learn that, in high Reynolds number ($Re_\lambda \sim 1300$) numerical simulations of the NS-α equations, while the correct scaling for the structure function was observed, the scaling of the energy spectrum was k^1 instead of k^{-1} [37].

The reason for this is that the NS-α fluid is comprised of both regions undergo-

ing the Navier-Stokes dynamics of vorticity transport and stretching, and regions of 'rigid rotators' where stretching is inhibited [37]. These rigid-rotators do not contribute to the scaling of the velocity structure function since by definition, they contain no relative motion. Thus the structure function scaling follows l^3 as anticipated. On the other hand, rigid rotators do have kinetic energy and would therefore contribute to the scaling of the energy spectrum, $E_\alpha(k)$. What would this scaling be? Following Graham et al. [37], we write

$$u\tilde{u} \sim kE_\alpha(k), \tag{2.41}$$

and use the relationship $u \sim (1+\alpha^2k^2)\tilde{u}$ to arrive at $E_\alpha(k) \sim (\tilde{u}^2\alpha^2)k$ when $\alpha k \gg 1$. Rigid rotators have a constant velocity u, which means for a given α^2 the scaling of the energy spectrum is $E_\alpha(k) \sim k$. Thus while both scalings are valid, the k^{-1} scaling is subdominant, and it is the k^1 scaling which is observed in practice. This implies that the scaling for the energy spectrum $E_{\tilde{u}}(k)$ would be

$$E_{\tilde{u}}(k) \sim \epsilon^{2/3}k^{-1},$$

which is shallower that that of the Navier-Stokes equations. One might interpret this as implying that the degrees of freedom are greater than the Navier-Stokes equation, which would make this a very poor candidate for an LES model. However, since rigid rotators possess no internal degrees of freedom, it seems the energy spectrum alone is not necessarily an appropriate measure of DOF. On the other hand the energy spectrum does suggest there would be a pile up of energy at the high wavenumbers, hardly a desirable feature for a subgrid model to have. Graham et al. [37] suggest this should not be a problem provided that the build-up does not contaminate the large energy containing motions that are typically the dominant contribution to the first and second order statistics. However, a similar conclusion could be reached for dissipative models, in that if they do have excessive dissipation, as long as the quantities of interest are not affected there is no problem.

On the other hand we recall the earlier results of Mohseni et al. [92] and Chen et al. [10] that found the energy spectrum for $E_\alpha(k)$ to be steeper than that of the Navier-Stokes equations for wavenumbers greater than $1/\alpha$, in contradiction to the k^1 spectrum found at higher resolutions. Note that because these earlier simulations were at lower Reynolds numbers and had inertial ranges spanning only about a decade of wavenumbers the model would mostly affect the dissipation scales and you would not see the change in slope because the energy transfer is dominated by

viscous dissipation [37]. For example, in the DNS of Chen et al. [10] the transfer spectrum is attenuated only in the dissipation range of wavenumbers. One picture emerging from these studies is that it may be necessary for α to be close to the end of the inertial subrange. This makes the model potentially less attractive computationally, and implies it may not be useful for high Reynolds number turbulence.

While box turbulence studies are an important part of model investigation and validation, real-world turbulence is rarely isotropic or even homogeneous. Many models have been found to work well in the idealized box turbulence case, but have been later found to have poor performance in more complex flows. A major objective of this thesis was to investigate the NS-α model in scenarios of more practical relevance. The first studies in this direction were by those by Nadiga and Margolin [98] and Holm and Nadiga [51] where they looked at using the model as a non-dissipative parameterization of mixing in a gyre, and Geurts and Holm [32] where they studied a transitional mixing layer. In both cases the NS-α model performed better than the traditional dissipative closures. In particular, the NS-α model captured the mixing layer transition better than even the dynamic model at a comparable cost, a very promising result. More recently the model has been used as a parameterization in simulations of mesoscale eddies with considerable success [105, 44, 45].

In numerical simulations it is necessary to choose a physical value or relationship to determine α^2. For isotropic turbulence α can be chosen to be a specific fraction of the mesh size, corresponding to a length scale in the inertial subrange. In the more general case, the length scales of the flow are not known as precisely. Since α^2 can be thought of as a smoothing scale, or filter width, it is logical to start by relating α^2 to the mesh spacing. This brings up the question of what is the required scale separation between α and the mesh size? This question was addressed by Geurts and Holm [32] in their mixing layer study. In these simulations, the levels of turbulent kinetic energy in the later stages of transition were too high when the NS-α model was used. By keeping α^2 constant and subsequently refining the mesh they were able to lower the fluctuation levels until good agreement with the DNS data was found. In this way the overprediction was attributed to insufficient subgrid resolution (where the subgrid resolution refers to number of grid points per filter width, and indicates the scale separation between the cut-off wavenumber of the model, and that of the computational mesh). Similar problems were seen in the study of forced and decaying isotropic turbulence by Mohseni et al. [92]. For the

case where $1/\alpha$ was close to the energy containing range there was a significant build up of large scale energy. This was alleviated by increasing the grid resolution. In the study of Geurts and Holm, the recommended subgrid resolution was $\alpha \sim h$ for the NS-α model, determined through trial and error. This resolution can be understood more readily in light of what we have discussed above. While the NS-α model is expected to attenuate triad interactions associated with the forward energy transfer, it would not do so abruptly at a wavenumber corresponding to $k_\alpha = 1/\alpha$. It can be expected that a scale separation between the grid scale cut-off and α would be required to allow for this attenuation. If we consider that we still need to resolve the scales that eddies of size $1/\alpha$ transfer their energy to, this means[3] $k_{max} = 2/\alpha$. Since the maximum wavenumber is also related to the grid spacing as $k_{max} = \pi/h$ this gives, $\alpha/h \sim 2/\pi \sim 1$.

While the mixing layer study addressed the important question of free transition, successful application of the model to a wall-bounded flow with no-slip boundary conditions has not yet been realized. An excellent study in this direction, and indeed the study that first attempted to use the NS-α equations as a model for turbulence, was the analytical study of pipe and channel flow by Chen et al. [7, 8, 9]. Using the ansatz that the smoothed velocity in the NS-α can be interpreted as a Reynolds average, they simplified the NS-α equations to yield the streamwise momentum balance for a channel flow, as is customary in turbulent flow studies of this geometry. The mean velocity profile from this simplified momentum equation was in good agreement with experimental and DNS data. The analysis also yielded an expression for the shear stress as a function of Reynolds number that exhibited the correct trends when compared with the data. Numerical simulations of the NS-α equations did not follow soon after the analytical study. The first attempt came seven years later in an *a priori* [4] study by Zhao and Mohseni [153] where they developed a dynamic version of the subgrid model used previously for box turbulence [92]. This model is based on the isotropic, constant α equations. Clearly, this is inappropriate for a wall-bounded flow, and it was expected that using the dynamic procedure to determine α would correct this deficiency. In the *a priori* results the dynamically determined α was found to decrease linearly from the wall in the viscous sublayer and lower buffer layer, after which it became constant. The

[3]Here we have used a factor of two again based on the evidence the eddies transfer their energy most effectively to scales half their size.

[4]An *a priori* study refers to one where the subgrid model terms are computed but not added to the momentum equations as source terms. Thus the velocity field evolves without the effect of the model, and the subgrid terms and model performance are assessed. In contrast an *a postereori* study is one where the model terms added to the momentum equations.

a postereori results were less promising [152] showing little improvement over the dynamic Smagorinsky model. Because the base model, NS-α, is more expensive than the Smagorinsky model, it is difficult to justify using the NS-α model with a dynamic procedure unless is shows remarkably improved results. However, Zhao and Mohseni did not show or comment on the model performance using the default model without the dynamic procedure, which is surprising. It is possible that they found (as we did) that it is not possible to obtain a converged result when using the default isotropic model near a solid wall.

Based on their experience we felt it was a good time to investigate the anisotropic, non-constant α equations as a subgrid model for wall-bounded flows. One of the principle difficulties in this endeavor was determining what equations to use. There are at least two versions in the literature [47, 84], the derivation of neither of which is easily accessible to the engineer or model practitioner. Zhao and Mohseni did not pursue this path because they felt it was too early. Here we felt that by solving one of the equations numerically, we could at least generate insight into how it performs as a turbulence model, and perhaps contribute a different dimension to the problem. To this end we first sought a more accessible derivation of the Eulerian-averaged equations from Hamilton's principle, and this is given in the next chapter.

Chapter 3

Derivation of the model from Hamilton's Principle

3.1 Introduction

The NS-α model is derived by applying Hamilton's principle to an averaged Lagrangian. While this method of averaging is new in the context of turbulence modeling, there are several examples where it has been used before in fluid mechanics. In particular, in studying the interaction between a slowly-varying mean flow, and a rapidly varying wave field [148], for which one practical result has been improved understanding of energy transfer in the ocean [101]. In a sense, the application of variational principles to develop a turbulence model which can be used in practical situations represents an attempt to bridge many of the ideas in mechanics to those in turbulence theory, and in turn to use these in an applied setting. It remains to be seen what we can learn about turbulence using such an approach.

We start by giving a bit of background about functionals and Hamilton's principle. This is followed by a discussion of material and spatial representations of fluid flow. Finally, a derivation of the NS-α equation from an Eulerian perspective is given. In this method variations are taken with respect to the Eulerian coordinates and averaging is carried out at a fixed spatial location. There are several reasons for choosing this instead of the Lagrangian (particle-following) method. In engineering applications of fluid mechanics we are used to working with the Eulerian description of a fluid, and it is more intuitive to develop a model from this perspective. Eulerian-averaging is also more consistent with the manner in which the data we are comparing against are averaged.

Since the term 'Lagrangian' can have two meanings in this Chapter, one being the difference between the kinetic and potential energies, and the other 'particle following', we will refer to the particle following representation as the material description of the fluid. The method is given here for an incompressible flow of constant density, since this is the form of the NS-α equations that we will be looking at in this thesis. For extensions to stratified and rotating fluids see Holm [47], and for compressible flow see Bhat [3].

3.2 Hamilton's principle and Newton's Law

Hamilton's principle is an example of a variational principle, which is a principle that seeks to find the stationary point (for example a minimum or maximum) of a given functional. There are only a few things that we will need to know about functionals here, so we will discuss them briefly first. A good discussion of these preliminaries can be found in the text by Gelfand and Fomin [27].

A functional, often called a 'function of functions', can be thought of as an operation that maps a function (or a set of functions) onto a scalar value. The general form is usually given as

$$J[y] = \int_a^b F(x, y, y')dx, \tag{3.1}$$

where y' is dy/dx. Note that the square brackets are used for a functional to signify the fact that it is acting on a function. As an example of a functional consider

$$J[y] = \int_a^b \sqrt{1 + y'^2}\, dx, \tag{3.2}$$

which is the functional that describes the length of a curve $y(x)$ from a to b, and is a function of the slope, y'. Minimizing this functional is then equivalent to finding the function, $y(x)$ (satisfying the imposed boundary conditions), which will yield the shortest distance between $[a, y(a)]$ and $[b, y(b)]$. This turns out to be the straight line, $y' = constant$. Evaluating the functional for a given y' then gives you the distance between a and b, which is a scalar.

The functional we will be interested in here is called the action, S, and is defined as the integral between beginning and end times of the difference between the kinetic and potential energies of a system. The difference between the kinetic

energy (T) and potential energy (Φ) is called the Lagrangian, L. The action can be written as

$$S[x] = \int_{t_1}^{t_2} \underbrace{(T - \Phi)}_{L}\, dt. \tag{3.3}$$

Hamilton's principle can be thought of as a special variational principle in that it leads to Newton's second law. Because the functional, S, is called the action Hamilton's principle is often called the 'principle of stationary action'. In a finite-dimensional system we can think of our system as being composed of a number of particles, and consider the state of the system to be specified when the position and velocity of these particles is known. It is then assumed that the initial and final configurations of the system are specified, which means that the variations are zero at t_1 and t_2. The question then is, for all possible trajectories from an initial configuration, $\boldsymbol{x}(t_1), \dot{\boldsymbol{x}}(t_1)$, to a final configuration, $\boldsymbol{x}(t_2), \dot{\boldsymbol{x}}(t_2)$, which is the one for which S is stationary? To see that this question leads us to Newton's Law consider the following action for a general N-particle system,

$$S = \int_{t_1}^{t_2} \sum_{n=1}^{N} \left(m_n \frac{1}{2} \frac{\partial \boldsymbol{x}_n}{\partial t} \cdot \frac{\partial \boldsymbol{x}_n}{\partial t} - \Phi(\boldsymbol{x}_n) \right) dt. \tag{3.4}$$

To find the stationary point of the action we need to consider the difference between the action on a varied trajectory $S[\boldsymbol{x} + \delta\boldsymbol{x}]$, and that on a true trajectory $S[\boldsymbol{x}]$. This difference is called the increment, ΔS. For our action in (3.4) the increment is

$$\Delta S = \int_{t_1}^{t_2} \sum_{n=1}^{N} \left(m_n \frac{\partial \boldsymbol{x}_n}{\partial t} \frac{\partial (\delta \boldsymbol{x}_n)}{\partial t} - \frac{\partial \Phi}{\partial \boldsymbol{x}_n} \delta \boldsymbol{x}_n + O(\delta \boldsymbol{x}_n)^2 \right) dt. \tag{3.5}$$

Integrating the first term by parts and applying the condition $\delta\boldsymbol{x}_n(t_1) = \delta\boldsymbol{x}_n(t_2) = 0$

$$\Delta S = \int_{t_1}^{t_2} \sum_{n=1}^{N} \left[\left(-m_n \frac{\partial^2 \boldsymbol{x}_n}{\partial t^2} - \frac{\partial \Phi}{\partial \boldsymbol{x}_n} \right) \delta \boldsymbol{x}_n + O(\delta \boldsymbol{x}_n)^2 \right] dt \tag{3.6}$$

The condition that the functional is stationary corresponds to vanishing of the first variation, defined as the first order terms in the increment. Similar to a regular derivative, this can be done by taking the limit, in this case as the true and varied trajectories approach each other. We do this by denoting the difference between the two as the area ϵ^2, see Figure 3.1. We then consider the limit [1]

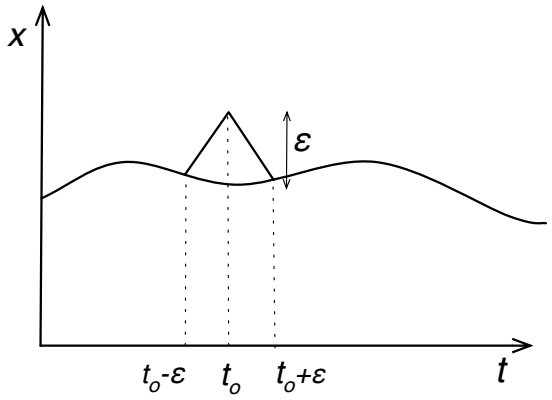

Figure 3.1: Sketch of the trajectory variation.

$$\frac{\delta S}{\delta \boldsymbol{x}} \equiv= \lim_{\epsilon^2 \to 0} \frac{S(\boldsymbol{x}+\delta\boldsymbol{x}) - S(\boldsymbol{x})}{\epsilon^2} \tag{3.7}$$

$$= \lim_{\epsilon^2 \to 0} \int_{t_1}^{t_2} \frac{1}{\epsilon^2} \sum_{n=1}^{N} \left[\left(-m_n \frac{\partial^2 \boldsymbol{x}_n}{\partial t^2} - \frac{\partial \Phi}{\partial \boldsymbol{x}_n} \right) \underbrace{\epsilon}_{\delta \boldsymbol{x}_n} + \underbrace{O(\epsilon^2)}_{(\delta \boldsymbol{x})^2} \right] \underbrace{\epsilon}_{dt} \tag{3.8}$$

$$= \left[\sum_{n=1}^{N} \left(-m_n \frac{\partial^2 \boldsymbol{x}_n}{\partial t^2} - \frac{\partial \Phi}{\partial \boldsymbol{x}_n} \right) \right]_{t=t_o} \tag{3.9}$$

Since the time $t = t_o$ is arbitrary this must be true for all times $t \in (t_1, t_2)$ and when the first variation is zero we are left with Newton's Law

$$\sum_{n=1}^{N} \left(-m_n \frac{\partial^2 \boldsymbol{x}_n}{\partial t^2} - \frac{\partial \Phi}{\partial \boldsymbol{x}_n} \right) = 0 \tag{3.10}$$

3.3 Moving from material to spatial representations

In the previous section we considered the action principle for an $N-$particle system. This is different from the approach we will use to develop the NS-α equations in that *i*) it is a discrete representation of the system and *ii*) it is given in terms of material coordinates, which are particle positions and velocities. The transformation from discrete to continuous can be made by replacing the sum over discrete particles to an integral over particle labels (where the label can be, for example, the position

[1]For a more thorough discussion see Gelfand pg. 27 [27].

of the particle at an initial time)

$$S[\boldsymbol{x}, \dot{\boldsymbol{x}}] = \int_{t_1}^{t_2} \int_{V(\boldsymbol{a})} L(\boldsymbol{x}, \dot{\boldsymbol{x}}) d^3a \, dt, \tag{3.11}$$

while the transformation from the material to spatial frame is done by reformulating the Lagrangian in terms of Eulerian coordinates. In the general case the Lagrangian can be written as a function of the velocity, density and entropy (c.f. [5, 122]),

$$S[\boldsymbol{u}, \rho, s] = \int_{t_1}^{t_2} \int_{V(\boldsymbol{x})} L(\boldsymbol{u}, \rho, s) d^3x \, dt. \tag{3.12}$$

In the material representation (3.11) variations are taken with respect to the particle position. This is a very natural way to apply Hamilton's principle, since it is a method which seeks to find the trajectory for which the action is stationary. This trajectory is usually described in terms of generalized coordinates, which do not necessarily have to coincide with physical coordinates. However, for the system described here, this trajectory is in fact a physical displacement trajectory, and is the familiar pathline we learn about in undergraduate fluid mechanics. So we can look at this as having fixed endpoints, and considering all possible pathlines between these endpoints. The pathline of interest is the one for which the action is stationary. In the previous section we saw this is the one that is governed by Newton's law.

In the spatial picture (3.12) variations of the Eulerian coordinates $(\boldsymbol{u}, \rho, s)$ are taken at a fixed point. The first question is then, how are variations of a particle trajectory reflected in these coordinates? Consider that if we are sitting at a fixed point watching particles being advected past, we have different particles passing through our fixed point. We can anticipate that the variation of an Eulerian variable will be composed of two parts, one will be the associated with the variation of a particle trajectory (as seen from a fixed position) while the second will be due to the fact that different labels will occupy that position.

To make this clear we need to define a function that connects the field position $\boldsymbol{x}$ to a label $\boldsymbol{a}$. Such a function is given by the trajectory, which we will denote by $\boldsymbol{\eta}$. More formally, let $\boldsymbol{\eta}$ be the function that maps particles with labels $\boldsymbol{a}$ to the field points they occupy at time t. For our purposes here we will assume this map is one-to-one, invertible and sufficiently smooth that we may differentiate it

as many times as necessary. The particle position $\boldsymbol{x}$ is then

$$\boldsymbol{x} = \boldsymbol{\eta}(\boldsymbol{a}, t). \tag{3.13}$$

Similarly, let $\boldsymbol{\eta}^{-1}$ be the map that tells you the label $\boldsymbol{a}$ of the particle occupying the field point $\boldsymbol{x}$ at time t,

$$\boldsymbol{a} = \boldsymbol{\eta}^{-1}(\boldsymbol{x}, t), \tag{3.14}$$

$\boldsymbol{\eta}^{-1}$ is often called the 'back-to-labels' map in the literature. As an example consider the mapping [2]

$$\boldsymbol{x} = \boldsymbol{\eta}(\boldsymbol{a}, t) = \boldsymbol{a}(1 + 2t)^{1/2}. \tag{3.15}$$

From this mapping we know that a particle with label $(2, 0, 0)$ will be at $(2\sqrt{5}, 0, 0)$ at time $t = 2$. In general, if we know the labels, then at a given time we would also know the particle positions. The inverse map for our example is given by $\boldsymbol{a} = \boldsymbol{\eta}^{-1}(\boldsymbol{x}, t)$,

$$\boldsymbol{a}(\boldsymbol{x}, t) = \frac{\boldsymbol{x}}{(1 + 2t)^{1/2}}. \tag{3.16}$$

From the inverse map we know the particle at $\boldsymbol{x} = (2\sqrt{5}, 0, 0)$ at time $t = 2$ has label $\boldsymbol{a} = (2, 0, 0)$.

The Eulerian and Lagrangian velocities at a given point are related through the identity

$$\boldsymbol{u}(\boldsymbol{x}, t) = \frac{d}{dt}\boldsymbol{\eta}(\boldsymbol{a}, t). \tag{3.17}$$

This states that the velocity at a given point is equal to the velocity of the particle which occupies that point at that time. This can be written as

$$\boldsymbol{u} = \dot{\boldsymbol{\eta}}(\boldsymbol{\eta}^{-1}(\boldsymbol{x}, t), t), \tag{3.18}$$

or

$$\boldsymbol{u} = \dot{\boldsymbol{\eta}} \circ \boldsymbol{\eta}^{-1} \tag{3.19}$$

where the $\circ$ operator denotes a composition of maps (the dot indicates a time derivative). Consider that if we only know the mapping $\boldsymbol{\eta}$, then to find the velocity, $\boldsymbol{u}(\boldsymbol{x}, t)$, at a given field point $\boldsymbol{x}$, we can evaluate $\boldsymbol{a} = \boldsymbol{\eta}^{-1}(\boldsymbol{x}, t)$ at our field point to find the particle occupying that point at time t. Knowing the particle (de-

[2] A excellent introduction to Eulerian and Lagrangian descriptions of fluid flow is given in the monograph by James Price, 'Lagrangian and Eulerian Representations of fluid flow: Kinematics and the equations of motion', *http : //ocw.mit.edu/ans7870/resources/price/essay3_sum.pdf*. The notation used here follows more closely that used in the NS-α literature [3, 50].

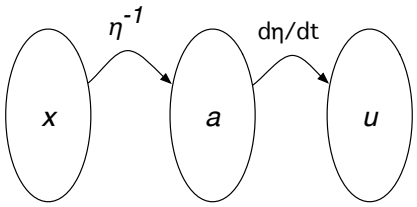

Figure 3.2: Mapping from a field point, to a label, and finally to the velocity field

noted by the label $\boldsymbol{a}$ we can then evaluate $\dot{\boldsymbol{\eta}}(\boldsymbol{a}, t)$ to get the velocity at that point. A sketch of this is given in Figure 3.2. The central idea to keep in mind here is that in the Eulerian framework the dependence of the velocity field on the particle trajectory comes into play in two places, one in calculating the rate of change of the trajectory and the other in evaluating the label. This means when we vary the velocity field we need to take both of these into account.

For our variational principle we will also need to vary the volume element, defined as [47]

$$D = det(d\boldsymbol{a}/d\boldsymbol{x}) \tag{3.20}$$

which is the ratio of the volume in the initial configuration to that in the current configuration. This is related to the Jacobian, $J = det(\nabla\boldsymbol{\eta})$ according to

$$D(\boldsymbol{x}, t) = \frac{1}{det(\nabla\boldsymbol{\eta})}. \tag{3.21}$$

To take variations we will also write the LHS in terms of the trajectory $\boldsymbol{\eta}$

$$D \circ \boldsymbol{\eta} = \frac{1}{det(\nabla\boldsymbol{\eta})}. \tag{3.22}$$

From these expressions for the velocity (3.19) and volume element (3.22) we will be able to relate variations of the Eulerian coordinates to the particle trajectory.

3.4 Derivation of the NS-α equations

The NS-α equations have been proposed in the literature as a turbulence model, and are considered to be different from other approaches in that the effects of turbulence are introduced at the level of the variational principle. To incorporate the effects of turbulence within the framework of Hamilton's principle consider that in the material description of a fluid, the state of the fluid is specified by the particle

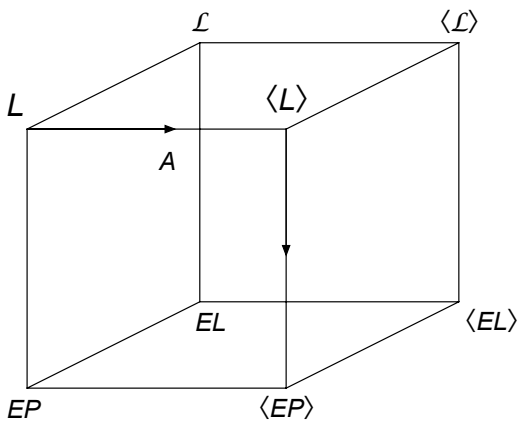

Figure 3.3: Different paths to the Euler-Poincaré equations (from Holm 2002 [49]).

displacements $\boldsymbol{x}(\boldsymbol{a}, t)$ and their velocities, $\dot{\boldsymbol{x}}(\boldsymbol{a}, t)$. It is natural then to incorporate turbulence by adding a random component to the displacement of a fluid particle, and, given that this random component is a function of time, to its velocity.

On the other hand, the vast majority of turbulence models are derived by working with the Eulerian description of a fluid, where the state of the (isentropic) fluid is described by $\boldsymbol{u}(\boldsymbol{x}, t)$ and $\rho(\boldsymbol{x}, t)$. For example, the well-known RANS equations for an incompressible flow are developed by decomposing the velocity field into mean and fluctuating components, substituting into the Navier-Stokes equations, and averaging. This suggests a different way of using the variational principle, which is to write it in terms of Eulerian coordinates and decompose these coordinates (instead of the particle position) into a mean and a fluctuation.

The goal in developing a turbulence model is usually to find a closed set of equations for the average state of the fluid. For both methods described above the equations that describe this average state are developed by averaging the Lagrangian and applying Hamilton's principle. The final momentum equation can thus be reached by different routes. Qualitatively, this is best illustrated using the diagram in Figure 3.3. In this Figure $\langle\cdot\rangle$ denotes an averaging operation, EL the Euler-Lagrange equation (equation for which the action is stationary, in the material frame) and EP the Euler-Poincaré equation (equation for which the action is stationary, in the spatial frame). Thus moving from left to right means an average is being applied, back to front is a transformation from the material to spatial frame and top to bottom indicates an application of Hamilton's principle (moving from the action integral to the differential equation). The route we will follow here is indicated by

the arrows. We start with the Lagrangian in the spatial frame (denoted by the plain uppercase L), decompose the Eulerian velocity into a mean and a fluctuation and average the Lagrangian $\langle L \rangle$, then apply Hamilton's principle to obtain the averaged Euler-Poincaré equations $\langle EP \rangle$. Following Holm, the derivation will be given for an incompressible, constant density flow. Following the objective of this thesis, we will try to keep things as simple as possible without resorting to undue assumptions and leaps of faith. The full details are well beyond the scope of this thesis and can be found in Holm [47] and references therein.

The general form for the Lagrangian in Eulerian coordinates is [5]

$$S = \int_{t_1}^{t_2} \int_V \left(\frac{\rho(\boldsymbol{x},t)}{2} u_i(\boldsymbol{x},t) u_i(\boldsymbol{x},t) - E(\rho(\boldsymbol{x},t), s(\boldsymbol{x},t)) - \phi(\boldsymbol{x},t) \right) d^3x\, dt \quad (3.23)$$

where E is the internal energy, s is the entropy and ϕ is the potential energy. Here we will consider an incompressible, constant density fluid of uniform entropy with no sources of potential energy. In the action principle we then remove the internal and potential energy functions and add an equation constraining the density to be constant

$$S = \int_{t_1}^{t_2} \int_V \left(\frac{\rho(\boldsymbol{x},t)}{2} u_i(\boldsymbol{x},t) u_i(\boldsymbol{x},t) + p\,(\rho_o - \rho(\boldsymbol{x},t)) \right) d^3x\, dt. \quad (3.24)$$

Using conservation of mass we can relate the density ratio to the volume element D by $D = \rho/\rho_o$, where ρ_o is the reference density. Using this we arrive at the action

$$S = \int_{t_1}^{t_2} \int_V \left(\frac{D}{2} u_i(\boldsymbol{x},t) u_i(\boldsymbol{x},t) + p\,(1 - D) \right) d^3x\, dt, \quad (3.25)$$

where we have divided through by ρ_o.

To incorporate turbulence the velocity is then expressed as the sum of a mean component and a random fluctuation, (here ω is a random variable)

$$u_i(\boldsymbol{x},t;\omega) = \overline{u}_i(\boldsymbol{x},t) + u_i'(\boldsymbol{x},t;\omega), \quad (3.26)$$

where the averaging operator $\langle \cdot \rangle$ and $\overline{\boldsymbol{u}}$ are defined as [47]

$$\overline{\boldsymbol{u}}(\boldsymbol{x},t) = \langle \boldsymbol{u}(\boldsymbol{x},t;\omega) \rangle = \lim_{T\to\infty} \frac{1}{T} \int_0^T \boldsymbol{u}(\boldsymbol{x},t;\omega)\, d\omega. \quad (3.27)$$

The manner in which the velocity fluctuation is defined is a significant source of debate in the α modeling community. Here we will start by reviewing the method given in Holm [47]. In this method the expression for the velocity fluctuation is determined by equating Eulerian and Lagrangian velocities at a point $\boldsymbol{x}+\boldsymbol{\xi}$ where $\boldsymbol{\xi}$ represents a random particle displacement from its mean trajectory,

$$u_i(\boldsymbol{x}+\boldsymbol{\xi};\omega) = \frac{D(x_i+\xi_i(\boldsymbol{x},t;\omega))}{Dt}. \tag{3.28}$$

Note that on the LHS the dependence on the random variable ω is contained in the velocity field, while on the RHS it is contained in the particle displacement field. To first order in $\boldsymbol{\xi}$ equation (3.28) can be written

$$u_i(\boldsymbol{x},t;\omega) + \xi_j(\boldsymbol{x},t;\omega)\frac{\partial u_i(\boldsymbol{x},t;\omega)}{\partial x_j} = \frac{D(x_i+\xi_i(\boldsymbol{x},t;\omega))}{Dt}. \tag{3.29}$$

Substituting in the velocity from (3.26)

$$\overline{u}_i(\boldsymbol{x},t) + \xi_j(\boldsymbol{x},t;\omega)\frac{\partial \overline{u}_i}{\partial x_j} + u_i'(\boldsymbol{x},t;\omega) + \xi_j(\boldsymbol{x},t;\omega)\frac{\partial u_i'}{\partial x_j} = \frac{Dx_i}{Dt} + \frac{D\xi_i(\boldsymbol{x},t;\omega)}{Dt}. \tag{3.30}$$

It is then assumed that the random displacement $\boldsymbol{\xi}$ is small and that the velocity fluctuation is of the same order of magnitude as this displacement so that we have

$$\underbrace{\overline{u}_i(\boldsymbol{x})}_{O(1)} + \underbrace{\xi_j\frac{\partial \overline{u}_i}{\partial x_j}}_{O(\xi)} + \underbrace{u_i'(\boldsymbol{x})}_{O(\xi)} + \underbrace{\xi_j\frac{\partial u_i'}{\partial x_j}}_{O(\xi^2)} = \underbrace{\frac{Dx_i}{Dt}}_{O(1)} + \underbrace{\frac{D\xi_i}{Dt}}_{O(\xi)}. \tag{3.31}$$

Equating terms of $O(\xi)$ gives:

$$\xi_j(\boldsymbol{x},t;\omega)\frac{\partial \overline{u}_i}{\partial x_j} + u_i'(\boldsymbol{x},t;\omega) = \frac{D\xi_i(x,t;\omega)}{Dt} \tag{3.32}$$

Now, recall that the RHS of this equation is the velocity due to changes in the particle position (material) while the LHS is the velocity at a fixed point (Eulerian). For the Eulerian-averaged equations Holm [47] then ascribes all of the turbulent fluctuations to those of the Eulerian velocity, which means the RHS of (3.32) is zero, leading to the two expressions

$$u_i' = -\xi_j\frac{\partial \overline{u}_i}{\partial x_j}, \tag{3.33a}$$

$$\frac{D\xi_i}{Dt} = 0. \tag{3.33b}$$

The first equation is the expression for the velocity fluctuation, which we will use in the kinetic energy term of the action principle. The second equation is interpreted in the literature as Taylor's hypothesis applied to the displacement field. From this equation we can obtain

$$\frac{D\langle \xi_k \xi_m \rangle}{Dt} = 0, \tag{3.34}$$

which states that each component of the particle displacement covariance advects like a scalar. A different equation for the displacement covariance is obtained when you apply the averaging along flow trajectories instead of at a fixed position. In this case, Holm's Lagrangian-averaged equations result in a displacement covariance that is Lie-advected

$$\frac{D\boldsymbol{\xi}}{Dt} - \boldsymbol{\xi} \cdot \nabla \overline{\boldsymbol{u}} = 0 \tag{3.35}$$

which follows from (3.32) when you set $\boldsymbol{u}' = 0$, or when you ascribe all of the fluctuation to the material coordinates. The same expression is obtained in Bhat [3] although in this case they explicitly choose the displacement covariance to be Lie-advected because it can be shown that this means the displacement field will remain divergence-free as it is advected along a trajectory.

The expression for the velocity fluctuation (3.33b) can be easily interpreted in the engineering sense if we think of $\boldsymbol{\xi}$ as a mixing length. For example, the velocity at a point $\boldsymbol{x} + \boldsymbol{\xi}$ can be written (to first order)

$$u_i(\boldsymbol{x} + \boldsymbol{\xi}) = u_i(\boldsymbol{x}) + \xi_j \frac{\partial u_i}{\partial x_j}. \tag{3.36}$$

Defining the velocity fluctuation as the difference between our smoothed velocity at two points, $\tilde{\boldsymbol{u}}(\boldsymbol{x}+\boldsymbol{\xi})$ and $\tilde{\boldsymbol{u}}(\boldsymbol{x})$ and choosing the sign such that if a parcel of low speed fluid at $\boldsymbol{x}$ is brought into a region of high speed fluid it at $\boldsymbol{x} + \boldsymbol{\xi}$ will be a negative fluctuation gives

$$u_i' = -\xi_j \frac{\partial \overline{u}_i}{\partial x_j}. \tag{3.37}$$

At the risk of belaboring this point, an alternative interpretation of this picture can be found by looking at $\boldsymbol{\xi}$ as the error between true and modeled trajectories. Given that

$$\frac{D\boldsymbol{x}}{Dt} = u \tag{3.38}$$

a simple first order discretization of the true trajectory $\boldsymbol{x}_t$ and the modeled trajectory $\boldsymbol{x}_m$ would be

$$\begin{aligned} \boldsymbol{x}_t^n &= \boldsymbol{x}_t^{n-1} + \boldsymbol{u}_t^{n-1}\left(\boldsymbol{x}_t^{n-1}\right)\Delta t, \\ \boldsymbol{x}_m^n &= \boldsymbol{x}_m^{n-1} + \boldsymbol{u}_m^{n-1}\left(\boldsymbol{x}_m^{n-1}\right)\Delta t, \end{aligned} \tag{3.39}$$

where the superscript n indicated the time level. Defining the error as the difference between the true and modeled trajectory we find [6]

$$\boldsymbol{\epsilon}^n = \boldsymbol{\epsilon}^{n-1} + \left(\boldsymbol{u}_t^{n-1}(\boldsymbol{x}_t^{n-1}) - \boldsymbol{u}_m^{n-1}(\boldsymbol{x}_m^{n-1})\right)\Delta t. \tag{3.40}$$

We can relate the true velocity to that at the modeled particle location using the definition of the error

$$\begin{aligned} \boldsymbol{u}_t^{n-1}(\boldsymbol{x}_t^{n-1}) &= \boldsymbol{u}_t^{n-1}(\boldsymbol{x}_m^{n-1} + \boldsymbol{\epsilon}^{n-1}) \\ &\sim \boldsymbol{u}_t^{n-1}(x_m^{n-1}) + \boldsymbol{\epsilon}^{n-1}\cdot\nabla\boldsymbol{u}_t^{n-1} \end{aligned} \tag{3.41}$$

then split the true velocity into a large and small scale component, and assume the large component is equal to the modeled field to obtain

$$\boldsymbol{\epsilon}^n = \boldsymbol{\epsilon}^{n-1} + \left(\boldsymbol{u}_s^{n-1}(\boldsymbol{x}_m^{n-1}) + \boldsymbol{\epsilon}^{n-1}\cdot\nabla\boldsymbol{u}_l^{n-1}\right)\Delta t \tag{3.42}$$

which is a discrete form of the equation for the fluctuation equation (3.32)

$$\frac{D\boldsymbol{\xi}}{Dt} = \boldsymbol{u}' + \boldsymbol{\xi}\cdot\nabla.\tilde{\boldsymbol{u}} \tag{3.43}$$

Looking at things from this perspective does not give us any new tools, but is an interpretation some may find more concrete. If we look at $\boldsymbol{\xi}$ as a background error field, when we set $D\boldsymbol{\xi}/Dt = 0$ this means the error is frozen along a particle trajectory. When we neglect the mean of $\boldsymbol{\xi}$, ie. $\langle\boldsymbol{\xi}\rangle = 0$ we are assuming this error has zero mean (there is no bias).

Substituting the velocity fluctuation into the Lagrangian in (3.25) and using $\langle\boldsymbol{\xi}\rangle = 0$ yields the averaged Lagrangian,

$$\langle L\rangle = \int_V \left(\frac{D}{2}\left(\overline{u}_i\overline{u}_i + \langle\xi_k\xi_l\rangle\frac{\partial\overline{u}_i}{\partial x_k}\frac{\partial\overline{u}_i}{\partial x_l}\right) + p(1-D)\right)d^3x. \tag{3.44}$$

Here we have followed the notation used in Holm [47] where the averaged velocity is $\overline{\boldsymbol{u}}$, but where we keep the brackets for the averaged displacement covariance $\langle\xi_k\xi_l\rangle$.

The action principle is

$$S = \int_{t_1}^{t_2} \langle L \rangle \, dt. \tag{3.45}$$

To apply Hamilton's principle, start by considering variations with respect to $\overline{u}_i$, D and $\langle \xi_k \xi_l \rangle$. The first variation of the action is

$$\delta S = \int_{t_1}^{t_2} \int_V \left(\frac{\partial \langle l \rangle}{\partial \overline{u}_i} \delta \overline{u}_i + \frac{\partial \langle l \rangle}{\partial D} \delta D + \frac{\partial \langle l \rangle}{\partial \langle \xi_k \xi_l \rangle} \delta \langle \xi_k \xi_l \rangle \right) d^3x \, dt, \tag{3.46}$$

where (l) is the Lagrangian density (Lagrangian/unit volume). The partial derivatives with respect to the volume element and particle displacement are

$$\frac{\partial \langle l \rangle}{\partial D} = \frac{\overline{u}_i \overline{u}_i}{2} + \frac{\langle \xi_k \xi_l \rangle}{2} \frac{\partial \overline{u}_i}{\partial x_k} \frac{\partial \overline{u}_i}{\partial x_l} - p, \tag{3.47}$$

$$\frac{\partial \langle l \rangle}{\partial \langle \xi_k \xi_l \rangle} = \frac{D}{2} \frac{\partial \overline{u}_i}{\partial x_k} \frac{\partial \overline{u}_i}{\partial x_l}. \tag{3.48}$$

For the velocity

$$\int_V \frac{\partial \langle l \rangle}{\partial \overline{u}_i} \delta \overline{u}_i \, dV = \int_V D \overline{u}_i \delta \, \overline{u}_i + D \frac{\langle \xi_k \xi_l \rangle}{2} \left(\frac{\partial}{\partial x_k} \left(\delta \overline{u}_i \right) \frac{\partial \overline{u}_i}{\partial x_l} + \frac{\partial \overline{u}_i}{\partial x_k} \frac{\partial}{\partial x_l} \left(\delta \overline{u}_i \right) \right) d^3x \tag{3.49}$$

$$= \int_V D \overline{u}_i \delta \overline{u}_i + D \langle \xi_k \xi_l \rangle \left(\frac{\partial \overline{u}_i}{\partial x_l} \frac{\partial}{\partial x_k} \left(\delta \overline{u}_i \right) \right) d^3x. \tag{3.50}$$

Integrating by parts

$$\int_V \frac{\partial \langle l \rangle}{\partial \overline{u}_i} \delta \overline{u}_i \, d^3x = \int_V D \overline{u}_i \delta \overline{u}_i + D \langle \xi_k \xi_l \rangle \left(\frac{\partial \overline{u}_i}{\partial x_l} \frac{\partial}{\partial x_k} \left(\delta \overline{u}_i \right) \right) d^3x, \tag{3.51}$$

$$= \int_A D \langle \xi_k \xi_l \rangle \frac{\partial \overline{u}_i}{\partial x_l} \delta \overline{u}_i \, dA_k + \int_V \left(D \overline{u}_i - \frac{\partial}{\partial x_k} \left(D \langle \xi_k \xi_l \rangle \frac{\partial \overline{u}_i}{\partial x_l} \right) \right) \delta \overline{u}_i \, d^3x. \tag{3.52}$$

If we apply the boundary condition that the normal component of $\langle \xi_k \xi_l \rangle$ is zero, the surface integral in (3.52) is zero and we have

$$\int_V \frac{\partial \langle l \rangle}{\partial \overline{u}_i} \delta \overline{u}_i \, d^3x = \int_V D \overline{u}_i - \frac{\partial}{\partial x_k} \left(D \langle \xi_k \xi_l \rangle \frac{\partial \overline{u}_i}{\partial x_l} \right) \delta \overline{u}_i \, d^3x. \tag{3.53}$$

The reason for showing this is that later we will use the boundary condition $\langle \xi_k \xi_l \rangle n_k = 0$ when we solve this equation numerically.

In our varied action (3.46) we have variations of the Eulerian coordinates $\delta\overline{u}_i, \delta D$ and $\delta\langle\xi_k\xi_l\rangle$. To take the limit as the varied trajectory approaches the true one we need to relate the variations, $\delta\overline{u}_i$, δD and $\delta\langle\xi_k\xi_l\rangle$ to variations in the particle trajectory. The particle trajectory variation is defined as [3]

$$\delta\boldsymbol{\eta} := \left.\frac{d}{d\epsilon}\right|_{\epsilon=0} \underbrace{(\boldsymbol{\eta} + \epsilon\,\delta\boldsymbol{\eta})}_{\boldsymbol{\eta}^\epsilon} \tag{3.54}$$

From (3.19) the varied velocity is

$$\boldsymbol{u}^\epsilon = \dot{\boldsymbol{\eta}}^\epsilon \circ (\boldsymbol{\eta}^\epsilon)^{-1}. \tag{3.55}$$

Denoting the velocity variation as [3]

$$\delta\boldsymbol{u} := \left.\frac{d}{d\epsilon}\right|_{\epsilon=0} \boldsymbol{u}^\epsilon \tag{3.56}$$

and carrying out the chain rule (see Appendix A) gives the following expression for the velocity variation

$$\delta\boldsymbol{u} = \frac{\partial \boldsymbol{w}}{\partial t} + \boldsymbol{u}\cdot\nabla\boldsymbol{w} - \boldsymbol{w}\cdot\nabla\boldsymbol{u}, \tag{3.57}$$

where $\boldsymbol{w}$ is the trajectory variation expressed at a field point, $\boldsymbol{w} := \delta\boldsymbol{\eta}\circ\boldsymbol{\eta}^{-1}$. The corresponding velocity variation for the averaged velocity is

$$\delta\overline{\boldsymbol{u}} = \frac{\partial \boldsymbol{w}}{\partial t} + \overline{\boldsymbol{u}}\cdot\nabla\boldsymbol{w} - \boldsymbol{w}\cdot\nabla\overline{\boldsymbol{u}}. \tag{3.58}$$

The first two terms in (3.58) are the substantial derivative of $\boldsymbol{w}$. In Appendix A it is shown that the substantial derivative can be expressed as $\delta\dot{\boldsymbol{\eta}}\circ\boldsymbol{\eta}^{-1}$, and since this is evaluated for $\boldsymbol{\eta}^{-1}$ (the unvaried inverse trajectory) this is the fixed label part. The third term is the change due to the label variation. This is not obvious from looking at the term itself, since the label dependence is hidden, as it should be, but can be seen from the calculations in Appendix A. In the Appendix A it is also shown that the variations of the volume element and displacement covariance are

$$\delta D = -\nabla\cdot(D\,\boldsymbol{w}), \tag{3.59}$$

and

$$\delta\langle\xi_k\xi_l\rangle = -\boldsymbol{w}\cdot\nabla\langle\xi_k\xi_l\rangle. \tag{3.60}$$

Substituting these variations (3.58),(3.59),(3.60) into (3.46)

$$\delta S = \left(\int_{t_1}^{t_2} \int_V \frac{\partial \langle l \rangle}{\partial u_i} \left(\frac{\partial w_i}{\partial t} + \overline{u}_j \frac{\partial w_i}{\partial x_j} - w_j \frac{\partial \overline{u}_i}{\partial x_j} \right) - \frac{\partial}{\partial x_i}(D w_i) \frac{\partial \langle l \rangle}{\partial D} - \frac{\partial \langle l \rangle}{\partial \langle \xi_k \xi_l \rangle} \frac{\partial \langle \xi_k \xi_l \rangle}{\partial x_i} w_i \right) d^3x \, dt. \tag{3.61}$$

Integrating by parts and changing sign

$$\begin{aligned} \delta S = & \int_{t_1}^{t_2} \int_V \left[\left(\frac{\partial}{\partial t} + \overline{u}_j \frac{\partial}{\partial x_j} \right) \frac{\partial \langle l \rangle}{\partial \overline{u}_i} + \frac{\partial \langle l \rangle}{\partial \overline{u}_j} \frac{\partial \overline{u}_j}{\partial x_i} - D \frac{\partial}{\partial x_i} \frac{\partial \langle l \rangle}{\partial D} + \frac{\partial \langle l \rangle}{\partial \langle \xi_k \xi_l \rangle} \frac{\partial \langle \xi_k \xi_l \rangle}{\partial x_i} \right] w_i d^3x \, dt \\ & \underbrace{- \int_V \frac{\partial \langle l \rangle}{\partial \overline{u}_i} w_i \, dV \Big|_{t_1}^{t_2}}_{I} \underbrace{- \int_{t_1}^{t_2} \int_A \frac{\partial \langle l \rangle}{\partial \overline{u}_i} \overline{u}_j w_i \, dA_j}_{II} + \underbrace{\int_{t_1}^{t_2} \int_A \frac{\partial \langle l \rangle}{\partial D} w_i \, dA_i}_{III} \end{aligned} \tag{3.62}$$

The last three terms are zero for the following reasons:
(I) variations are zero at beginning and end times (same as for Newton's law),
(II) velocity is either periodic or has zero normal component for a solid surface,
(III) trajectory variation ($\boldsymbol{w}$) is tangent to the bounding surface [96].

Setting the first variation to zero and imposing the constraint $D = 1$ yields the Euler-Poincaré equation

$$0 = \left(\frac{\partial}{\partial t} + \overline{u}_j \frac{\partial}{\partial x_j} \right) \frac{\delta \langle L \rangle}{\delta \overline{u}_i} + \frac{\delta \langle L \rangle}{\delta \overline{u}_j} \frac{\partial \overline{u}_j}{\partial x_i} - D \frac{\partial}{\partial x_i} \frac{\delta \langle L \rangle}{\delta D} + \frac{\delta \langle L \rangle}{\delta \langle \xi_k \xi_l \rangle} \frac{\partial \langle \xi_k \xi_l \rangle}{\partial x_i}. \tag{3.63}$$

The Euler-Poincaré equation (3.63) can be written in the more familiar form (to see this substitute the partial derivatives (3.53), (3.47), (3.48) into (3.61) and take the limit as d^3x,w_i, and dt go to zero)

$$\frac{\partial v_i}{\partial t} + \overline{u}_j \frac{\partial v_i}{\partial x_j} + v_j \frac{\partial \overline{u}_j}{\partial x_i} = - \frac{\partial p^\alpha}{\partial x_i} - \frac{1}{2} \frac{\partial \langle \xi_k \xi_l \rangle}{\partial x_i} \frac{\partial \overline{u}_m}{\partial x_k} \frac{\partial \overline{u}_m}{\partial x_l} \tag{3.64}$$

where the following variables have been defined (using the constraint $D = 1$)

$$v_i = \frac{\delta \langle L \rangle}{\delta \overline{u}_i} = \overline{u}_i - \frac{\partial}{\partial x_k} \left(\langle \xi_k \xi_l \rangle \frac{\partial \overline{u}_i}{\partial x_l} \right) \tag{3.65}$$

$$p^\alpha = p - \frac{1}{2} \overline{u}_m \overline{u}_m - \langle \xi_k \xi_l \rangle \frac{\partial \overline{u}_i}{\partial x_k} \frac{\partial \overline{u}_i}{\partial x_l}. \tag{3.66}$$

If we impose isotropy $\langle \xi_k \xi_l \rangle = \alpha^2 \delta_{kl}$ and assume α^2 is constant, we arrive at the

inviscid form of the NS-α equations found in the literature [51, 32]

$$\frac{\partial v_i}{\partial t} + \overline{u}_j \frac{\partial v_i}{\partial x_j} + v_j \frac{\partial \overline{u}_j}{\partial x_i} = -\frac{\partial p^\alpha}{\partial x_i}, \tag{3.67}$$

with

$$v_i = \overline{u}_i - \alpha^2 \frac{\partial^2 \overline{u}_i}{\partial x_k^2}. \tag{3.68}$$

There are a few things to note here. The first is that the averaged velocity $\overline{\boldsymbol{u}}$ becomes the smoothed velocity when we consider that $\boldsymbol{v}$ and $\overline{\boldsymbol{u}}$ are related through a Helmholtz operator. This is what is meant in the literature by 'temporal averaging in the variational principle implies a spatial smoothing in the momentum equation' [47], although one could anticipate this from the expression for the velocity fluctuation. Another aspect to note is that if we had not considered the functional dependence on $\langle \xi_k \xi_l \rangle$ we would not have obtained the $\partial \langle \xi_i \xi_l \rangle / \partial x_i$ term in the final momentum equation (3.64). This term is necessary to conserve momentum, which you can see either by considering Noether's theorem for the action principle, or by removing this term and trying to write the momentum equation in conservative form. Some studies of the NS-α equations have not included this term in their analyses yielding incorrect results, as pointed out in the literature [112, 52]. Finally, by following through with this method we are able to understand how the boundary conditions for the NS-α equations arise.

The reader may have noticed that we have at times applied incompressibility to the averaged (or smoothed) velocity $\nabla \cdot \overline{\boldsymbol{u}} = 0$. This does not come from the variational principle itself but from the equation for the volume element [47]

$$\frac{\partial D}{\partial t} + \nabla \cdot (D \overline{\boldsymbol{u}}) = 0. \tag{3.69}$$

Imposing the constraint $D = 1$ then gives $\nabla \cdot \overline{\boldsymbol{u}} = 0$, or $\nabla \cdot \tilde{\boldsymbol{u}} = 0$ when we recognize $\overline{\boldsymbol{u}}$ is the smoothed velocity according to the Helmholtz operation.

Note that other methods can also be used to derive the equations from Hamilton's principle. For alternative examples on the use of variational principles in fluid mechanics see Salmon [122] and Finlayson [24]. When using their methods the advection equation (3.34) needs to be added as a constraint equation to obtain the last term on the RHS of Equation (3.64) that contains the gradient of the particle displacement covariance.

Chapter 4

The Subgrid Model

4.1 Model Formulation

For the subgrid model the anisotropic Eulerian-averaged equations from Holm [47] (equation 280) are used as a starting point. These equations were derived in Chapter 3 (see equation (3.64)) and are written as

$$\frac{\partial \tilde{u}_i}{\partial x_i} = 0, \tag{4.1}$$

$$\frac{\partial u_i}{\partial t} + \tilde{u}_j \frac{\partial u_i}{\partial x_j} + u_m \frac{\partial \tilde{u}_m}{\partial x_i} = -\frac{\partial p^\alpha}{\partial x_i} - \frac{1}{2}\frac{\partial \langle \xi_k \xi_l \rangle}{\partial x_i}\left(\frac{\partial \tilde{u}_m}{\partial x_k}\frac{\partial \tilde{u}_m}{\partial x_l}\right), \tag{4.2}$$

with the modified pressure,

$$p^\alpha = p - \frac{1}{2}(\tilde{u}_m \tilde{u}_m) - \frac{1}{2}\langle \xi_k \xi_l \rangle \left(\frac{\partial \tilde{u}_m}{\partial x_k}\frac{\partial \tilde{u}_m}{\partial x_l}\right) \tag{4.3}$$

and the following relationship between the smoothed and unsmoothed velocity,

$$u_i = \left(1 - \frac{\partial}{\partial x_k}\left(\langle \xi_k \xi_l \rangle \frac{\partial}{\partial x_l}\right)\right)\tilde{u}_i. \tag{4.4}$$

Using the vector identity

$$u_m \frac{\partial \tilde{u}_m}{\partial x_i} + \frac{\partial p^\alpha}{\partial x_i} + \frac{1}{2}\frac{\partial \langle \xi_k \xi_l \rangle}{\partial x_i}\left(\frac{\partial \tilde{u}_m}{\partial x_k}\frac{\partial \tilde{u}_m}{\partial x_l}\right) = \frac{\partial p}{\partial x_i} - \frac{\partial}{\partial x_l}\left(\langle \xi_k \xi_l \rangle \frac{\partial \tilde{u}_m}{\partial x_i}\frac{\partial \tilde{u}_m}{\partial x_k}\right), \tag{4.5}$$

the momentum equation can also be written in momentum-conservation form

$$\frac{\partial u_i}{\partial t} + \tilde{u}_j \frac{\partial u_i}{\partial x_j} = -\frac{\partial p}{\partial x_i} + \frac{\partial}{\partial x_l}\left(\langle \xi_k \xi_l \rangle \frac{\partial \tilde{u}_m}{\partial x_i}\frac{\partial \tilde{u}_m}{\partial x_k}\right). \tag{4.6}$$

The form of equation used as a starting point to develop a subgrid model depends on the goal. Here, the objective is to derive a subgrid model for the primitive variables $[\tilde{u}_i, \tilde{p}]$ with the subgrid term written as the divergence of a tensor. The motivation behind this is so that the subgrid model can be easily implemented in a finite-volume formulation in a manner similar to most subgrid models. For this purpose, we will start with the equation in momentum conservation form (4.6). However, if vorticity was to be used as the dependent variable, it is easier to start with (4.2) and rewrite it in rotational form before taking the curl to obtain a vorticity equation.

The derivation of the governing equations for the NS-α model is done using Hamilton's principle and does not incorporate non-conservative forces. This is why the above equation does not have a viscous term, which means one must be added after the derivation. Holm [47] suggests the following viscous term with a modified Laplacian

$$\underbrace{\nu\left(\frac{\partial}{\partial x_k}\left(\langle \xi_k \xi_l \rangle \frac{\partial}{\partial x_l}\right)\right)}_{\tilde{\Delta}} u_i. \tag{4.7}$$

The reason for chosing this form of viscous term is that the contribution from this term to the conserved energy, $e_\alpha = \int_V u_i \tilde{u}_i \, dV$, is always negative [47], and thus the viscous term always provides a sink of energy. However, this also means the viscous term is dependent on the model parameter. In particular if $\langle \xi_k \xi_l \rangle \to 0$, as is required near a no-slip boundary, the viscous forces will also be zero.

In practice, most studies [8, 10, 32] use the standard Laplacian operator acting on the momentum velocity, u_i. This is the approach used here. When we develop the smoothed momentum equation we will be looking at it from the point of view of an LES model, following a similar methodology as that used in other applications. Our equation will have $\tilde{u}_i$ as a dependent variable and will contribute viscous sink to the resolved flow energy equation of the form $-\nu \partial_k \tilde{u}_i \partial_k \tilde{u}_i$ as it is in other LES studies.

To develop an equation with the smoothed velocity as the dependent variable we

follow the approach taken in Holm and Nadiga [51] and use the commutator between the substantial derivative and the smoothing operator, where the substantial derivative is defined using a smoothed advecting velocity, $D/Dt = \partial_t + \tilde{u}_j\partial_j$ [47]. For our subgrid model we would like to have the substantial derivative acting on the smoothed velocity. This is done by rewriting the advective terms in (4.6) as

$$\frac{\partial u_i}{\partial t} + \tilde{u}_j\frac{\partial u_i}{\partial x_j} = [D/Dt, H]\tilde{u}_i + H\left(\frac{\partial \tilde{u}_i}{\partial t} + \tilde{u}_j\frac{\partial \tilde{u}_i}{\partial x_j}\right). \tag{4.8}$$

Here $[D/Dt, H]$ is the commutator between the substantial derivative and the Helmholtz operator, H and is defined as $[D/Dt, H]\tilde{u}_i = D/Dt(H(\tilde{u}_i)) - H(D/Dt(\tilde{u}_i))$. Recall that the Helmholtz operator relates the smoothed and unsmoothed velocities according to

$$u_i = \underbrace{\left(1 - \frac{\partial}{\partial_{kk}}\left(\langle\xi_k\xi_l\rangle\frac{\partial}{\partial x_l}\right)\right)}_{H,\text{ Helmholtz operator}}\tilde{u}_i. \tag{4.9}$$

Using the commutator and adding a viscous term, the momentum equation (4.6) can be written

$$\frac{\partial \tilde{u}_i}{\partial t} + \tilde{u}_j\frac{\partial \tilde{u}_i}{\partial x_j} = H^{-1}\left(\frac{\partial p}{\partial x_i} + \nu\frac{\partial^2 u_i}{\partial x_k^2} + \frac{\partial}{\partial x_l}\left(\langle\xi_k\xi_l\rangle\frac{\partial \tilde{u}_m}{\partial x_i}\frac{\partial \tilde{u}_m}{\partial x_k}\right) - [D, Dt, H]\tilde{u}_i\right). \tag{4.10}$$

Expanding and simplifying the commutator we found it could be expressed as,

$$\left[\frac{\partial}{\partial t} + \tilde{u}_j\frac{\partial}{\partial x_j}, \left(1 - \frac{\partial}{\partial x_k}\left(\langle\xi_k\xi_l\rangle\frac{\partial}{\partial x_l}\right)\right)\right]\tilde{u}_i = \frac{\partial}{\partial x_j}\left(\langle\xi_k\xi_l\rangle\frac{\partial \tilde{u}_i}{\partial x_k}\frac{\partial \tilde{u}_j}{\partial x_l} + \langle\xi_j\xi_l\rangle\frac{\partial \tilde{u}_k}{\partial x_l}\frac{\partial \tilde{u}_i}{\partial x_k}\right) - \frac{\partial}{\partial x_k}\left(\left(\frac{\partial\langle\xi_k\xi_l\rangle}{\partial t} + \tilde{u}_j\frac{\partial\langle\xi_k\xi_l\rangle}{\partial x_j}\right)\frac{\partial \tilde{u}_i}{\partial x_l}\right). \tag{4.11}$$

Note that for constant, isotropic fluctuations ($\langle\xi_k\xi_l\rangle = \alpha^2\delta_{kl}$), the first two terms on the RHS of (4.11) are the Leray model found in the literature [32]. Thus, we can look at these two terms here as an anisotropic Leray model, although this is not strictly true since we applied $\partial_j\tilde{u}_j = 0$ in deriving the commutator, while the continutity equation for the Leray model is $\partial_j u_j = 0$ [32].

For the NS-α model the last term on the RHS of (4.11) can *in theory* be neglected, because for the Eulerian-averaged equations each component of the particle dis-

placement is transported by the mean flow like a scalar (Chapter 3, equation (3.34)),

$$\frac{D\langle \xi_k \xi_l \rangle}{Dt} = 0. \tag{4.12}$$

In the context of LES modelling, this term represents the explicit change in filter width. It is customary in the LES community to neglect these types of terms in preliminary evaluations of a subgrid model, a simplification discussed in detail in the literature (see [137] and references therein). As is the case with all subgrid terms, these terms will lead to energy transfer between resolved and subgrid modes, and neglecting these terms therefore changes the subgrid transfer dynamics. For the equation above this is clearly seen by considering the isotropic case, where the last term in (4.11) can be written,

$$\frac{\partial}{\partial x_k}\left(\left(\frac{D\alpha^2}{Dt}\right)\frac{\partial \tilde{u}_i}{\partial x_k}\right). \tag{4.13}$$

The substantial derivative of α^2 can be seen to play the role of a variable eddy viscosity. It will dissipate energy when α^2 increases along a flow path and backscatter energy when it decreases. It is interesting that this is exactly the method suggested in the literature [137] to model the commutation error in LES. The idea being that when a flow scale is advected into a region where the grid is coarser, it will go from being resolved to modelled, leading to dissipation, and vice versa when the grid is refined.

Whether or not these terms can be neglected depends on their magnitude to the other subgrid terms. If we consider the one-dimensional case and only spatial variations in α^2 this term can be neglected if

$$\begin{aligned} \tilde{u}\frac{\partial \alpha^2}{\partial x} &\ll \alpha^2 \frac{\partial \tilde{u}}{\partial x}, \\ \frac{1}{\alpha^2}\frac{\partial \alpha^2}{\partial x} &\ll \frac{1}{\tilde{u}}\frac{\partial \tilde{u}}{\partial x}, \end{aligned} \tag{4.14}$$

which means that the filter field must be smoother than the flow field. We found that while this is not always true for the test cases considered here, including the $D\alpha^2/Dt$ term does not lead to improved results[1]. This term tends to be large in regions where the resolved flow advection terms are also large. We found it does

[1]This may be because in the present work α^2 is a function of the spatially varying grid size. Including only the advective part of the substantial derivative of α^2 means the equations are no longer Galilean invariant.

not have as significant of an impact as the third term on the RHS of equation (4.10) (which comes from the tilting term in the momentum equation) because the latter tends to be large when the resolved flow advection terms are small, so there is little to counter it other than the pressure gradient.

With equation (4.12) the momentum equation (4.10) can be written (here we are assuming the filter commutes with differentiation for the pressure gradient and viscous term [2]),

$$\frac{\partial \tilde{u}_i}{\partial t} + \tilde{u}_j \frac{\partial \tilde{u}_i}{\partial x_j} = -\frac{\partial \tilde{p}}{\partial x_i} + \nu \frac{\partial^2 \tilde{u}_i}{\partial x_k^2} - H^{-1}\left(\frac{\partial m_{ij}}{\partial x_j}\right) \tag{4.15}$$

with the subgrid stress

$$m_{ij}^{FULL} = \underbrace{\langle \xi_k \xi_l \rangle \frac{\partial \tilde{u}_i}{\partial x_k} \frac{\partial \tilde{u}_j}{\partial x_l}}_{A_{ij}} + \underbrace{\langle \xi_j \xi_l \rangle \frac{\partial \tilde{u}_k}{\partial x_l} \frac{\partial \tilde{u}_i}{\partial x_k}}_{B_{ij}} - \underbrace{\langle \xi_k \xi_j \rangle \frac{\partial \tilde{u}_m}{\partial x_i} \frac{\partial \tilde{u}_m}{\partial x_k}}_{C_{ij}}. \tag{4.16}$$

The A_{ij} term is an anisotropic version of the gradient model, $A_{ij}+B_{ij}$ an anisotropic Leray model (with $\partial_j \tilde{u}_j = 0$ as we noted earlier) and $A_{ij} + B_{ij} - C_{ij}$ the anisotropic NS-α model. The subgrid stress in (4.16) is composed of three terms, each of which is a second order tensor. In contrast, the subgrid model used by Geurts and Holm [32], which was based on the isotropic, constant α^2, equations, has three terms, each of which is a third order tensor. Since the isotropic equations are considered to be as expensive to solve as the Dynamic Smagorinsky model [32], it is desirable at this stage to simplify the expression for the subgrid stress to reduce the computational effort. We then proceed by retaining only the diagonal components of $\langle \xi_k \xi_l \rangle$. This gives us a formulation similar to that derived using second order reconstruction methods [149, 145] where the lack of diagonal terms arises when the three-dimensional filter is applied as the composition of three one-dimensional filters, $L = l_1 \circ l_2 \circ l_3$, where l_j $(j = 1, 2, 3)$ represents a one dimensional filter in the x_j-direction [120].

Retaining only the diagonal components of $\langle \xi_k \xi_l \rangle$, the subgrid stress (4.16) becomes

$$m_{ij}^{ANISO} = \alpha_k^2 \delta_{kl} \frac{\partial \tilde{u}_i}{\partial x_k} \frac{\partial \tilde{u}_j}{\partial x_l} + \alpha_l^2 \delta_{jl} \frac{\partial \tilde{u}_k}{\partial x_l} \frac{\partial \tilde{u}_i}{\partial x_k} - \alpha_k^2 \delta_{kj} \frac{\partial \tilde{u}_m}{\partial x_i} \frac{\partial \tilde{u}_m}{\partial x_k} \tag{4.17}$$

[2] While commutation error has been recently discussed in the literature [137] for the advective terms, other terms in the filtered Navier-Stokes equation are still a subject of future work for the community.

where we have used $\alpha_k^2 = \langle \xi_k \xi_k \rangle$. For the isotropic case the expression for the subgrid stress reduces to the form given already in the literature [32],

$$m_{ij}^{ISO} = \left(\alpha^2 \frac{\partial \tilde{u}_i}{\partial x_k} \frac{\partial \tilde{u}_j}{\partial x_k} + \alpha^2 \frac{\partial \tilde{u}_k}{\partial x_j} \frac{\partial \tilde{u}_i}{\partial x_k} - \alpha^2 \frac{\partial \tilde{u}_k}{\partial x_i} \frac{\partial \tilde{u}_k}{\partial x_j} \right) \tag{4.18}$$

We now have a source term which can be incorporated into a standard primitive-variable finite volume code. This has been done by starting with the most general form of the Eulerian-averaged equation, where $\langle \xi_k \xi_l \rangle$ is a function of space and time and the fully anisotropic form is used. This is a useful exercise because the assumptions used to obtain the simplified form are clear.

4.2 Resolved flow energy equation

From the momentum equation

$$\frac{\partial \tilde{u}_i}{\partial t} + \tilde{u}_j \frac{\partial \tilde{u}_i}{\partial x_j} = -\frac{\partial \tilde{p}}{\partial x_i} + \nu \frac{\partial^2 \tilde{u}_i}{\partial x_k^2} - H^{-1} \left(\frac{\partial m_{ij}}{\partial x_j} \right) \tag{4.19}$$

we can obtain an equation for the resolved flow energy $\tilde{e} = \tilde{u}_i \tilde{u}_i / 2$. For the moment let us assume the filter width (here proportional to α_k or α) is constant which means the filtering and differentiation operators commute and we can write

$$H^{-1} \left(\frac{\partial m_{ij}}{\partial x_j} \right) = \frac{\partial \tilde{m}_{ij}}{\partial x_j}. \tag{4.20}$$

The equation for the resolved flow energy, $\tilde{e} = \tilde{u}_i \tilde{u}_i / 2$, then takes the form

$$\underbrace{\frac{\partial \tilde{e}}{\partial t}}_{I} + \underbrace{\frac{\partial}{\partial x_j} (\tilde{e} \tilde{u}_j)}_{II} = - \underbrace{\frac{\partial}{\partial x_i} (\tilde{u}_i \tilde{p})}_{III} + \underbrace{\nu \frac{\partial^2 \tilde{e}}{\partial x_k^2}}_{IV} - \underbrace{\nu \frac{\partial \tilde{u}_i}{\partial x_k} \frac{\partial \tilde{u}_i}{\partial x_k}}_{V} - \underbrace{\frac{\partial}{\partial x_j} (\tilde{u}_i \tilde{m}_{ij})}_{VI} + \underbrace{\tilde{m}_{ij} \frac{\partial \tilde{u}_i}{\partial x_j}}_{VII} \tag{4.21}$$

The physical meaning of the different terms is [126]
(I) and (II) total (local and convective) change in the resolved flow kinetic energy
(III) redistribution due to pressure/velocity interactions
(IV) redistribution due to viscous effects
(V) energy dissipation due to molecular viscosity
(VI) redistribution due to interactions between the resolved velocity and the subgrid stress
(VII) subgrid transfer term (T_{SGS}).

Assessment of a subgrid model generally focuses on the subgrid transfer term (T_{SGS}), which also appears with an opposite sign in the equation for the subgrid energy (c.f. Sagaut [120]). This term is often referred to in the literature as the subgrid dissipation, but we prefer to call it a transfer term because it can be both positive and negative. When it is negative we say it is a dissipative term (energy drain from the resolved to subgrid scales) while when it is positive we say it is backscattering energy (reverse transfer from subgrid to resolved scales). The emphasis on this term in the literature is due to the prevalent view that the primary role of a subgrid model is to accurately capture the energy transfer from large to small scales. This was the central design criteria for the early Smagorinsky model [127, 77], and more recently for the velocity estimation model by Park and Mahesh [103]. A significant difference between older and newer approaches is that in the past it was believed to be sufficient to model the net energy transfer from large to small scales using a dissipative term, while more recently the emphasis is on properly accommodating both forward transfer and backscatter.

However, the emphasis on the subgrid transfer term alone may at times be misleading. In particular the redistribution term involving the subgrid stress (term VI in equation 4.21) indicates the subgrid model interacts with and can modify the distribution of mean flow energy, which will in turn affect the subgrid dissipation indirectly. In the subgrid model of Park and Mahesh [103] the subgrid dissipation was constrained to match that of the dynamic Smagorinsky model, but their model outperformed the dynamic model for a plane channel flow. They found the subgrid redistribution term was over twice as big as the transfer term in the near wall region, and their results suggest the term plays an important role, thus affecting the overall statistics.

When the filter width is not constant we should leave the filter acting on the divergence term and we cannot split the energy transfer into a redistribution term and a source/sink term. In this case the energy transfer due to the subgrid model is

$$\tilde{u}_i H^{-1} \left(\frac{\partial m_{ij}}{\partial x_j} \right). \tag{4.22}$$

4.3 Physical Interpretation of the subgrid force

When written as a subgrid stress the effect of the m_{ij} term is not easily interpreted physically. This term provides a force to the momentum equation, and we will now rewrite it such that the form of this forcing function is a clarified. To keep things simple in this section we will assume $\langle \xi_k \xi_l \rangle = \alpha^2 \delta_{kl}$ and that α^2 is constant. We will also make use of the difference between the unsmoothed and smoothed velocity,

$$u_i^{ST} = -\alpha^2 \frac{\partial^2 \tilde{u}_i}{\partial x_k^2}. \tag{4.23}$$

In the LES literature this velocity would be called the subgrid fluctuation. In the NS-α literature it is referred to as the 'Stokes velocity' [47, 10], due to its relationship with the Stokes drift velocity [47], which is the first order difference between the averaged Lagrangian and Eulerian velocities [69]. For the NS-α model the velocity averaged at a fixed point was $\tilde{u}$, so we can consider this to be the Eulerian velocity. The velocity associated with the particles being advected (u) is the Lagrangian velocity. The difference between the two $u_i - \tilde{u}_i$ is equation (4.23) given above. For a more detailed discussion on this see Holm [47] Section 4.

Using the Stokes velocity, we found the commutator can be written in more intuitive way

$$[D/Dt, H]\, \tilde{u}_i = 2\, \partial_j A_{ij} - u_j^{ST} \frac{\partial \tilde{u}_i}{\partial x_j}. \tag{4.24}$$

This means that the first two terms of the subgrid tensor can be written as

$$\partial_j (A_{ij} + B_{ij}) = 2\, \partial_j A_{ij} - u_j^{ST} \frac{\partial \tilde{u}_i}{\partial x_j}. \tag{4.25}$$

We can now see that the cross derivative term in B_{ij}, which has the form $\tilde{u}_j \partial_j$, is related to the advection of the resolved velocity due to the Stokes drift. If we go back to the momentum equation (4.6) it can now be written

$$H\left(\frac{\partial \tilde{u}_i}{\partial t} + \tilde{u}_j \frac{\partial \tilde{u}_j}{\partial x_i}\right) = -\frac{\partial p^\alpha}{\partial x_i} - 2\frac{\partial A_{ij}}{\partial x_j} + u_j^{ST} \frac{\partial \tilde{u}_i}{\partial x_j} - u_k \frac{\partial \tilde{u}_k}{\partial x_i}. \tag{4.26}$$

Using the identity

$$u_j^{ST} \frac{\partial \tilde{u}_i}{\partial x_j} = -\boldsymbol{u}^{ST} \times \tilde{\boldsymbol{\omega}} + u_k^{ST} \frac{\partial \tilde{u}_k}{\partial x_i} \tag{4.27}$$

the momentum equation can be written

$$\frac{\partial \tilde{u}_i}{\partial t} + \tilde{u}_j \frac{\partial \tilde{u}_j}{\partial x_i} = -\frac{\partial \tilde{p}^*}{\partial x_i} - H^{-1}\left(2\frac{\partial A_{ij}}{\partial x_j} + \boldsymbol{u}^{ST} \times \tilde{\boldsymbol{\omega}}\right) \tag{4.28}$$

where p^* is a modified pressure. We can now see that the subgrid model is composed of two forcing terms. The first term, A_{ij}, is well known in the literature where it goes by many names, such as the Clark model [36], filtered gradient model [144] and Tensor-Diffusivity term [149]. Here we will refer to it as the gradient model, because the Clark model and Tensor-Diffusivity model both technically contain an additional Smagorinsky-like term [145, 149]. It is a generic subgrid closure which can be derived by expanding the subgrid stress τ_{ij} in a Taylor series expansion and retaining terms up to $O(\Delta^2)$, where Δ is the filter width. When the Helmholtz operator is approximated by a box filter, $\alpha_k^2 \approx \Delta_k^2/24$, where Δ_k is the width of a box filter in the $k-$direction, this term is identical to the model used commonly in the literature [149]

$$\begin{aligned} 2A_{ij} &= 2\alpha_k^2 \frac{\partial \tilde{u}_i}{\partial x_k}\frac{\partial \tilde{u}_j}{\partial x_k} \\ &= \frac{\Delta_k^2}{12}\frac{\partial \tilde{u}_i}{\partial x_k}\frac{\partial \tilde{u}_j}{\partial x_k}. \end{aligned} \tag{4.29}$$

This suggests an alternative (more approximate) way of deriving an equation for the smoothed velocity, which would be to start with the momentum equation, rewrite it with the Stokes vortex force on the RHS, apply a filter to the equations, and close the resulting τ_{ij} term with an explicitly filtered gradient model. For alternative forms of the governing equations for the NS-α model see Domaradzki and Holm [17].

The vortex force is what makes the NS-α model different from other approaches. To highlight how a vortex forcing term is fundamentally different than, for example, a Smagorinsky model, consider a simple two-dimensional mixing layer with $u = \tanh(y)$. The Smagorinsky model will add a diffusion term to the momentum equation with diffusivity,

$$\nu_T = (C_s\Delta)^2 |S_{ij}| \sim (C_s\Delta)^2 \operatorname{sech}^2 y. \tag{4.30}$$

The diffusivity will be highest at the middle of the mixing layer, and it is not surprising that such a model cannot be used for studies of mixing layer transition, where it damps out the small amplitude perturbations preventing transition [144].

On the other hand, due the presence of the mean shear $\partial\tilde{u}/\partial y$, the vortex force would make its most significant contribution to the vertical momentum equation, with a vertical forcing term

$$u^{ST}\tilde{\omega}_z \sim \alpha^2 \frac{\partial^2 \tilde{u}}{\partial y^2}\tilde{\omega}_z. \tag{4.31}$$

At the very early stages of transition this term would provide equal and opposite vertical forcing to the mixing layer, and therefore leaves the mixing layer unchanged. However, as soon as undulations in the layer appear the flow is no longer symmetric and such a terms would serve to 'push' the mixing layer back and forth. Unlike the Smagorinsky model, the NS-α model was found to correctly capture the growth of a transitional mixing layer [32].

Kinematically we can see how the vortex force can affect the flow in the process of mixing layer transition, but is there any link with fully-developed 3D turbulence? The Stokes velocity defined by equation (4.23) means $\boldsymbol{u}^{ST}$ scales as $\alpha^2|\boldsymbol{k}|^2$ (where $\boldsymbol{k}$ is a wavenumber) and can be interpreted as a small scale velocity component. Thus the vortex force $\boldsymbol{u}^{ST} \times \tilde{\boldsymbol{\omega}}$ represents the nonlinear interaction between a small-scale velocity and a large scale vorticity. These types of interactions were studied by Kerr et al. [57] and were found to be responsible for $70 - 90\%$ of the energy transfer from the large to small scales in isotropic box turbulence, giving some support to the idea of using such a term as a subgrid model.

Chapter 5

Numerical Methods

5.1 The STREAM code

The STREAM code is a colocated finite-volume method that has been used extensively in testing Reynolds-stress and k-ϵ turbulence models [75]. The version of the code used in this thesis is simpler than the original STREAM code [74] in that it is for Cartesian geometries and a fluid of constant density. The algorithm is outlined briefly below.

We start with the continuous form of the momentum equation with a source term S_u

$$\frac{\partial \tilde{u}_i}{\partial t} + \frac{\partial}{\partial x_j}\left(\tilde{u}_i \tilde{u}_j\right) = -\frac{\partial \tilde{p}}{\partial x_i} + \frac{\partial}{\partial x_k}\left(\nu \frac{\partial \tilde{u}_i}{\partial x_k}\right) + S_u. \tag{5.1}$$

In our case the source term is the subgrid force $H^{-1}\left(\partial_j m_{ij}\right)$ (see equation (4.15)). Integrating the momentum equation over a control volume, using Gauss's theorem to express the divergence terms as surface integrals

$$\int_V \frac{\partial \tilde{u}_i}{\partial t}\, dV + \int_{CS} \tilde{u}_i \tilde{u}_j\, A_j = -\int_V \frac{\partial \tilde{p}}{\partial x_i}\, dV + \int_{CS} \left(\nu \frac{\partial \tilde{u}_i}{\partial x_k}\right) A_k + \int_V S_u\, dV. \tag{5.2}$$

We now write this in discrete form, using the $x-$momentum equation in two dimensions as an example. The extension to three dimensions is straightforward. For the time derivative we use a three-level scheme [23]

$$\int_V \frac{\partial \tilde{u}_i}{\partial t}\, dV \sim \left(\frac{3\tilde{u}_P^{n+1} - 4\tilde{u}_P^{n} + \tilde{u}_P^{n-1}}{2\Delta t}\right) V_P \tag{5.3}$$

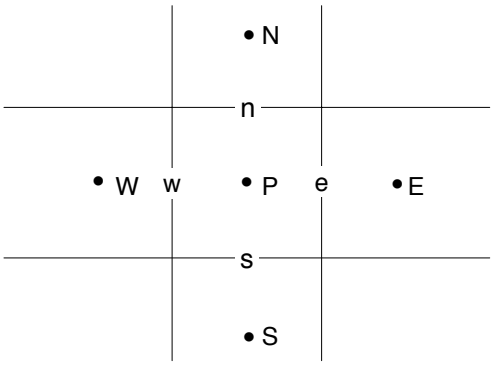

Figure 5.1: Variable arrangement for the colocated finite volume method, shown here in 2D. The nodes are marked by capitals letters, and the faces by lowercase letters.

where the subscript 'P' denotes the node and the superscript 'n' denotes the time level. Nodal variables are denoted by the upper case subscripts P,E,W,N,S while values at control volume faces are denoted with the lower case subscripts, e,w,n,s. Note that in the current colocated grid arrangement variables are only defined at the nodes, thus all face values are obtained by interpolating nodal values. A sketch of the variable arrangement is given in Figure 5.1 for clarification.

The advection terms in the momentum eqution (5.2) can be written

$$\int_{CS} \tilde{u}_i \tilde{u}_j A_j = \tilde{u}_e \dot{m}_e - \tilde{u}_w \dot{m}_w + \tilde{u}_n \dot{m}_n - \tilde{u}_s \dot{m}_s \tag{5.4}$$

where $\dot{m}_e, \dot{m}_w, \dot{m}_n \dot{m}_s$ are the mass fluxes through the east, west, north and south faces of the control volume. The method used to calculate the mass fluxes will be discussed below with the pressure correction scheme, at this time we will leave them in symbolic form. The face velocities are interpolated from nodal values using the QUICK scheme (c.f. Ferziger [23]) for the cavity flow and a second order central difference scheme (CDS) for the channel, unless otherwise noted. As an example of the implementation consider CDS for a non-uniform mesh,

$$\tilde{u}_e = \tilde{u}_E \lambda_e + \tilde{u}_P (1 - \lambda_e) \tag{5.5a}$$

$$\tilde{u}_w = \tilde{u}_W \lambda_w + \tilde{u}_P (1 - \lambda_w) \tag{5.5b}$$

$$\tilde{u}_n = \tilde{u}_N \lambda_n + \tilde{u}_P (1 - \lambda_n) \tag{5.5c}$$

$$\tilde{u}_s = \tilde{u}_S \lambda_s + \tilde{u}_P (1 - \lambda_s) \tag{5.5d}$$

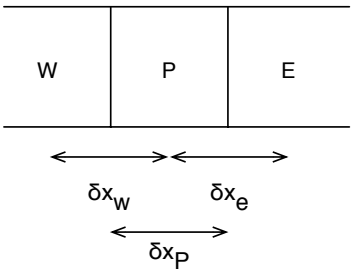

Figure 5.2: Notation used for distances between control volume nodes and faces

where $\lambda_e, \lambda_w, \lambda_n$ and λ_s are the linear interpolation factors. The QUICK scheme is implemented using a deferred correction approach, full details are given in Lien [73]. The implementation of both advection schemes along with the time-stepping method was verified by advecting wavepackets and comparing the numerical group velocity to that obtained analytically using the method described in Trefethen [135].

The diffusion terms are discretized using central differences (recall that the viscosity is constant)

$$\int_{CS} \left(\nu \frac{\partial \tilde{u}}{\partial x_k} \right) A_k = \left[\nu \frac{\partial \tilde{u}}{\partial x} A_x \right]_e - \left[\nu \frac{\partial \tilde{u}}{\partial x} A_x \right]_w + \left[\nu \frac{\partial \tilde{u}}{\partial y} A_y \right]_n - \left[\nu \frac{\partial \tilde{u}}{\partial y} A_y \right]_s \tag{5.6a}$$

$$= \nu \left[(\tilde{u}_E - \tilde{u}_P) \frac{A_{xe}}{\delta x_e} - (\tilde{u}_P - \tilde{u}_W) \frac{A_{xw}}{\delta x_w} + (\tilde{u}_N - \tilde{u}_P) \frac{A_{yn}}{\delta y_n} - (\tilde{u}_P - \tilde{u}_S) \frac{A_{ys}}{\delta y_s} \right]. \tag{5.6b}$$

Here we have introduced the notation δx_e to denote the distance between the centers of the P and E nodes, as shown in Figure 5.2, $\delta x_w, \delta y_n$ and δy_s are defined in a similar fashion. Combining (5.3),(5.4),(5.5a)-(5.5d), and (5.6b), we now have the $u-$momentum equation in discrete form

$$A_p \tilde{u}_p^{m+1} = \sum_{nb} A_{nb} \tilde{u}_{nb}^{m+1} - \frac{\tilde{p}_e^m - \tilde{p}_w^m}{\delta x_P} + S_u^m \tag{5.7}$$

where the subscript nb denotes the control volumes neighbouring P. In 2D this is E,W,N and S. The coefficients in the discrete equation are

$$A_E = -\lambda_e \dot{m}_e + \nu A_{xe}/\delta x_e \tag{5.8a}$$

$$A_W = -\lambda_w \dot{m}_w + \nu A_{xw}/\delta x_w \tag{5.8b}$$

$$A_N = -\lambda_n \dot{m}_n + \nu A_{yn}/\delta y_n \tag{5.8c}$$

$$A_S = -\lambda_s \dot{m}_s + \nu A_{ys}/\delta y_s \tag{5.8d}$$

$$A_P = A_E + A_W + A_N + A_S + \tfrac{3}{2}\tfrac{V_p}{\Delta t} \tag{5.8e}$$

$$S_u = \left(2\tilde{u}_p^n - \tfrac{1}{2}\tilde{u}_p^{n-1}\right)\tfrac{V_p}{\Delta t} - H^{-1}\textstyle\sum_{CS} m_{1j} A_j, \tag{5.8f}$$

where the last term in S_u is the subgrid model integrated over the control volume (see section 5.2). In equation (5.7) we have written the velocity field at iteration level $m+1$ to reflect the inner iteration level within the timestep. The $\tilde{u}$ momentum equation is solved implicitly at iteration level $m+1$ using the pressure field, mass fluxes and source term from the previous iteration level m. This is followed by solution of the $\tilde{v}$ and $\tilde{w}$ momentum equations and finally the pressure correction equation. If the maximum residual from one of the equations exceeds the convergence criteria, we return to the $\tilde{u}$ momentum equation and repeat the cycle until convergence is achieved. The simulation then proceeds to the next time level. The subgrid force was calculated each iteration level (m) priori to the $\tilde{u}$-momentum equation. This means the subgrid forces are held constant during the solution of the $\tilde{u}$,$\tilde{v}$ and $\tilde{w}$ momentum equations.

The $\tilde{v}$ and $\tilde{w}$ momentum equations are discretized in the same manner as the u equation. We then have three equations for $\tilde{u}, \tilde{v}, \tilde{w}$, but not yet a method to determine the unknown pressure field. To link the momentum equations with an equation for the pressure we use the SIMPLEC method, which we will now outline briefly.

The discrete momentum equations are solved in turn using a pressure field from the previous iteration level. The equations are solved without imposing the continuity constraint, thus the resulting momentum fields do not necessarily satisfy mass conservation. To reflect this we rewrite equation (5.7) in terms of new variables $\tilde{u}^*, \tilde{v}^*, \tilde{w}^*$ and $\tilde{p}^*$ (dropping the iteration level index for simplicity)

$$A_p \tilde{u}_p^* = \sum_{nb} A_{nb} \tilde{u}_{nb}^* - \frac{\tilde{p}_e^* - \tilde{p}_w^*}{\delta x_P} + S_u. \tag{5.9}$$

The true velocity fields are the sum of this approximate solution with an (unknown) correction

$$\tilde{u} = \tilde{u}^* + \tilde{u}' \tag{5.10a}$$

$$\tilde{p} = \tilde{p}^* + \tilde{p}'. \tag{5.10b}$$

Subtracting (5.9) from (5.7) yields an equation for the corrections

$$A_P \tilde{u}'_p = \sum_{nb} A_{nb} \tilde{u}'_{nb} - \frac{\tilde{p}'_e - \tilde{p}'_w}{\delta x_P}. \tag{5.11}$$

For the SIMPLEC method we approximate the first term on the RHS of (5.11) as

$$\sum_{nb} A_{nb} \tilde{u}'_{nb} \approx \tilde{u}'_P \sum_{nb} A_{nb}. \tag{5.12}$$

Because the corrections are zero at convergence this simplification does not affect the final result [138]. The equation relating the velocity correction to the pressure corrections is then

$$\tilde{u}'_p = -\frac{\tilde{p}'_e - \tilde{p}'_w}{\delta x_P (A_P - \sum_{nb} A_{nb})}. \tag{5.13}$$

Taking the divergence of both sides of (5.13) and requiring the velocity u to satisfy continuity (which means $0 = D(\tilde{u}^*) + D(\tilde{u}')$ where D is the discrete divergence operator) yields an equation that can be solved for the pressure corrections

$$D(\tilde{u}^*_P) = D\left(\frac{(\tilde{p}'_e - \tilde{p}'_w)}{\delta x_P (A_P + \sum_{nb} \tilde{u}'_{nb})}\right). \tag{5.14}$$

We recognize the left hand side as the divergence of the nodal velocity, or the mass flux. To calculate the mass flux we need the face velocities. Because of the colocated variable arrangement used here, a simple interpolation of nodal velocities to the control volume faces in (5.14) can lead to a decoupling between the velocity and pressure fields, in which the velocity field cannot sense a pressure difference on the order of the mesh spacing, leading to grid-scale oscillations. This was discussed by Rhie and Chow [114] and in this thesis we follow their method in which an additional pressure smoothing term is included in the calculation of the face velocities, see [73] for details.

With these face velocities the mass flux is calculated to obtain the LHS of the pressure correction equation (5.14). The pressure correction equation is then solved

using a preconditioned conjugate gradient solver [23] to obtain the pressure correction field. From this we calculate the velocity corrections using (5.13) and then update the guessed velocity and pressure fields using $\tilde{u} = \tilde{u}^* + \tilde{u}'$ and $\tilde{p} = \tilde{p}^* + \tilde{p}'$.

Before moving on to the subgrid model a few remarks regarding the advection schemes should be made. One of the key differences between the LES methodology and RANS models is that in LES the turbulent flow statistics (eg. rms velocities) are computed directly from the resolved flow. This means the method is more sensitive to the numerical methods used. For example if first-order upwinding is used with a Smagorinsky model the contribution of the numerical dissipation associated with the truncation error could be larger than that from the subgrid stress, and your results may not reflect the true performance of the model. It is common practice in LES to use central differencing schemes that contain only dispersive, not dissipative errors, and (in theory) therefore do not compete directly with the (dissipative) model. However, this does not remove the problem because dispersion errors can also contaminate the results. In the context of LES this is usually interpreted in terms of the modified wavenumber associated with the central difference operator [31]. Dispersion errors can also lead to higher numerical dissipation indirectly, by increasing flow gradients [43].

In this thesis we use the QUICK scheme used for the lid driven cavity flow, and second-order central differences for the channel flow. The QUICK scheme can be written as the sum of a second-order CDS and a third-order upwinding, hence it contains dissipative and dispersion errors [147]. The CDS scheme used for the channel flow contains only dispersion errors. For both the cavity and channel flow the time-stepping method is a second-order scheme weighted backwards in time, and contains some numerical dissipation.

In practice, to determine if the discrepancy between the LES results and DNS or experimental results is due to numerical error or modeling deficiencies a common strategy is to refine the mesh while keeping the filter width constant [30, 32]. This is referred to as increasing the subgrid resolution, which is the scale separation between the filter width (Δ) and the mesh spacing (h). As $\Delta/h \to \infty$, the solution approaches a state where the numerical errors are negligible and any errors left are due to the model itself. In this thesis we encountered difficulties when attempting to increase the filter width for some cases, and were limited in our ability to carry out a systematic study of this nature. Similar problems with increasing the physical

size of α^2 have been found by others using the NS-α model [105]. It was however, ensured that the main problems encountered, numerical oscillations for the cavity flow and high skin friction for the channel, could be reproduced on various meshes and with at least two different subgrid resolutions.

5.2 Model Implementation

In the finite volume formulation the source term appears on the right-hand side of the momentum equation (Equation (4.15)) as

$$\int_V H^{-1} \left(\frac{\partial m_{ij}}{\partial x_j} \right) \, dV \tag{5.15}$$

where H is the Helmholtz operator and m_{ij} is the subgrid stress. If we first calculate the subgrid stress m_{ij} at cell centers and then compute the divergence, this means the velocity gradients in the m_{ij} terms would be computed at cell centers. It was found that doing this using second-order central differences made the model more susceptible to numerical oscillations. As an alternative, the method used here is to write the source term in a manner consistent with the other terms in the momentum equation

$$H^{-1} \int_V \frac{\partial}{\partial x_j} \left(m_{ij} \right) \, dV = H^{-1} \int_{CS} m_{ij} A_j. \tag{5.16}$$

The velocity gradients are now computed at control volume faces, which means the source term is computed from velocity differences between adjacent nodes. Thus the procedure is to first compute the subgrid force at all interior nodes

$$F_i = \int_{CS} m_{ij} A_j, \tag{5.17}$$

and then find the filtered force $\tilde{F}_i$. This can be done either by solving the Helmholtz equation

$$F_i = \tilde{F}_i - \frac{\partial}{\partial x_k} \left(\alpha_k^2 \frac{\partial \tilde{F}_i}{\partial x_k} \right), \tag{5.18}$$

or by using another method to apply the filter. In this thesis both Helmholtz inversion and a simple box filter were used. Each will now be discussed in turn.

For the cavity flow Helmholtz inversion was carried out by first discretizing the equation using central differences, and then solving the discrete system using a

conjugate gradient solver [23]. For the channel flow an FFT solver was used in the periodic directions while a direct solver was used in the wall-normal direction (see Appendix B). For both the direct solver and the conjugate gradient solver values of the force F_i were not required at the solid boundaries because the boundary value of F_i is multiplied by the boundary value of the normal component of α_k^2, which is zero according to the specified boundary condition (see Chapter 3). To make this more clear consider a 1-D discretization of the Helmholtz equation

$$F_P = \tilde{F}_P - \frac{1}{\delta x_P}\left(\alpha_e^2 \left.\frac{\partial \tilde{F}}{\partial x}\right|_e - \alpha_w^2 \left.\frac{\partial \tilde{F}}{\partial x}\right|_w\right). \tag{5.19}$$

If there is a solid boundary at the east face $\alpha_e^2 = 0$ we do not need to specify the gradient $\partial\tilde{F}/\partial x$ at the boundary. Note that the Helmholtz filter can be implemented in the same manner for both the anisotropic and isotropic models. For the isotropic model we used $\alpha^2 = 0$ on the boundary.

While the Helmholtz equation can be solved efficiently using FFTs on a periodic domain, the conjugate gradient method used in the more general case (here cavity flow) is expensive. For this reason it is preferable to approximate Helmholtz inversion by using an equivalent operator. This issue has been discussed in the literature [32, 105]. Because of the similarity between their transfer functions, it is common to use a box filter to approximate Helmholtz inversion. Recall that when solving the Helmholtz equation the relationship between the filtered and unfiltered variables is (for the case of isotropic, constant filter width)

$$\phi = \left(1 - \alpha^2\nabla^2\right)\tilde{\phi}. \tag{5.20}$$

For Helmholtz inversion the transfer function is

$$\hat{G}_{Helm} = \frac{1}{1 + \alpha^2 k^2}. \tag{5.21}$$

When $(\alpha k)^2 < 1$ this can be written

$$\hat{G}_{Helm} = 1 - (\alpha k)^2 + (\alpha k)^4 - ... \tag{5.22}$$

For the box filter the relationship between the filtered and unfiltered variables is

$$\tilde{\phi} = \int_{-\infty}^{\infty} \phi(\xi) G(x - \xi)\, d\xi, \tag{5.23}$$

with the kernel,

$$G_{box}(x-\xi) = \begin{cases} \frac{1}{\Delta} & \text{if} \quad |x-\xi| \leq \frac{\Delta}{2} \\ 0 & \text{otherwise} \end{cases} \tag{5.24}$$

The transfer function for the box filter is

$$\hat{G}_{box} = \frac{\sin(k\Delta/2)}{k\Delta/2}, \tag{5.25}$$

which can be written

$$\hat{G}_{box} = 1 - \frac{1}{3!}\left(\frac{k\Delta}{2}\right)^2 + \frac{1}{5!}\left(\frac{k\Delta}{2}\right)^4 - ... \tag{5.26}$$

If $(\alpha k)^2 \ll 1$ and we retain only terms to second order, equating (5.22) with (5.26) yields $\alpha^2 \approx \Delta/24$, a relationship used in the literature when comparing the NS-α model to other models [32]. A picture of the two transfer functions is shown in Figures 5.3, where we have used $\alpha = \Delta/5$ to plot $\hat{G}_{helm}$. We can see that for low values of Δk the box filter is a good approximation to Helmholtz inversion, while at higher αk values the box filter displays oscillatory behaviour. Most of our simulations used a Δk value of ≈ 6 (based on $k_{max} = \pi/h$ and $\Delta = 2h$ where h is the grid spacing), and we found very little difference between the two filters. In the study by Petersen et al. [105] they used Δk values as high as ≈ 27 and found a stronger attenuation of small scale activity (expressed in their study as the level of eddy kinetic energy) with the box filter as compared to Helmholtz inversion. We can also see from Figure 5.3 that the transfer function for the box filter is not strictly positive. In the paper by Petersen et al. [105] it was found the box filter can lead to problems with negative energy and instability. In this thesis we did not encounter any problems with the explicit filtering operation. At times the subgrid model was found to lead to a numerical instability through excessive backscatter. In these cases it was verified that the filter had a stabilizing effect.

The box filter given by equation (5.23) with kernel (5.24) can be evaluated using either the trapezoidal rule or Simpson's rule. For a uniform mesh and an integration interval of $2h$ the two approximations in one-dimension are:

trapezoidal rule

$$\tilde{\phi}_P = \frac{1}{4}\left(\phi_W + 2\phi_P + \phi_E\right) \tag{5.27}$$

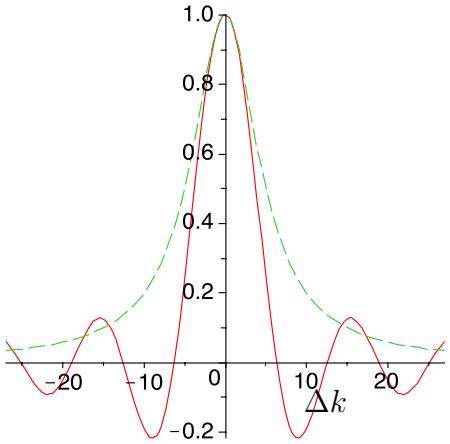

Figure 5.3: Filter transfer functions; solid line, box filter (5.25); dashed line Helmholtz inversion (5.21)

Simpson's rule

$$\tilde{\phi}_P = \frac{1}{6}\left(\phi_W + 4\phi_P + \phi_E\right). \tag{5.28}$$

If you substitute e^{ikx} for ϕ_P and $e^{ik(x-h)}$ and $e^{ik(x+h)}$ for ϕ_W and ϕ_E respectively you arrive at the discrete transfer functions:

trapezoidal rule

$$\hat{G}_{trap} = \frac{1+\cos(kh)}{2} \tag{5.29}$$

Simpson's rule

$$\hat{G}_{Simp} = \frac{2+\cos(kh)}{3} \tag{5.30}$$

A plot of the two transfer functions is shown in Figure 5.4 over the range of resolvable wavenumbers. We can see that using the trapezoidal rule the transfer function effectively decays to zero at the Nyquist frequency, and will be more effective at attenuating high wavenumber components, which can be contaminated with numerical errors. For this reason the trapezoidal rule is often chosen in practice [99]. For the box filter three-dimensional filters were constructed as the composition of three one-dimensional filters, $L = l_1 \circ l_2 \circ l_3$, where l_j $(j = 1, 2, 3)$ represents a one dimensional filter in the x_j-direction [121]. The cavity flow used nonuniform meshes in the x and y directions while the channel flow used a nonuniform mesh in the y direction only. In these directions the one-dimensonal filter followed the trapezoidal rule for a nonuniform mesh (recall δx_e and δx_w are defined in Figure

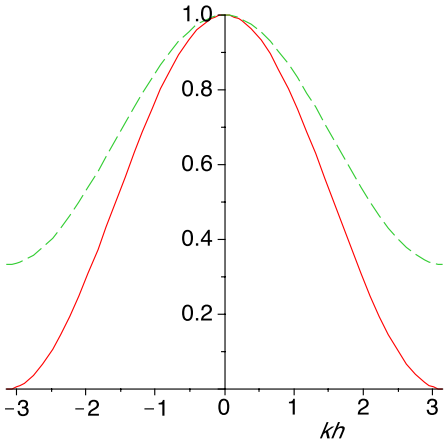

Figure 5.4: Discrete transfer functions for the box filter; solid line, trapezoidal rule Eqn. (5.29); dashed line, Simpson's rule Eqn. (5.30).

5.2)

$$\tilde{\phi}_P = \frac{\phi_E \delta x_e + \phi_P(\delta x_e + \delta x_w) + \phi_W \delta x_w}{2(\delta x_e + \delta x_w)}. \tag{5.31}$$

The box filter was used only for the anisotropic model. For the isotropic model the filter width should be the same size in each direction. To implement this on a stretched mesh you would have to adjust your stencil in each direction to be the correct physical size. This could lead to a stencil that does not even contain one grid cell if the mesh is highly stretched in a given direction. For the isotropic model only Helmholtz inversion was used. While the isotropic model was not generally stable, it should be noted that the performance was better when the correct filter was used. For example, it was found you cannot use an anisotropic filter with an isotropic model and vice versa.

Comparing transfer functions is one way to look at the differences between the box filter and Helmholtz inversion. Another way that may be more meaningful here is to compare the filter width computed from the actual filter coefficients used in the numerical simulation. For example, for the trapezoidal rule the filter coefficients are $(1/4, 1/2, 1/4)$ while for Simpson's rule they are $(1/6, 2/3, 1/6)$. For Helmholtz inversion the filter coefficients can be determined from the discrete Green's function [105]. This is the solution of the Helmholtz equation given $u = \delta(x - x_o)$ (impulse response). Once the filter coefficients, W_j, are known the filter width can

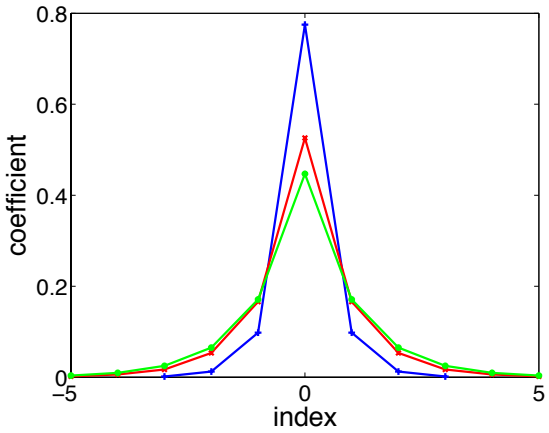

Figure 5.5: Filter coefficients returned by the conjugate gradient solver; blue +, $\alpha^2 = h^2/6$; red x, $\alpha^2 = 2h^2/3$; green *, $\alpha^2 = h^2$.

be computed from [80]

$$\frac{\Delta}{h} = \sqrt{12 \sum_{j=-(N-1)/2}^{(N-1)/2} j^2 W_j}. \tag{5.32}$$

Lund used this definition to show that apparent discrepancies in the *type* of filter used in the dynamic Smagorinsky model could in fact be accounted for by properly defining the filter width.

In the discussion of the results in this thesis we consider the filter width for the box filter to be the interval over which the trapezoidal rule is evaluated. For Helmholtz inversion the relationship from the transfer functions $\alpha^2 = \Delta^2/24$ is used to relate a chosen value of α^2 or α_k^2 to an effective filter width. For example, if we set $\alpha_x^2 = h_x^2$ we interpret this as a filter width $\Delta_x = \sqrt{24}h_x \approx 4.9h_x$. One question is then, if we calculate the filter width from the coefficients, does this relationship still hold? For the trapezoidal rule the coefficients evaluated over $2h$ and $4h$ are $(1/4, 1/2, 1/4)$ and $(1/8, 1/4, 1/4, 1/4, 1/8)$ respectively. From equation (5.32) the filter widths for these two cases are $2.5h$ and $4.2h$, slightly larger than expected. For Helmholtz inversion a plot of the filter coefficients for the conjugate gradient solver are shown in Figure 5.5 for three different values of α^2 and the filter widths from equation (5.32) are given in Table 5.2. We can see that the discrete filter widths are very close to the ones from the estimate $\alpha^2 = \Delta^2/24$. In this thesis we primarily used filters of widths $\Delta \approx 2h$ and found little difference between the box filter and Helmholtz inversion for both the cavity flow and channel flow. Therefore, while a more detailed analysis of filters could be done, we will leave this to a later

α^2	Δ/h based on $\alpha^2 = \Delta^2/24$	Δ/h based on Eq. (5.32)
$h^2/6$	2.0	2.0
$2h^2/3$	4.0	4.0
h^2	4.9	4.6

Table 5.1: Filter widths for Helmholtz inversion.

study employing larger filter widths.

Chapter 6

Lid-driven cavity flow

6.1 Physical problem

The application of the NS-α model to a practical problem is studied here using a lid-driven cavity flow at Reynolds numbers of 3,200 and 10,000, where the Reynolds number is based on the lid velocity and cavity length. The chosen cavity has a spanwise aspect ratio (SAR) of 1 (it is a cube) and has been studied before both experimentally [111, 64, 63, 62] and numerically [151, 4, 71]. The three-dimensional cavity flow contains a variety of flow structures and is a challenging test case for a subgrid model due to the lack of homogeneous directions, the presence of both laminar and turbulent flow regions, and the anisotropic nature of the flow.

At the lower Reynolds number of 3,200 the flow is transitional and the primary features are the primary eddy (PE), upstream and downstream secondary eddies (referred to as USE and DSE respectively), corner vortices and the Taylor-Goertler-like (TGL) vortices. A schematic of the test case is shown in Figure 6.1. While the primary and secondary eddies and corner vortices are ubiquitous features of the three-dimensional lid-driven cavity flow, the TGL vortices are specific to the flow around this Reynolds number. These vortices are known to form around $Re = 1,000$ due to the instability of the concave shear layer which is present at the interface between the primary eddy and downstream secondary eddy [125]. In the simulations the vortices were found to 'meander to and fro' along the bottom of the cavity, similar to what is described in the experimental studies [111]. A picture of the streamwise vorticity contours is shown in Figure 6.2 showing a single pair of TGL vortices for the cubical cavity ($SAR = 1$) and 8 pairs for a wider cavity of $SAR = 3$ (although the focus is on the $SAR = 1$ case, a few simulations were done on wider

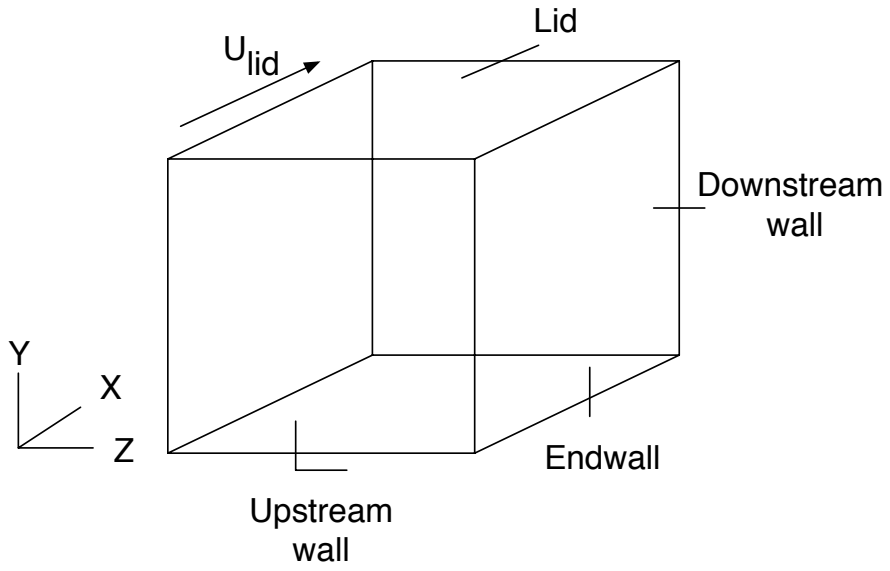

(a) Geometry of the cavity

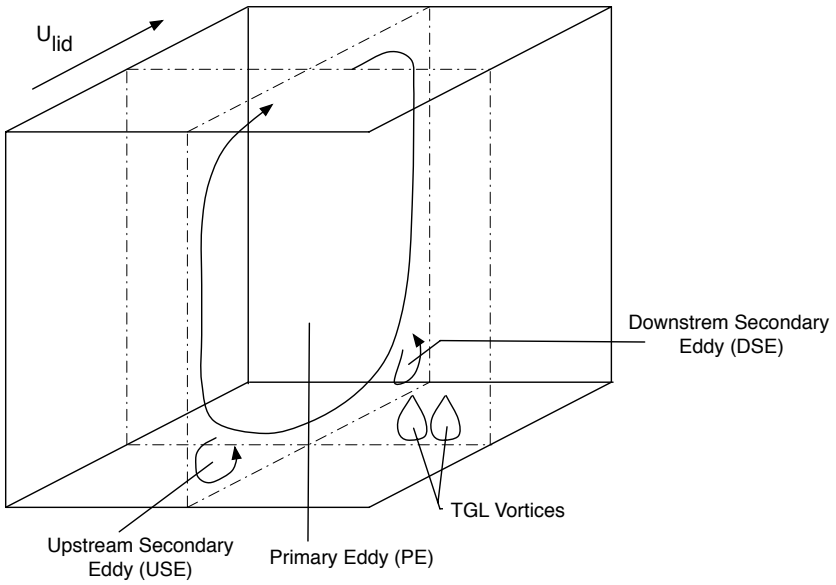

(b) Sketch of flow structures in the lid-driven cavity flow. The TGL vortices are present for the $Re = 3,200$ case only.

Figure 6.1: The lid-driven cavity flow

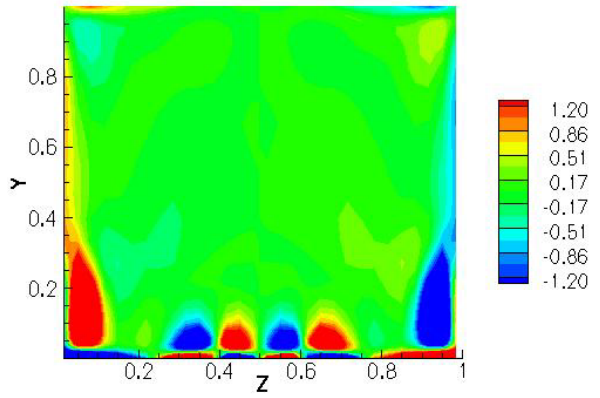

(a) $SAR = 1$

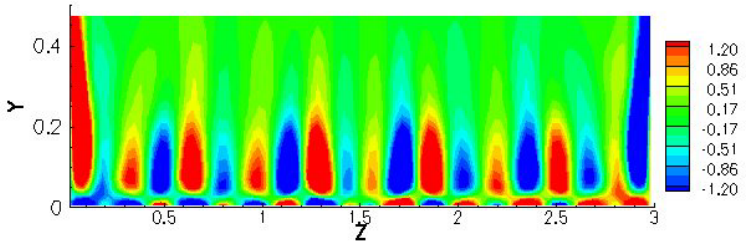

(b) $SAR = 3$

Figure 6.2: TGL vortices shown using vorticity contours on the $x = .75$ plane. Red indicates positive vorticity while blue is negative.

cavities). It is important to note that at a Reynolds number of $3,200$ the observed fluctuations are largely coming from the unsteadiness of the vortex structures in the cavity, and are not turbulent in nature. The inherent unsteadiness of the cavity at this Reynolds number is closely related to the TGL vortices. When the movement of these vortices is inhibited the rms fluctuations in the cavity are negligible. This was shown experimentally [111] when a cavity with a narrower span ($SAR = 0.5$) was used. In this case the TGL vortices were locked in position at the cavity center, which was attributed to the fact that at a narrower span the drag due to the endwalls becomes more significant relative to the momentum transferred by the lid.

The TGL vortices become less coherent with increasing Reynolds number. In the experiments, it was found that their presence could no longer be detected at $Re = 7,500$ [111]. For the higher Reynolds number test case considered here, $Re = 10,000$, the key feature of the flow is the formation of two jets which separate off the downstream wall and impinge on the cavity bottom. After impingement the

wall jets spread along the cavity bottom before encountering the upstream wall. The experimental measurements reported a small inertial subrange in the impingement region.

The lid driven cavity has been studied previously using Large Eddy Simulations. Zang, Street and Koseff [151] used the dynamic mixed model to study the cavity flow at both $Re = 3,200$ and $Re = 10,000$, although for the higher Reynolds number they looked at a narrower cavity (SAR=0.5), for which the flow is not turbulent. Thus both of their test cases should be considered quasi-laminar. Nevertheless, it can be difficult to use a model in such a regime, and from this point of view the study is useful. Their results showed that the Smagorinsky coefficient C_s determined from the dynamic procedure was non-zero only near the downstream secondary eddy, where the flow is transitional. Their mean flow and rms profiles were also in good agreement with the experimental data. A more recent LES study was carried out by Bouffanis and Deville [4] for the cubical cavity at $Re = 10,000$ using a spectral element method. They used both the dynamic model and the dynamic mixed model and found little difference between the two. The mean flow and rms profiles were also in good agreement with DNS data from an earlier study of the same cavity which used twice the resolution as the LES [71]. The models were found to be active in the turbulent parts of the flow, and mostly inactive in the laminar regions, as they should be.

The objective of using the NS-α model for this test case was to determine how suitable the model is for a complex flow. Both of the previous studies used dynamic models, in some cases with additional similarity terms. These models are of similar cost to the NS-α model [32], but in a study of a transitional mixing layer the NS-α model was found to have better performance. We would like to see if we can still obtain better results with the NS-α model in a case now containing solid boundaries, where it is not appropriate to use a constant α^2 as was done for the mixing layer.

6.2 Numerical Description

The lid-driven cavity flow is studied numerically using the methods described in Chapter 5. The mesh used is stretched in the x and y directions to resolve the shear layers near the walls, but uniform in the spanwise since the relevant flow physics (TGL vortices for the low Reynolds number and wall jets for the high Reynolds

Re	(Nx, Ny, Nz)	h_{min}	h_{max}/h_{min}
3,200	(32,32,32)	5.6×10^{-3}	12.4
10,000	(48,48,48)	3.6×10^{-3}	12.5
10,000	(64,64,64)	2.6×10^{-3}	12.9

Table 6.1: Mesh parameters for the lid-driven cavity flow

number) are not clustered near the endwalls, but distributed along the span. The parameters pertaining to the mesh are given in Table 6.1. Different stretching ratios were tested for the x and y directions, the ones chosen provided the best compromise between near wall resolution and a reasonable mesh size in the interior. Note that for the high Reynolds numbers, two different resolutions were used, 64^3 and 48^3.

To assess the time step and total sampling time we first compare our parameters to those used in the experiments. For the lid-driven cavity all quantities are non-dimensionalized by the cavity length (L) and lid velocity (U). The characteristic time scale is then L/U. This can be written in terms of the Reynolds number (since the lid velocity was not reported in the experiments)

$$\frac{L}{U} = \frac{L^2}{\nu}\frac{\nu}{UL} = \frac{1}{Re}\frac{L^2}{\nu}.$$

Estimating the kinematic viscosity of water at room temperature as $1 \times 10^{-6}\mathrm{m}^2/\mathrm{s}$ and knowing the length of the cavity to be 150 mm gives $L/U = 7.31s$ for the $Re = 3,200$ case and $L/U = 2.25s$ for the $Re = 10,000$ case. A time step of 0.01 then corresponds to physical time of $0.0731s$ and $0.025s$ or physical frequencies of $13Hz$ and $44Hz$ respectively. The power spectra shown from the experiments for all cases have very little frequency content above $1Hz$. Therefore, it was expected that the timestep chosen would be adequate. This was verified by the fact that simulation results showed very little difference when run at a timestep half as big.

The timestep is important because a smaller time step will obviously mean more steps to achieve a total simulation time. It was found in particular for the high Reynolds number case long integration times were needed to achieve a statistically stationary state, which was assessed by monitoring the rolling averages of the mean and rms velocities, as well as the total kinetic energy. Once a statistically steady state was achieved, statistics were collected over $20L/U$. This was found to be adequate for converged statistics.

The procedure used to initialize the simulations was as follows. On each mesh a simulation with the model turned off was started from a state of rest. Thus, at time $t = 0$ the lid was set into motion at a uniform velocity and a recirculating flow slowly developed in the cavity. When the flow was statistically steady the instantaneous fields were written to a file. This flow state was then used to initialize the runs with the NS-α model. With the NS-α model active a new statistically steady state was established before samples were collected.

Following the convention in the literature, we have dropped the tilde on the filtered variables in reported results. In this chapter averaging is carried out with respect to time. Time averages are denoted by the overbar $\bar{\cdot}$ and a fluctuation about this mean is denote with a prime.

6.3 Results with no model

We will begin by showing some sample results from running the code without a turbulence model. The mean flow, rms and shear stress profiles are shown in Figure 6.3 for the $Re = 3,200$ case using both the QUICK [23] and the UMIST [76] advection scheme. The UMIST scheme is a TVD (total-variation diminishing) version of QUICK and is shown here for comparison because it will be used later when we look at the numerical oscillations encountered with the model. We can see the mean flow profiles are well captured for both schemes, while the rms and shear stress profiles are slightly underpredicted for the UMIST scheme. Looking at these results, the reader might wonder why use a subgrid model at all if the flow is well-predicted without one? One thing to keep in mind is that in a complex flow situation, eg. a flow with laminar, transitional and fully turbulent regions, it is required that the flow remain inactive during the laminar flow regime. Thus, it is useful to know what effect the NS-α model will have, if any, at this relatively low Reynolds number.

In Figure 6.4 contours of the spanwise vorticity show the primary recirculation cell, the DSE and the USE. If we compare the u_{rms} profiles in Figure 6.3 with these contours we can see the upper peak in the u_{rms} profile ($y \approx 0.2$) comes from the unsteadiness of the wall jet that separates off the downstream wall. For this Reynolds number the wall jet does not impinge on the cavity bottom. On the other hand, the lower peak in the u_{rms} profile ($y \approx 0.05$) is related to the movement of

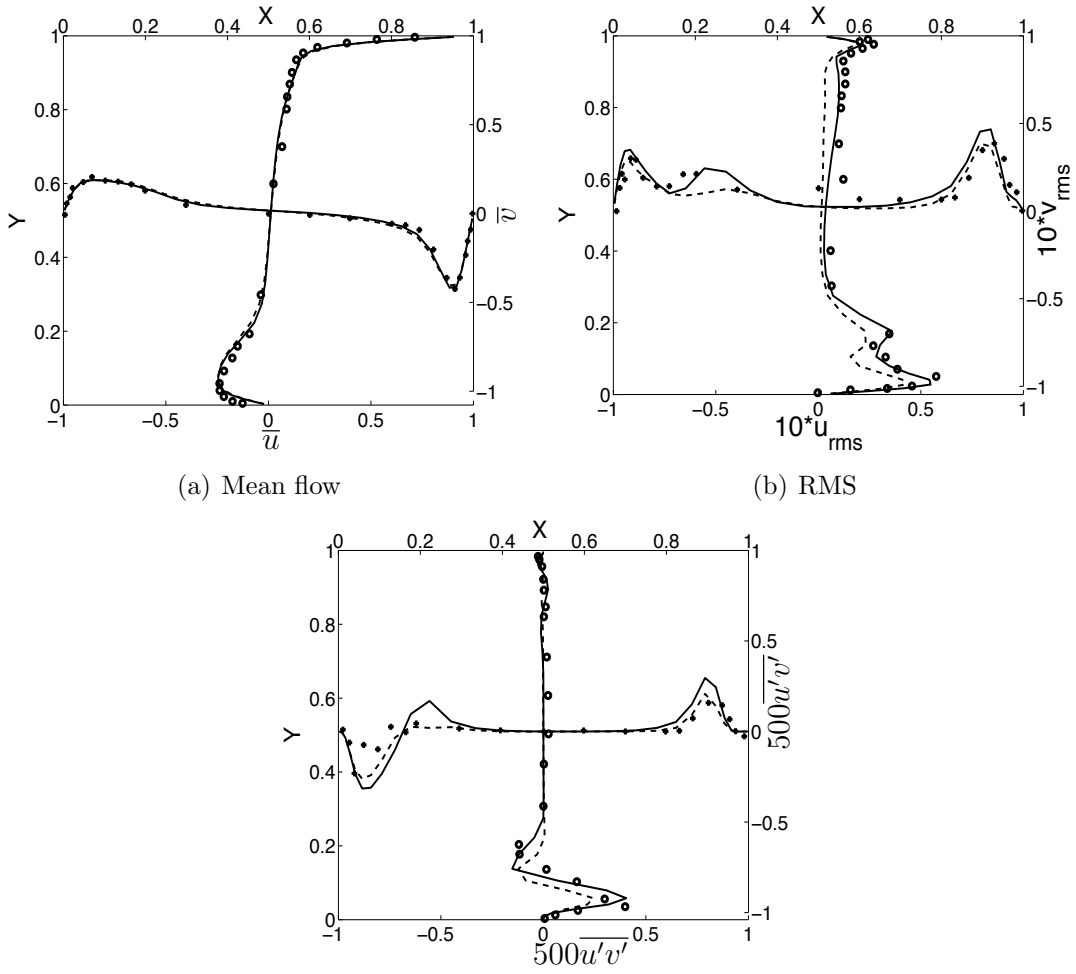

(a) Mean flow

(b) RMS

(c) Shear stress

Figure 6.3: Comparison of no model run and experimental data for $Re = 3,200$. Profiles are along the centerlines on the cavity midplane. Solid line is the QUICK scheme, dashed line is the UMIST scheme, symbols are experimental data [111].

the DSE and USE pulling on the boundary layer and the TGL vortices moving back and forth [111]. The movement of these vortices is reflected in a time trace of the velocity taken near the cavity center and close to the bottom, shown in Figure 6.5. The trace using the UMIST scheme is qualitatively similar to that shown in the experimental study of Prasad and Koseff [111] in that there is a low frequency modulation with a few higher frequency peaks. However, the lower frequency we measure here $f \approx 1/50 = 0.02$ is lower than that in the experiments $f \approx 0.04$. The trace from using the QUICK scheme has some additional high frequency peaks, but is qualitatively similar to that from the UMIST scheme. Similar sensitivity of the TGL vorticies to the advection scheme was found in the GAMM workshop on the lid-driven cavity flow [125]. Before looking at the higher Reynolds number we will note that as a means of verifying the code further a simulation of a narrower cavity ($SAR = 0.5$) with a finer mesh $(128, 128, 32)$ was also carried out. We found that the TGL vortices were locked in position at the cavity center, and that the rms fluctuations are negligible in agreement with the experimental data [111]. The narrow span cavity was chosen for a higher resolution study because for this case we could use enough grid points to have a uniform mesh in the $x - y$ plane. This test case was then used later to troubleshoot problems with the NS-α model (by having a uniform mesh we eliminate α_k^2 gradients in the domain interior, but discontinuities at the endwalls, where $\alpha_k^2 = 0$ remain a problem).

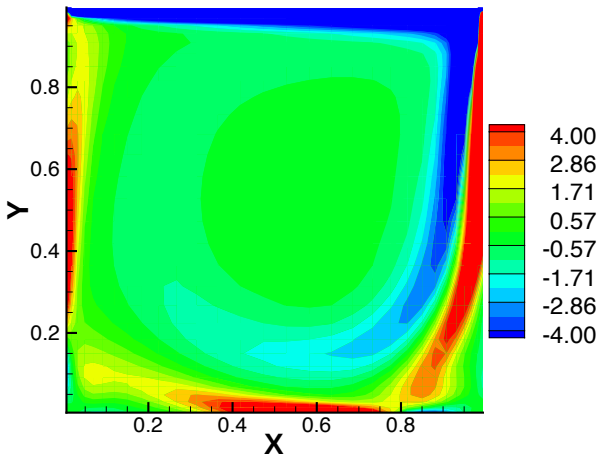

Figure 6.4: Spanwise vorticity, ω_z on the cavity midplane $z = 0.5$ for $Re = 3,200$

For the higher Reynolds number case of $Re = 10,000$ the mean flow, rms and shear stress profiles are shown in Figure 6.6 for the two different meshes. We can

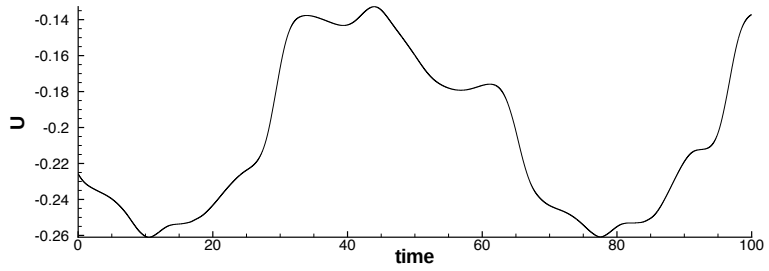

(a) UMIST scheme

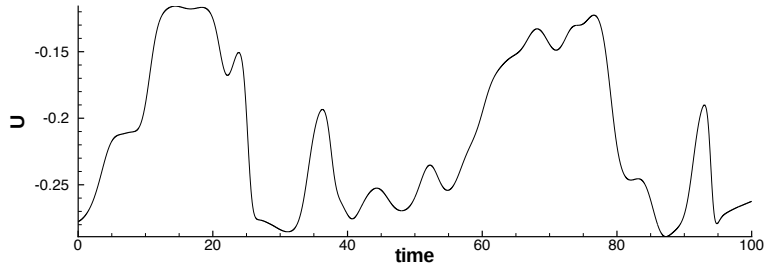

(b) QUICK scheme

Figure 6.5: Time traces of u velocity taken at a point on the midplane at a height of 7mm ($y = 0.047$) from the cavity bottom as in the experiments [111].

see that on both meshes the rms and shear stress profiles are underpredicted, with the $(64)^3$ results being better than those at $(48)^3$. The mean flow profile for the $u-$velocity on the 48^3 mesh also has a nose that is peaked and more closely resembles a laminar flow profile (turbulent profile is flatter due to enhanced mixing).

6.4 NS-α model results

Since α_k^2 is a smoothing scale we start with a simple definition based on the grid size

$$\alpha_k^2 = C\left(h_k^2\right) \tag{6.1}$$

where h_k is the grid spacing in the k-direction and C is a constant denoting what fraction of the grid spacing to use. Because α_k^2 can be related to the filter width, Δ_k, of a box filter via $\alpha_k^2 = \Delta_k^2/24$ [32], we choose $C = 1/6$, which corresponds to a filter width that is twice the grid size.

Initially when we turned on the NS-α model for the lid driven cavity flow we

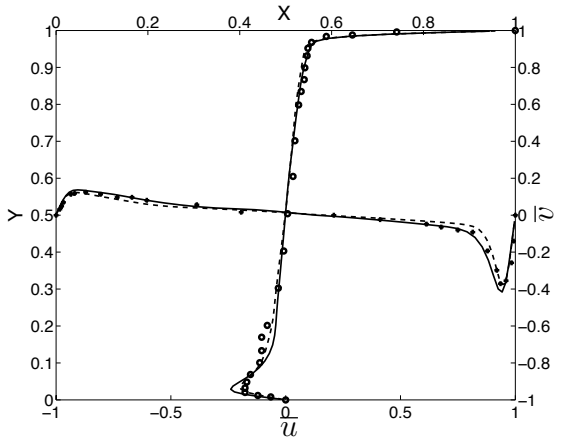

(a) Mean flow

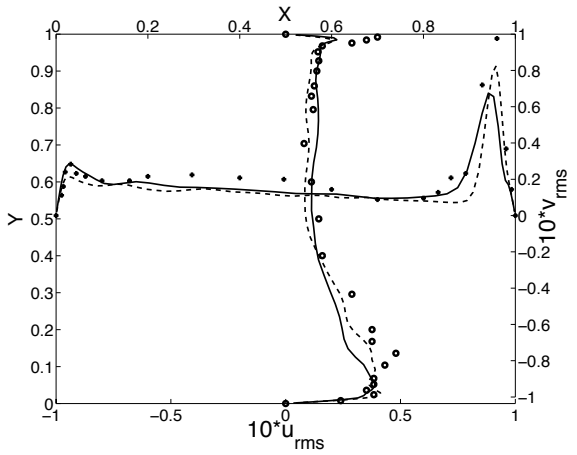

(b) RMS

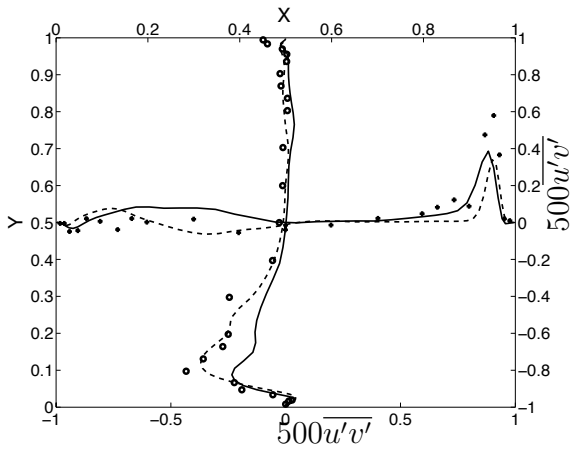

(c) Shear stress

Figure 6.6: Profiles along the centerlines on the cavity midplane with no model for the $Re = 10,000$ case. Solid line is the $(48)^3$ mesh, dashed line is the $(64)^3$ mesh, symbols are experimental data [111].

encountered some perplexing model behavior. The model generated small-scale activity that, at a first glance, could be interpreted as turbulence. There were difficulties in increasing the physical size of α, counter to our intuition instead of increased smoothing this often led to even more small-scale activity. This has been seen in previous studies, where it was attributed to either numerical error [32] or the fact that the model allows more energetic structures to exist near the grid-scale [105, 33]. The initial poor performance of the model was not altogether surprising, the lid-driven cavity is a challenging flow, and many models have serious difficulties when they are run in a wall-bounded flow for the first time. However, the failure mode of the NS-α model was found to be different than that described in the literature for dissipative models, which tend to damp too much near boundaries and lead to flow that is too laminar-like. In this section we discuss the problems encountered with the NS-α model, their physical interpretation, and a proposed solution.

6.4.1 Problems Encountered when α^2 is based on the mesh

Numerical oscillations

Before we begin we will show some representative results that led us to suspect numerical oscillations were contaminating the solution. Initially, when the NS-α model was applied to the cavity flow there were two persistent results that were problematic. The first was high fluctuation levels in the downstream wall jet region for the low Reynolds number ($Re = 3,200$) test case. This was accompanied by premature separation of the wall jet, which in turn affects the shape of the $\overline{u}$ and u_{rms} profiles on the midplane. A sample of the mean flow and rms profiles on the cavity midplane is shown in Figure 6.7. The second problematic result was more prominent for the high Reynolds number case ($Re = 10,000$) where the wall jet was found to be pushed out too far from the wall, as shown in Figure 6.8. These problems were observed for both isotropic and anisotropic models (where isotropic is with a scalar model parameter α^2, and the anisotropic model is with separate model parameter for each direction, α_k^2), on both coarse and refined meshes, over a few different α_k^2 values, and with both Helmholtz inversion and box filtering.

Initially both of these problems were attributed to the model itself. The rationale behind this is easier to follow if we recall that we can rewrite the subgrid term, $H^{-1}\left(\partial_j m_{ij}\right)$, in the form

$$H^{-1}\left(2\,\partial_j A_{ij} + \boldsymbol{u}^{ST} \times \tilde{\boldsymbol{\omega}}\right), \tag{6.2}$$

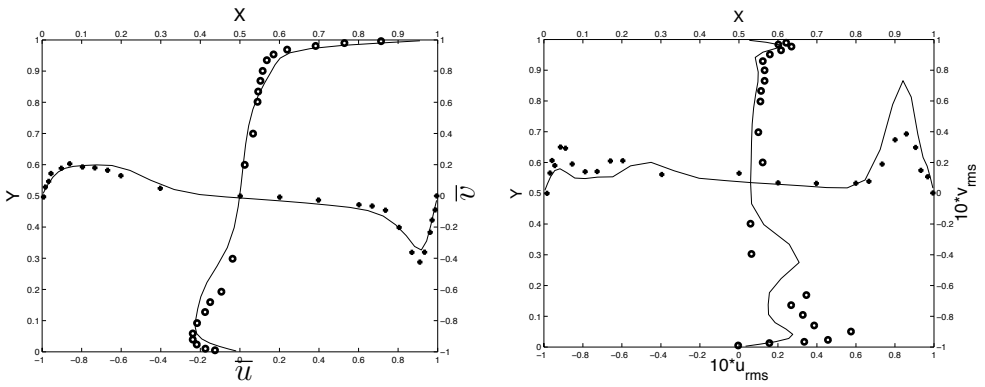

(a) Mean flow (b) RMS

Figure 6.7: Profiles along the centerlines on the cavity midplane for the $Re = 3,200$ case, anisotropic NS-α model. Symbols are experimental data [111].

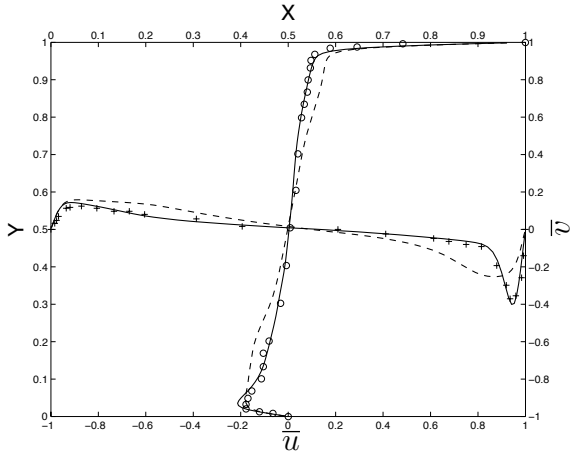

Figure 6.8: Mean flow profiles on the midplane for the $(64)^3$ mesh. Solid line, no model; dashed line, NS-α model, symbols are experimental data [111].

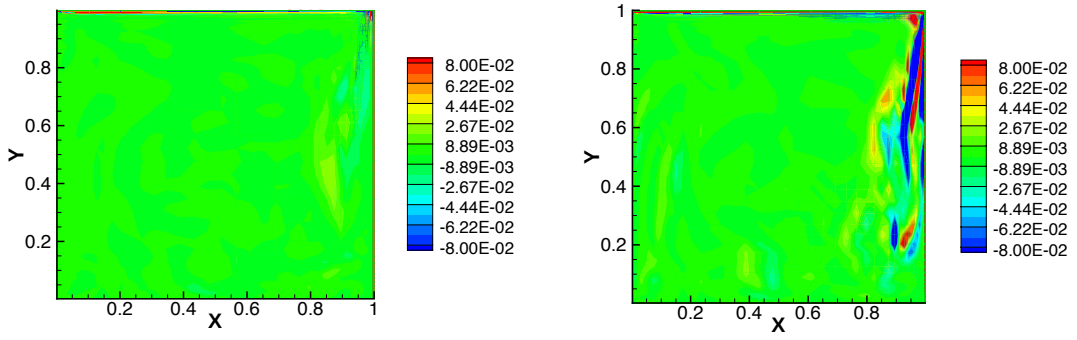

(a) $\partial_j A_{1j}$ (b) x-component of $\boldsymbol{u}^{ST} \times \boldsymbol{\omega}$

Figure 6.9: Vortex force (x component) and $\partial_j A_{1j}$ term for the $Re = 3,200$ case, anisotropic model.

with the Stokes velocity

$$\boldsymbol{u}^{ST} = -\alpha_k^2 \frac{\partial^2 \tilde{\boldsymbol{u}}}{\partial x_k^2}. \tag{6.3}$$

A plot of the two source terms in the symmetry plane is shown in Figure 6.9, we can see that the vortex force term is much larger than the $\partial_j(A_{ij})$ term. Because the wall jet is pushed too far out from the downstream wall in the x-direction, we now look at the contribution of the vortex force to the $\tilde{u}$-momentum equation

$$v^{ST}\tilde{\omega}_z - w^{ST}\tilde{\omega}_y. \tag{6.4}$$

Near the downstream wall $\tilde{\omega}_z \gg \tilde{\omega}_y$ and $\partial_x \gg \partial_y, \partial_z$ and it was expected that the problem was coming from following component of the vortex force,

$$\alpha_x^2 \frac{\partial^2 \tilde{v}}{\partial x^2}\tilde{\omega}_z. \tag{6.5}$$

Given that the vorticity field is unsteady this will be an unsteady forcing term which could cause the wall jet to oscillate back and forth, leading to high fluctuation levels. Depending on the balance between the positive and negative forcing, it is possible that that this could lead to the jet being pushed too far out from the wall in the mean. For the anisotropic model this hypothesis could be easily tested by turning off α_x^2. This was done for the high Reynolds number test case, and to our surprise this did not help the situation. Instead, it was turning off α_z^2 which solved this problem.

A closer examination of the flow fields corresponding to the $\alpha_z^2 \neq 0$ and $\alpha_z^2 = 0$

cases showed that the main difference between the two is the appearance of streamwise vortices (along the downstream wall these are in the vertical direction, $\tilde{\omega}_y$) in the downstream wall jet region when $\alpha_z^2 \neq 0$, as shown in Figure 6.10. These

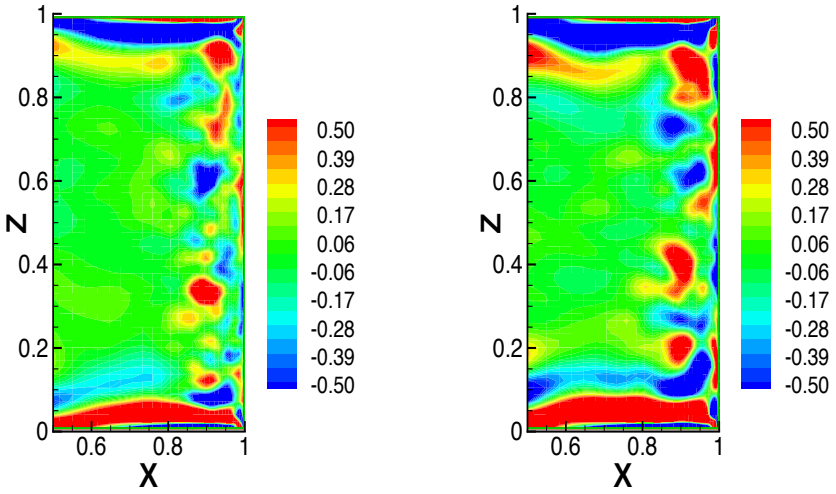

(a) anisotropic model, $C = 1/6$

(b) anisotropic model, $C = 1$

(c) isotropic model, $C = 1/6$

(d) no model

Figure 6.10: Vertical vorticity ($\tilde{\omega}_y$) on the $y = 0.6$ plane near the downstream wall for the $Re = 10,000$ case. All simulations are done with the $(64)^3$ mesh.

vortices do not appear when a model is not used or when the Leray model is used and are a numerical artifact of the NS-α model [1]. The presence of these vortices can be understood if there is significant modulation of the velocity in the spanwise

[1]Some simulations were done with the Leray model, which means only the $A_{ij} + B_{ij}$ terms in the subgrid stress were used. The model was able to run stably long enough to collect some statistics, but later diverged.

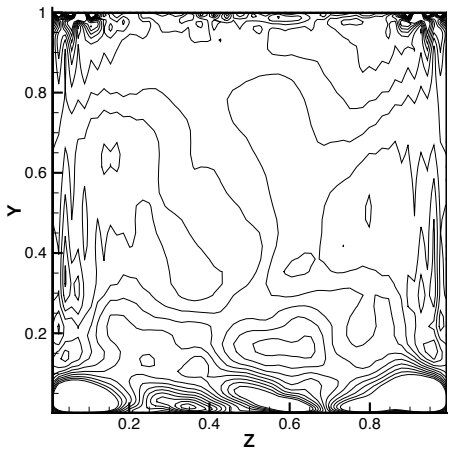

Figure 6.11: Spanwise velocity ($\tilde{w}$) in a $y-z$ plane near the downstream wall for $Re = 10,000$, anisotropic model, 64^3 mesh.

direction, as for example could be caused by spanwise numerical oscillations. Recall that the vortex force in the momentum equations appears as advection and stretching/tilting terms in the vorticity equations. In particular the stretching/tilting term in the vertical vorticity equation is

$$\tilde{\omega}_x \frac{\partial v^{ST}}{\partial x} + \tilde{\omega}_y \frac{\partial v^{ST}}{\partial y} + \tilde{\omega}_z \frac{\partial v^{ST}}{\partial z}. \tag{6.6}$$

Since we know it is α_z^2 that is causing the problem, we can see that spanwise oscillations leading to $\tilde{v}^{ST} \approx \alpha_z^2 \partial^2 \tilde{v}/\partial^2 z$ might be leading to the generation of vertical vorticity. A closer inspection of the flow fields for the NS-α model shows there are numerical oscillations in the spanwise direction, which are most easily seen in the weak spanwise velocity component, as shown in Figure 6.11. In particular if spanwise oscillations manifest themselves as $\partial \tilde{v}/\partial z$ this will generate both v^{ST} and ω_x and the first term in (6.6) will tilt this x-component of vorticity into the vertical.

There is an interesting analogy between the behavior seen here, and an alternative interpretation of the NS-α equations. It has been pointed out [47] that these equations are similar to the Craik-Leibovich equations, which are used to account for the long-time averaged effect of surface waves on mean momentum transfer [87]. The effect of surface waves is to create a relative velocity between a fluid particle (Lagrangian) and the background current (Eulerian) [69]. This relative velocity is called the Stokes drift velocity. The effect of this relative velocity is to tilt verti-

cal vorticity into the streamwise direction to create streamwise vortices (Langmuir cells) which transport momentum perpendicular to the free surface and flatten the velocity profile below the surface, leading to a mixed layer. A schematic of this (called the CL2 mechanism) is shown in Figure 6.12(a) following the review article by Leibovich [70]. The basic ingredients are, the Stokes velocity, seed vorticity, and a feedback mechanism. Kinematically the seed vorticity is tilted by the Stokes velocity. For the physical surface mixed layer you find in oceans and lakes, the Stokes velocity is the relative velocity described above, the seed vorticity (which is in the vertical direction) comes from planetary vorticity and/or wave-breaking [130], and the feedback mechanism is that the tilted vortices (Langmuir cells) lead to further inhomogenites in the spanwise direction, promoting further the formation of vertical vorticity - which is the seed vorticity. If we take this picture and now rotate it 90^o about the spanwise axis (and apply a no-slip condition for the cavity flow) we have Figure 6.12(b). Now we have a vertical Stokes drift velocitiy, tilting the $x-$component of vorticity into the vertical direction. This generates large streamwise vortices which transport momentum away from the downstream wall, generating the flat velocity profile we see in Figure 6.8. In this scenario the seed vorticity is the numerical oscillations, the Stokes velocity is coming from the subgrid model, and the feedback is again that the streamwise vortices promote further disturbances in the spanwise direction (the spanwise perturbation would actually be very small so there would be numerous perturbations creating an array of vorticies). Thus, this result is not erroneous in the sense that it is a real solution to the given equations in the presence of small scale spanwise oscillations which generate the necessary seed vorticity and/or Stokes velocity. However, the problem is that the oscillations are not coming from something physical, but from an unwanted numerical effect. It should be noted that although the source term due to the model is not large in the spanwise direction, there is little to balance its effect in the spanwise direction. It was found that the flat velocity profile seen in Figure 6.8 developed slowly over time, indicating that the long-time average effect of the vertical vortices is a mixing out of the velocity profile. Similar problems were observed in cases where the numerical oscillations were not visually obvious, again showing that since the effect builds up over time, small oscillations can have a significant impact.

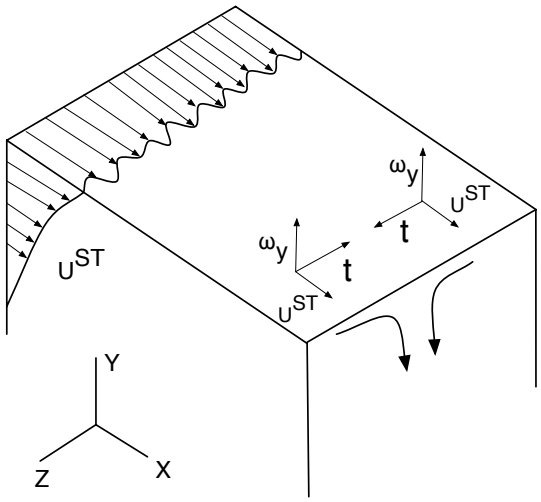

(a) Spanwise perturbations generate vertical vorticity. In the momentum equation opposing torques ($\boldsymbol{t}$) are created from the $\boldsymbol{u}^{ST} \times \boldsymbol{\omega}$ term. This creates a convergence zone and streamwise vorticity. In the vorticity equation, vertical vorticity is tilted by u^{ST} into the streamwise direction. After Leibovich [70].

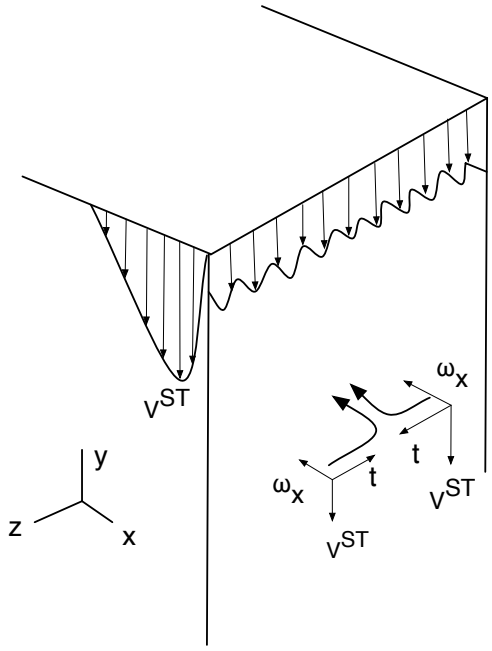

(b) Spanwise perturbations generate ω_x. In the momentum equation opposing torques $\boldsymbol{t}$ are created from the $\boldsymbol{u}^{ST} \times \boldsymbol{\omega}$ term. This creates a convergence zone and vertical vorticity. In the vorticity equation, streamwise vorticity is tilted by v^{ST} into the vertical direction.

Figure 6.12: Creation of streamwise vorticity through the vortex force.

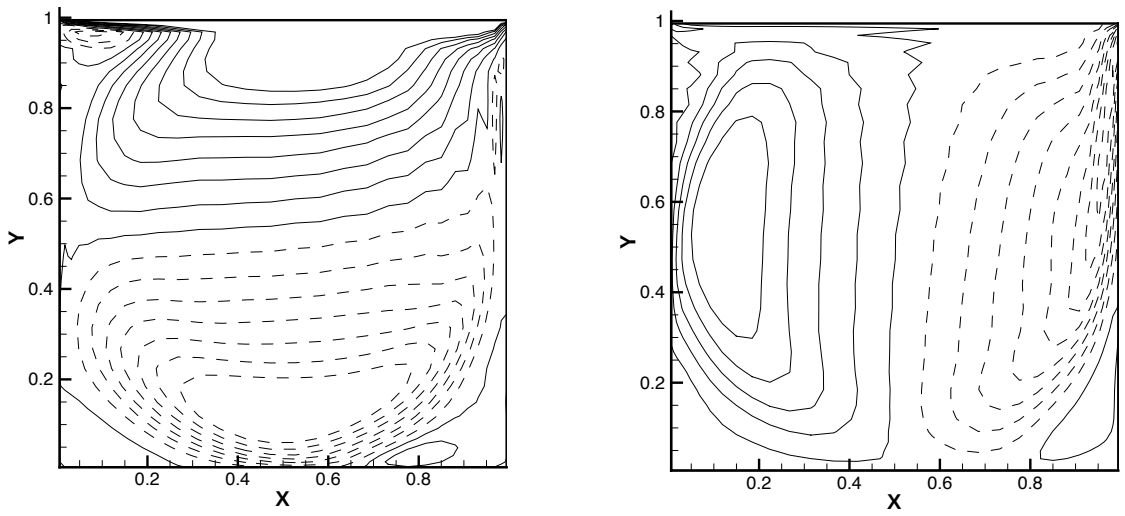

Figure 6.13: 2D cavity, velocity contours for the anisotropic model, $\tilde{u}$-velocity (left) and $\tilde{v}$-velocity (right). Solid and dashed lines indicated positive and negative contours respectively.

At this point it is clear that it is not possible to interpret the physical behavior of the NS-α model until the numerical oscillations can be understood and dealt with appropriately. For the purpose of understanding this problem further we turned to 2D simulations to see if we could recreate the problem in a simpler setting. It was found upon reducing the mesh stretching ratio that two problematic regions emerged, as can be seen in Figure 6.13. Both are found in the vicinity of the zero contours of the $\tilde{u}$ and $\tilde{v}$ velocity respectively. The contours shown in Figure 6.13 are for the anisotropic model with α_k^2 taken to be proportional to the grid spacing (the mesh is stretched in both directions). Similar results are found when the isotropic model is used, and when a uniform mesh is used, in which case they are much worse. Recall that the subgrid model can be written (see Equation (6.13)) as

$$m_{ij} = A_{ij} + B_{ij} - C_{ij}, \tag{6.7}$$

where the first two terms constitute the Leray model, and the NS-α model is comprised of all three. Since the Leray model does not have this problem, we know it is coming from the C_{ij} term. By trial and error it was found that the oscillations near the lid are coming from the following term in the $\tilde{v}$ momentum equation,

$$\frac{\partial C_{22}}{\partial y} \approx \frac{\partial}{\partial y}\left(\alpha_y^2 \frac{\partial \tilde{u}}{\partial y}\frac{\partial \tilde{u}}{\partial y}\right), \tag{6.8}$$

while those near the downstream wall are coming from the following term in the $\tilde{u}$ momentum equation,

$$\frac{\partial C_{11}}{\partial x} \approx \frac{\partial}{\partial x}\left(\alpha_x^2 \frac{\partial \tilde{v}}{\partial x}\frac{\partial \tilde{v}}{\partial x}\right). \tag{6.9}$$

Note that it is gradients of the $\tilde{u}$ velocity which are acting as source terms in the $\tilde{v}$ momentum equation and vice versa (which makes this problem a bit different than some more standard sources of numerical oscillations, such as the Peclet number problem [116] and oscillations in central differencing schemes [135]).

Since the oscillations near the lid are very pronounced, we will now look at this region in more detail. The $y-$momentum balance at $x = 0.47$ near the lid is shown in Figure 6.14. When the model is turned off, it can be seen in Figure 6.14(a) that the balance is between the streamwise advection $\tilde{u}\,\partial\tilde{v}/\partial x$ and the vertical pressure gradient $\partial\tilde{p}/\partial y$, and that both decrease monotonically as the lid is approached. From Figure 6.14(b) we can see that the model generates a large source term near the lid. This source term is balanced by the vertical pressure gradient, and leads to non-monotonic behaviour near the lid and the oscillations we see in Figure 6.13. This problem is coming from the near wall behavior of the model parameter α^2. While the grid stretching means that $\alpha^2 \to 0$ at a solid wall, when α^2 is based on the mesh it is not possible to have $\partial\alpha^2/\partial y \to 0$ as well. As we move from a highly stretched mesh to a uniform mesh, but continue to impose the Dirichlet condition, $\alpha^2 = 0$, we create a jump in $\partial\alpha^2/\partial y$ at the boundary. If the balance is between the pressure gradient and $\partial_y C_{22}$, the vertical momentum equation becomes

$$\frac{\partial \tilde{p}}{\partial y} = \frac{\partial}{\partial y}\left(\alpha_y^2 \left(\frac{\partial \tilde{u}}{\partial y}\right)^2\right). \tag{6.10}$$

When we integrate this over the control volume adjacent to the lid (here n and s indicate the north and south faces) we obtain,

$$\tilde{p}_n - \tilde{p}_s = \left[\alpha_y^2 \left(\frac{\partial \tilde{u}}{\partial y}\right)^2\right]_n - \left[\alpha_y^2 \left(\frac{\partial \tilde{u}}{\partial y}\right)^2\right]_s. \tag{6.11}$$

The first term on the right-hand side will be zero if the north face is a solid wall ($\alpha_y^2|_n = 0$), which means the pressure gradient will be negative. If we were to require $\partial\alpha_y^2/\partial y = 0$ at the boundary, then we would not have this problem. To demonstrate this the 2D cavity flow case was run again explicitly setting $\alpha_y^2|_n = \alpha_y^2|_s$ for the control volume adjacent to the upper and lower boundaries. The

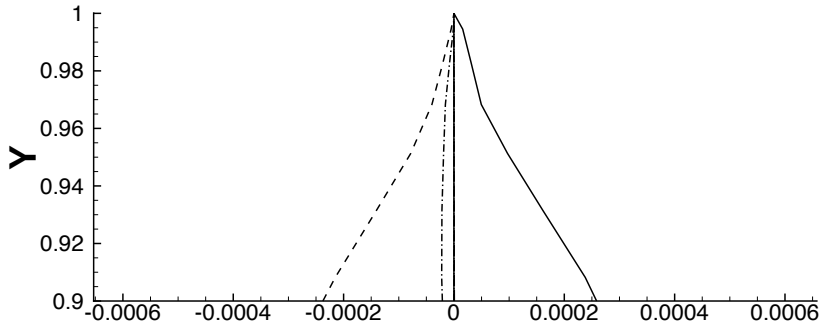

(a) No model

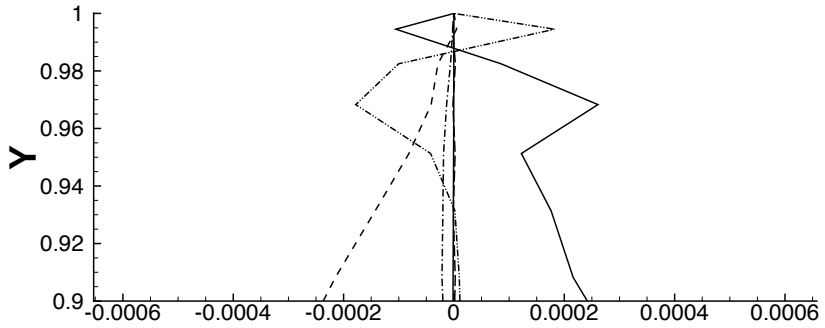

(b) NS-α model, $\alpha^2 = 0$ at $y = 1$

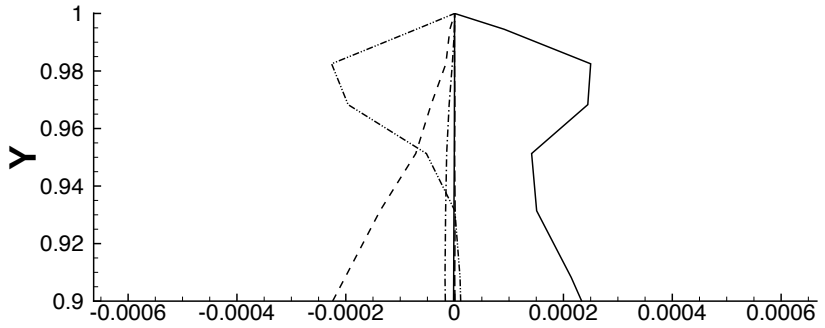

(c) NS-α model, $\partial\alpha^2/\partial y = 0$ at $y = 1$

Figure 6.14: Momentum balance near the lid for the 2-D cavity flow, $Re = 3,200$. Solid line is $\partial\tilde{p}/\partial y$, dashed line is $\tilde{u}\,\partial\tilde{v}/\partial x$, dash-dot is $\tilde{v}\,\partial\tilde{v}/\partial y$; and dash-dot-dot is $\partial\widetilde{(C_{22})}/\partial y$.

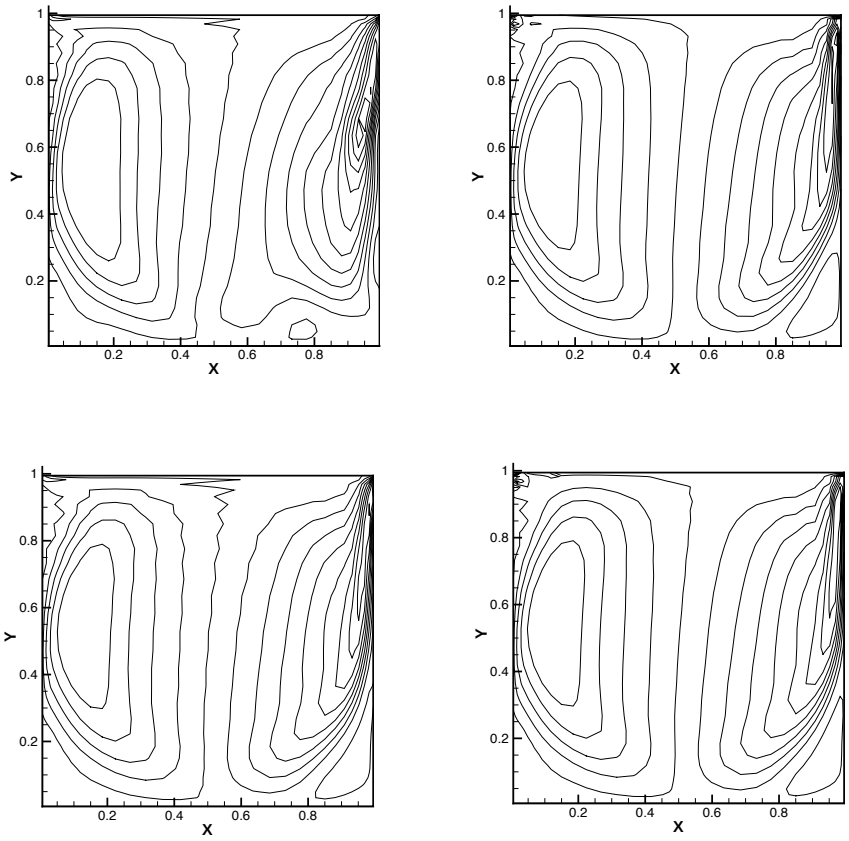

Figure 6.15: Vertical velocity contours for the 2D cavity, $Re = 3,200$. Top row is the isotropic model while lower half is the anisotropic model. Left column is with the homogeneous Dirichlet boundary condition while right column is with the homogeneous Neuman condition for α^2 (isotropic) and α_k^2 (anisotropic).

numerical oscillations are significantly reduced, as shown in Figure 6.15. The flow is also now in agreement with the no model case, as it should be for a 2D laminar flow. Alternatively we can remove the oscillations by setting α^2 on the boundary according to the value that will give $p_n - p_s = 0$. For example at the top boundary

$$\alpha_n^2 = \alpha_s^2 \frac{(\partial \tilde{u}/\partial y)_s}{(\partial \tilde{u}/\partial y)_n}$$

This also removed oscillations, but effectively shifts the boundary condition to the requirement that $u = \tilde{u}$ instead of having the normal component of $\alpha_k^2 = 0$. When we derived these equations in Chapter 3 it was the latter condition that we used, so we feel it is more correct to enforce this in the simulations.

For the 3D cavity flow the mesh used is sufficiently stretched in the $x-y$ plane to avoid any problems associated with the $N/S/E/W$ boundaries. The problem arises instead because the mesh is uniform in the spanwise direction. When we use the NS-α model for this case in its present form and set α_z^2 to be proportional to the mesh spacing h_z^2, when we get to an endwall the boundary condition $\alpha_z^2 = 0$ implies $\partial_z \alpha_z^2 \neq 0$ and we find oscillations are generated in the spanwise direction. Out of interest, we also tried solving the Helmholtz equation in the spanwise direction keeping α_z^2 constant, in which case the boundary values do not arise when you discretize the Helmholtz equation. Similar to the study by Petersen et al. [105] we found that this led strong damping near the walls. For the $Re = 3,200$ cavity, this completely suppressed the motion of the TGL vortices, which we know is not physically correct.

Finally, it should be noted that the oscillations seen are not just a boundary problem but will occur whenever α^2 changes too abruptly. As a simple example a laminar Couette flow was also tested. In this case there are two walls at $y = \pm h$ moving in equal and opposite directions and the velocity gradient is uniform. An α_y^2 discontinuity was introduced in the middle at $y = 0$. When the model was turned on there was a jump in the vertical velocity at the discontinuity. This was from the C_{ij} term, and was balanced partly by the unsteady term and partly by the pressure gradient. Clearly, α^2 is supposed to be a smoothing parameter, and abrupt changes are not physical, leading to unphysical results.

Near-lid Backscatter

For the lid-driven cavity flow it was found that the isotropic model overpredicts the mean flow velocity and was particularly susceptible to divergence. These problems were found to be due to excessive backscatter of energy near the cavity lid, which was easily confirmed by turning the model off in this region. This backscatter not only increases the energy of the resolved flow (leading to the overacceleration) but can also lead to divergence. A picture of the velocity profiles is shown in Figure 6.16 for both the low and high Reynolds numbers.

We found the backscatter problem could be reproduced when α^2 is constant. This means we can write the contribution of the subgrid model to the resolved flow energy equation as the sum of a redistribution term and a subgrid transfer term

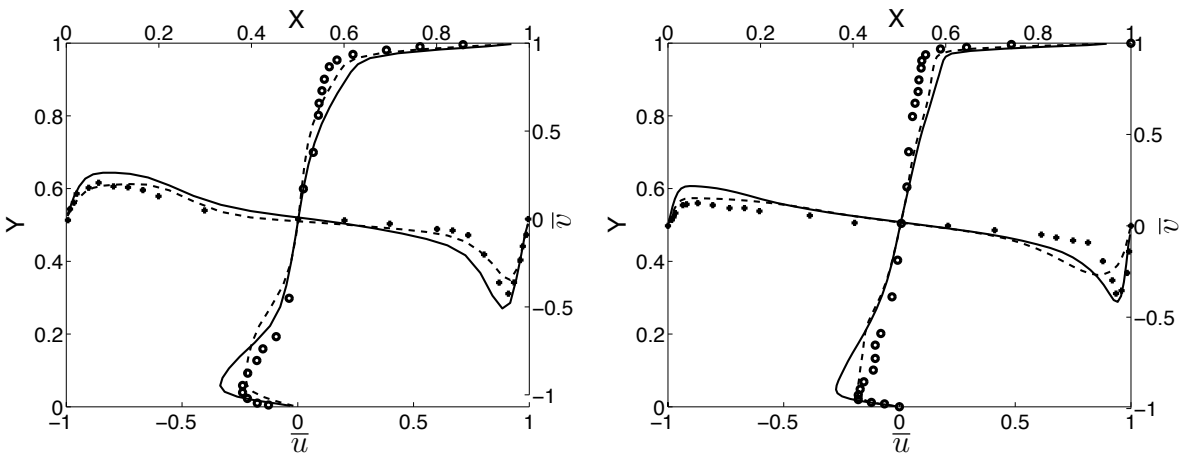

(a) $Re = 3,200$ (b) $Re = 10,000$

Figure 6.16: Mean flow profiles for anisotropic and isotropic models showing the tendency of the isotropic model to overpredict the mean flow. Solid line is the isotropic model and dashed line the anisotropic model.

(T_{SGS})

$$\int_V \tilde{u}_i \frac{\partial}{\partial x_j} \widetilde{m}_{ij}\, dV = \int_V \Big(\underbrace{\frac{\partial}{\partial x_j}\left(\tilde{u}_i \widetilde{m}_{ij}\right)}_{redistribution} - \underbrace{\widetilde{m}_{ij} \frac{\partial \tilde{u}_i}{\partial x_j}}_{T_{SGS}} \Big)\, dV. \tag{6.12}$$

In Figure 6.17 we show the total energy transfer for the isotropic and anisotropic versions of the subgrid model, and the decompositions into the redistribution and T_{SGS} terms. It can be seen that the energy transfer is much higher for the isotropic model in the laminar flow regions near the lid and downstream wall. This is from the redistributive part of the transfer (negative redistribution corresponds to a positive source term in the resolved flow energy equation). Further decomposing the energy transfer into contributions from the A_{ij}, B_{ij} and C_{ij} terms respectively in Figure 6.18 shows that the dominant contribution to the energy transfer is the gradient term (A_{ij}). This is the first term in the subgrid stress

$$m_{ij}^{ISO} = \Big(\underbrace{\alpha^2 \frac{\partial \tilde{u}_i}{\partial x_k} \frac{\partial \tilde{u}_j}{\partial x_k}}_{A_{ij}} + \underbrace{\alpha^2 \frac{\partial \tilde{u}_k}{\partial x_j} \frac{\partial \tilde{u}_i}{\partial x_k}}_{B_{ij}} - \underbrace{\alpha^2 \frac{\partial \tilde{u}_k}{\partial x_i} \frac{\partial \tilde{u}_k}{\partial x_j}}_{C_{ij}} \Big). \tag{6.13}$$

The gradient model has been the subject of various analyses in the literature and in particular it has been shown that it should be applied to wall bounded flows with care due to a negative viscosity problem which can arise if the model length scale is too large close to the wall [143, 40, 59]. The most popular remedies for this problem are clipping [144], which means turning off the model when it is backscattering, and

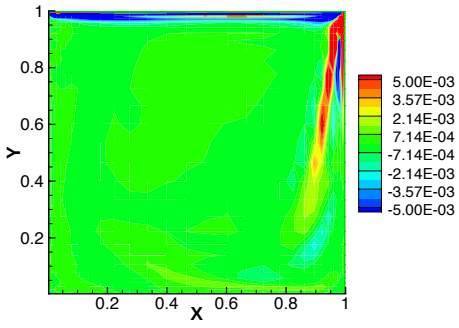

(a) total energy

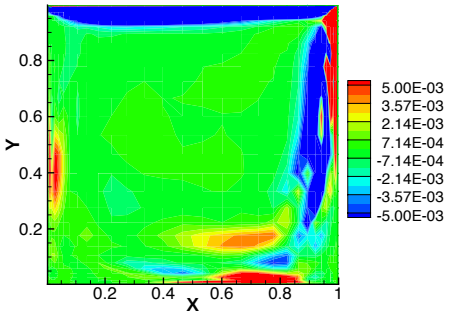

(b) total energy

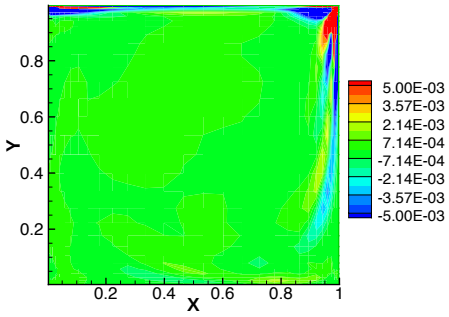

(c) redistribution

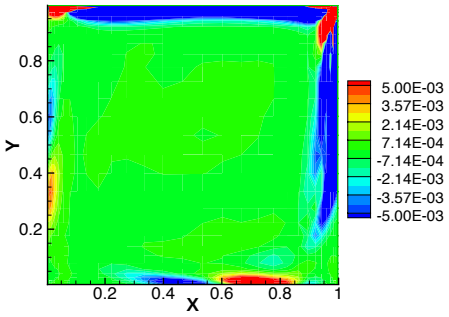

(d) redistribution

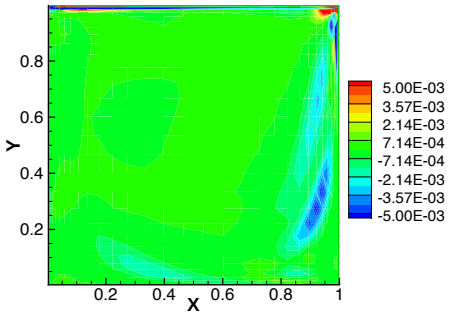

(e) T_{SGS}

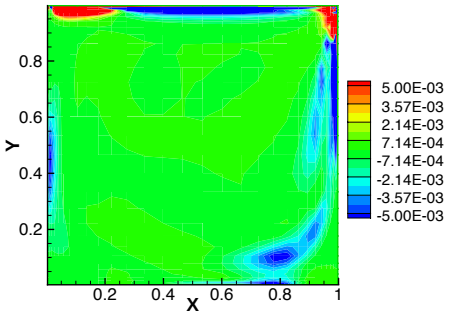

(f) T_{SGS}

Figure 6.17: Energy transfer for the $Re = 3,200$ case. Left panel, anisotropic model; right panel, isotropic model. Note that for this isotropic model there is strong evidence that the model is active in the laminar flow regions (near the lid along the upper part of the downstream wall).

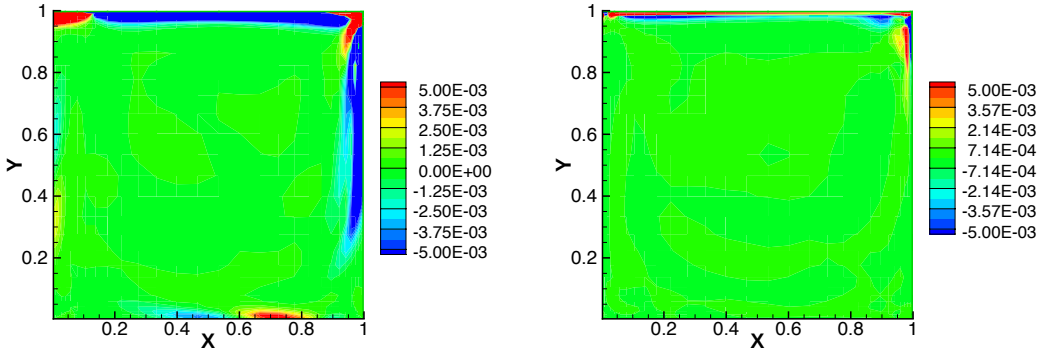

(a) redistribution, A_{ij}

(b) redistribution, B_{ij}

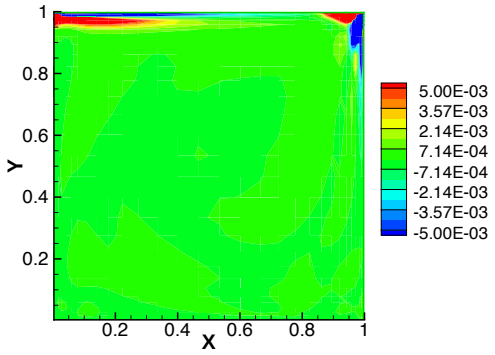

(c) redistribution, C_{ij}

Figure 6.18: SGS redistribution term, isotropic model, $Re = 3,200$. Note that the A_{ij} term is large in the laminar flow regions near the lid and the upper part of the downstream wall.

using near wall damping functions [149]. Part of the appeal of using the NS-α model is its ability to naturally accomodate backscatter, so in this thesis we will not use clipping. Wall-damping functions may be of interest for a channel flow case, but are difficult to develop (and not entirely appropriate) for the complex lid-driven cavity flow. Fortunately, we found the instability was not a problem when the anisotropic model was used for an acceptable range of α_k^2 values. For example, for value ranging from a filter width between two to 5 times the grid size. This motivated the emphasis on the anisotropic model over the isotropic one.

6.4.2 An alternative defnition of α^2

The results shown in the previous section highlight some of the problems encountered when we use a definition of α^2 which is based on the mesh size. It was found that physically relevant results are associated with having both α^2 and $\partial\alpha^2/\partial y \to 0$ at the wall, and that abrupt changes in α^2 can lead to unphysical numerical oscillations. It was also found that the model can generate excessive backscatter near the cavity lid, though this was not a significant problem for the anisotropic model.

Since the problems we see are associated with near-wall behaviour another logical approach would be to introduce a damping factor which reduces the magnitude of α^2 near the wall. However, the lid-driven cavity is a complex flow, and is far from canonical wall-bounded flows, such as the turbulent boundary layer or channel flow. As such, it is not really an appropriate test case for near wall behavior (the boundary layers are not generally turbulent). Damping factors based on this flow would probably have little relevance to other situations. Instead, it was found more useful to move in a direction more appropriate to a complex flow situation. Here, this meant moving away from a grid based definition for α^2 to one where α^2 is a function of the flow.

In doing this we first recall that α^2 is, in theory, a measure of the mean-squared displacement of a particle from an averaged trajectory. Particle displacements in turbulent flows were discussed in a very insightful manner by Taylor [132] for the one-dimensional case. The relationship between the NS-α model and Taylor's work has been pointed out earlier [50], and there are two results from his paper which we would now like to use. The first one is that when the time over which the particle has travelled from an initial to final point, T, is sufficiently short such that the particle velocities at the beginning and end of motion are well-correlated, the

mean-squared displacement of the particle from its initial position is

$$[X^2] \sim [u^2]T^2 \tag{6.14}$$

where u is the particle velocity and the square brackets denote a statistical average. Based on this we let α^2 be defined according to

$$\alpha^2 = [u^2]T^2. \tag{6.15}$$

If we take T to be a timescale indicative of the resolved flow a reasonable choice would be

$$T = \left(\tilde{g}_{ij}\tilde{g}_{ij}\right)^{-1/2}, \tag{6.16}$$

where $\tilde{g}_{ij}$ is the resolved velocity gradient.

To determine u^2 we will draw on a second argument given in Taylor's paper which is that in considering the dispersion of a particle due to turbulent motion it is not the total kinetic energy of the particle, u^2, that is relevant, but the number of times the particle switches direction (or effectively, the number of zero crossings about the mean). In one dimension this can be captured by $\left(\partial_x u\right)^2$ or $\left(\partial_t u\right)^2$. In the more general case a second-order structure function could be used. In the anisotropic case this would be [72]

$$F_2^{aniso}(\mathbf{x}, L, t) = \frac{1}{6}\sum_{i=1}^{3}[|\mathbf{u}(\mathbf{x},t)-\mathbf{u}(\mathbf{x}+L_{xi}\mathbf{e}_i,t)|^2-|\mathbf{u}(\mathbf{x},t)-\mathbf{u}(\mathbf{x}-L_{xi}\mathbf{e}_i,t)|^2]\left(\frac{L}{L_{xi}}\right)^{2/3}. \tag{6.17}$$

Here $\mathbf{e}_i$ denotes a unit vector and L is a length scale based on an appropriate volume. For homogeneous, isotropic turbulence this is similar to using the turbulent kinetic energy to estimate u^2 since in that case there is a simple relationship between the second order structure function and the energy spectral density (see Batchelor p. 120 [2])

$$F_2^{iso}(\boldsymbol{x}, L_x) = 4\int_0^{k_c} E(k)\left[1 - \frac{\sin(kL_x)}{kL_x}\right]\, dk. \tag{6.18}$$

Putting the velocity and time scales together we would then arrive at the following definition for α_k^2,

$$\alpha_k^2 = \frac{F_2^{aniso}(\mathbf{x}, L, t)}{\tilde{g}_{ij}\tilde{g}_{ij}}. \tag{6.19}$$

In practice F_2 is computed using the six closest neighbors to a given mesh point [22] ($L_x = h_x$). This means such a definition of α_k^2 would reduce to the wall normal spacing in a uniform shear flow such as a Couette flow, which will result in little improvement over the simple grid-based definition. This problem can be anticipated because in a wall bounded flow, for example a channel flow with $\partial\tilde{u}/\partial y$ as the shear, the velocity difference associated with $\tilde{u}(y + \Delta y) - \tilde{u}(y)$ contains a contribution from the mean flow gradient which should not be included in the computation of F_2. This problem has been discussed in the literature in applications of the structure function model to channel and boundary layer flows [22]. In this case the problem was resolved by not including $\tilde{u}(y + \Delta y) - \tilde{u}(y)$ in the calculation of F_2. In the more complex situation other strategies, such as high pass filtering, are often used [22].

Instead of using the second order structure function the definition that was found to work well was

$$\alpha_x^2 = \max\left[(\delta_x\tilde{u})^2, (\delta_y\tilde{u})^2, (\delta_z\tilde{u})^2\right]\ T^2 \tag{6.20}$$

$$\alpha_y^2 = \max\left[(\delta_x\tilde{v})^2, (\delta_y\tilde{v})^2, (\delta_z\tilde{v})^2\right]\ T^2 \tag{6.21}$$

$$\alpha_z^2 = \max\left[(\delta_x\tilde{w})^2, (\delta_y\tilde{w})^2, (\delta_z\tilde{w})^2\right]\ T^2 \tag{6.22}$$

where again T^2 is $(\tilde{g}_{ij}\tilde{g}_{ij})^{-1}$ and the δ symbol denotes a velocity increment. In practice this can computed as the velocity difference between adjacent mesh points. The *max* function in equation (6.20)-(6.22) was chosen to allow the simulation to use the largest length scale, and hence the maximum smoothing. The objective here was not to arrive at a rigorous method to determine α_k^2, but to see if a simple intuitive definition can improve the results. In the future a more rigorous method could be used to determine α_k^2 such that it fulfills specific requirements, such as ensuring the model contribution is zero in a laminar flow region.

Whereas a structure function is based on the velocity difference in a given direction and tells us about energy contained in eddies of a given size, this definition tells us about the energy in the horizontal, vertical and spanwise velocity fluctuations. The idea with the definition in equations (6.20)-(6.22) was then that horizontal particle displacements should be based on fluctuations in the horizontal velocity, and similarly for the vertical and spanwise components.

6.4.2.1 Results for Re=3,200

Mean flow and rms profiles with the alternative definition of α_k^2 are shown in Figure 6.19. It can be seen that for the low Reynolds number case the effect of the model on the first and second order statistics is negligible. This is not a bad result because the flow is laminar over most of the cavity at this Reynolds number. We can see from the energy transfer in Figure 6.20 that the model is active in the transitional flow regions, and inactive in the laminar ones, as it should be. The exception to this is the high source terms generated in the top right corner. We did not find this to have a significant impact in that turning off the model in this corner did not change the results. Previous studies have also found a relative insensitivity to the corner singularity in the flow field away from the corner [125].

While not investigated in detail in this thesis, it was found that the NS-α model can have a significant impact on the TGL vortices. Time traces of the streamwise velocity from a probe at a height $y = 0.047$ from the cavity bottom and in the middle of the $x - y$ plane are shown in Figure 6.21. Both of these are taken from a simulation where the UMIST scheme was used. The trace with no model is qualitatively similar to that shown in the experimental study of Prasad and Koseff [111] in that there is a low frequency modulation with a few higher frequency peaks (this was mentioned earlier at the beginning of this Chapter). The ratio between the two frequencies is ≈ 4, the same as that measured in the study by Freitas and Street [26]. In this study they found the slow part of the system was associated with oscillations of the TGL pair at the cavity center, which does not meander but is fixed. The shorter time scale was thought to be due to a a secondary instability of the TGL vortices offset from the center.

With the model we no longer see the slow oscillation in the time trace in Figure 6.21 but record only one frequency (which is the same as the higher frequency without the model). The frequency and appearance of the time trace with the model is in fact almost identical to that measured experimentally by Koseff and Street [62] in the shear layer separating the DSE and the PE (upstream of where we are measuring here). We can also see in Figure 6.22, which are plots of the streamwise vorticity contours with time, that the pattern is similar to the no model case, but occurs at a faster rate. It is not clear why the model has this effect on the TGL vortices. One possibility is because it is backscattering energy in the vicinity of the vortices, enhancing the faster oscillation such that the slow one is no longer detected at the cavity center. A plot of the energy transfer is shown in Figure 6.24

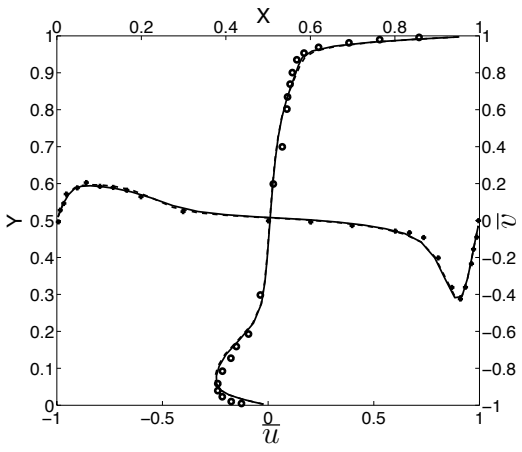

(a) Mean

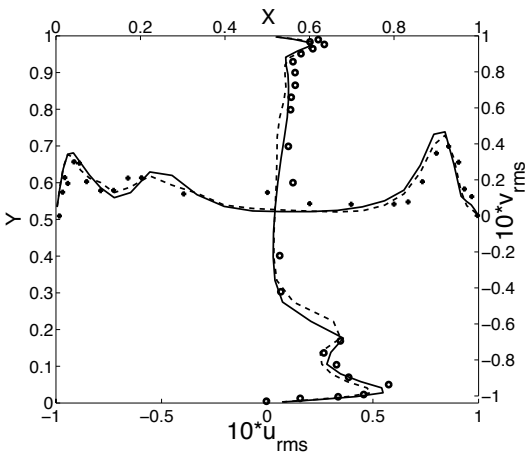

(b) RMS

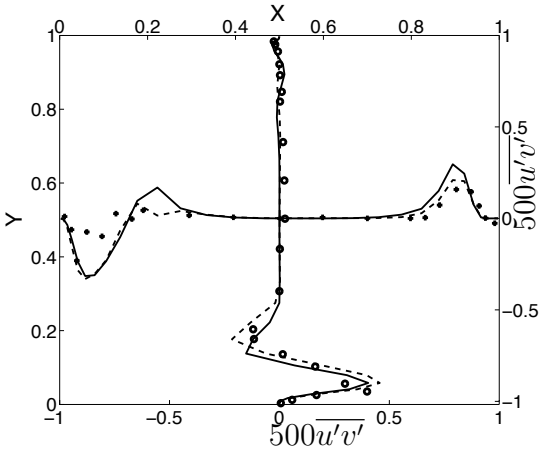

(c) Shear stress

Figure 6.19: Mean flow, rms and shear stress profiles with the flow-dependent definition of α_k^2 for $Re = 3,200$. Solid lines are without the model, dotted lines are the NS-α model, symbols are experimental data [111].

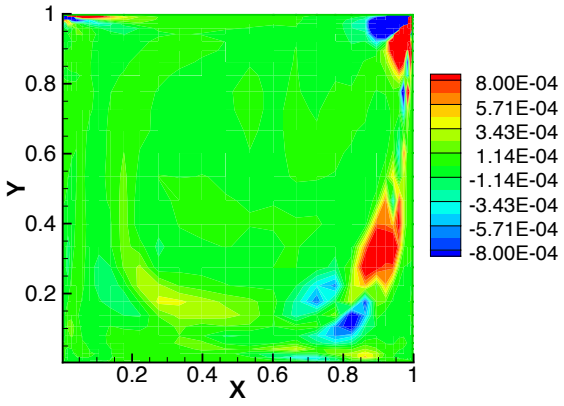

Figure 6.20: Energy transfer for the anisotropic model with α_k^2 based on the flow dependent definition, $Re = 3,200$. In contrast with the mesh-based definition (Figure 6.17(b)) the high energy transfer in the laminar regions near the lid and upper part of the downstream wall are no longer present, with the exception being the top right corner.

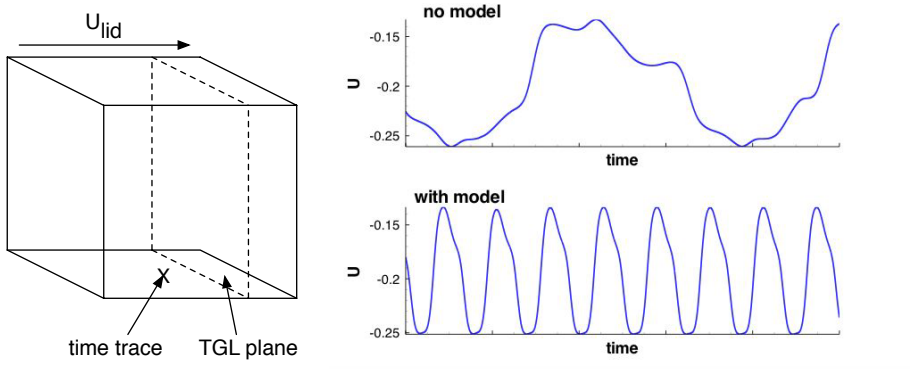

Figure 6.21: Time traces of the streamwise velocity measured near the cavity bottom at $(0.50, 0.047, 0.5)$.

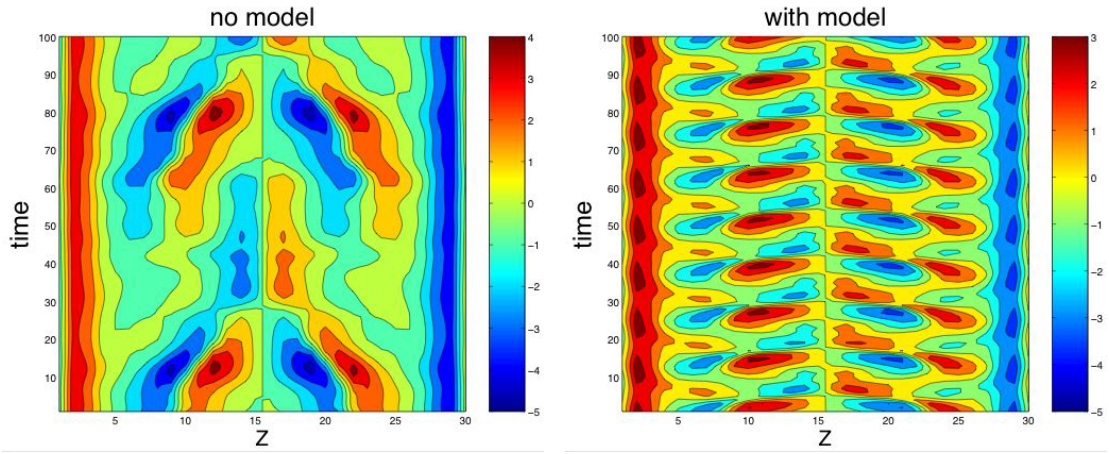

(a) no model (b) NS-α

Figure 6.22: Streamwise vorticity with time, $Re = 3,200$, 32^3 mesh.

Figure 6.23: Contours of streamwise vorticity with time both without a model and with the model. Notice how the pattern is similar with and without the model, but with the model it occurs at a higher frequency.

with contours of streamwise vorticity superimposed. There is a high concentration of backscatter where the TGL vortices are located, $x \approx 0.78$, as shown in figure 6.24.

6.4.2.2 Results for $Re = 10,000$

We now look at the performance of the model with the alternative definition of α_k^2 given in equations (6.20)-(6.22) for the higher Reynolds number case. For comparison, results are also shown for the case where no subgrid model is used. There are several ways the performance of a subgrid model can be assessed. We start by

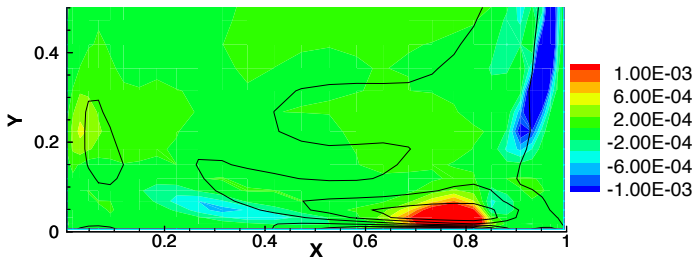

Figure 6.24: Energy transfer term T_{SGS} in the bottom half of the cavity. Streamwise vorticity contours are superimposed to show the coincidence between backscatter (red) and the TGL vortices. $Re = 3,200$, 32^3 mesh.

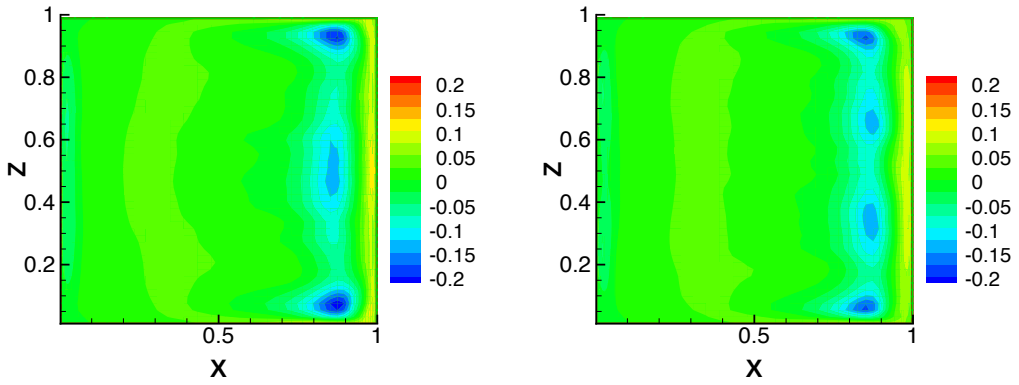

(a) Without model

(b) With model

Figure 6.25: Contours of $\overline{v}$ looking down at the cavity bottom (on the $y = .005$ plane) for $Re = 10,000$ on the 48^3 mesh. This figure shows that the wall jet correctly splits into two when the model is used, but does not split without the model.

looking at how well the mean flow is captured, which is reflected in the wall jet structure. Recall that the flow should split into two wall jets, which impinge on the cavity bottom. We can see in Figure 6.25 that when a model is not used the flow does not split into two jets, and that this situation is corrected when we used the NS-α model. We found that even on the coarse mesh of $(32)^3$ the NS-α model with the alternative definition of α_k^2 can correctly produce the splitting into two wall jets. However, because the energy spectra at such a coarse resolution did not exhibit a $k^{-5/3}$ slope, no results from this test case are shown. The mean flow, rms and shear stress profiles are shown in Figure 6.26 for the 48^3 mesh and in Figure 6.27 for the 64^3 mesh. In Figure 6.26 we also show the mean flow profile from using the mesh-based α_k^2. It can be clearly seen that with the flow-dependent definition we are able to obtain the correct mean flow profile. It can also be clearly seen that the new model does a good job of capturing the velocity fluctuations near the lid and in the downstream wall jet region, and that the shear stress profiles are in excellent agreement with the experimental data [111]. In contrast, without the model (solid line) the fluctuations are too low, and the shear stress is underpredicted. For the finer mesh results shown in Figure 6.27 the differences with and without the model are small, indicating that as $\alpha_k^2 \to 0$ the simulation moves towards a DNS as it should.

The highly inhomogeneous and anisotropic nature of lid driven cavity flow was well documented in the DNS study of Leriche and Gavrilakis [71] and LES carried

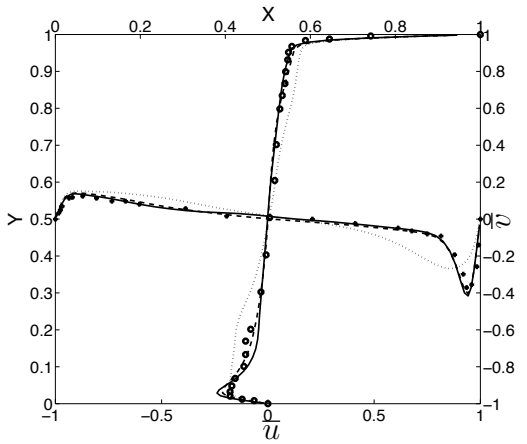

(a) Mean

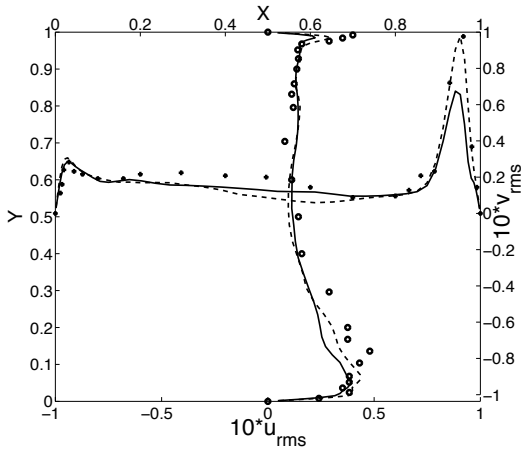

(b) RMS

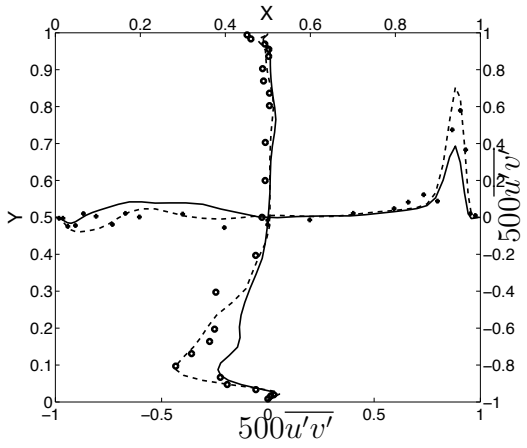

(c) Shear stress

Figure 6.26: Mean flow, rms and shear stress profiles on the midplane for the 48^3 mesh, $Re = 10,000$. Solid line is no model, dotted line (first plot only) is NS-α with the mesh-based definition of α_k^2 and dashed line is NS-α with alternative definition of α_k^2. Symbols are experimental data.[111]

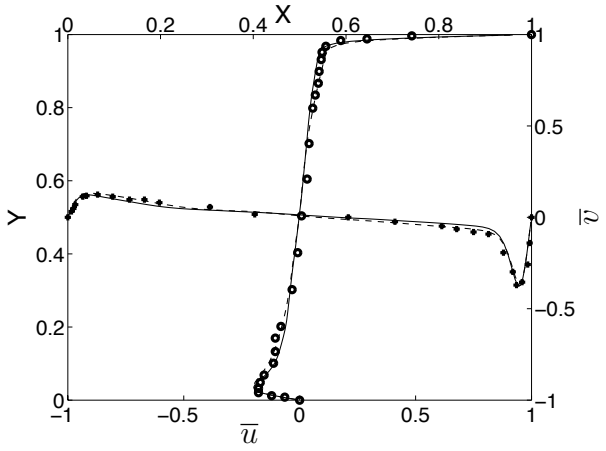

(a) Mean flow

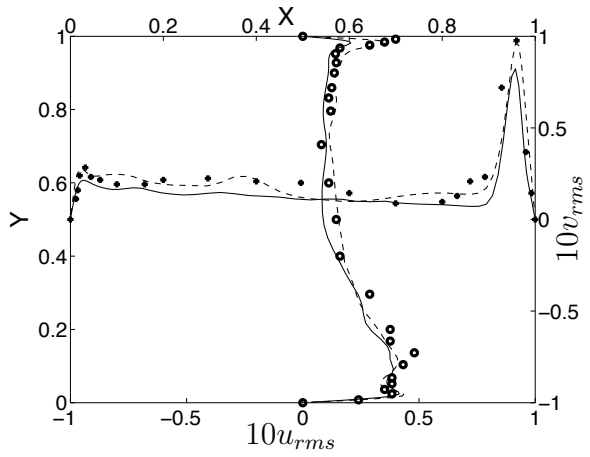

(b) RMS

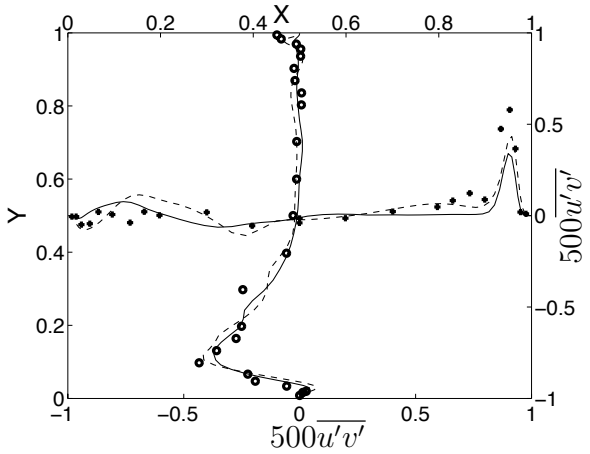

(c) Shear stress

Figure 6.27: Mean flow, rms and shear stress profiles on the midplane for the 64^3 mesh, $Re = 10,000$. Solid line is no model, dashed line is with alternative definition of α_k^2. Symbols are experimental data. [111]

	$1 : \int_V \overline{u}^2/\overline{v}^2\, dV : \int_V \overline{u}^2/\overline{w}^2\, dV$
DNS (Lauriche 2000)	1:1.22:50
no model (coarse DNS)	1:1.23:118
NS-α with α^2 based on (6.20)-(6.22)	1:1.22:60

Table 6.2: Relative ratios of the volume-averaged mean velocity components.

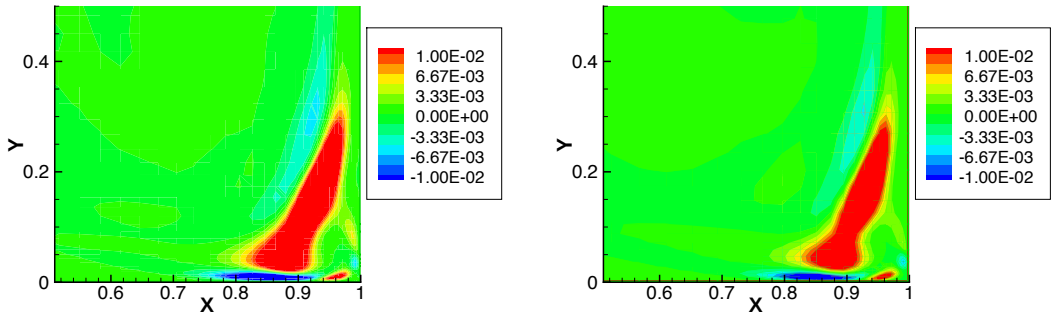

(a) no model, 64^3

(b) flow-dependent NS-α, 48^3

Figure 6.28: Turbulent kinetic energy production near the jet impingement region on the $z = 0.3$ plane, $Re = 10,000$.

out by Bouffanais and Deville [4]. One measure of anisotropy they used is the relative ratios of the volume-averaged mean velocity components. In the present study it was found the ratios with the model compare much more favorably with the DNS study, see Table 6.2. In particular, without the model there is not enough energy associated with the spanwise component. As we have seen in Figure 6.25 when a model is not used the flow does not correctly split into the two wall jets, consequently there is not enough momentum transfer in the spanwise direction.

The flow in the downstream wall jet region is characterized by positive and negative turbulent energy production [71]. Plots of the total production are shown in Figure 6.28. As the downstream wall is approached the dominant contribution to turbulent kinetic energy production is from the $-\overline{v'v'}\partial_y\overline{v}$ terms, and is positive as the flow decelerates. In the impingement region the contributions from the $-\overline{u'u'}\partial_x\overline{u}$ and $-\overline{w'w'}\partial_z\overline{w}$ terms dominate, and these are negative as the flow accelerates. This scenario is in good agreement with the description in the DNS study [71], and we can see from Figure 6.28 that the NS-α model is able to capture this on a fairly coarse mesh of (48^3). It is interesting to contrast the turbulent kinetic energy production with the contribution to the subgrid model. For the lid-driven

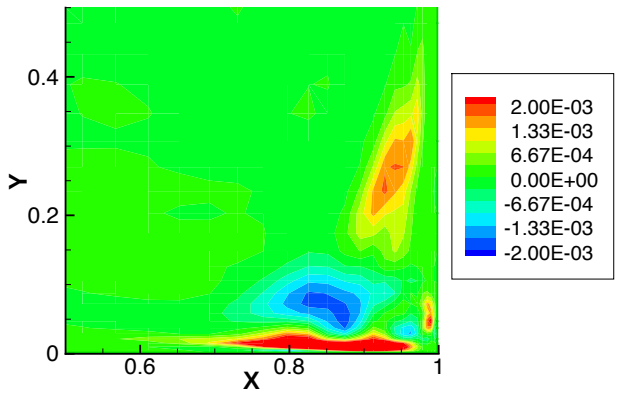

Figure 6.29: Energy transfer term $\tilde{u}_i\tilde{F}_i$ on the $z = 0.03$ plane for the 48^3 mesh, $Re = 10,000$.

cavity the filter width (α_k^2) is not constant and we cannot split the energy transfer into a redistribution term and a source/sink term. Instead we plot the total SGS contribution, $\tilde{u}_i\tilde{F}_i$ divided by the control volume, where the subgrid force is

$$\tilde{F}_i = H^{-1} \int_V \frac{\partial m_{ij}}{\partial x_j}\, dV. \tag{6.23}$$

Contour plots of $\tilde{u}_i\tilde{F}_i$ on a plane near the cavity bottom are shown in Figure 6.29. Note that the energy transfer is an order of magnitude smaller than the turbulent kinetic energy production in Figure 6.28.

To compare the current definition of α_k^2 given in (6.20)-(6.22) with the mesh-based definition from equation (7.14), plots of α_k^2/h_k^2 are shown in Figure 6.30. We can see that α_y^2/h_y^2 is high in the jet impingement region, while α_x^2/h_x^2 and α_z^2/h_z^2 reflect the spreading of the jet on cavity bottom, and the impingement on the upstream wall. Considering that the relationship between the unsmoothed and smoothed velocity in Fourier space is $\hat{u}_i(\boldsymbol{k}) = (1 + \alpha^2|\boldsymbol{k}|^2)\hat{\tilde{u}}_i(\boldsymbol{k})$ we can also look at this as the range of $(\alpha k)^2$ values. When $(\alpha k)^2 = 0$ the model is inactive, while in the turbulent regions we expect $(\alpha k)^2 \sim 1$. This is reflected in the plots shown in Figure 6.30. The actual force experienced by the flow due to the subgrid model is also of interest. In Figure 6.31 we plot the subgrid force contribution to the $x-$momentum equation, which can be compared to the mesh based definition discussed earlier. It can be seen that the high source terms near the lid and in the downstream wall jet region are eliminated when the flow dependent version of α_k^2 is used, and instead the flow is active in the turbulent regions near the cavity bottom.

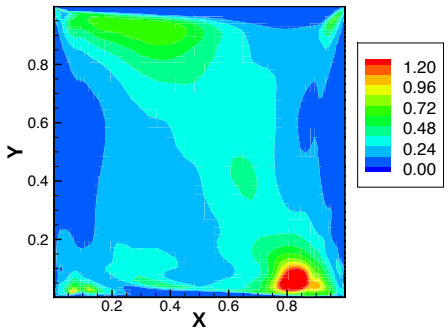

(a) (α_y^2/h_y^2) on the $z = 0.3$ plane

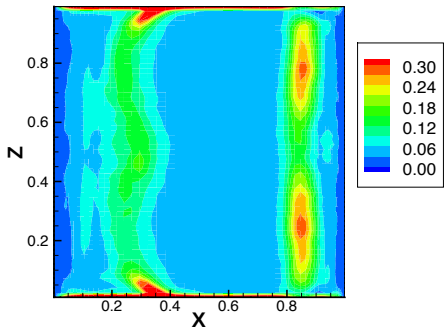

(b) (α_x^2/h_x^2) on the $y = 0.01$ plane

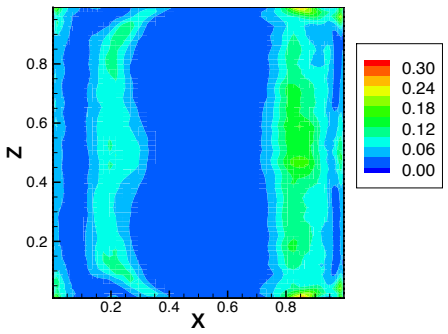

(c) (α_z^2/h_z^2) on the $y = 0.01$ plane

Figure 6.30: Contour plots of α_j^2/h_j^2 highlighting the wall jet impingement and spreading regions for the 64^3 mesh, $Re = 10,000$.

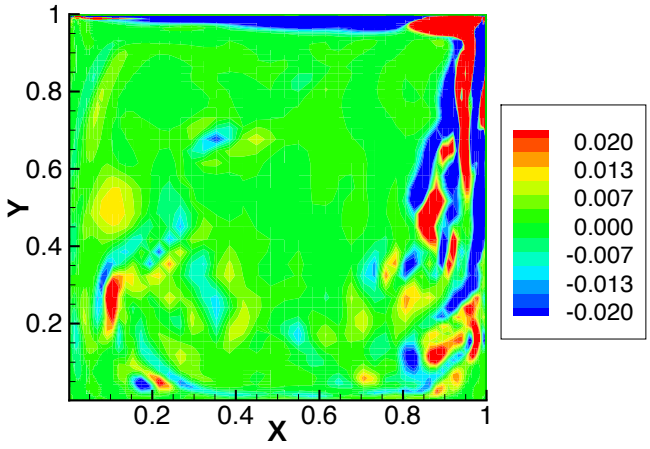

(a) α_k^2 based on the grid.

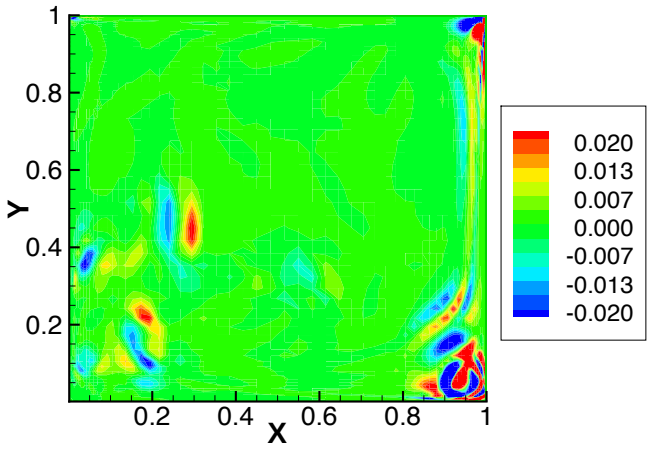

(b) alternative definition of α_k^2

Figure 6.31: Subgrid force to the $x-$momentum equation on the $z = 0.3$ plane (through the impingement region) for the 64^3 mesh, $Re = 10,000$. With α_k^2 based on the grid the force is high in the laminar regions (near the lid and downstream wall), whereas with the alternative definition (equations (6.20)-(6.22)) the force is high only in the turbulent regions.

The previous plots were from simulations where the explicit filter was applied using Helmholtz inversion. For the cavity flow this method was very expensive, adding an overhead of 90% to the computation time. Because Helmholtz inversion is the true operator used in the model development, these initial simulations were done with this filter to ensure that the problems encountered were not due to approximating the Helmholtz operator using another method. In Figure 6.32 we show the mean flow, rms and shear stress profiles comparing the box filter and Helmholtz filter for the $(48)^3$ mesh when that flow-dependent version of α_k^2 is used. It can be seen that the differences between the two are negligible. However, when the box filter is used the model overhead (30%) is much lower than with Helmholtz inversion (90%). This makes the model comparable to other advanced methods [106] that are used for complex flows. Similar results were found by Petersen et al. [105], where they found that to make the model competitive it is necessary to use a box filter, and also reported a computational overhead of 27%.

6.5 Summary

At a Reynolds number of $3,200$ the flow is reasonably well-captured without a model, hence a subgrid model should remain relatively inactive. With the mesh-based definition of α^2 and α_k^2 neither the isotropic or anisotropic model were able to fulfill this requirement. The isotropic model generated excessive backscatter near the lid and was very susceptible to divergence. The anisotropic model performed much better in this respect. However both models experience problems due to the α discontinuity encountered at the endwalls when the boundary condition $\alpha^2 = 0$ or $\alpha_z^2 = 0$ is enforced. For the complex flow used here we decided to use a simple definition of α_k^2 as a function of the flow to overcome this problem. With this definition the model remained largely inactive for the low Reynolds number case, and produced results for the higher Reynolds number that were a significant improvement over the no model case for a fairly coarse mesh of 48^3 (as compared to 64^3 used in the literature [151, 4]).

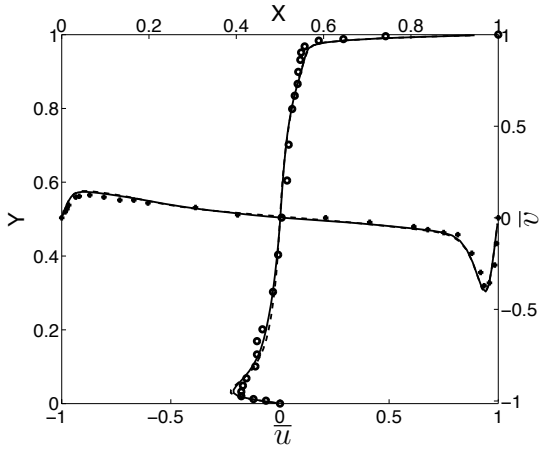

(a) mean

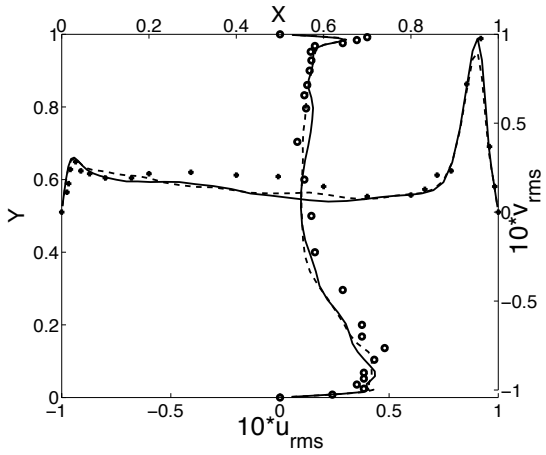

(b) rms

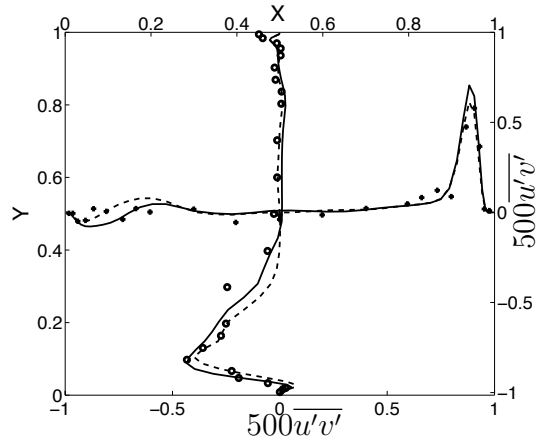

(c) shear stress

Figure 6.32: Mean flow, rms and shear stress profiles for the 48^3 mesh with the flow dependent definition of α^2, $Re = 10,000$. The solid line is with Helmholtz inversion; dashed line is with the box filter, symbols are experimental data [111].

Chapter 7

Channel Flow

7.1 Introduction

Turbulent channel flow (also known as plane Poiseuille flow) is a pressure-driven flow between two flat plates. A sketch is shown in Figure 7.1. It was one of the first test cases to be considered in the pioneering LES studies of the 1970s and early 1980s [16, 124, 93] and remains popular due to its simplicity and relevance to the fundamental problem of flow near solid boundaries. There are many similarities between the channel flow and boundary layers, and both form a basic building block for more complex cases such as the flow over aircraft wings, turbine blades, and the atmospheric boundary layer. However, the test case is not as simple as it looks. Consider that the underlying idea in LES is to capture the large energetic scales, while confining modeling assumptions to the small, unresolved ones. In model development, the filter width is typically assumed to be in the inertial subrange, separating the energy containing and dissipative scales. A fundamental

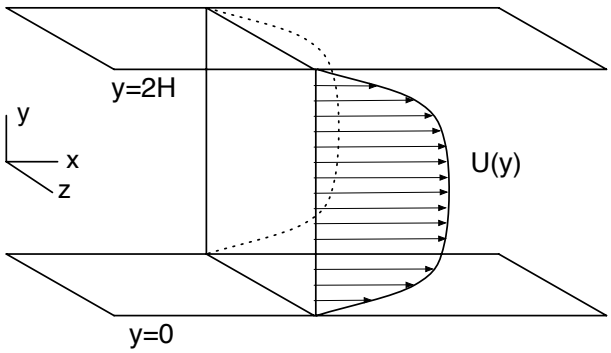

Figure 7.1: Sketch of the plane channel flow

problem encountered in the channel flow test case is that there is no inertial subrange close to the wall and the energetic and dissipative scales overlap [56]. To reduce the effect of the model on the energy-containing scales near the wall it is often necessary to decrease the filter width in this region. Damping functions are a popular way to accomplish [41, 83, 107], but are rarely suitable for more complex flows. Another difficulty with wall-bounded flows is the anisotropy of the near-wall region. The early LES of Schumann [124] used two eddy viscosities, one for the isotropic flow and a second to deal with anisotropy and inhomogenity. A similar model was used by Moin and Kim [93] with reasonable results. Recent models are more sophisticated, incorporating for example dynamic procedures, scale-similarity terms, and velocity reconstruction techniques, but some still have difficulty with even the mean flow profile [20, 39, 123].

The LES literature regarding the channel flow test case can be confusing for the newcomer. Simulation results exhibit a high sensitivity to the mesh resolution [39, 83, 99]. A recent paper by Meyers and Sagaut [91] showed that the convergence towards a DNS result is not monotonic with grid spacing. Their study looked at two different vertical resolutions and two different Reynolds numbers and investigated convergence towards DNS as a function of the streamwise and spanwise grid spacing [1]. The convergence was quantified primarily in terms of skin friction error, but the rms velocities were also studied. In all cases the convergence was not monotonic, and cases that had negligible error for skin friction did not necessarily produce the correct rms fluctuations. The sensitivity to the horizontal mesh resolution is not surprising given the anisotropy of the near-wall structures, however it took them considerable computational effort ($\approx$ 700 simulations) to demonstrate this clearly, and it is likely that the error map would be different for a different numerical method. It has long been a tradition in the LES community to test a subgrid model using a coarse-grid channel flow, and to base the success of the model largely on its ability to reproduce the correct log-law. This study brings into question (finally) the use of plane channel flow as the primary test case for subgrid models, and in particular the emphasis on the logarithmic law. While the study by Sagaut and Meyers was only published recently, the inconsistencies in the literature regarding the channel flow test case were part of the motivation in the

[1] The emphasis on the streamwise and spanwise spacing is because for the channel flow the mesh in these directions is coarse, while a finer mesh is usually used in the wall-normal direction. The fine mesh in the vertical is used so the vertical scales are well resolved and a filter is not required in this direction. This avoids having to deal with non-uniform filter widths that would arise because the mesh is stretched in the vertical

present thesis to include a study of the cavity flow.

The outline of this chapter is as follows. We will start by giving an overview of the physical problem and the numerical description. We will then present results from using the NS-α model for this flow with α_k^2 based on the mesh, along with a discussion of one possible reason why the model has difficulty in this flow. Finally, damping factors and the flow-dependent definition of α^2 will be tested and recommendations for future work will be made.

The notation in the reported results is the same as that used for the cavity flow. An averaged quantity is denoted by an overbar, and a fluctuation about this state is denoted with a prime. For the velocity, vorticity and other profiles reported (quantities that are a function of the vertical coordinate) the averaging is taken over the statistically homogeneous directions x and z as well as with time to increase the statistical sample.

In this chapter quantities are non-dimensionalized using the channel half-height, H, and the shear velocity u_τ

$$u_\tau \equiv \sqrt{\tau_w}, \tag{7.1}$$

where τ_w is the wall shear stress

$$\tau_w \equiv \nu \left. \frac{\partial u}{\partial y} \right|_w \tag{7.2}$$

These non-dimensional quantities are denoted

$$u^+ = \frac{u}{u_\tau} \qquad y^+ = \frac{y u_\tau}{\nu} \qquad Re_\tau = \frac{u_\tau H}{\nu}. \tag{7.3}$$

In the discussion we will refer at times to the different regions of the turbulent velocity profile, shown in Figure 7.2. The focus in this thesis was on wall-resolving LES, thus we are going to consider Reynolds numbers at the low end of the turbulent regime. These channels have only a very small logarithmic region, therefore the discussion herein we will be primarily concerned with the viscous sublayer and buffer region. An alternative approach would have been to focus on high Reynolds number boundary layers, using a wall model. This is beyond the scope of the present work, but should be investigated in a future study.

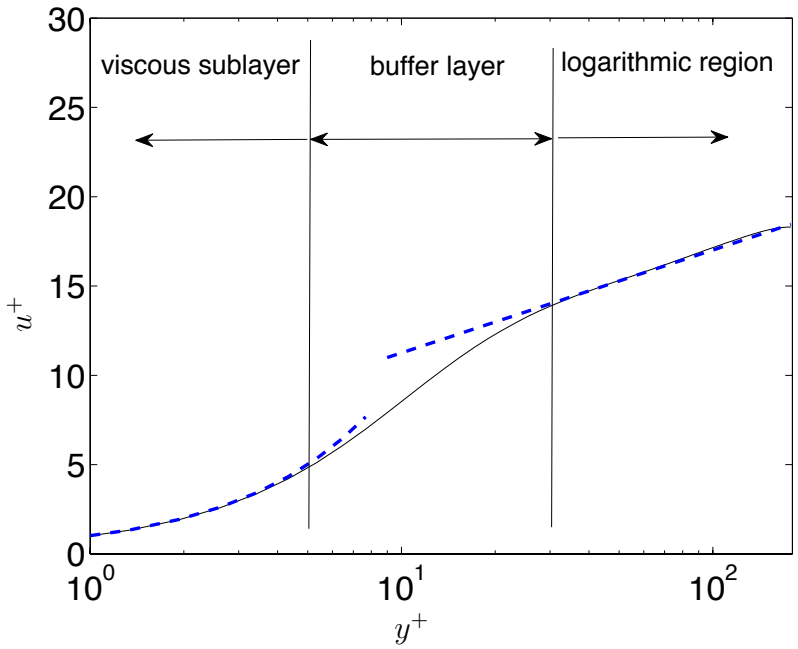

Figure 7.2: Regions of the channel flow. Dashed lines represent $u^+ = y^+$ in the viscous sublayer and $u^+ = 2.5\,lny^+ + 5$ in the logarithmic region. After Tennekes and Lumley [133], chapter 5.

7.2 Physical Problem

In the channel flow test case the solid walls decelerate the flow, and this drag force is balanced by the driving pressure gradient. In a numerical computation the pressure gradient is supplied through a source term in the streamwise momentum equation, while in the laboratory it is supplied by the pump or fan driving the flow. When the flow is fully developed it can be considered statistically homogeneous in the streamwise direction and with time. Typically, in a numerical experiment, it is assumed the duct is very wide, and thus the flow is taken to be statistically homogeneous in the spanwise direction as well. Together these assumptions mean the derivatives of all averaged quantities in these directions is zero

$$\frac{\partial \bar{\cdot}}{\partial x} = \frac{\partial \bar{\cdot}}{\partial z} = \frac{\partial \bar{\cdot}}{\partial t} = 0. \tag{7.4}$$

For the purpose of analysis this allows the governing equations to be simplified considerably. Employing the Reynolds decomposition of the flow velocity into a

mean and fluctuating quantity, the streamwise momentum equation simplifies to

$$0 = -\frac{\partial \overline{p}}{\partial x} + \frac{1}{Re}\frac{\partial^2 \overline{u}}{\partial y^2} - \frac{\partial \overline{u'v'}}{\partial y}. \tag{7.5}$$

A similar simplification of the vertical momentum equation will tell you the driving pressure gradient is independent of the vertical coordinate. Integrating (7.5), applying boundary condition $\overline{u'v'} = 0$ at $y = \pm H$ and using the definition of wall shear stress (7.2) gives you a relationship between the driving pressure gradient and the drag force

$$\frac{\partial \overline{p}}{\partial x} = \frac{\tau_w}{H}. \tag{7.6}$$

Based on the above momentum balance, the turbulent channel flow appears to be very simple. However, the near-wall region of this flow is populated with coherent structures that interact in a complex way to sustain turbulence [54]. The most well known of these structures are the so-called horseshoe vortices postulated first by Theodorsen [134]. It is thought that these vortices form from a perturbation or kink in the spanwise vorticity [117, 102]. Through self-induction this kink is lifted up to from the wall which brings the tip of the vortex into a region of high-speed fluid relative to the legs. The velocity difference between the tip and the legs stretches the vortex to form the hairpin shape.

In recent years improvements in DNS capabilities and experimental methods have enabled a more accurate picture of boundary layer flows. While classic hairpin vortices have been found, most consist of a single leg, or cane shape [117]. In the near-wall region, additional structures have been found. These are streamwise vortices and streaks. The streaks are long bands of alternating low and high speed fluid, where low and high speed is relative to the mean streamwise velocity. A picture is shown in Figure 7.3. The streamwise vortices (which may be related to the legs of the hairpins, or may arise from other mechanisms [102, 56]) are thought to play a crucial role in the formation of these streaks by bringing up low-speed fluid from the near-wall region and returning high-speed fluid. The streaks are known to periodically eject their fluid away from the wall in a process known as bursting. There are different hypotheses as to why the streaks eject fluid [102], one hypothesis being that a low-speed streak creates a local inflection point in the streamwise velocity profile, and the burst is a manifestation of the subsequent instability. The fluid ejected in a burst is replaced by high speed fluid carried into the streak region from the outer region, in an event known as a sweep. Together bursts and sweeps are responsible for the production of Reynolds stresses and hence turbulent kinetic

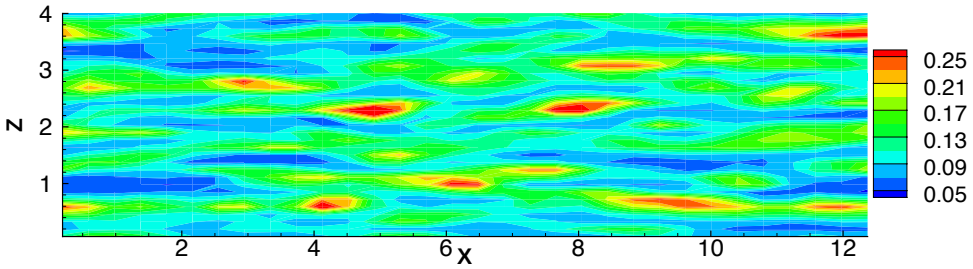

Figure 7.3: Velocity streaks on an $x-z$ plane in the viscous sublayer. The red color indicates high speed fluid while blue indicates low speed fluid, where high and low speed are relative to the mean.

energy. In the context of subgrid modeling they are also associated with forward energy transfer and backscatter respectively [109].

Given this complex taxonomy of structures is is worthwhile to consider which aspects of a turbulent boundary layer a model should be able to capture (keeping in mind that one of the benefits of using LES over RANS is the resolution of energy-containing structures). The streaks are not turbulent in nature and are very long, $L_x^+ \approx 10^3 - 10^4$, with an average spanwise spacing of $L_z^+ \approx 100$ [56]. Each streak has several streamwise vortices associated with it. The vortices are inclined to the wall and typically interact with the near-wall region over a distance of of $x^+ \approx 200$ [56]. Experience has shown that the mesh must be fine enough to sense these large-scale features, $\Delta_z^+ \approx 30$ and $\Delta_x^+ \approx 80$ with three grid points in the viscous sublayer are recommended as minimum values [150] in a wall-resolving LES. The bursts, sweeps and dynamics of the streamwise and hairpin vortices are not typically fully resolved, and their effect on the first and second order statistics (notably turbulent energy production) then needs to be captured by the model. This is complicated by the fact that several studies have shown both forward energy transfer and backscatter are associated with the streamwise and hairpin vortices [100, 108, 109]. Given this, it is not surprising that the Smagorinsky model has difficulty in this flow [42, 108]. Adding a stochastic backscatter term to the Smagorinsky model in the near wall region can compensate for the under-resolved energy production, yielding improved results [85, 19]. This may be because high dissipation near the wall (due to the model) leads to overly-stable streaks. Adding backscatter can serve to destabilize these streaks, leading to the bursting processes necessary for turbulent energy production. Mason [85] has pointed out that accounting for backscatter near the wall is especially important because the lack of the inertial range in this region means

the backscatter will affect the energy containing scales directly.

7.3 Numerical Description

The channel flow is studied using the STREAM code described in Chapter 25. Periodic boundary conditions are applied in the homogeneous directions (streamwise and spanwise) while no-slip conditions are used for the solid boundary located at $y = \pm H$. The mesh is uniformly spaced in the homogeneous directions but stretched in the wall-normal directions using a hyperbolic tangent profile

$$y_i = \frac{1}{2}\left(1 + \frac{\tanh(\Gamma(2i/N_y - 1))}{\tanh(\Gamma)}\right), i = 0..N_y \tag{7.7}$$

where Γ is the stretching parameter. A stretching parameter of 2.0 was used as this gives reasonable resolution near the wall (first node around $y^+ \approx 1 - 2$). A summary of the mesh spacing and domain size used is given in Table 7.1 where the non-dimensionalization for the $^+$ units is with the Reynolds number $Re_\tau = 180$.

(L_x, L_y, L_z)	(N_x, N_y, N_z)	h_x^+	$h_y^+(min)/h_y^+(max)$	h_z^+
$(4\pi, 2, 4\pi/3)$	(32,48,32)	71	1.2/16	35

Table 7.1: Mesh parameters for the channel flow

In our simulations a constant mean mass flux was enforced at a Reynolds number of 4160 based on the centerline velocity of a laminar flow and the channel half-height H. This is equivalent to a bulk flow Reynolds number of $Re_b = 2773$. The Reynolds number was chosen to correspond to $Re_\tau = 180$ for which DNS data is available for comparison. The relationship between the bulk flow and friction Reynolds numbers is given by the empirical formula [15]

$$Re_\tau = 0.175(Re_b)^{0.875}. \tag{7.8}$$

The driving pressure gradient is supplied to the flow through a body force in the streamwise momentum equation. This is done by splitting the pressure gradient term into the sum of a constant driving force (f_x) and a periodic contribution, p_{per}, giving the following streamwise momentum equation (assuming for simplicity that filtering and differentiation commute)

$$\frac{\partial \tilde{u}}{\partial t} + \frac{\partial}{\partial x_j}\left(\tilde{u}\tilde{u}_j\right) = -\frac{\partial \tilde{p}_{per}}{\partial x} - f_x + \frac{1}{Re}\frac{\partial^2 \tilde{u}}{\partial x_k^2} - \frac{\partial \tilde{m}_{1j}}{\partial x_j}. \tag{7.9}$$

Integrating over the domain and applying the periodic and no slip conditions yields

$$\int_V \frac{\partial \tilde{u}}{\partial t}\, dV = -f_x V + 2\tau_w A_y. \tag{7.10}$$

where τ_w is the wall shear stress defined in equation (7.2). Equation (7.10) tells us that for steady flow the applied body force $f_x V$ is balanced by the drag force. For the channel flow the height is $2H$ where $H = 1$, therefore $2A_y = V$ and we can write

$$\int_V \frac{\partial \tilde{u}}{\partial t}\, dV = -f_x V + \tau_w V. \tag{7.11}$$

Thus our unknown force that appears as a source term in the momentum equation can be calculated from

$$f_x V = \tau_w V - \int_V \frac{\partial \tilde{u}}{\partial t}\, dV. \tag{7.12}$$

To maintain a constant mass flux the procedure is as follows. For each time step to first calculate τ_w and U_{bulk} based on the velocity field at the previous time level and then for each control volume calculate the source term

$$f_x V = \tau_w V - K \frac{u_{target} - u_{bulk}}{\Delta t} V \tag{7.13}$$

where the constant K is used to control how much of the correction is applied each time step. This is in essence a simple proportional controller. For $K = 0.01$ the mass flux usually wanders by about $< 0.5\%$ during a simulation, having a negligible impact on the overall statistics [2]

There are number of different ways the turbulent channel flow can be initialized. While the method used does not affect the fully developed solution (the flow is by definition homogeneous with respect to time), it does affect the time required to reach a statistically steady state where averaging can begin. One method widely used because it is simple is to begin with a laminar (parabolic) profile with white noise superimposed to trigger the transition to turbulence. Here instead we used a parabolic profile with a superimposed Tollmien-Schlicting (T-S) wave to provide a 2D disturbance. A T-S wave with amplitude of 10% of the centerline velocity and wavenumber 2 (made dimensionless with the channel half-height) was found to bring the flow to a turbulent state quickly. This method also provided a means to check the periodic boundary conditions. While the transition to turbulence is not physical, in that the planar Poiseuille flow is linearly stable to small perturbations

[2] This method to control the flowrate was suggested to the author by J. Larsson, 2007.

for $Re_b < 3848$ [21] (and for this reason the T-S wave used corresponds to a higher Reynolds number flow), by initializing the flow with a large scale disturbance nonlinear interactions quickly generate a cascade of energy towards the small scales. In addition, because the flow initially develops into an array of periodic structures, any errors in the boundary conditions become immediately apparent. This method was preferred over white noise because it was found the noise had a tendency to either decay before generating a turbulent state, or require a longer time to reach a turbulent state. Although a thorough study was not carried out here, initialization methods should be studied systematically in a separate study.

The method described above was used to initialize all simulations where a model was not used. Simulations with the NS-α model were initialized both using the method described above and also by reading in instantaneous fields from a simulation with the model turned off. Both methods produce the same converged statistics, but the latter method is faster.

7.4 Full Channel Flow Results

7.4.1 No model results

We begin by looking at results with the model turned off. This is important because in some cases a numerical code will produce good results even without a model, and the model results are in fact not a large deviation from this state. In our case, the STREAM code is a very flexible code that is used for a wide variety of geometries and applications, and is not optimized for channel flow. In Figure 7.4 we can see that when a model is not used the logarithmic law is overpredicted although the slope is correct. This means the viscous sublayer is too thick. The skin friction is also underpredicted by 13%, see Table 7.2. The streamwise velocity fluctuations shown in Figure 7.4 are too high, while the vertical and spanwise fluctuations are too low. These results are typical at such low grid resolutions [67] and are probably due to insufficient resolution of the streamwise vortices and/or overly stable streaks.

Vorticity fluctuations with the model turned off are shown in Figure 7.5. We can see that while the spanwise fluctuations are well predicted, the streamwise and vertical fluctuations are too low. An important part of the self-sustaining cycle of near-wall

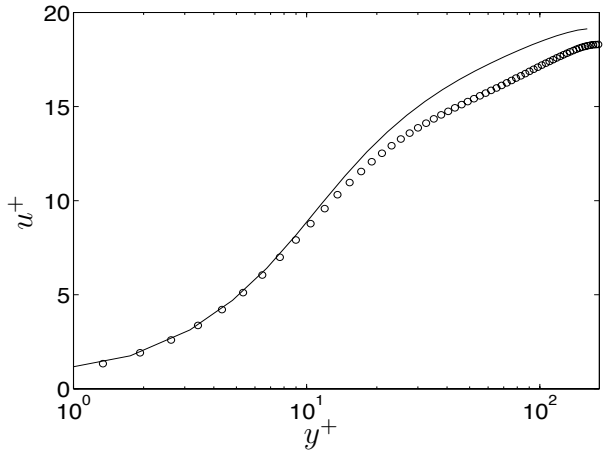

(a) Mean flow

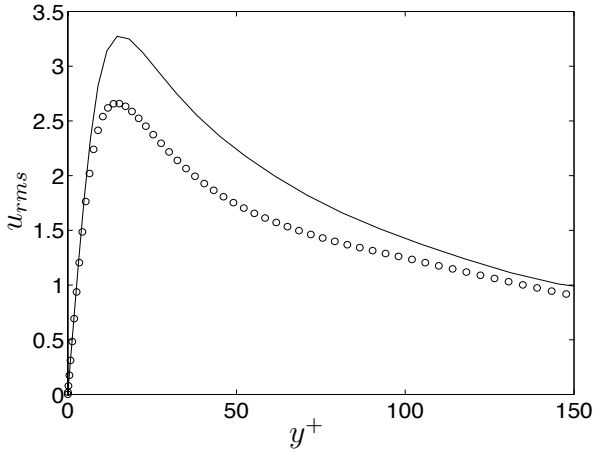

(b) Streamwise

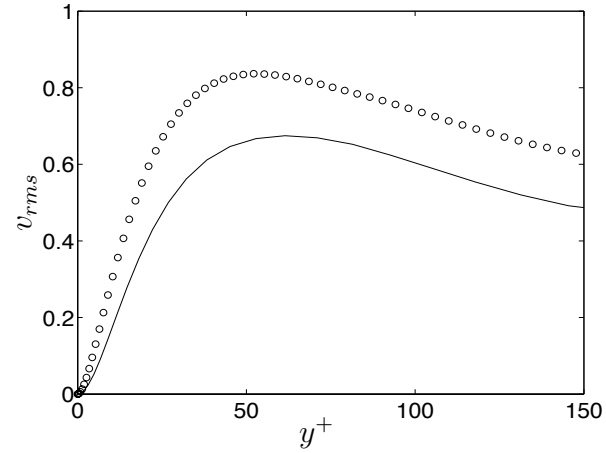

(c) Wall normal

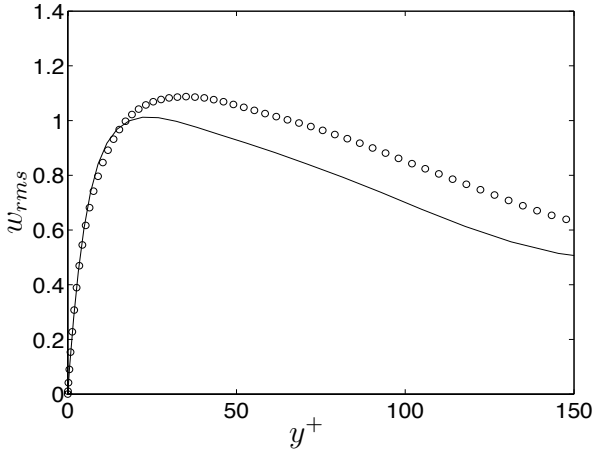

(d) Spanwise

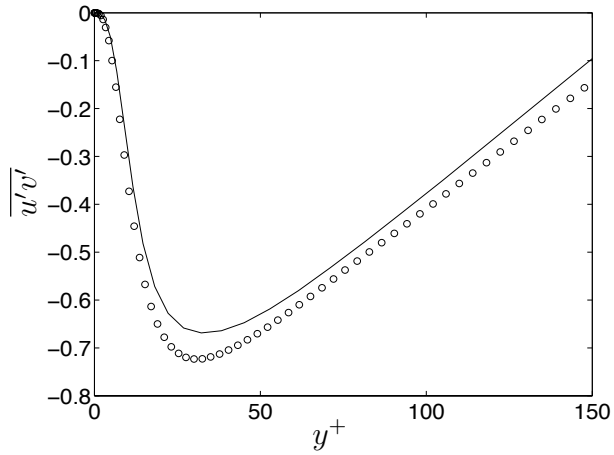

(e) Shear stress

Figure 7.4: Mean flow, rms and shear stress profiles with no model, full channel. Symbols are DNS data[58].

turbulence is the streamwise vorticies, and these are thought to be generated primarily by the lifting up of transverse vorticity, defined as $(\omega_y^2 + \omega_z^2)^{1/2}$, away from the wall where it is tilited into the streamwise direction by the mean flow gradient [53]. The fact that the vertical and streamwise vorticity are underpredicted is not surprising given that the mesh is too coarse to properly resolve these details.

7.4.2 NS-α model results

The situation changes dramatically when we use the NS-α model. The results in this section are with α_k^2 equal to a filter width of twice the grid spacing. This corresponds to $C = 1/6$ for

$$\alpha_k^2 = C\left(h_k^2\right) \tag{7.14}$$

where h_k is the grid spacing in the k-direction. We will refer to this as the default NS-α model. In Figure 7.6 there is a significant undershoot of the logarithmic law, corresponding to high skin friction, see Table 7.2 (recall the velocity is non-dimensionalized with the friction velocity, which is proportional to the skin friction). Note also that the peaks for the vertical velocity fluctuations and shear stress are in good agreement with the DNS data, although the slopes are incorrect, because the channel is too wide in viscous units. The streamwise fluctuations are slightly reduced as compared to the no model case (Figure 7.4), and the peak is closer to the wall than the DNS data, indicating a thin viscous layer. This is in sharp contrast to results with a Smagorinsky model, which typically produces a thick viscous region and low spanwise fluctuations [83].

The most surprising result with the NS-α model is the overshoot of the spanwise fluctuations in Figure 7.6(d). Initially it was thought this problem might be related to α_y^2 given the problems encountered for the cavity flow regarding the wall-normal

Case	Skin Friction (C_f)	C_f error
full channel DNS [58]	3.73×10^{-3}	-
no model	3.25×10^{-3}	-12.9%
NS-α-default	7.46×10^{-3}	100 %
NS-α-default with $\alpha_y^2 = 0$	7.10×10^{-3}	90.3%
NS-α-default with $\alpha_z^2 = 0$	4.63×10^{-3}	24%

Table 7.2: Skin friction for the full channel with and without the NS-α model. Our results are for a $(32, 48, 32)$ mesh, the DNS used a spectral method with a resolution of $(192, 129, 160)$.

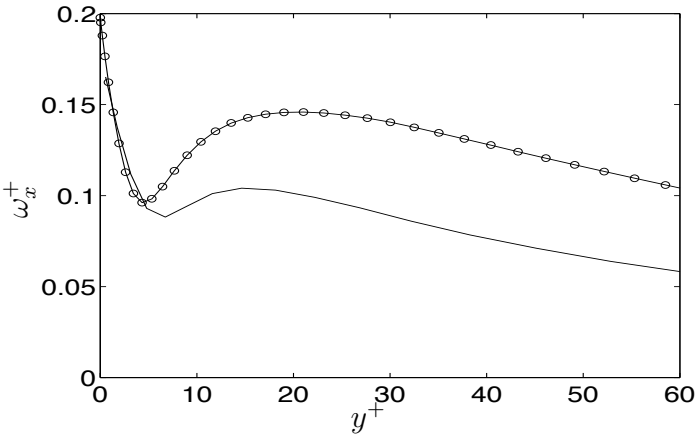

(a) Streamwise

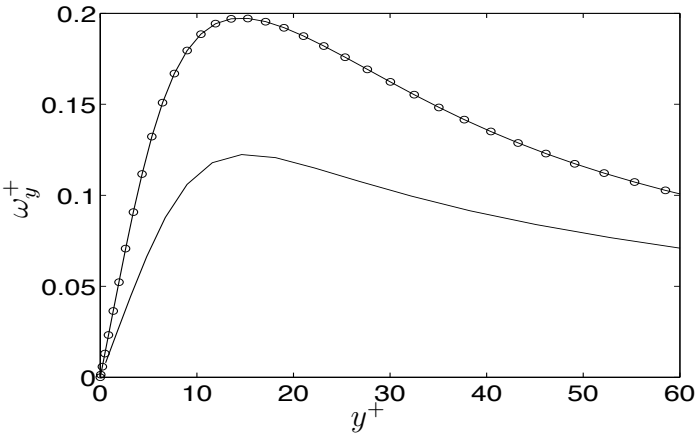

(b) Vertical

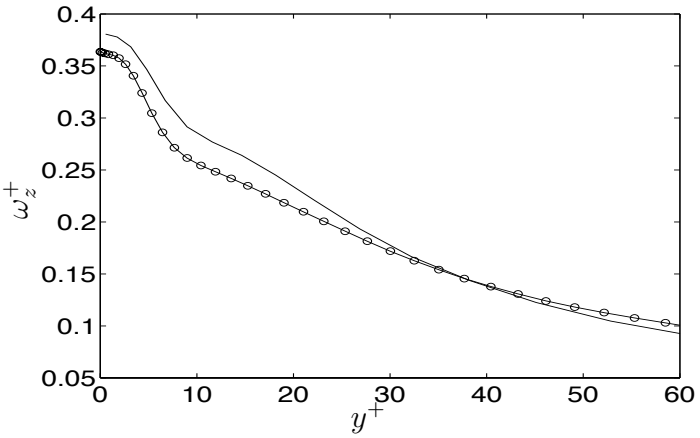

(c) Spanwise

Figure 7.5: RMS vorticity profiles with no model, full channel. Symbols are DNS data [58].

component of α_k^2. To investigate further the model was turned off first in the wall normal direction ($\alpha_y^2 = 0$), and then in the spanwise direction ($\alpha_z^2 = 0$). We can see from the mean velocity profiles in Figure 7.6 and the skin friction coefficients given in Table 7.2 that it was not α_y^2 but α_z^2 causing the problem. It should be noted that checks were made to ensure this was not a simple implementation error, for example by switching the coordinate directions, and also by comparing analytical solutions for the m_{ij} term with computed solution using a simple test field. We can see from the rms and shear stress profiles that turning off α_y^2 does smooth out some slight oscillations in the shear stress profiles, but otherwise does not have a significant impact on the results, while turning off α_z^2 removes the near-wall peak in the w_{rms} profile. In fact, because the DNS data from Kim et al. [58] underpredicts the spanwise velocity fluctuations as compared to the experimental data [68], the spanwise fluctuations with $\alpha_z^2 = 0$ are actually fairly good. Turning off α_z^2 also moves the peak in the streamwise fluctuations farther from the wall. The peak is at $y^+ \approx 10$ for the default model, while for $\alpha_z^2 = 0$ it is at $y^+ \approx 14$. In the DNS study [58] the peak in the u_{rms} profile is at $y^+ \approx 15$. It was also verified that the results are not due to a problem with the explicit filter. In Figure 7.7 we can see the results are almost identical when a box filter is used. The only difference between the two is that the spanwise fluctuations are slightly lower when Helmholtz inversion is used.

High fluctuation levels have been reported before in the literature for the NS-α model [32]. In this case their remedy was to refine the mesh, increasing the subgrid resolution. They found using $\alpha \sim h$ to yield reasonable results. Due to the fact that our numerical code was not parallelized, increasing the mesh resolution was not an option for this channel. Instead we set $\alpha_k = h_k$, thus increasing the subgrid resolution (scale separation between filter width and smallest grid size) by increasing the physical size of α_k^2. The results with this increased scale separation are shown in Figure 7.7, and we can see that this does not improve the situation. The problematic high spanwise fluctuations are still present, and the underprediction of the logarithmic law is even more severe.

To put the results from the NS-α model without wall modification into perspective we recall that when the default Smagorinsky model is used without near-wall damping or a dynamic procedure the flow relaminarizes [129]. A comparison with the NS-α model would be to use the isotropic NS-α model without any near-wall modifications, for example either setting α^2 to a constant, or to the grid-cell volume. We found in this case the simulation diverged quickly. Using the anisotropic model allows for numerically stable solutions, but basing α_k^2 on the mesh does not

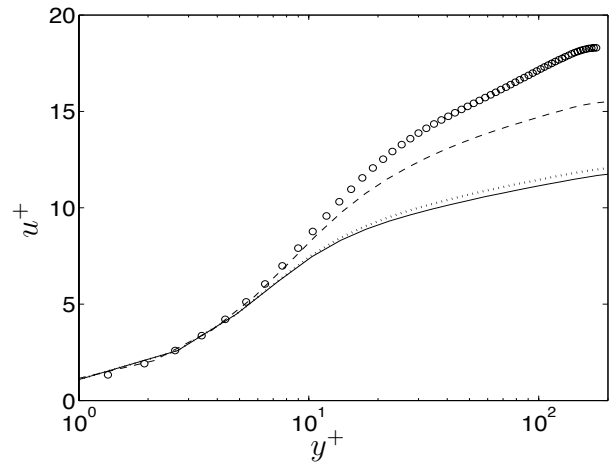

(a) Mean flow

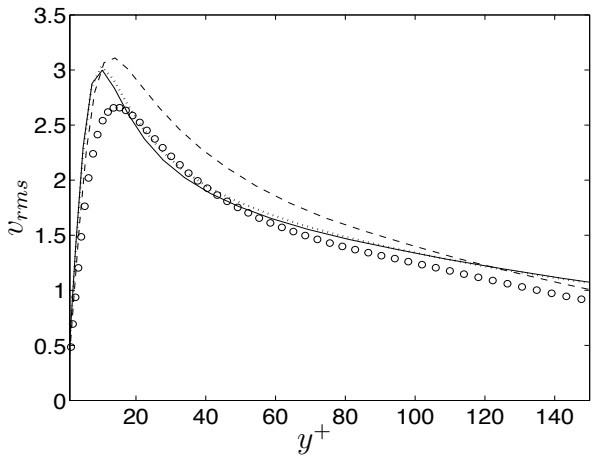

(b) Streamwise

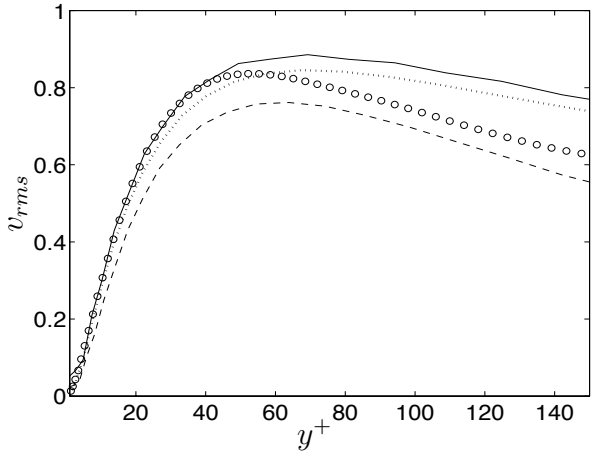

(c) Wall normal

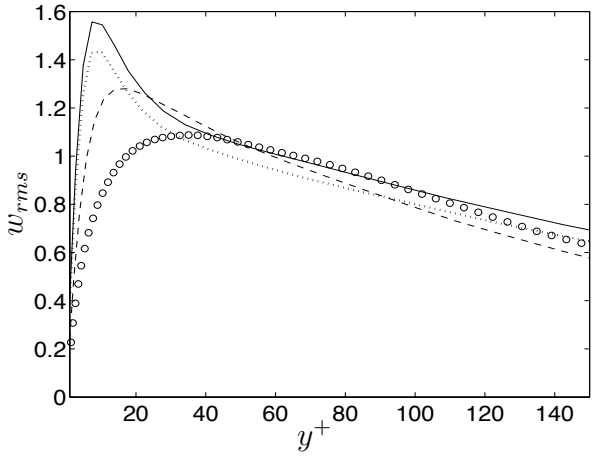

(d) Spanwise

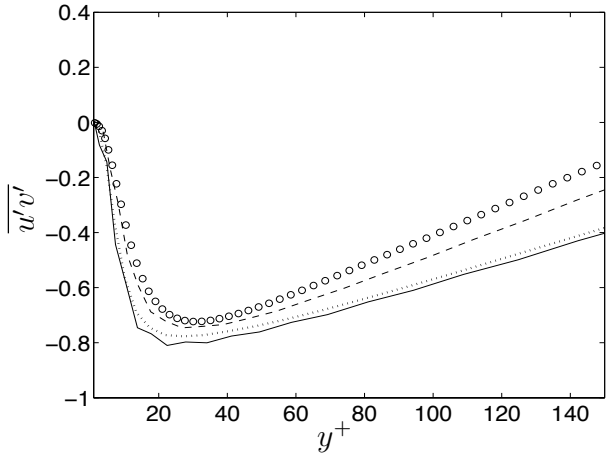

(e) Shear stress

Figure 7.6: Results with α_k^2 based on the mesh. Solid line is default model, dashed line is with $\alpha_z^2 = 0$ while dotted line is with $\alpha_y^2 = 0$. Symbols are DNS data [58].

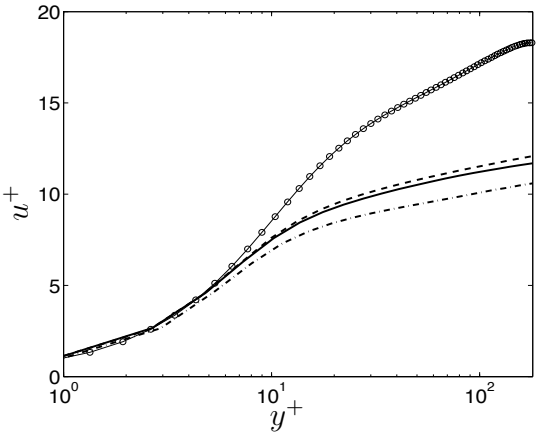

(a) Mean flow

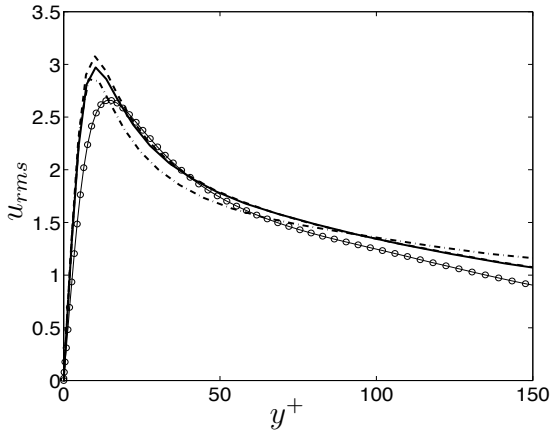

(b) Streamwise

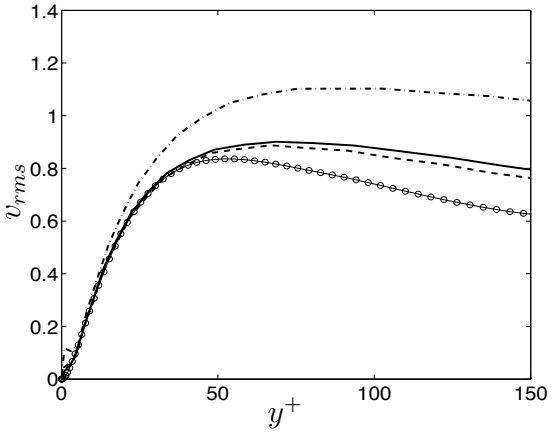

(c) Wall normal

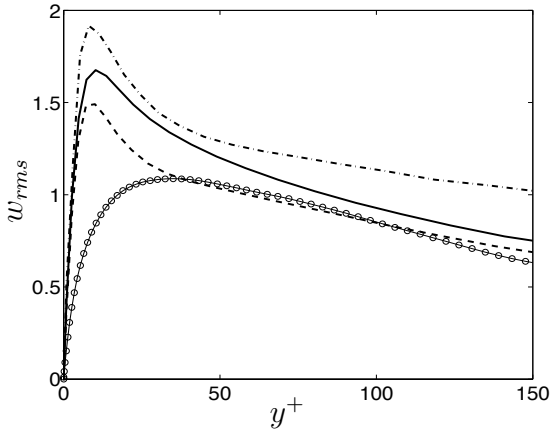

(d) Spanwise

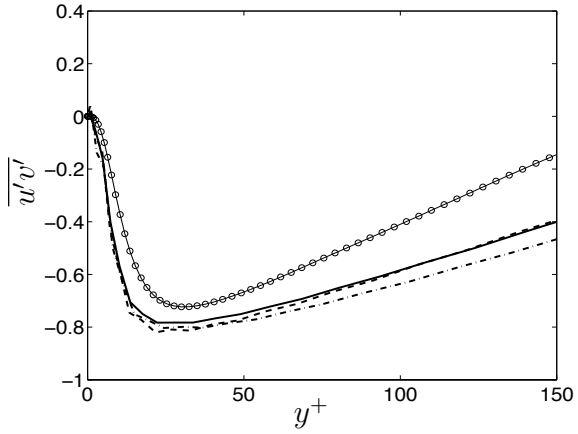

(e) Shear stress

Figure 7.7: Results with two different filters; α_k^2 based on the mesh. Dashed line is Helmholtz inversion with $\alpha_k^2 = h_k^2/6$; solid line is a box filter with $\alpha_k^2 = h_k^2/6$; dash-dotted line is Helmholtz inversion with $\alpha_k^2 = h_k^2$.

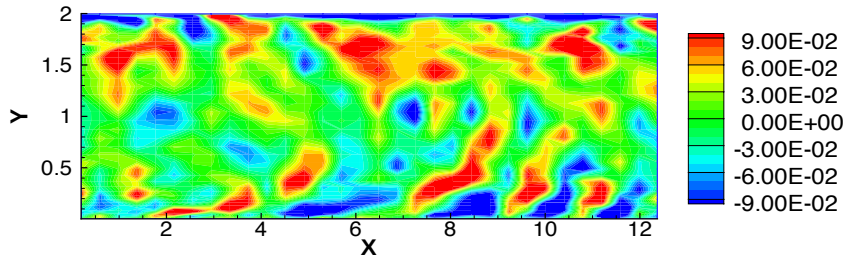

(a) NS-α

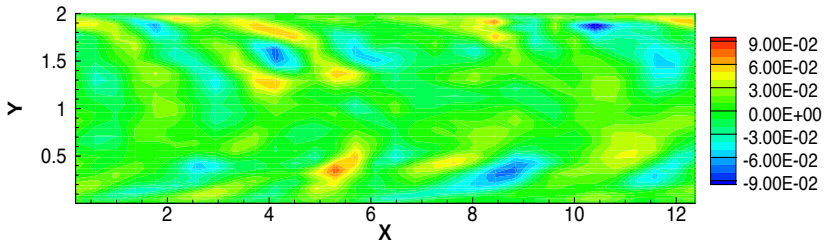

(b) no model

Figure 7.8: Contours of the instantaneous spanwise velocity. Contour levels ± 0.08.

necessarily lead to physically relevant results.

It is interesting to compare snapshots of the instantaneous spanwise velocity with and without the NS-α model. These are shown in Figure 7.8. We can see the velocity field for the NS-α contains more small-scale activity and coherent structures close to the grid scale. This is consistent with what is found in other studies [45, 32]. While the activity appears to be poorly resolved, the energy spectrum shown later in section 7.7 does not show any build-up in the high wavenumbers, thus we don't believe that this result is dominated by numerical error at the small scales. In contrast, we can see that without a model the velocity contours are very diffuse.

While the current results for the NS-α model are not encouraging in that the skin friction is too high and there is clearly a problem associated with the near-wall region, it should be pointed out that there are some promising aspects to these results. The NS-α model clearly has an entirely different behavior than that reported for eddy viscosity models [83]. If we can understand this behavior then there is potential for the model to produce very good results. Working towards this understanding is the focus of the next section.

	Re	(L_x, L_y, L_z)	(N_x, N_y, N_z)	h_x^+	$h_y^+(min)/h_y^+(max)$	h_z^+
I	4,160	$(\pi, 2, 0.3\pi)$	(16,64,16)	35.3	0.875/11.6	10.6
II	4,160	$(\pi, 2, 0.3\pi)$	(24,64,24)	23.6	0.875/11.6	7.07
III	4,160	$(\pi, 2, 0.3\pi)$	(32,64,32)	17.7	0.875/11.6	5.30
IV	4,160	$(\pi, 2, 0.3\pi)$	(32,128,32)	17.7	0.424/5.80	5.30

Table 7.3: Mesh parameters for the minimal channel flow.

7.5 Minimal channel flow

To look at the channel flow over a wider range of parameters an investigation was done using the minimal channel flow. This channel is much smaller than the one used in the previous section, allowing us to use a fine grid (resolution almost equivalent to a DNS). The meshes used are summarized in Table 7.3. The term 'minimal channel' refers to the smallest flow unit that has been found able to sustain turbulence for a given Reynolds number [53]. Such a flow unit consists of a single low-speed streak (or more accurately, a section of such a streak) along with a pair of quasi-streamwise counter-rotating vortices. While it is not large enough to provide a realistic description of the dynamics of the outer region, Jimenez [53, 54] has shown that it provides a valid representation of the near-wall region. Hence, these channels are often used in studies of near-wall turbulence.

For this purpose we chose a channel of dimension $(\pi, 2, 0.3\pi)$ with Reynolds number $Re_\tau = 180$. This means the spanwise dimension in viscous units will be $L_z^+ \sim 180$. This is wide enough to sustain turbulence, which is estimated by Jimenéz [53] to be $L_z^+ \sim 85 - 110$. Note that the channel width required to sustain turbulence corresponds to the width of a streak. Jimenez [53] showed that narrower channels had a tendency to relaminarize.

The DNS here was initialized in the same manner as for the full channel simulations in the previous section. Simulations were run for $t = 400U_b/h$ before beginning to collect statistics (at this time the total skin friction was oscillating with time about a mean value and the time-averaged total shear stress exhibited a linear variation across the channel width). Statistics were then collected over $t = 400U_b/h$. For the minimal channel long integration times are required since you are essentially sampling only one or two turbulent structures instead of a larger array as you would have in a larger domain.

7.5.1 Mean flow and RMS and shear stress profiles

Mean flow, rms and shear stress profiles are shown in Figure 7.9 for the no model case with the $(24, 64, 24)$ mesh. We can see that all quantities are in good agreement with the full channel DNS [58]. The rms profiles deviate slightly from the full channel DNS data near the channel center. This is to be expected for the minimal channel flow, because it is towards the center that the presence of the missing outer flow is felt [53] . Reynolds stress budgets were also computed (not shown) and were in good agreement with those reported for the full channel DNS [58].

Simulation results with the NS-α model are shown in Figure 7.10. For the results shown $\alpha_y^2 = 0$ to keep the comparison with the two different C values on the $(16, 64, 16)$ and $(32, 64, 32)$ meshes exact in the sense that the α_k^2 values on the two meshes are identical (recall from earlier results also that α_y^2 does not significantly impact the results). We have already seen for the full channel turning off α_y^2 has a negligible impact on the results, and preliminary tests found this to be the case also for the minimal channel. Consistent with the results at the lower mesh resolution, NS-α model severely underpredicts the log-law. The rms profiles are somewhat different than those at the lower resolution (compare Figure 7.10 with Figure 7.6). We now have an underprediction of the streamwise velocity fluctuations, and high spanwise and vertical fluctuations.

There are two main features the reader should be aware of when looking at Figure 7.10. The first is that when C is maintained at a constant value of $1/6$, corresponding to a filter width of twice the mesh spacing, and the mesh is refined, the results do not approach the DNS data. Instead, they become slightly worse in that the u_{rms} and v_{rms} increasingly deviate from the DNS data. While this might seem counter-intuitive, other studies have also found that decreasing the filter width (and thus the model contribution) does not necessarily mean the simulation results monotonically approach a DNS [32]. The reason for this is at a finer mesh numerical errors that may have been compensating for modeling deficiencies (eg. numerical dissipation) are smaller. Here we also have a model composed of products of velocity gradients. Refining the mesh, and improving the resolution of these gradients, may be increasing the subgrid contribution more than decreasing the actual value of α_k^2. The second feature to note is that varying the subgrid resolution by altering the C value while keeping the physical size of α_k^2 constant significantly worsens the results. Again, this could be due to the fact that on the finer mesh the gradient are higher. When we keep the physical value of α_k^2 the same the overall effect would then be a

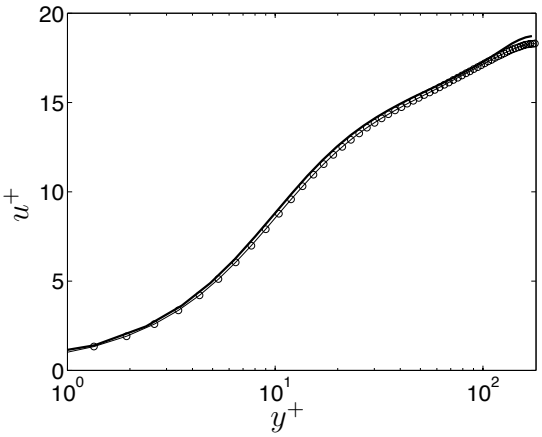

(a) Mean flow

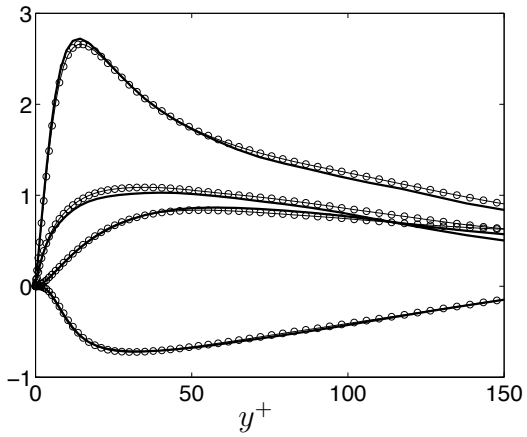

(b) Rms velocities and shear stress profiles. Top to bottom; u_{rms},w_{rms},v_{rms},$\overline{u'v'}$.

Figure 7.9: Mean, rms and shear stress profiles with no model for the $(24, 64, 24)$ mesh; symbols full channel DNS [58].

higher subgrid stress. Pictures of the instantaneous spanwise velocity are shown in Figure 7.11. Unlike the full channel where we could clearly see grid-resolution effects, for the minimal channel the small-scales are well resolved. However, once again there is too much small-scale activity for the NS-α model, especially in the near-wall region.

To investigate the effect of the model on the flow structures further in Figure 7.12 we plot PDFs of the coherent structure function F_{CS}. The coherent structure function is defined as [60],

$$F_{CS} = \frac{Q}{E}, \tag{7.15}$$

where Q is defined as

$$Q = \frac{1}{2}\left(\tilde{W}_{ij}\tilde{W}_{ij} - \tilde{S}_{ij}\tilde{S}_{ij}\right), \tag{7.16}$$

and E is

$$E = \frac{1}{2}\left(\tilde{W}_{ij}\tilde{W}_{ij} + \tilde{S}_{ij}\tilde{S}_{ij}\right). \tag{7.17}$$

The tensors $\tilde{W}_{ij}$ and $\tilde{S}_{ij}$ are the rotation and strain tensors

$$\tilde{S}_{ij} = \frac{1}{2}\left(\frac{\partial \tilde{u}_j}{\partial x_i} + \frac{\partial \tilde{u}_i}{\partial x_j}\right), \tag{7.18}$$

$$\tilde{W}_{ij} = \frac{1}{2}\left(\frac{\partial \tilde{u}_j}{\partial x_i} - \frac{\partial \tilde{u}_i}{\partial x_j}\right). \tag{7.19}$$

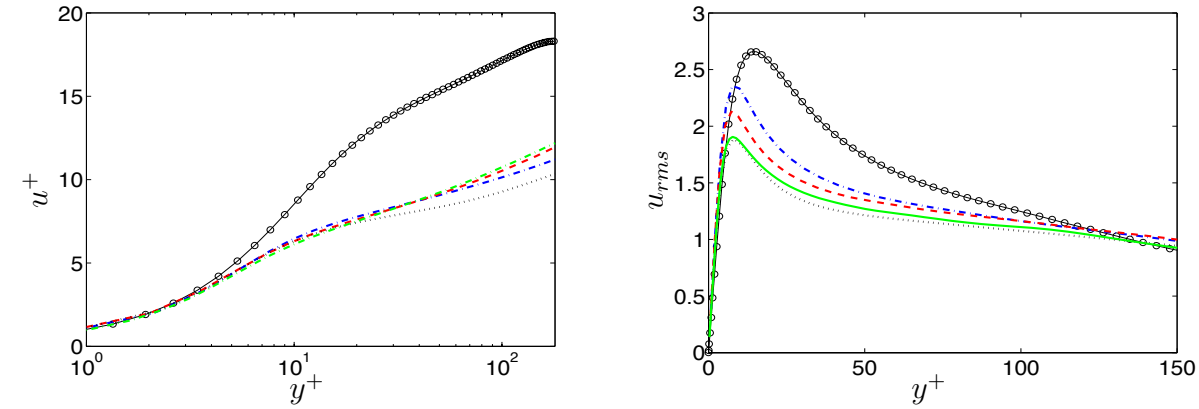

(a) Mean flow

(b) Streamwise

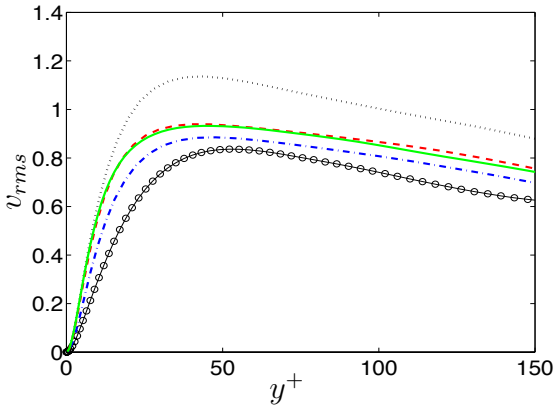

(c) Vertical

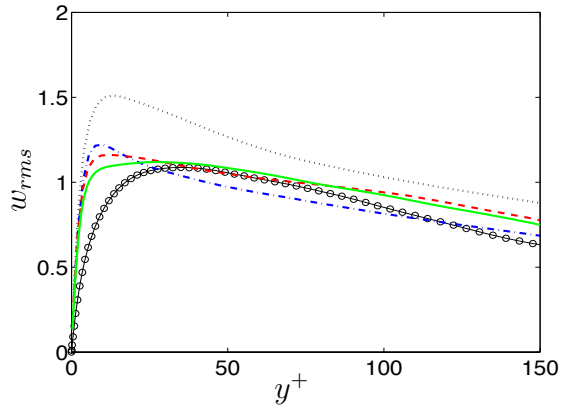

(d) Spanwise

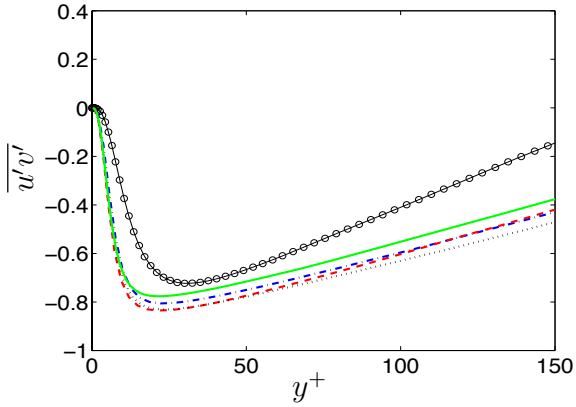

(e) Shear stress

Figure 7.10: Mean, rms and shear stress profiles. Dash-dotted line (blue), $C = 1/6$, $(16, 64, 16)$; dashed line (red), $C = 1/6$, $(24, 128, 24)$; dotted line (black), $C = 2/3$, $(32, 64, 32)$; green line (solid) $C = 1/6$, $(32, 128, 32)$; symbols full channel DNS [58]. To look at the effect of refining the mesh while keeping the subgrid resolution constant the blue, red and green lines can be compared. To look at the effect of keeping the physical size of α_k^2 constant while refining the mesh (hence increasing the subgrid resolution) the blue and black lines can be compared.

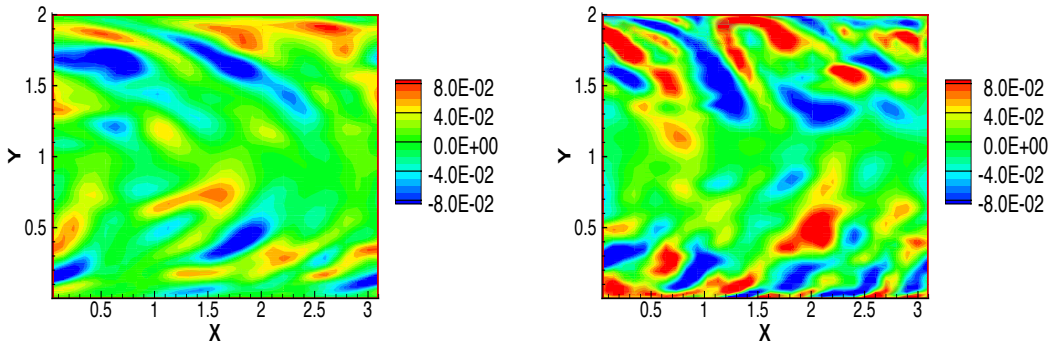

(a) DNS (b) NS-α

Figure 7.11: Contours of the instantaneous spanwise velocity for the minimal channel for the $(32, 128, 32)$ mesh.

The parameter Q is often used to identify coherent structures in a turbulent flow and measures the relative strength of rotation vs. strain [14]. The parameter F_{CS} is then a normalized measure of rotation vs. strain with

$$-1 \leq F_{CS} \leq 1. \tag{7.20}$$

By looking at PDFs of F_{CS} we can get an idea of the distribution of the flow structures. These PDFs are shown in Figure 7.12 for two wall-normal locations. The first, at $y^+ \approx 18$ is in the buffer layer, while the second, at $y^+ \approx 85$ is in the upper buffer or lower logarithmic region. We can see that for the full channel when a model is not used there is a narrower distribution of flow structures as compared to the minimal channel indicating the coarse resolution used for the full channel fails to capture the full range of F_{CS} (assuming the minimal and full channels would have roughly the same PDFs at equivalent resolutions). When the NS-α model is used the distribution in the buffer layer is too wide, indicating the intermittent nature of the flow (in fact part of this may be because the buffer layer is most likely closer to the wall for the default NS-α model, so at $y^+ = 18$ we are already outside the buffer layer). On the other hand the PDF farther from the wall is in better agreement with the DNS, indicating the model influences the flow structures mostly in the near-wall region on this fine mesh. For the full channel we also show results for the NS-α model with a wall-normal damping function (the specific function will be discussed later). The important aspect to take note of here is that with wall damping the NS-α model produces PDFs on a coarse mesh that are in good agreement with those without a model for the minimal channel (mesh II) at both wall-normal locations. Because the minimal channel has a finer mesh than the full

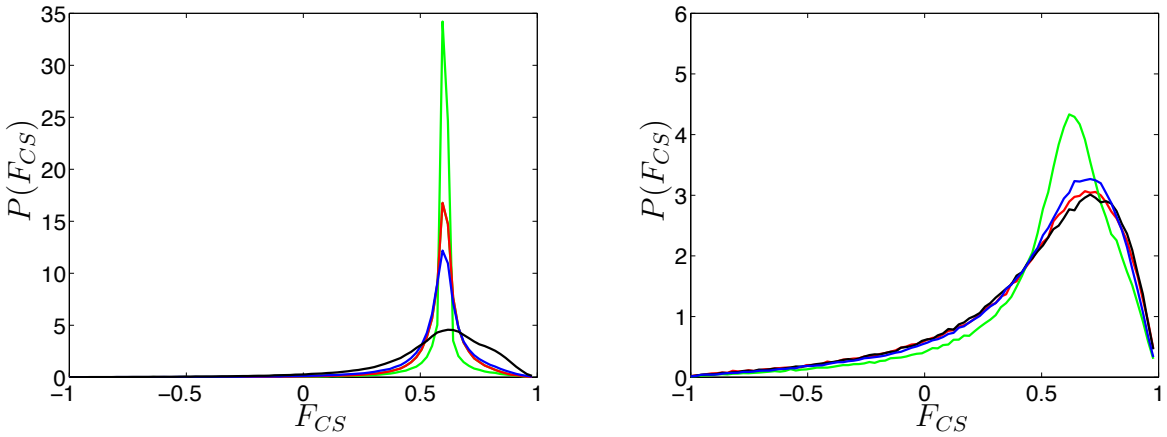

(a) $y^+ \approx 18$ (b) $y^+ \approx 85$

Figure 7.12: F_{CS} PDFs at two different wall normal locations. Blue line, minimal channel DNS (mesh II); black line, minimal channel NS-α (mesh II); green line, full channel no model; red line, full channel NS-α with damping. Meshes are given in Tables 7.1 and 7.3 for the full channel and minimal channel respectively.

channel (compare Tables 7.1 and 7.3) this indicates the NS-α does a good job of capturing vortex structures at a coarser grid resolution, in qualitative agreement with other studies [44, 32]. While concrete conclusions could only be made with a full channel DNS and using a more thorough investigation of definitions of coherent structures, these preliminary results do indicate there is a clear benefit to using the model with regards to statistics of flow structures.

As discussed earlier in Section 4.2 the subgrid energy transfer term, $T_{SGS} = \tilde{m}_{ij}\partial_j\tilde{u}_i$, is important in the assessment of a subgrid model because it represents the energy transfer from the resolved to subgrid scles. In this section α_x^2 and α_z^2 are constant, while α_y^2 is zero, and we can split the energy transfer into the source/sink term (T_{SGS}) and redistribution term (see Equation (4.21)). Plots of T_{SGS} as a function of the wall normal distance are shown in Figure 7.13. Both the total transfer due to the m_{ij} term and the individual contributions from the $\tilde{A}_{ij}$, $\tilde{B}_{ij}$ and $\tilde{C}_{ij}$ terms (see eg. (4.16)) are shown. Note that the contributions from both the $\tilde{A}_{ij}$ and $\tilde{B}_{ij}$ terms are net dissipative, while the $\tilde{C}_{ij}$ term produces net backscatter. For all three terms the instantaneous values (not shown) fluctuated about these mean values by an order of magnitude, exhibiting both forward transfer and backscatter.

In Figure 7.13 for the case where $C = 1/6$ (filter width of twice the grid size) the minimum subgrid transfer (or maximum SGS dissipation) is $T_{SGS}^+ \approx -0.06$

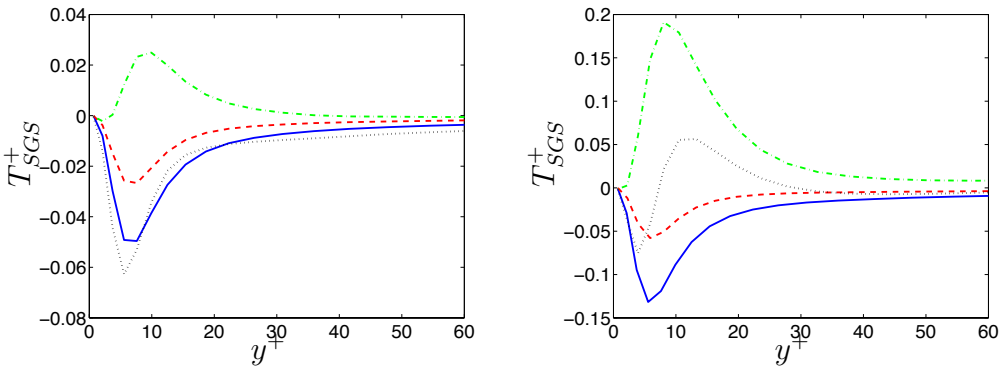

(a) $C = 1/6$ (b) $C = 2/3$

Figure 7.13: Energy transfer T^+_{SGS} for two different subgrid resolutions. Dashed line (red), T^+_{SGSA}; solid line (blue), T^+_{SGSB}; dash-dotted line (green) T^+_{SGSC}; dotted (black), total.

which is in good agreement with that reported in the literature from filtering DNS data for a channel flow at the same Reynolds number with the same filter [41, 109]. This is interesting because, while it is tempting to try to improve the performance of the NS-α model by adding dissipation, as is the usual remedy for non-dissipative model, this result suggests that is not the correct approach for this particular problem. The main problem instead is that the dominant physics is too close to the wall. The peak transfer in our simulations occurs at $y^+ \approx 5$, as compared to that in the literature at $y^+ \approx 10$.

For the $C = 2/3$ case (filter width four times the grid size), the net transfer switches from dissipative very close to the wall ($y^+ \approx 5$) to backscatter farther away ($y^+ \approx 12$). This is technically incorrect as the filtered DNS results in the literature demonstrate the net transfer should always be dissipative. It is interesting that although the physical size of α_k^2 is the same in both cases, the energy transfer with $C = 2/3$ is substantially higher than for the $C = 1/6$ case. This may be because on the finer mesh the velocity gradients are well resolved, thus the subgrid force itself may be higher.

7.5.2 Vorticity Fluctuations

The normalized vorticity fluctuations, $\omega^+ = \omega_{rms}\nu/u_\tau^2$, are shown in Figure 7.14 for the $(24, 64, 24)$ and $(32, 128, 32)$ meshes, both use $C = 1/6$. Again the minimal channel DNS is in good agreement with the data from the full channel DNS [58], while the NS-α model significantly overpredicts the streamwise and spanwise

vorticity fluctuations very close to the wall. The peak in the streamwise vorticity fluctuation at the edge of the buffer layer (at $y^+ \approx 20$ for the DNS) is much closer to the wall for the NS-α model (here at $y^+ \approx 9$) and higher in magnitude. As we mentioned earlier, this peak is indicative of the streamwise vortices in the buffer layer [58]. This indicates the streamwise vortices are stronger for the NS-α model (which is expected also from the high vertical and spanwise velocity fluctuations) and that the viscous layer is very thin, bringing the buffer layer closer to the wall. This is reflected also in the vertical vorticity fluctuations, which peak too close to the wall.

The high streamwise vorticity peak at the wall for the NS-α model was particularly surprising because, according to the streamwise vortex model of Kim et al. [58], the ratio between the streamwise vorticity peak at the wall to that in the buffer layer should be ≈ 1.3. Here we have instead a ratio of ≈ 2 (taking the peak at $y^+ \approx 10$ to be the buffer layer vortices). The wall value of the streamwise vorticity for the NS-α model is $\omega_x^+|_w \approx 0.4$, twice that in the DNS where $\omega_x^+|_w \approx 0.18$. This discrepancy can be accounted for by including a vortex tilting term to analyze the NS-α model results. Streamwise vorticity can be created by tilting of the spanwise vorticity into the streamwise direction, as can be accomplished for example by the $\omega_z \frac{\partial u}{\partial z}$ term in the spanwise vorticity equation. For the NS-α model this term is augmented by the $\omega_z \frac{\partial u^{ST}}{\partial z}$. We can compare the two by writing the tilting term for the Navier-Stokes equation as

$$\omega_{tiltx}^{NS} \approx \omega_z^{NS} \left(\frac{\partial u}{\partial z} \right)^{NS}, \tag{7.21}$$

and that for the NS-α equation as

$$\omega_{tiltx}^{\alpha} \approx \omega_z^{\alpha} \left(\frac{\partial \tilde{u}}{\partial z} \right)^{\alpha} + \omega_z^{\alpha} \left(\frac{\partial u^{ST}}{\partial z} \right). \tag{7.22}$$

Although we do not know the spanwise velocity gradient, $\partial u / \partial z$, close to the wall the most significant contribution to this term would be from the streaks, thus we take this velocity gradient to be proportional to the rms streamwise velocity fluctuation divided by the streak spacing. The streak spacing can be measured from the two point correlation R_{uuz} [58], which is shown in Figure 7.15 for both the present minimal channel DNS and the NS-α model results. We can see the average streak spacing is narrower with the NS-α model. At $y^+ \approx 7$ the minimum in R_{uuz} is at $L_z^+ \sim 20$ with the model, indicating a streak spacing of $L_z^+ \approx 40$. In comparison, the DNS here has a streak spacing of $L_z^+ \approx 80$. In comparison, for the full

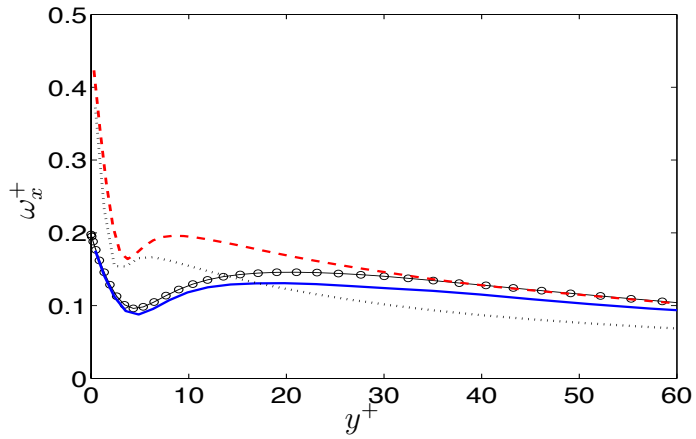

(a) Streamwise

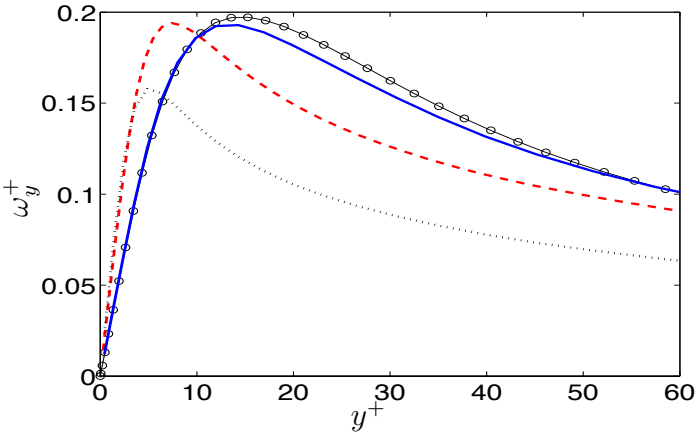

(b) Vertical

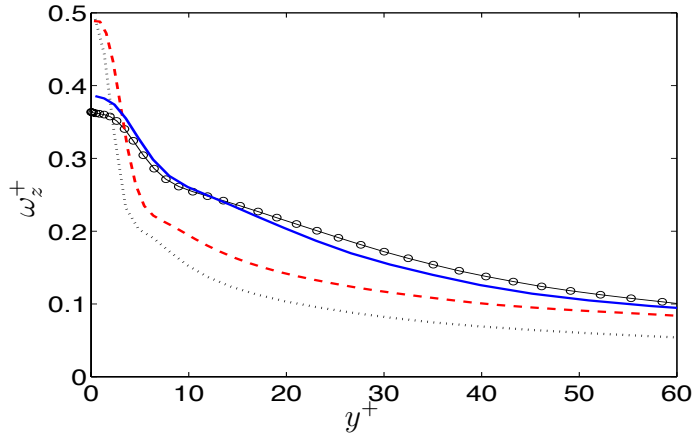

(c) Spanwise

Figure 7.14: RMS vorticity profiles. Solid line (blue), no model $(24, 64, 24)$; dashed line (red), NS-α model $(32, 128, 32)$; dotted line (black), NS-α model $(24, 64, 24)$; symbols full channel DNS [58]

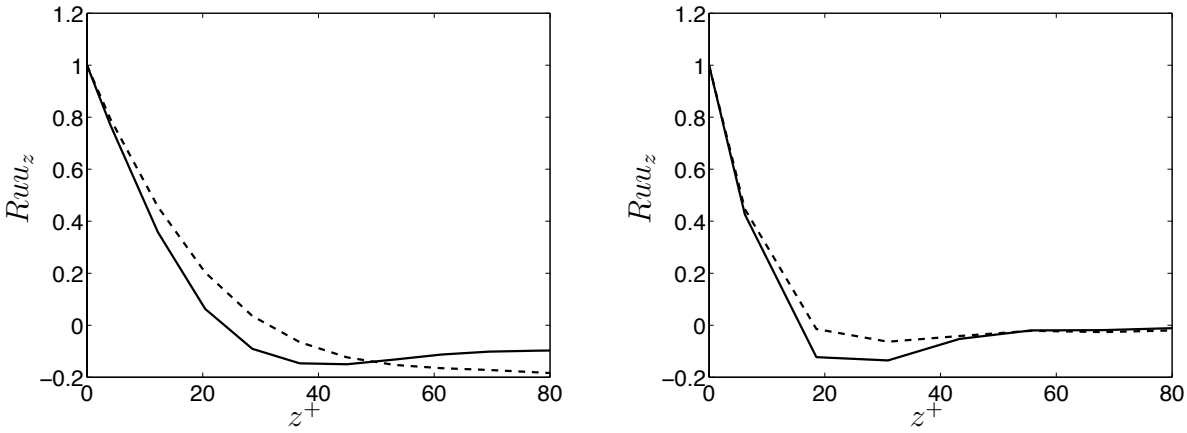

(a) DNS (b) NS-α

Figure 7.15: Two point correlations in the spanwise direction, left panel is DNS and right panel is the NS-α model. Solid line is at $y^+ \approx 7$, dashed line is $y^+ \approx 18$.

channel DNS in the literature it is $L_z^+ \approx 100$. For the NS-α model the spacing is too small by about a factor of two. It is not clear at this point why this is the case [3].

Returning to our streamwise vortex model, and using the streamwise velocity values from Figures 7.9 and 7.10, for the minimal channel DNS $\partial u/\partial z$ is approximately $2.7/80 = 0.035$ while for the NS-α model it is $2/40 = 0.05$. If we then take the contribution for the spanwise gradient of the Stokes velocity ($\partial_z u^{ST} \approx \partial_z \left(\alpha_z^2 \partial_{zz}^2 \tilde{u}\right)$ to be proportional to $(\alpha^2/h_z^2)(d\tilde{u}/dz)^\alpha$ we arrive at the following relationship between the two source terms

$$\frac{\omega_{tiltx}^{\alpha}}{\omega_{tiltx}^{NS}} = \frac{\omega_z^{\alpha}(d\tilde{u}/dz)^{\alpha}(1+\alpha^2/h_z^2)}{\omega_z^{NS}(d\tilde{u}/dz)^{NS}} \tag{7.23}$$

Substituting $(d\tilde{u}/dz)^\alpha/(du/dz)^{NS} \sim 0.05/0.035$, $\alpha^2/h_z^2 \approx 1/6$ and $\omega_z^\alpha/\omega_z^{NS} = 0.48/0.38$ (wall values from Figure 7.14) into Equation (7.23) we arrive at

$$\frac{\omega_{tiltx}^{NS}}{\omega_{tiltx}^{\alpha}} = 2.1 \tag{7.24}$$

[3]One possibility is, given that the streak spacing is believed to emerge from a secondary instability of the Tollmein-Schlicting wave (Jimenez pg. 219 [53]), the spacing we see here may be related to possible differences that would arise through a stability analysis of the NS-α equation as compared to the same anaylysis for the Navier-Stokes equation. For example, it has been shown that the model lowers the critical wavenumber for baroclinic instability in a two-layer quasi-geostrophic model. Although the initialization here was not representative of a true transition process, there were significant differences observed in how the flow became turbulent from the perturbed laminar state when the NS-α model was used, as compared to without.

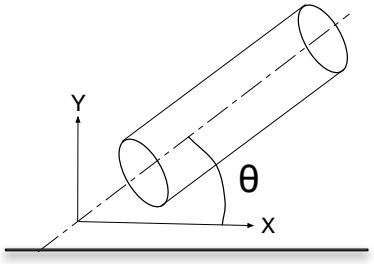

Figure 7.16: Definition of the vorticity inclination angle θ.

which agrees well with the values from the minimal channel of 0.38/0.18. While this is a very simple model, and does not explain other features, for example the high spanwise fluctuations near the wall, it is still enlightening. The streamwise vortices and streaks are considered the major physical features of the near-wall region at this Reynolds number, and streamwise vortices are strongly correlated with skin friction [66]. Because the skin friction is also so high for the NS-α model, we felt if the problem with the streamwise vorticity could be corrected, other anomalies may follow suit.

To investigate the streamwise vortices in the NS-α model further, in Figure 7.17 we compare probability density functions (PDFs) of the vorticity angle $\theta = \arctan(\tilde{\omega}_y/\tilde{\omega}_x)$ at three different heights from the wall. This is loosely defined as the streamwise vortex inclination angle, a sketch is shown in Figure 7.16. For the DNS the PDFs were measured using the instantaneous vorticity vector on three $x-z$ planes, at vertical locations of $y^+ \approx 7$, $y^+ \approx 18$ and $y^+ \approx 72$. The first is in the viscous sublayer, the second is in the buffer layer, and the last is in the upper buffer or lower logarithmic layer. In the viscous sublayer we can see two peaks in the PDF at $\pm 90^o$ corresponding to the low-speed streaks. (Consider that alternating bands of high and low speed u velocity in the spanwise direction will produce vertical vorticity). As you move into the buffer region a shoulder appears near $25^o/-155^o$ that corresponds to the streamwise vortices, and farther from the wall we see the peaks merge into a broader peak around $+45^o/-135^o$ indicating the average inclination angle of the streamwise vortices (and possibly hairpin vortex legs) in this region. These results are in good agreement with those from the literature [94].

For the NS-α model the PDFs were initially measured at the same y^+ values as in the DNS. They did not show any evidence of low-speed streaks, but all peaked in the range $40^o - 50^o$. Additional measurements were then made closer to the

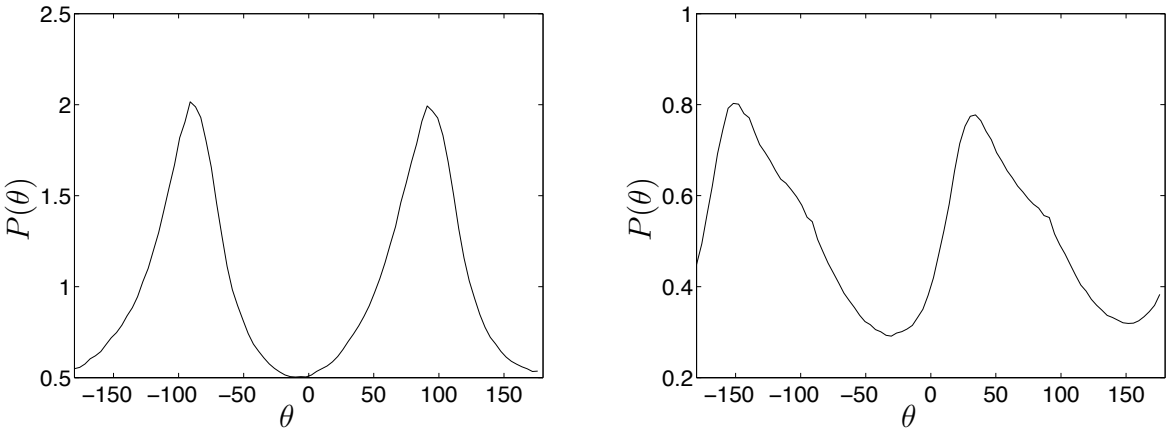

(a) $y^+ \approx 7.0$

(b) $y^+ \approx 5.4$

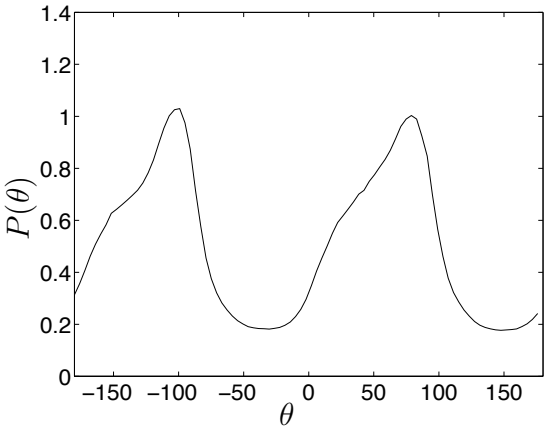

(c) $y^+ \approx 18$

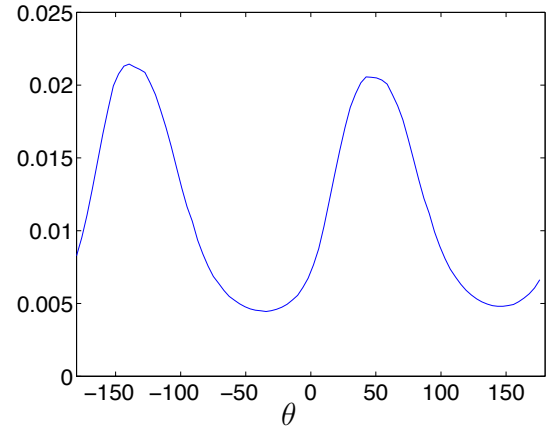

(d) $y^+ \approx 7.0$

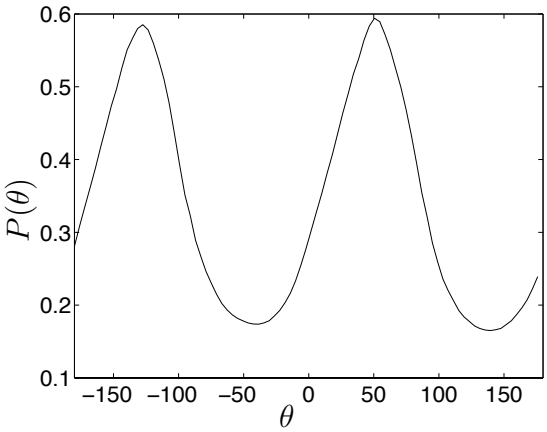

(e) $y^+ \approx 72$

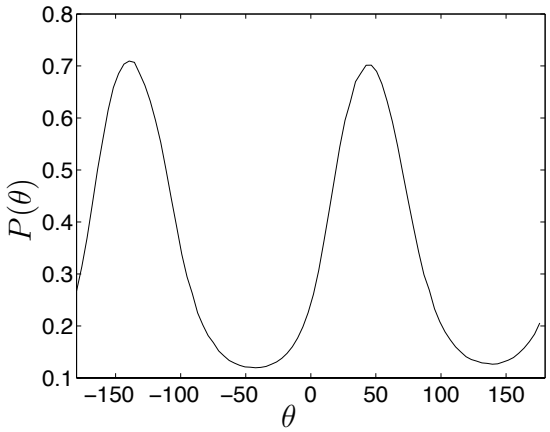

(f) $y^+ \approx 9.7$

Figure 7.17: Streamwise vorticity PDFs. Left column is DNS and right column is NS-α model.

wall, and are shown in Figure 7.17. At $y^+ \approx 5.4$ we can see there are shoulders near $\theta \approx \pm 90^o$ and more distinct peaks at $\theta \approx +20^o/-160^o$, the former indicating streamwise streaks and the latter indicating streamwise vortices. PDFs measured closer to the wall (not shown) had a single peak at $\theta \approx 0$ (zero vertical vorticity, as required by the no-slip condition at the wall). Thus we did not see any PDFs indicating a region dominated by low-speed streaks (similar to the one at $y^+ \approx 7$ for the DNS). For the NS-α model the PDFs farther from the wall (beyond about $y^+ \approx 8$) peak at $\approx +45^o/-135^o$ which is in good agreement with the DNS farther from the wall.

These results suggest that the $\tilde{\omega}_z \frac{\partial u^{ST}}{\partial z}$ term in the NS-α model provides an additional mechanism for producing vorticity in the near-wall region by tilting spanwise vorticity directly into the streamwise direction. This is physically incorrect in two respects. First, vortex tilting and stretching processes should occur farther away from the wall, in the buffer region, not in the viscous sublayer which is what we see here. Second, the path of streamwise vorticity creation is incorrect. In the literature the streamwise vorticity comes from *first* lifting up the transverse vorticity into the buffer layer and *then* tilting of the vorticity into the streamwise direction [53], while here we have a direct tilting of spanwise vorticity into the streamwise direction. On the other hand, the ability of the model to alter the vorticity field directly is interesting and possibly advantageous.

7.6 Results with the alternative α_k^2 and with damping

The results in the previous section indicate damping of α_k^2 in the near wall region may be necessary. In the study by Zhao and Mohseni [153] they found in an *a priori* study using a dynamic procedure that α followed a linear variation from zero at the wall to a constant value of 0.02 around $y^+ \approx 10$. In a later study [152] they tested this distribution for α (now turning off the dynamic procedure and fixing α to follow the specified profile), but their results were not very promising. Similar to what we found, their spanwise velocity fluctuations were excessively high. This is not surprising because their α distribution was determined using an *a priori* study, which does not account for the feedback of the model on the flow. For example, in the previous section we saw that the effect of having the streamwise vortices closer to the wall is to increase skin friction. This is the type of effect you will not see in

an *a priori* study.

Following Zhao and Mohseni we also used a linear variation of α and α_k from zero at the wall to a constant value at a specified wall-normal distance. However, the damping was applied over the region $y^+ < 60$ instead of the region $y^+ < 10$ that was used in their study. This choice was motivated by the study by Jimenez that demonstrated in the region $y^+ < 60$ the low-speed streaks are a critical part of the autonomous cycle of near-wall turbulence [54]. Thus we consider this to be the 'streak-affected' region, and since the problem is related to the velocity gradients from the streaks, $\partial\tilde{u}/\partial z$, it is logical to apply the damping factor through this region. Other values were tested along with exponential damping profiles instead of the simple linear one. The shape of the damping profile was found to be insignificant, with the wall-normal distance being the important factor. Damping over the streak affected region was found to consistently provide the best results. The damping function used was

$$f(y^+) = \begin{cases} \left(y^+/60\right)^2 & \text{if} \quad y^+ \leq 60 \\ 1 & \text{otherwise.} \end{cases} \tag{7.25}$$

Results with damping are shown in Figure 7.18 for the isotropic and anisotropic models. For the isotropic model α^2 was specified as $\alpha^2 = f\left(y^+\right)(0.02)^2$, where $f\left(y^+\right)$ is given by equation (7.25) and 0.02 is the value of α away from the wall determined by Zhao and Mohseni using a dynamic procedure. For the anisotropic model $\alpha_k^2 = f\left(y^+\right) C h_k^2$ was used for α_x^2 and α_z^2 while α_y^2 was set to zero. Initially a C value of $1/6$ was used such that it is a damped version of the default model. However, with this value the logarithmic law was significantly underpredicted (in terms of the y-intercept), so the results reported here used $C = 1/12$. Even with this value the skin friction is still overpredicted. To have the same physical equivalent α for the isotropic and anisotropic models you would need to use $C = 1/24$ or $\Delta = h$. This was tested (results not shown) and it did bring the mean velocity profile into good agreement with the DNS data, but it does not seem to make good physical sense because this would mean the filter width is equal to the grid spacing.

We can see in Figure 7.18 that damping removes the problem with the high spanwise fluctuations, and improves some quantities slightly (eg. mean flow profile, shear stress and streamwise velocity fluctuations) but overall the differences between the

no model and NS-α model results are very small when damping is used. Changes in the numerical scheme or grid resolution would probably impact the results within a similar degree as the model. Similar conclusions can be made for the vorticity fluctuations in Figure 7.19. The damping factor does remove the high peak in the streamwise vortices near the wall, but also reduced the strength of the vortices in the buffer layer, such that they are now too weak, similar to the no model result.

Results with the Leray model (with $\partial_j \tilde{u}_j$ enforced) and with the flow-dependent α_k^2 are shown in Figures 7.20 and 7.21. Note that no damping was used for the Leray model. For comparison results with no model and the default NS-α model are also shown. The no model and default NS-α model results were shown earlier at the beginning of this chapter. We can see in Figure 7.20 that the results with the default Leray model (only the first two terms, A_{ij} and B_{ij} in the subgrid stress are significantly different than those from the default NS-α model. Although we have not focused specifically on the Leray model in the thesis, it provides a means of isolating the problem with the NS-α model. With the Leray model the prediction of the mean flow is improved as compared to the no model case but there is only a slight improvement to the RMS profiles. It should be noted that there is no anisotropic Leray model previously reported in the literature. Channel flow results with the isotropic Leray model were presented by van Reeuwijk [139] following a different methodology (using the unsmoothed velocity as the dependent variable). In that case it was found the model generated a thick boundary layer near the wall, and this was due to enforcing continuity using the unsmoothed velocity. Here we enforce continuity with the smoothed velocity, and do not encounter that problem. However, we did find the Leray model to be less stable numerically than the NS-α model. For example we were unable to run the model over as wide of a range of α_k^2 values as for the NS-α model.

Results with the flow-dependent definition of α_k^2 are also shown in Figure 7.20. In this case the mean flow gradient was not considered in the calculation of α_x^2, a similar strategy is used in implementing the structure function model in boundary-layer flows [22]. The results with the flow-dependent definition are disappointing in that they remove the near-wall problem, but do not yield a visible improvement as compared to the no model case. In some cases (eg. vertical fluctuations) the results with the Leray model are better.

The vorticity fluctuations are shown in Figure 7.21. Using the flow-dependent

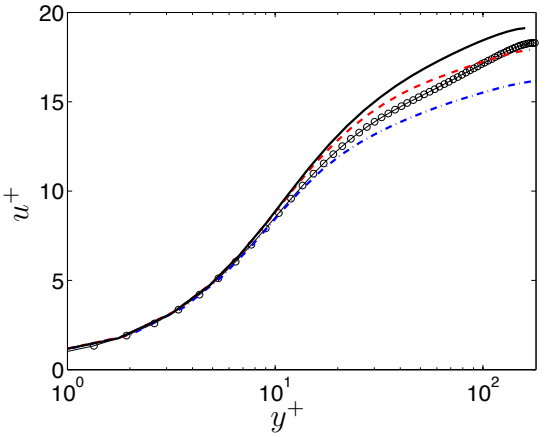

(a) Mean flow

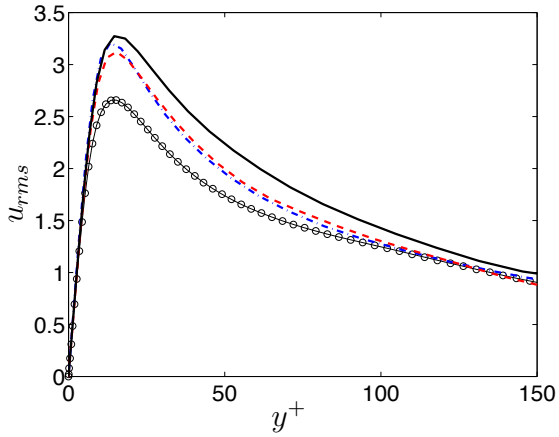

(b) Streamwise

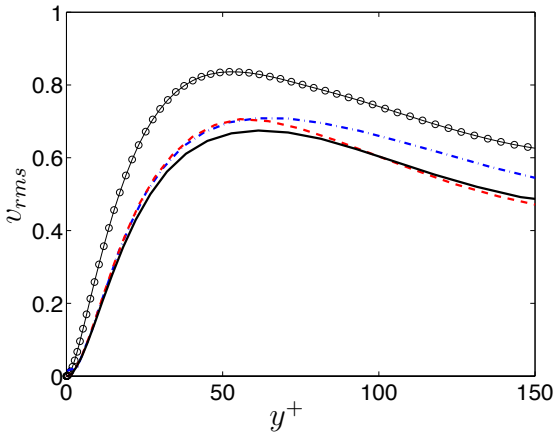

(c) Vertical

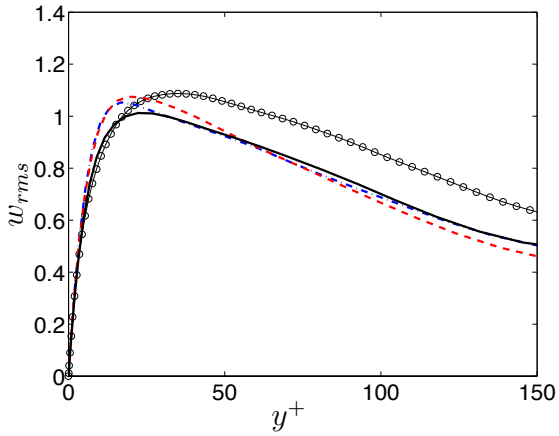

(d) Spanwise

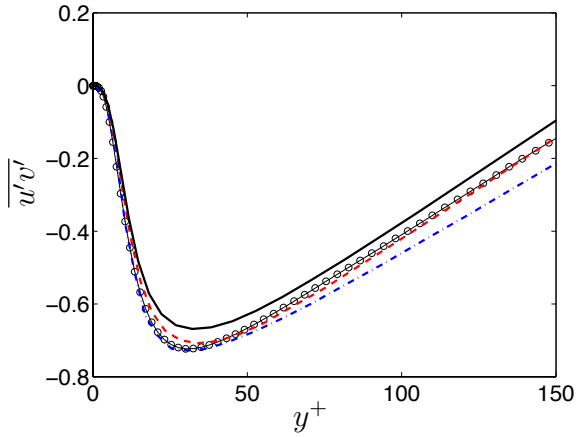

(e) Shear stress

Figure 7.18: Mean flow, rms and shear stress profiles; no model (solid black); isotropic NS-α with damping (dashed red); anisotropic NS-α with damping (dash-dot blue). Symbols are DNS data [58].

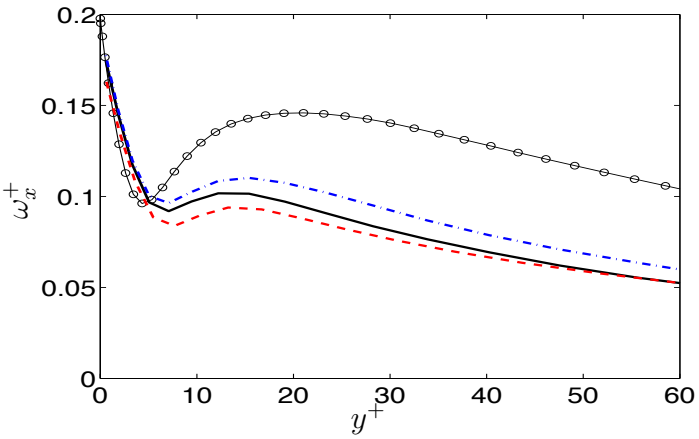

(a) Streamwise

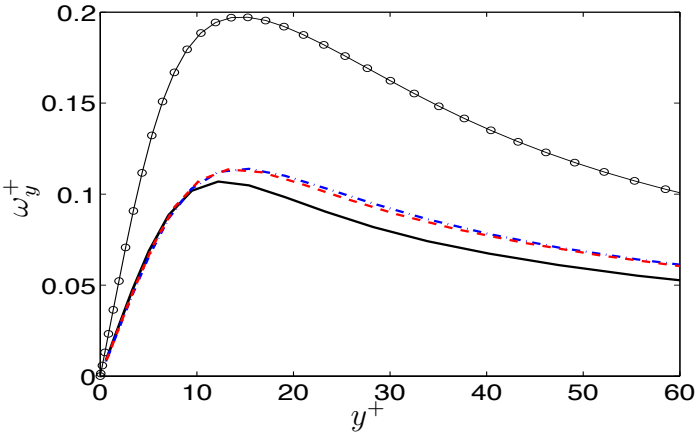

(b) Vertical

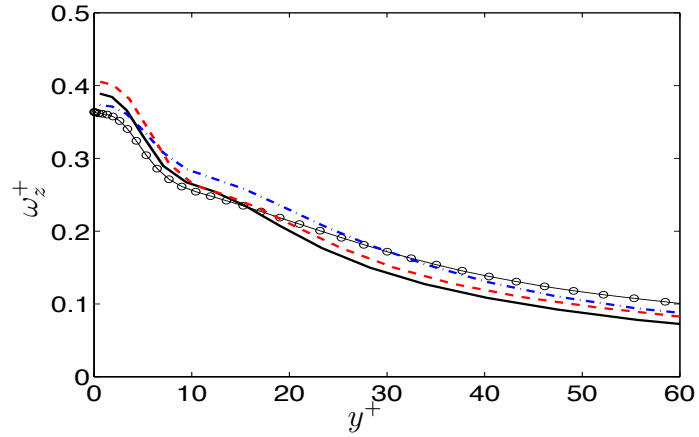

(c) Spanwise

Figure 7.19: RMS vorticity profiles; no model (solid black); isotropic NS-α with damping (dashed red); anisotropic NS-α with damping (solid blue). Symbols are DNS data [58].

definition of α_k^2 removes the problematic high streamwise vorticity fluctuations in the region $y^+ < 10$ but also reduces the strength of the streamwise vorticies farther from the wall such that they are now underpredicted. It is disappointing that none of the models show an improvement in predicting the vorticity fluctuations over the no model result.

7.7 A preliminary look at nonlinear activity

The NS-α model is an example of a nonlinear regularization model [4]. In theory these models smooth the nonlinear term in such a way that the energy transfer to the small scales is attenuated. We would expect evidence for this to be found for example in a steeper energy spectrum, although the recent work by Graham et al. [37, 36] has shown this may not be the case for the NS-α model. In the present thesis it was not possible to test the scaling arguments discussed in Chapter 2 because this requires very fine mesh resolutions. The study by Graham et al. [36] used $(2048)^3$ mesh points for box turbulence, far beyond our resolution capabilities. In addition, neither the channel flow or cavity flow are appropriate test cases for a careful validation the theoretical results based on isotropic turbulence theory, although a future study of energy transfer in the channel flow could be interesting (c.f. Domaradzki [18] for a study of interscale interactions in wall-bounded flows using the Navier-Stokes equations.).

The streamwise velocity spectrum is shown in Figure 7.22 for the full channel. Other spectra that were measured were similar. From this spectrum we can see the model does not damp the high wavenumber region, but instead has reduced energy at the lower wavenumbers (this was found also in the study by Graham et al. for some cases [37]). It is possible that this is related to the observation [10] that vortex structures are shorter and fatter in 3D NS-α turbulence than in regular Navier-Stokes turbulence.

Both the spectrum without the model and the one with the NS-α model exhibit a small inertial subrange. The latter being at higher wavenumbers. We also see the spectrum with the model begins to drop off around the wavenumber $k_\alpha = 1/\alpha_x$

[4] Mathew et al.[86] define a regularization model as 'an ad hoc modification of a model problem to keep it well behaved at all times'. For a turbulent flow the solution can diverge when the small scales are not accounted for, thus regularization in this context refers to a method to prevent divergence.

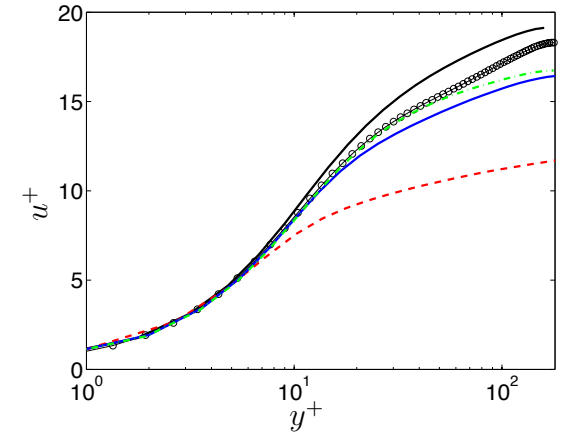

(a) Mean flow

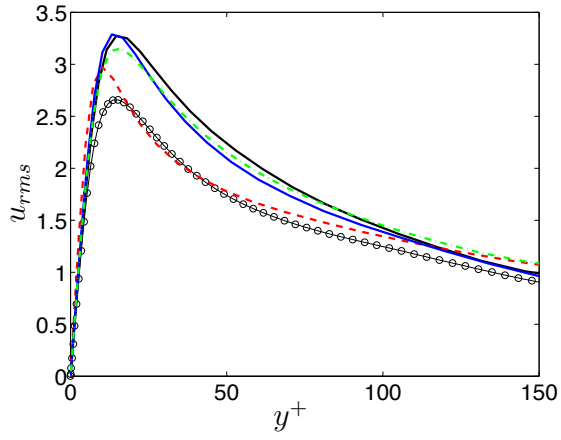

(b) Streamwise

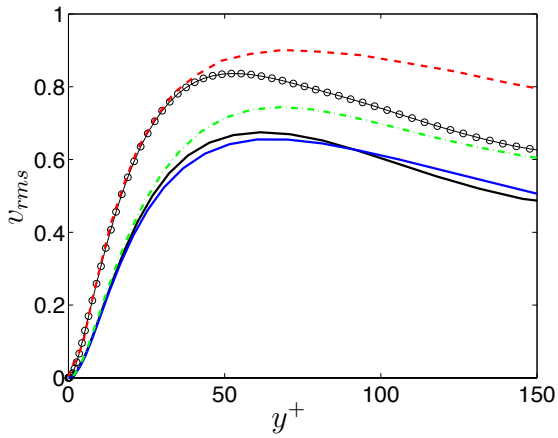

(c) Wall normal

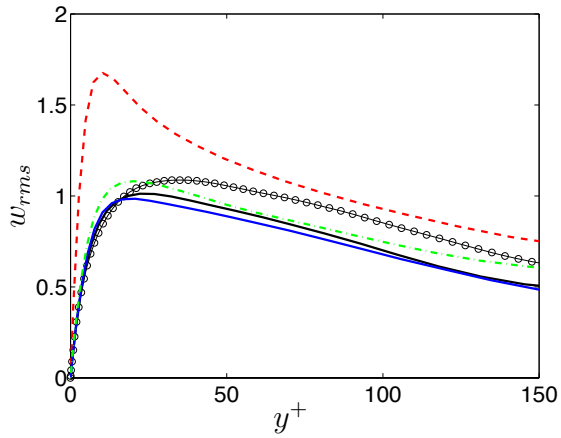

(d) Spanwise

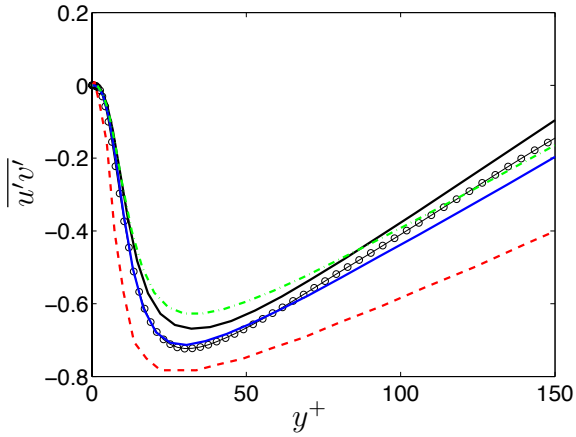

(e) Shear stress

Figure 7.20: Mean flow, shear stress and rms profiles; no model (solid black); NS-α with α_k^2 based on the mesh (dashed red); NS-α with flow-dependent α_k^2 (solid blue); Leray model with α_k^2 based on the mesh (dash-dotted green). Symbols are DNS data [58].

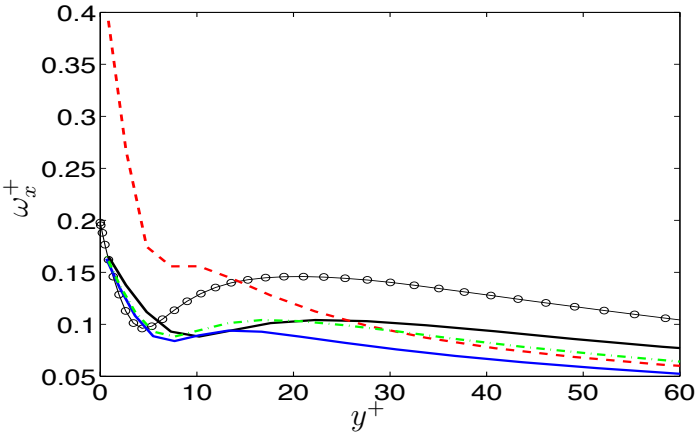

(a) Streamwise

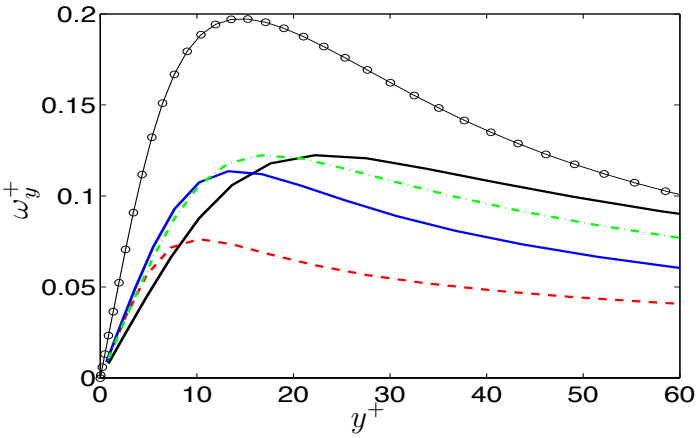

(b) Vertical

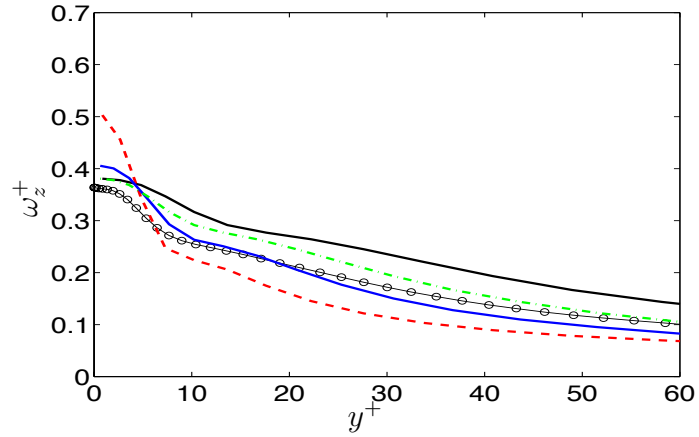

(c) Spanwise

Figure 7.21: RMS vorticity profiles. Results with no model (solid black); NS-α with α_k^2 based on the mesh (dashed red); NS-α with flow-dependent α_k^2 (solid blue); Leray model with α_k^2 based on the mesh (dash-dotted green). Symbols are DNS data [58].

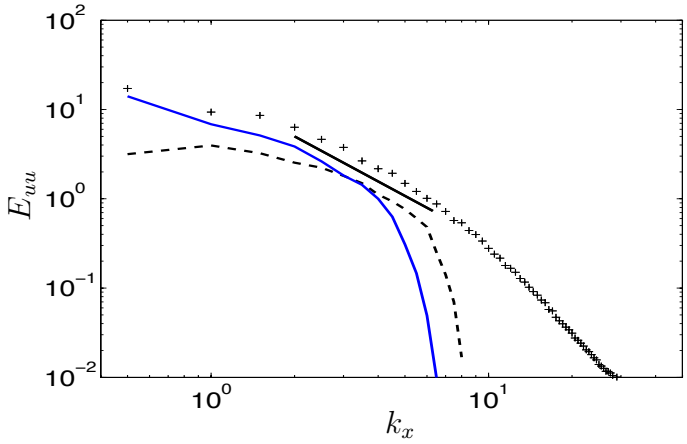

Figure 7.22: Streamwise spectra for the full channel measured at $y^+ \approx 80$. Black crosses are DNS [58]; blue is without a model; black dashed is the default NS-α model. A slope of $-5/3$ is also shown.

(here $k_\alpha = 6.2$) similar to what has been seen in other studies [10].

To investigate the possibility that the NS-α model exhibits altered nonlinear properties as compared to the Navier-Stokes equations we looked at the relative helicity PDFs. The relative helicity is a dimensionless quantity defined as [118]

$$h = \frac{\boldsymbol{u} \cdot \boldsymbol{\omega}}{|\boldsymbol{u}||\boldsymbol{\omega}|}. \tag{7.26}$$

The relationship between nonlinearity and helicity can be seen when we consider that in rotational form the Navier-Stokes equation can be written

$$\frac{\partial \boldsymbol{u}}{\partial t} + \boldsymbol{\omega} \times \boldsymbol{u} = -\nabla \left(p + \frac{1}{2} \boldsymbol{u} \cdot \boldsymbol{u} \right) + \nu \nabla^2 \boldsymbol{u}. \tag{7.27}$$

For the NS-α model in the LES-template we can write

$$\frac{\partial \tilde{\boldsymbol{u}}}{\partial t} + \tilde{\boldsymbol{\omega}} \times \tilde{\boldsymbol{u}} = -\nabla \left(p + \frac{1}{2} \tilde{\boldsymbol{u}} \cdot \tilde{\boldsymbol{u}} \right) + \nu \nabla^2 \tilde{\boldsymbol{u}} - H^{-1} \left(\frac{\partial m_{ij}}{\partial x_j} \right). \tag{7.28}$$

Combining the nonlinear term $\tilde{\boldsymbol{u}} \times \tilde{\boldsymbol{\omega}}$ with the definition of relative helicity in terms of the smoothed velocity and vorticity (which we will denote by $\tilde{h}$) we arrive at

$$\frac{(\tilde{\boldsymbol{u}} \cdot \tilde{\boldsymbol{\omega}})^2}{|\tilde{\boldsymbol{u}}|^2 |\tilde{\boldsymbol{\omega}}|^2} + \frac{(\tilde{\boldsymbol{u}} \times \tilde{\boldsymbol{\omega}})^2}{|\tilde{\boldsymbol{u}}|^2 |\tilde{\boldsymbol{\omega}}|^2} = 1. \tag{7.29}$$

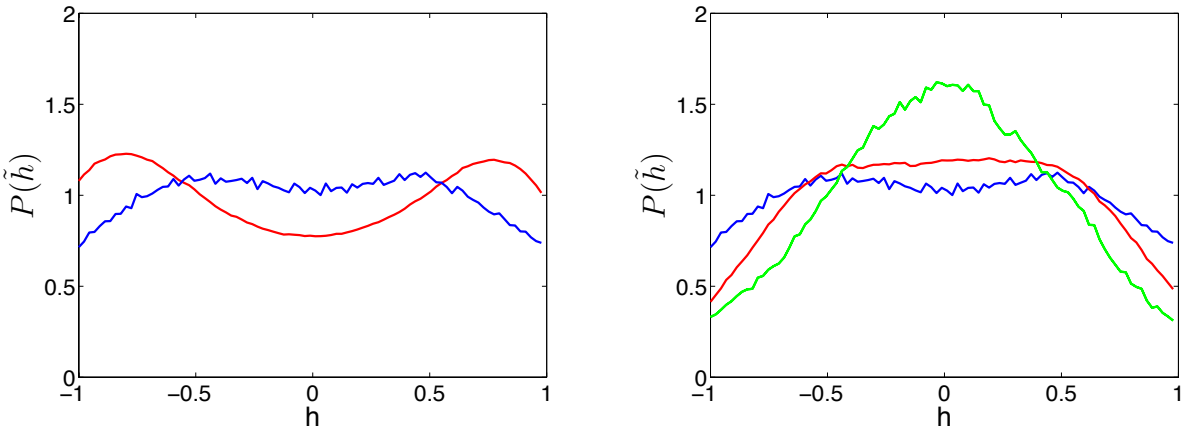

(a) minimal channel, $y^+ \approx 90$

(b) full channel, $y^+ \approx 90$

Figure 7.23: PDFs of the relative helicity, (a) minimal channel; DNS (meshII), blue; default NS-α, red; (b) full channel; NS-α with damping (anisotropic model), red; no model, green. Blue line is from the minimal channel DNS, shown for comparison.

This relationship is often used to relate regions of high helicity to a depleted nonlinearity, and long-lived coherent structures [118]. Given that the NS-α equations are described as having a reduced nonlinearity [17], we might expect they may also have high relative helicity. The PDFs shown in Figure 7.23 were measured away from the walls at $y^+ \approx 90$. We can see for the minimal channel the default NS-α model (red) has two shoulders near $+/-1$ indicating a higher probability of increased helicity relative to the Navier-Stokes equations (blue). Values of $\overline{\tilde{h}^2}$ are given in Table 7.4. A uniform distribution would correspond to $\overline{\tilde{h}^2} = 0.33$. For the full channel we can see when a model is not used the PDF is too peaked and $\overline{\tilde{h}^2}$ is too low, but when the damped NS-α model is used the results are closer to the minimal channel DNS. Because we expect the minimal channel DNS to be representative of a full channel at a finer mesh spacing, this suggests that the NS-α model can produce helicity statistics on a coarse mesh that are comparable to those from a finer mesh without a model. We also carried out a few simulations with a standard Smagorinsky model with wall damping for the full channel, and found they did not improve the helicity statistics as compared to the no model case.

7.8 Summary

The results presented here show that the NS-α model with a mesh-based definition of α_k^2 (anisotropic) does not perform well in that it significantly overpredicts the

model	$\overline{\tilde{h}^2}$
DNS (minimal channel)	0.31
NS-α (default, minimal channel)	0.37
NS-α (damping, full channel)	0.29
no model (full channel)	0.21

Table 7.4: Values of $\overline{\tilde{h}^2}$.

skin friction, and produces erroneous near-wall behavior that is reflected primarily in high spanwise velocity fluctuations and high streamwise vorticity fluctuations. A possible explanation for this was proposed, which was that the vortex tilting term in the model was generating streamwise vorticity very close to the wall (in what should be the viscous sublayer) due to interaction between the model and the streaks. Damping through the streak-affected region was found to remove the problem, but the results did not yield a noticeable improvement over the no model case. It should be pointed out that the anisotropic model was able to achieve a numerically stable result, something which we found was not possible with the isotropic one when α^2 was based on the grid volume.

The poor performance of the default NS-α model with regards to skin friction is not entirely unexpected. Many models that do not incorporate either a dynamic procedure or a sensor to detect energy build up (along with an appropriate drain) also have difficulty in this flow. Future directions could be to either develop such a sensor within the NS-α framework, or move towards higher Reynolds number boundary layers, where the near wall region is not resolved. In the latter case approximate boundary conditions for the wall could be used (c.f. Sagaut [120]).

On the other had the ability of the NS-α model to reproduce the statistics of the coherent structure function and resolved flow helicity on a mesh that is coarser (in terms of mesh sizes in $^+$ units) than the DNS by a factor of $2-4$ in each direction is very promising. We found the computational overhead for the NS-α model in the channel flow to be about 30% for both the box and FFT filters, in agreement with other studies [105, 32]).

Chapter 8

Conclusions and Future Work

8.1 Outcomes of the thesis

At the time this thesis was proposed the NS-α model was emerging as a promising alternative to strictly dissipative closures. At that time (and continuing to the present day) the bulk of the literature was of a theoretical nature with simulation results available for only a few cases, isotropic turbulence [10, 92], the transitional mixing layer [32] and the wind-driven gyre [51]. Simulations of turbulent channel flow were carried out later by Zhao and Mohseni [153, 152], and more recently the model was used as a parameterization for mesoscale eddies [105, 44, 45]. All of the above studies used the isotropic equations with constant α^2 with the exception of Zhao and Mohseni [152] who used the isotropic NS-α equations with an α^2 distribution determined using a dynamic procedure in an *a priori* analysis. Similar to the situation found here, their results showed excessively high fluctuations in the spanwise velocity, though no explanation was given. The present thesis contributes to this picture by: (*i*) developing a subgrid model for the general case of an anisotropic and/or variable model parameter α_k^2, (*ii*) showing that the source of the poor performance in the turbulent channel flow when a mesh-based definition of α_k^2 is used is due to interaction between the model and the velocity streaks, thus damping through the streak-affected regions leads to improved results, (*iii*) proposing a preliminary (albeit ad-hoc) definition of α_k^2 that is not solely dependent on the mesh-spacing. This definition worked well for the lid-driven cavity flow.

Interpretation of the results in this thesis was at times confounded by the complexity of the test cases chosen. To simplify analysis of the results it would have been easier to build these test cases from simpler elements. For example, a turbu-

lent channel flow can be built by starting with a homogeneous shear flow [119] to look at shear production and anisotropy, before adding walls. On a similar note, the interaction between the NS-α model and solid walls could be carried out first without the complicating effects of the shear flow by following the study by Perot and Moin [104]. In this study they looked at the effect of solid boundaries on turbulence by using two separate types of boundary conditions in turn. The first was a free-slip wall (to investigate kinematic blocking), and the second was a permeable wall (to investigate the no-slip condition without the kinematic blocking).

It should also be pointed out that the first two terms in the anisotropic subgrid stress developed in this thesis (either Equation (4.16) or Equation (4.17)) can be used as an anisotropic Leray model if one enforces $\partial_j \tilde{u}_j = 0$. In fact, enforcing $\partial_j \tilde{u}_j = 0$ was one of the recommendations from the study by Van Reeuwijk on the Leray model in wall-bounded flows [140]. We found this anisotropic Leray model could be used in a turbulent channel flow without additional wall-damping.

8.2 Future directions regarding NS-α turbulence

Recent studies [37, 36, 33] have contributed significantly to our understanding of the NS-α equations as a turbulence model. Recall that the NS-α equations were found to generate rigid-rotators that do not participate in the energy cascade, leading to a shallower energy spectrum than that of the Navier-Stokes equations. However, a detailed understanding of interscale energy transfer in the NS-α model is still lacking. Analytical arguments (see Section 2.1.3) have yet to be verified through numerical simulations, and in fact are based on our understanding of the relevant triad interactions for the Navier-Stokes equations, not the NS-α equations. It would be useful to look into this in more detail as it may help guide our understanding of model results, or assist in the development of an appropriate energy drain to make the model more robust.

In the present thesis we have taken the approach of solving the NS-α equations with the smoothed velocity $\tilde{\boldsymbol{u}}$ as the dependent variable. One question then is, what is the implication of the resolved energy norm $\int_V u_i \tilde{u}_i \, dV$ when we solve the equations in this manner? Recall the equation for the resolved flow energy, $\tilde{e} = \tilde{u}_i \tilde{u}_i / 2$,

$$\frac{\partial \tilde{e}}{\partial t} + \frac{\partial}{\partial x_j}\left(\tilde{e}\tilde{u}_j\right) = -\frac{\partial}{\partial x_i}\left(\tilde{u}_i \tilde{p}\right) + \nu \frac{\partial^2 \tilde{e}}{\partial x_k^2} - \nu \frac{\partial \tilde{u}_i}{\partial x_k}\frac{\partial \tilde{u}_i}{\partial x_k} - \frac{\partial}{\partial x_j}\left(\tilde{u}_i \tilde{m}_{ij}\right) + \tilde{m}_{ij}\frac{\partial \tilde{u}_i}{\partial x_j}. \quad (8.1)$$

If we consider the inviscid case for simplicity and integrate over a control volume with periodic boundary conditions the conserved energy is

$$\int_V \frac{\partial \tilde{e}}{\partial t}\, dV = \int_V \tilde{m}_{ij} \frac{\partial \tilde{u}_i}{\partial x_j}\, dV. \tag{8.2}$$

Recall that for the NS-α equation with $\boldsymbol{u}$ as the dependent variable for the case of inviscid flow with periodic boundary conditions the conserved energy is

$$\int_V \frac{\partial \tilde{e}}{\partial t}\, dV + \int_V \frac{\partial}{\partial t}\left(\frac{\alpha^2}{2}|\nabla \tilde{u}_i|^2\right) dV = 0. \tag{8.3}$$

Subtracting Equation (8.2) from (8.3) yields

$$\int_V \frac{\partial}{\partial t}\left(\frac{\alpha^2}{2}|\nabla \tilde{u}_i|^2\right) dV = -\int_V \tilde{m}_{ij} \frac{\partial \tilde{u}_i}{\partial x_j}\, dV \tag{8.4}$$

from which we can see that the subgrid transfer term $\tilde{m}_{ij}\partial\tilde{u}_i/\partial x_j$ can be viewed as providing a source term to the equation for the resolved flow gradients, and therefore the resolved flow enstrophy, $\int_V \tilde{\omega}\cdot\tilde{\omega}$. In light of this it might be useful in the future to look more closely at how the NS-α model affects the resolved flow vortices (see da Silva et al. [13] for a study of this nature for other subgrid models). Studies in this direction have practical implications as well, for example in applications where it is the size, strength and location of the fluid vortices that is of interest.

8.3 Application of the model to practical problems

The question remains as to what types of problems we expect the NS-α model to be a useful approach. In the present thesis we have looked at the performance of the NS-α model in wall bounded flows where the approach taken has been to resolve the near-wall dynamics. We found that for the channel flow reasonable results can be obtained when we use a damping function. Though the mean flow and rms profiles are not better than those found using other approaches, the NS-α model also does not contain a sensor and drain mechanism which other models found to be successful do [29, 128]. Both the lid-driven cavity and the flow structures in the channel flow were found to be well captured with the NS-α model on a coarse mesh. In this respect the model performance is consistent with other studies [32, 45]. The picture emerging is that the model is promising for flows where integrity of the flow

structures would be compromised by a dissipative method (eg. growth and merging of vortex structures in mixing layer or boundary layer transition) and this poor resolution of the flow structures would directly impact the quantities of interest (eg. sound pressure level due to flow-resonant interaction between a mixing layer vortex and an acoustic field).

In all of the potential future studies a question that needs to be addressed is whether it is useful to interpret the model parameter as a filter width and tie it directly to the mesh. The problems encountered in this thesis (numerical oscillations for the lid-driven cavity and high skin friction for the channel flow) both arose when a simple mesh-dependent definition of α^2 (isotropic) or α_k^2 (anisotropic) was used. On a similar note Graham et al. [37] found for isotropic turbulence that choosing α to correspond to a length scale in the inertial subrange (as is done when following an LES methodology) led to high energy in the small scales.

Moving away from a simple interpretation of the model parameter as either a filter width or length scale in the inertial subrange would mean using another approach to determine α_k^2. For example, returning to the definition of α_k^2 as the mean-squared particle displacement from an average trajectory, solving an advection equation for α_k^2 within the channel flow may be one method to at least generate insight into how particle trajectories are altered by the presence of a solid wall. For the more general case of a complex flow, a dynamic procedure may be necessary. While using a dynamic procedure or solving an advection equation may be too expensive for practical implementation, the α_k^2 values determined using these methods could be used to generate insights into new modeling strategies.

Appendix A - Details of the Variations

The variation of the velocity and volume element are based on the discussion in Bhat's thesis [3] (although Bhat works with the density field, the mathematics is similar for the volume element).

The velocity variation is defined as

$$\delta \boldsymbol{u} := \left.\frac{d}{d\epsilon}\right|_{\epsilon=0} \boldsymbol{u}^{\epsilon} \tag{A-5}$$

with

$$\begin{aligned} \boldsymbol{u}^{\epsilon} =& \dot{\boldsymbol{\eta}}^{\epsilon} \circ (\boldsymbol{\eta}^{\epsilon})^{-1} \\ =& \dot{\boldsymbol{\eta}} \circ (\boldsymbol{\eta}^{\epsilon})^{-1} + \epsilon \delta \dot{\boldsymbol{\eta}} \circ (\boldsymbol{\eta}^{\epsilon})^{-1}. \end{aligned} \tag{A-6}$$

Differentiating with respect to ϵ and setting $\epsilon = 1$

$$\delta \boldsymbol{u} = \nabla \dot{\boldsymbol{\eta}} \cdot \left.\frac{d}{d\epsilon}\right|_{\epsilon=0} (\boldsymbol{\eta}^{\epsilon})^{-1} + \delta \dot{\boldsymbol{\eta}} \circ \boldsymbol{\eta}^{-1}. \tag{A-7}$$

The second part of (A-7) is the rate of change of the trajectory variation for the original label. We would like to find an expression for this in terms of the trajectory variation at a field point, $\boldsymbol{w} = \delta \boldsymbol{\eta} \circ \boldsymbol{\eta}^{-1}$. To do this follow Bhat [3] and calculate the time derivative of $\boldsymbol{w}$

$$\frac{\partial \boldsymbol{w}}{\partial t} = \delta \dot{\boldsymbol{\eta}} \circ \boldsymbol{\eta}^{-1} + \nabla \delta \boldsymbol{\eta} \cdot \frac{\partial}{\partial t} \left(\boldsymbol{\eta}^{-1} \right). \tag{A-8}$$

To evaluate the last derivative we make use of the property (where Id is the identity)

$$\boldsymbol{\eta} \circ \boldsymbol{\eta}^{-1} = Id \tag{A-9}$$

and differentiate both sides with respect to time

$$\frac{\partial}{\partial t} \left(\boldsymbol{\eta}^{-1} \circ \boldsymbol{\eta} \right) = 0 \tag{A-10}$$

$$\frac{\partial \boldsymbol{\eta}^{-1}}{\partial t} \circ \boldsymbol{\eta} + \nabla \boldsymbol{\eta}^{-1} \cdot \frac{\partial \boldsymbol{\eta}}{\partial t} = 0. \tag{A-11}$$

Composing both sides with $\boldsymbol{\eta}^{-1}$,

$$\frac{\partial \boldsymbol{\eta}^{-1}}{\partial t} \circ \boldsymbol{\eta} \circ \boldsymbol{\eta}^{-1} + \nabla \boldsymbol{\eta}^{-1} \cdot \dot{\boldsymbol{\eta}} \circ \boldsymbol{\eta}^{-1} = 0 \tag{A-12}$$

which gives

$$\frac{\partial \boldsymbol{\eta}^{-1}}{\partial t} = -\nabla \boldsymbol{\eta}^{-1} \cdot \dot{\boldsymbol{\eta}} \circ \boldsymbol{\eta}^{-1}. \tag{A-13}$$

Going back to (A-8) we now have an expression for $\delta\dot{\boldsymbol{\eta}} \circ \boldsymbol{\eta}^{-1}$,

$$\frac{\partial \boldsymbol{w}}{\partial t} = \delta\dot{\boldsymbol{\eta}} \circ \boldsymbol{\eta}^{-1} - \underbrace{\nabla \delta\boldsymbol{\eta} \cdot \nabla \boldsymbol{\eta}^{-1}}_{\nabla \boldsymbol{w}} \cdot \underbrace{\dot{\boldsymbol{\eta}} \circ \boldsymbol{\eta}^{-1}}_{\boldsymbol{u}} \tag{A-14}$$

or,

$$\delta\dot{\boldsymbol{\eta}} \circ \boldsymbol{\eta}^{-1} = \frac{\partial \boldsymbol{w}}{\partial t} + \boldsymbol{u} \cdot \nabla \boldsymbol{w} \tag{A-15}$$

which tells us that the rate of change of the trajectory variation with the label fixed (unvaried label is denoted by the $\boldsymbol{\eta}^{-1}$) is given by the substantial derivative.

The first part of the velocity variation in (A-7) is the change with respect to the label. To evaluate this we need to find

$$\left.\frac{d}{d\epsilon}\right|_{\epsilon=0} (\boldsymbol{\eta}^{\epsilon})^{-1} \tag{A-16}$$

This can be done by using

$$(\boldsymbol{\eta}^{\epsilon})^{-1} \circ (\boldsymbol{\eta}^{\epsilon}) = Id, \tag{A-17}$$

and differentiating both sides

$$\left.\frac{d}{d\epsilon}\right|_{\epsilon=0} (\boldsymbol{\eta}^{\epsilon})^{-1} \circ \boldsymbol{\eta} + \nabla \boldsymbol{\eta}^{-1} \cdot \underbrace{\frac{d}{d\epsilon}(\boldsymbol{\eta}^{\epsilon})}_{\delta\boldsymbol{\eta}} = 0 \tag{A-18}$$

Moving the last term over to the right hand side and composing both sides with $\boldsymbol{\eta}^{-1}$ (or in other words, applying the back to labels map, which brings our independent variable back to the field position $\boldsymbol{x}$ instead of the label $\boldsymbol{a}$), yields

$$\left.\frac{d}{d\epsilon}\right|_{\epsilon=0} (\boldsymbol{\eta}^{\epsilon})^{-1} = -\nabla \boldsymbol{\eta}^{-1} \cdot \delta\boldsymbol{\eta} \circ \boldsymbol{\eta}^{-1}. \tag{A-19}$$

This is the same as equation (20) in Bretherton [5] where it is consdered the relationship between infinitesimal changes between the forward mapping $\boldsymbol{\eta}$ and those

incurred in the inverse mapping $\boldsymbol{\eta}^{-1}$. Putting this together with the last term in (A-7)

$$\delta\boldsymbol{u} = \frac{\partial \boldsymbol{w}}{\partial t} + \boldsymbol{u}\cdot\nabla\boldsymbol{w} - \underbrace{\nabla\dot{\boldsymbol{\eta}}\cdot\nabla\boldsymbol{\eta}^{-1}}_{\nabla\boldsymbol{u}}\cdot\underbrace{\delta\boldsymbol{\eta}\circ\boldsymbol{\eta}^{-1}}_{\boldsymbol{w}}. \tag{A-20}$$

Finally we have arrived at the expression for the velocity variation

$$\delta\boldsymbol{u} = \frac{\partial \boldsymbol{w}}{\partial t} + \boldsymbol{u}\cdot\nabla\boldsymbol{w} - \boldsymbol{w}\cdot\nabla\boldsymbol{u} = 0. \tag{A-21}$$

For variations of the volume element start with the expression

$$D\circ\boldsymbol{\eta} = \frac{1}{det\nabla\boldsymbol{\eta}}. \tag{A-22}$$

To take variations of the LHS of equation (A-22) write

$$D^{\epsilon}\circ\boldsymbol{\eta}^{\epsilon} = D(\boldsymbol{\eta}^{\epsilon}) + \epsilon\,\delta D(\boldsymbol{\eta}^{\epsilon}) \tag{A-23}$$

differentiate with respect to ϵ

$$\left.\frac{d}{d\epsilon}\right|_{\epsilon=0}(D^{\epsilon}\circ\boldsymbol{\eta}^{\epsilon}) = \left[\frac{\partial D}{\partial\boldsymbol{\eta}^{\epsilon}}\cdot\delta\boldsymbol{\eta}\right]_{\epsilon=0} + \delta D\circ\boldsymbol{\eta}^{\epsilon}|_{\epsilon=0} \tag{A-24}$$

$$=\nabla D\cdot\delta\boldsymbol{\eta} + \delta D\circ\boldsymbol{\eta} \tag{A-25}$$

For the RHS of equation (A-22)

$$\left.\frac{\partial}{\partial\epsilon}\right|_{\epsilon=0}\left(\frac{1}{det(\nabla\boldsymbol{\eta}^{\epsilon})}\right) = -\frac{1}{(det\nabla\boldsymbol{\eta})^2}\cdot\left.\frac{\partial}{\partial\epsilon}\right|_{\epsilon=0} det(\nabla\boldsymbol{\eta}^{\epsilon}) \tag{A-26}$$

To differentiate the determinant a two-dimensional example will suffice

$$\left.\frac{d}{d\epsilon}\right|_{\epsilon=0}(det\nabla\boldsymbol{\eta}^{\epsilon}) = \begin{vmatrix} \frac{\partial\delta\eta_x}{\partial a} & \frac{\partial\delta\eta_x}{\partial b} \\ \frac{\partial\eta_y}{\partial a} & \frac{\partial\eta_y}{\partial b} \end{vmatrix} + \begin{vmatrix} \frac{\partial\eta_x}{\partial a} & \frac{\partial\eta_x}{\partial b} \\ \frac{\partial\delta\eta_y}{\partial a} & \frac{\partial\delta\eta_y}{\partial b} \end{vmatrix} \tag{A-27}$$

$$= \frac{\partial\delta\eta_x}{\partial a}\frac{\partial\eta_y}{\partial b} - \frac{\partial\delta\eta_x}{\partial b}\frac{\partial\eta_y}{\partial a} + \frac{\partial\eta_x}{\partial a}\frac{\partial\delta\eta_y}{\partial b} - \frac{\partial\eta_x}{\partial b}\frac{\partial\delta\eta_y}{\partial a} \tag{A-28}$$

$$= det\nabla\boldsymbol{\eta}\frac{\partial\eta_i^{-1}}{\partial x_j}\frac{\partial\delta\eta_j}{\partial a_i} \tag{A-29}$$

$$= det\nabla\boldsymbol{\eta}\frac{\partial}{\partial x_j}\left(\delta\boldsymbol{\eta}\circ\boldsymbol{\eta}^{-1}\right) \tag{A-30}$$

$$= det\nabla\boldsymbol{\eta}\cdot\boldsymbol{w}. \tag{A-31}$$

Putting the RHS and LHS together

$$\delta D\circ\boldsymbol{\eta} + \nabla D\cdot\delta\boldsymbol{\eta} = -\frac{1}{det\nabla\boldsymbol{\eta}}\nabla\cdot\boldsymbol{w}. \tag{A-32}$$

Composing both sides with $\boldsymbol{\eta}^{-1}$

$$\delta D = -\nabla D\cdot\underbrace{\delta\boldsymbol{\eta}\circ\boldsymbol{\eta}^{-1}}_{\boldsymbol{w}} - D\nabla\cdot\boldsymbol{w} \tag{A-33}$$

$$= -\nabla D\cdot\boldsymbol{w} - D\,\nabla\cdot\boldsymbol{w} \tag{A-34}$$

$$= -\nabla\cdot(D\boldsymbol{w}) \tag{A-35}$$

For variations of the particle displacement covariance write $D\langle\xi_k\xi_l\rangle/Dt$ in material form

$$\langle\xi_k\xi_l\rangle\circ\boldsymbol{\eta} = \langle\xi_k\xi_l\rangle_i \tag{A-36}$$

where the subscript i denotes the initial value. This equation tells us the displacement covariance is preserved along trajectories. Now vary both sides, and differentiate with respect to ϵ noting that the RHS is constant

$$\left.\frac{d}{d\epsilon}\right|_{\epsilon=0}(\langle\xi_k\xi_l\rangle^{\epsilon}\circ\boldsymbol{\eta}^{\epsilon}) = 0 \tag{A-37}$$

which gives

$$\nabla\langle\xi_k\xi_l\rangle\cdot\delta\boldsymbol{\eta} + \delta\langle\xi_k\xi_l\rangle\circ\boldsymbol{\eta} = 0. \tag{A-38}$$

Composing both sides with $\boldsymbol{\eta}^{-1}$

$$\delta\langle\xi_k\xi_l\rangle = -\nabla\langle\xi_k\xi_l\rangle \cdot \boldsymbol{w} \tag{A-39}$$

Appendix B - Helmholtz equation solver for the channel flow

In this Appendix the method used to solve the Helmholtz equation for the channel flow will be described. For the channel flow the mesh spacing was constant in the homogeneous directions x and z. This means when α_k^2 is based on the mesh spacing, α_x^2 and α_z^2 are both constant. In some cases a flow-dependent definition of α^2 was used. In these cases the plane-averaged values of α_x^2 and α_z^2 were used. For the isotropic model α^2 is a function of the vertical coordinate y only.

We begin with the Helmholtz equation in physical space, indicating the filtered and unfiltered variables by $\tilde{\phi}$ and ϕ respectively.

$$\phi = \tilde{\phi} - \alpha_x^2 \frac{\partial^2 \tilde{\phi}}{\partial x^2} - \frac{\partial}{\partial y}\left(\alpha_y^2 \frac{\partial \tilde{\phi}}{\partial y}\right) - \alpha_z^2 \frac{\partial^2 \tilde{\phi}}{\partial z^2} \tag{B-1}$$

After carrying out a Fourier transform in the periodic directions x and z we have and equation for $\hat{\phi}$

$$\hat{\phi} = \hat{\tilde{\phi}} + \alpha_x^2 k_x^2 \hat{\tilde{\phi}} - \frac{\partial}{\partial y}\left(\alpha_y^2 \frac{\partial \hat{\tilde{\phi}}}{\partial y}\right) + \alpha_z^2 k_z^2 \hat{\tilde{\phi}}. \tag{B-2}$$

Here $\hat{\phi} = \hat{\phi}(k_x, y, k_z)$ and $\hat{\tilde{\phi}} = \hat{\tilde{\phi}}(k_x, y, k_z)$. Discretizing the vertical derivative using finite differences

$$\begin{aligned}\frac{\partial}{\partial y}\left(\alpha_y^2 \frac{\partial \hat{\tilde{\phi}}}{\partial y}\right) =& \frac{1}{\delta y_P}\left[\alpha_y^2 \frac{\partial \hat{\tilde{\phi}}}{\partial y}\bigg|_{i,n,k} - \alpha_y^2 \frac{\partial \hat{\tilde{\phi}}}{\partial y}\bigg|_{i,s,k}\right] \\ =& \frac{1}{\delta y_P}\left[\alpha_y^2|_n \frac{\hat{\tilde{\phi}}(k_x, j+1, k_z) - \hat{\tilde{\phi}}(k_x, j, k_z)}{y_{j+1} - y_j} - \alpha_y^2|_s \frac{\hat{\tilde{\phi}}(k_x, j, k_z) - \hat{\tilde{\phi}}(k_x, j+1, k_z)}{y_j - y_{j-1}}\right]\end{aligned} \tag{B-3}$$

. Equation (B-2) can now be written in the form

$$a_P \hat{\tilde{\phi}}_P = a_N \hat{\tilde{\phi}}_N + a_S \hat{\tilde{\phi}}_S + S_\phi, \tag{B-4}$$

with

$$a_N = \frac{1}{\delta y_P}\left[\frac{\alpha_y^2|_n}{y_{j+1} - y_j}\right] \tag{B-5}$$

$$a_S = \frac{1}{\delta y_P}\left[\frac{\alpha_y^2|_s}{y_j - y_{j-1}}\right] \tag{B-6}$$

$$a_P = 1 + \alpha_x^2 k_x^2 + \alpha_z^2 k_z^2 + a_N + a_S \tag{B-7}$$

$$S_\phi = \hat{\phi}. \tag{B-8}$$

Equation (B-4) can be efficiently solved using an algorithm for tridiagonal matrices (TDMA [12]) for each k_x, k_z. The solution variable $\hat{\tilde{\phi}}(k_x, y, k_z)$ is transformed back to physical space $\tilde{\phi}(x, y, z)$. The Fourier transforms and inverse transforms were carried out using the routines in Numerical Recipes in Fortran [142]. The method was tested on two and three dimensional problems with known analytical solutions, such as a gaussian hump and a superposition of sinusoidal waves.

References

[1] J. Bardina, J.H. Ferziger, and W.C. Reynolds. Improved subgrid models for large eddy simulation. In *AIAA Paper 80-1357*, 1980.

[2] G.K. Batchelor. *The Theory of Homogeneous Turbulence*. Cambridge University Press, 1972.

[3] H.S. Bhat. *Lagrangian averaging, nonlinear waves, and shock regularization*. PhD thesis, California Institute of Technology, 2005.

[4] R. Bouffanais and M.O. Deville. Large-eddy simulation of the flow in a lid-driven cavity. *Physics of Fluids*, 19:055108, 2007.

[5] F.P. Bretherton. A note on Hamilton's principle for perfect fluids. *Journal of Fluid Mechanics*, 44:19–31, 1970.

[6] M. Buehner. *Lagrangian measurements and low-dimensional models for oceanographic atmospheric data ssimilation*. PhD thesis, Dalhousie University, 2000.

[7] S. Chen, C. Foias, D.D. Holm, E Olson, E.S. Titi, and S. Wynne. Camassa-Holm equations as a closure model for turbulent channel and pipe flow. *Physical Review Letters*, 81:5338–5341, 1998.

[8] S. Chen, C. Foias, D.D. Holm, E. Olson, E.S. Titi, and S. Wynne. The Camassa-Holm equations and turbulence. *Physica D*, 133:49–65, 1999.

[9] S. Chen, C. Foias, D.D. Holm, E. Olson, E.S. Titi, and S. Wynne. A connection between the Camassa-Holm equations and turbulent flows in pipes and channels. *Physics of Fluids*, 11:2343–2353, 1999.

[10] S. Chen, D.D. Holm, L.G. Margolin, and R. Zhang. Direct numerical simulations of the Navier-Stokes alpha model. *Physica D*, 133:66–83, 1999.

[11] R.A. Clark, J.H. Ferziger, and W.C. Reynolds. Evaluation of subgrid-scale models using an accurately simulated turbulent flow. *Journal of Fluid Mechanics*, 91:1–16, 1979.

[12] S.D. Conte and C deBoor. *Elementary Numerical Analysis*. McGraw-Hill, 1972.

[13] C.B. da Silva and J.C.F. Pereira. The effect of subgrid-scale models on the vortices computed from large-eddy simulations. *Physics of Fluids*, 16:4506, 2004.

[14] P.A. Davidson. *Turbulence: An introduction for scientists and engineers*. Oxford University Press, 2006.

[15] R.B. Dean. Reynolds number dependence of skin friction and other bulk flow variables in two-dimensional rectangular duct flow. *Journal Fluids Engineering*, 100:215–223, 1978.

[16] W.J. Deardorff. A numerical study of three-dimensional turbulent channel flow at large Reynolds numbers. *Journal of Fluid Mechanics*, 41:453–480, 1970.

[17] J.A. Domaradzki and D.D. Holm. Navier-Stokes alpha model: LES equations with nonlinear dispersion. In B.J. Geurts, editor, *Modern Simulation Strategies for Turbulent Flow*, chapter 6. R.T. Edwards, Inc., 2001.

[18] J.A. Domaradzki and W. Liu. Energy transfer in numerically simulated wall-bounded turbulent flows. *Physics of Fluids*, 6(4):1583–1599, 1994.

[19] J.A. Domaradzki and E.M. Saiki. Backscatter models for Large-Eddy-Simulations. *Theoretical and Computational Fluid Dynamics*, 9:75–83, 1997.

[20] J.A. Domaradzki and E.M. Saiki. A subgrid-scale model based on the estimation of unresolved scales of turbulence. *Physics of Fluids*, 9(7):2148–2164, 1997.

[21] P.G. Drazin and W.H. Reid. *Hydrodynamic Stability*. Cambridge University Press, 1981.

[22] F. Ducros, P. Comte, and M. Lesieur. Large-eddy simulation of transition to turbulence in a boundary layer developing spatially over a flat plate. *Journal of Fluid Mechanics*, 326:1–36, 1996.

[23] J.H. Ferziger and M. Peric. *Computational methods for fluid dynamics*. Springer, 3rd edition, 2002.

[24] B.A. Finlayson. *Method of weighted residuals and variational principles, with application in fluid mechanics, heat and mass transfer*. Academic Press, 1972.

[25] C. Foias, D.D. Holm, and E.S. Titi. The Navier-Stokes-alpha model of fluid turbulence. *Physica D*, 152-153:505–519, 2001.

[26] C.J. Freitas and R.L. Street. Non-linear transient phenomena in a complex recirculating flow: A numerical investigation. *International Journal for Numerical Methods in Fluids*, 8:769–802, 1988.

[27] I.M. Gelfand and S.V. Fomin. *Calculus of Variations*. Dover Publications, 1963.

[28] M. Germano. Differential filters for the large eddy numerical simulation of turbulent flows. *Physics of Fluids*, 29(6):1755–1757, 1986.

[29] M. Germano, U. Piomelli, P. Moin, and W.H. Cabot. A dynamic subgrid-scale eddy viscosity model. *Physics of Fluids*, 3:1790, 1991.

[30] B.J. Geurts and J. Frohlich. A framework for predicting accuracy limitations in large-eddy simulations. *Physics of Fluids*, 14(6):L41–L44, 2002.

[31] B.J. Geurts and D.D. Holm. Alpha-modeling strategy for LES of turbulent mixing. In *Turbulent Flow Computation*, pages 237–278. Kluwer:London, 2002.

[32] B.J. Geurts and D.D. Holm. Leray and LANS-alpha modelling of turbulent mixing. *Journal of Turbulence*, 7(10):1–33, 2006.

[33] B.J. Geurts, A.K. Kuczaj, and E.S. Titit. Regularization modeling for large-eddy simulation of homogeneous isotropic decaying turbulence. *Journal of Physics A*, 41:344008, 2008.

[34] S. Ghosal. Mathematical and physical constraints on Large-Eddy simulation of turbulence. *AIAA Journal*, 37(4):425–433, 1999.

[35] S. Goto. A physical mechanism of the energy cascade in homogeneous isotropic turbulence. *Journal of Fluid Mechanics*, 605:355–366, 2008.

[36] J. Graham, D. Holm, P. Mininni, and A. Pouquet. Three regularization models of the Navier-Stokes equations. *Physics of Fluids*, 20:035107, 2008.

[37] J. Graham, D.D. Holm, P.D. Mininni, and A. Pouquet. Highly turbulent solutions of LANS-alpha and their LES potential. *Physical Review E*, 756:056310, 2007.

[38] H.L. Grant, A. Moillet, and R.W. Stewart. Turbulent spectra from a tidal channel. *Journal of Fluid Mechanics*, 12:241–263, 1962.

[39] J. Gullbrand and F.K. Chow. The effect of numerical errors and turbulence models in large-eddy simulations of channel flow, with and without explicit filtering. *Journal of Fluid Mechanics*, 495:323–341, 2003.

[40] Kobayashi H. and Y. Shimomura. Inapplicability of the Clark model to the large eddy simulation of turbulent channel flows. *Physics of Fluids*, 15(3):L29–L32, 2003.

[41] C. Hartel and L. Kleiser. Analysis and modelling of subgrid-scale motions in near-wall turbulence. *Journal of Fluid Mechanics*, 356:327–352, 1998.

[42] C. Härtel, L. Kleiser, F. Unger, and R. Friedrich. Subgrid-scale energy transfer in the near-wall region of turbulent flows. *Physics of Fluids*, 6:3130–3143, 1994.

[43] M.W. Hecht, W.R. Holland, and P.J. Rasch. Upwind-weighted advection schemes for ocean tracer transport: An evaluation in a passive tracer context. *Journal of Geophysical Research*, 100:20,763–20,778, 1995.

[44] M.W. Hecht, D.D. Holm, M. R. Petersen, and B.A. Wingate. Implementation of the LANS-alpha turbulence model in a primitive equation ocean model. *Journal of Computational Physics*, 227(11):5691–5716, 2008.

[45] M.W. Hecht, D.D. Holm, M.R. Petersen, and B.A. Wingate. The LANS-alpha and Leray turbulence parameterizations in primitive equation ocean modeling. *Journal of Physics A*, 41:344009, 2008.

[46] D. Holm, C. Jeffery, S. Kurien, D. Livescu, M.A. Taylor, and B.A. WIngate. The LANS-alpha model for computing turbulence. Origins, results and open problems. *Los Alamos Science*, 29:152–171, 2005.

[47] D.D. Holm. Fluctuation effects on 3D Lagrangian mean and Eulerian mean fluid motion. *Physica D*, 133:215–269, 1999.

[48] D.D. Holm. Karman-Howarth theorem for the Lagrangian-averaged Navier-Stokes-alpha model of turbulence. *Journal of Fluid Mechanics*, 467:205–214, 2002.

[49] D.D. Holm. Lagrangian averages, averaged Lagrangians, and the mean effect of fluctutions in fluid dynamics. *Chaos*, 12(2):518–530, 2002.

[50] D.D. Holm. Taylor's hypothesis, Hamilton's principle and the LANS-alpha model for computing turbulence. *Los Alamos Science*, (29):172–180, 2005.

[51] D.D. Holm and B.T. Nadiga. Modeling mesoscale turbulence in the barotropic double-gyre circulation. *Journal of Physical Oceanography*, 33:2355–2366, 2003.

[52] D.D Holm, V. Putkaradze, P.D. Weidman, and B.A. Wingate. Boundary effects on exact solutions of the Lagrangian-Averaged Navier-Stokes-alpha equations. *Journal of Statistical Physics*, 113:841–854, 2003.

[53] J. Jimenez. The minimal flow unit in near-wall turbulence. *Journal of Fluid Mechanics*, 225:213–240, 1991.

[54] J. Jimenez. The autonomous cycle of near-wall turbulence. *Journal of Fluid Mechanics*, 389:335–359, 1999.

[55] J. Jimenez. On eddy-viscosity sub-grid models. In *Workshop on Direct and Large-Eddy Simulations*, pages 75–86, 1999.

[56] J. Jimenez and R.D. Moser. What are we learning from simulating wall turbulence? *Philosophical Transactions of the Royal Society A*, 365:715–732, 2007.

[57] R.M. Kerr, J.A. Domaradzki, and G. Barbier. Small-scale properties of non-linear interactions and subgrid-scale energy transfer in isotropic turbulence. *Physics of Fluids*, 8(1):197–208, 1996.

[58] J. Kim, P. Moin, and R. Moser. Turbulence statistics in fully developed channel flow at low Reynolds number. *Journal of Fluid Mechanics*, 177:133–166, 1987.

[59] H. Kobayashi and Y. Shimomura. Comment on 'Inapplicability of the dynamic Clark model to the large eddy simulation of incompressible turbulent channel flows'. *Physics of Fluids*, 16(2):492, 2004.

[60] Hiromichi Kobayashi. The subgrid-scale models based on coherent structures for rotating homogeneous turbulence and turbulent channel flow. *Physics of Fluids*, 17:045105–1,12, 2005.

[61] A.N. Kolmogorov. Dissipation of energy in locally isotropic turbulence. *Dokl. Acad. Nauk. SSSR*, 32:141, 1941. English translation in Proceedings of the Royal Society of London A, 434:15-17, 1991.

[62] J.R. Koseff and R.L. Street. The lid-driven cavity flow: A synthesis of qualitative and quantitative obseravtions. *Journal of Fluids Engineering*, 106:390–398, 1984.

[63] J.R. Koseff and R.L. Street. On end wall effects in a lid-driven cavity flow. *Journal of Fluids Engineering*, 106:385–389, 1984.

[64] J.R. Koseff and R.L. Street. Visualization studies of a shear driven three-dimensional recirculating flow. *Journal of Fluids Engineering*, 106:21–27, 1984.

[65] R.H. Kraichnan. Inertial ranges in two-dimensional turbulence. *Physics of Fluids*, 10:1417–1423, 1967.

[66] A.G. Kravchenko, H. Choi, and P. Moin. On the relation of near-wall streamwise vortices to wall friction in turbulent boundary layers. *Physics of Fluids A*, 5(2):3309–3311, 1993.

[67] A.G. Kravchenko, P. Moin, and R. Moser. Zonal embedded grids for numerical simulations of wall-bounded turbulent flows. *Journal of Computational Physics*, 127:412–423, 1996.

[68] H. Kreplin and H. Eckelmann. Behavior of the three fluctuating velocity components in the wall region of turbulent channel flow. *Physics of Fluids*, 22:1233, 1979.

[69] P.K. Kundu. *Fluid Mechanics*. Academic Press Inc., 1990.

[70] S. Leibovich. The form and dynamics of Langmuir circulations. *Annual Review of Fluid Mechanics*, 15:715–724, 1983.

[71] E. Leriche and S. Gavrilakis. Direct numerical simulations of the flow in a lid-driven cubical cavity. *Physics of Fluids*, 12:1363, 2000.

[72] M. Lesieur and O. Metais. New trends in large-eddy simulations of turbulence. *Annual Review of Fluid Mechanics*, 28:45–82, 1996.

[73] F.S. Lien. *Computational modelling of 3D flow in complex ducts and passages.* PhD thesis, University of Manchester, 1992.

[74] F.S. Lien and M.A. Leschziner. A general non-orthogonal collocated FV algorithm for turbulent flow at all speeds incorporating second moment closure. Part 1: Computational implementation. *Computer Methods for Applied Mechanics and Engineering*, 114:123–148, 1994.

[75] F.S. Lien and M.A. Leschziner. A general non-orthogonal collocated FV algorithm for turbulent flow at all speeds incorporating second moment closure. Part 2: Application. *Computational Methods for Applied Mechanics and Engineering*, 114:149–167, 1994.

[76] F.S. Lien and M.A. Leschziner. Upstream monotonic interpolation for scalar transport with application to complex turbulent flows. *International Journal for Numerical Methods in Fluids*, 19:527–548, 1994.

[77] D.K. Lilly. The representation of small-scale turbulence in numerical simulation experiments. In *Proceedings IBM Scientific Computing Symposium on Environmental Sciences*, pages 195–210, 1967.

[78] D.K. Lilly. A proposed modification of the Germano subgrid-scale closure method. *Physics of Fluids A*, 34:633, 1992.

[79] S. Liu, C. Meneveau, and J. Katz. On the properties of similarity subgrid-scale models as deduced from measurements in a turbulent jet. *Journal of Fluid Mechanics*, 275:83–119, 1994.

[80] T.S. Lund. On the use of discrete filters for large eddy simulation. In *Annual Research Briefs 1997*, pages 83–95. Center for Turbulence Research, 1997.

[81] T.S. Lund. The use of explicit filters in large eddy simulation. *Computers and Mathematics*, 46:603–616, 2003.

[82] J.C. Magnient and P. Sagaut. A study of built-in filter for some eddy viscosity models in large-eddy simulation. *Physics of Fluids*, 13(5):1440–1449, 2001.

[83] P. Majander and T. Siikonen. Evaluation of Smagorinsky-based subgrid-scale models in a finite-volume computation. *International Journal for Numerical Methods in Fluids*, 40:735–744, 2002.

[84] J.E. Marsden and S. Shkoller. The Anisotropic Lagrangian Averaged Euler and Navier-Stokes equations. *Archives of Rational Mech. Analysis*, 66:27–46, 2003.

[85] P.J. Mason. Large-eddy simulation: A critical review of the technique. *Quarterly Journal of the Royal Meteorological Society*, 120:1–26, 1994.

[86] J. Mathew, R. Lechner, H. Foysi, J. Sesterhenn, and R. Friedrich. An explicit filtering method for large eddy simulation of compressible flows. *Physics of Fluids*, 15(8):2279–2289, 2003.

[87] J.C. McWilliams, P.P. Sullivan, and C.H. Moeng. Langmuir turbulence in the ocean. *Journal of Fluid Mechanics*, 334:1–30, 1997.

[88] C. Meneveau and T.S. Lund. On the Lagrangian nature of the turbulence energy cascade. *Physics of Fluids*, 8:2820–2825, 1994.

[89] C. Meneveau, T.S. Lund, and W.H. Cabot. A Lagrangian dynamic subgrid-scale model of turbulence. *Journal of Fluid Mechanics*, 319:353–385, 1996.

[90] S. Menon, P.-K. Yeung, and W.-W. Kim. Effect of subgrid models on the computed interscale energy transfer in isotropic turbulence. *Computers and Fluids*, 25(2):165–180, 1996.

[91] J. Meyers and P. Sagaut. Is plane-channel flow a friendly case for the testing of large-eddy simulation subgrid-scale models? *Physics of Fluids*, 19:048105, 2007.

[92] K. Mohseni, B. Kosovic, S. Shkoller, and J.E. Marsden. Numerical simulations of the Lagrangian Averaged Navier-Stokes equations for homogeneous isotropic turbulence. *Physics of Fluids*, 15(2):524–544, 2003.

[93] P. Moin and J. Kim. Numerical investigation of turbulent channel flow. *Journal of Fluid Mechanics*, 118:341–377, 1982.

[94] P. Moin and J. Kim. The structure of the vorticity field in turbulent channel flow. Part 1: Analysis of the instantaneous fields and statistical correlations. *Journal of Fluid Mechanics*, 155:441–464, 1985.

[95] D.C. Montgomery and A. Poquet. An alternative interpretation for the Holm alpha model. *Physics of Fluids*, 14(9):3365–3366, 2002.

[96] P.J. Morrison. Hamiltonian description of the ideal fluid. *Reviews of Modern Physics*, 70:467–521, 1998.

[97] S. Murakami and S. Iizuka. CFD analysis of turbulent flow past square cylinder using dynamic LES. *Journal of Fluids and Structures*, 13:1097–1112, 1999.

[98] B.T. Nadiga and Margolin L.G. Dispersive-dissipative eddy parameterization in a barotropic model. *Journal of Physical Oceanography*, 31:2525=2531, 2001.

[99] F.M. Najjar and D.K. Tafti. Study of discrete test filters and finite difference approximations for the dynamic subgrid-scale stress model. *Physics of Fluids*, 8(4):1076–1088, 1996.

[100] V.K. Natrajan and K.T. Christensen. The role of coherent structures in subgrid-scale energy transfer within the log layer of wall turbulence. *Physics of Fluids*, 18:065104–1,14, 2006.

[101] D.J. Olbers. Nonlinear energy transfer and the energy balance of the internal wave field in the deep ocean. *Journal of Fluid Mechanics*, 74:375–399, 1976.

[102] R.L. Panton. Overview of the self-sustaining mechanisms of wall turbulence. *Progress in Aerospace Sciences*, 37:341–383, 2001.

[103] N. Park and K. Mahesh. A velocity-estimation model constrained by subgrid scale dissipation. *Journal of Computational Physics*, 227:4190–4206, 2008.

[104] B. Perot and P. Moin. Shear-free turbulent boundary layers. 1. Physical insights into near-wall turbulence. *Journal of Fluid Mechanics*, 295:1999–227, 1995.

[105] M.R. Petersen, M.W. Hecht, and B.A. Wingate. Efficient form of the LANS-alpha turbulence model in a primitive equation ocean model. *Journal of Computational Physics*, 227(11):5717–5735, 2008.

[106] U. Piomelli. Large-eddy simulation: achievements and challenges. *Progress in Aerospace Sciences*, 35:335–362, 1999.

[107] U. Piomelli and E. Balaras. Wall-layer models for Large-Eddy simulations. *Annual Review of Fluid Mechanics*, 34:349–374, 2002.

[108] U. Piomelli, W.H. Cabot, P. Moin, and S. Lee. Subgrid-scale backscatter in turbulent and transitional flows. *Physics of Fluids A*, 7(3):1766–1771, 2001.

[109] U. Piomelli and Y. Yu. Subgrid-scale energy transfer and near wall turbulence structure. *Physics of Fluids*, 8(1):215–224, 1996.

[110] S.B. Pope. *Turbulent Flows*. Cambridge University Press, 2000.

[111] A.K. Prasad and J.R. Koseff. Reynolds number and end-wall effects on a lid-driven cavity flow. *Physics of Fluids A*, 1(2):208–218, 1988.

[112] V. Putkaradze and P. Weidman. Turbulent wake solutions of the Prandtl α equations. *Physical Review E*, 67:036304–1,7, 2003.

[113] S. Radhakrishnan and U. Piomelli. Large eddy simulation of oscillating boundary layers: Model comparison and validation. *Journal of Geophysical Research*, 113:C02022, 2008.

[114] C.M. Rhie and W.L. Chow. Numerical study of the turbulent flow past an airfoil with trailing edge separation. *AIAA*, 21(11):1525–1532, 1983.

[115] L.F. Richardson. Atmospheric diffusion shown on a distance-neighbour graph. *Proceedings of the Royal Society of London A*, 110:709–737, 1926.

[116] Patrick J. Roache. *Computational Fluid Dynamics*. Hermosa Publishers, 1972.

[117] S.K. Robinson. Coherent motions in the turbulent boundary layer. *Annual Review of Fluid Mechanics*, 23:601–639, 1991.

[118] M. Rogers and P. Moin. Helicity fluctuations in incompressible turbulent flows. *Physics of Fluids*, 30(9):2662–2771, 1987.

[119] M. Rogers and P. Moin. The structure of the vorticity field in homogeneous turbulent flows. *Journal of Fluid Mechanics*, 176:33–66, 1987.

[120] P. Sagaut. *Large Eddy Simulation for Incompressible Flows*. Springer-Verlag, 2002.

[121] P. Sagaut and R. Grohens. Discrete filters for large eddy simulations. *International Journal for Numerical Methods in Fluids*, 31:1195–1220, 1999.

[122] Rick Salmon. *Lectures on Geophysical Fluid Dynamics*. Oxford University Press, 1998.

[123] F. Sarghini, U. Piomelli, and E. Balaras. Scale-similar models for large-eddy simulations. *Physics of Fluids*, 11:1596–1607, 1999.

[124] U. Schuman. Subgrid scale models for finite difference simulations of turbulent flows in plane channels and annuli. *Journal of Computational Physics*, 18:376–404, 1975.

[125] P.N. Shankar and M.D. Deshpande. Fluid mechanics in the driven cavity. *Annual Review of Fluid Mechanics*, 32:93–136, 2000.

[126] C.B. Silva and O. Metais. On the influence of coherent structures upon interscale interactions in turbulent plane jets. *Journal of Fluid Mechanics*, 473:103–145, 2002.

[127] J. Smagorinsky. General circulation experiments with the primitive equations I. The basic experiment. *Monthly Weather Review*, 91:99–164, 1963.

[128] S. Stolz, N.A. Adams, and L. Kleiser. An approximate deconvolution model for large-eddy simulations with application to incompressible wall-bounded flows. *Physics of Fluids*, 13(6):997–1014, 2001.

[129] S. Stolz, P. Schlatter, and L. Kleiser. High-pass filtered eddy-viscosity models for large-eddy simulations of transitional and turbulent flow. *Physics of Fluids*, 17:065103–1,14, 2005.

[130] P.P. Sullivan, J.C. McWilliams, and K. Melville. Surface gravity wave effects in the oceanic boundary layer: large-eddy simulation with vortex force and stochastic breakers. *Journal of Fluid Mechanics*, 593:405–452, 2007.

[131] B. Tao, J. Katz, and C. Meneveau. Statistical geometry of subgrid scale stresses determined from holographic PIV measurements. *Journal of Fluid Mechanics*, 467:35–78, 2002.

[132] G.I. Taylor. Diffusion by continuous movements. *Proceedings of the London Mathematical Society*, 20:196–212, 1922.

[133] H. Tennekes and J.L. Lumley. *A first course in turbulence*. MIT Press, 1973.

[134] T. Theodorsen. Mechanism of turbulence. In *Proceedings of the Second Midwestern Conference on Fluid Mechanics*, pages 1–18, 1952.

[135] L.N. Trefethen. Group velocity in finite-difference schemes. *SIAM Review*, 24:113–136, 1982.

[136] A. Tsinober, L. Shtilman, and H. Vaisburd. A study of properties of vortex stretching and enstrophy generation in numerical and laboratory turbulence. *Fluid Dynamics Research*, 21:477–494, 1997.

[137] F. van der Bos and B.J. Geurts. Commutator errors in the filtering approach to large-eddy simulation. *Physics of Fluids*, 17:035108, 2005.

[138] J.P. Van Doormall and G.D. Raithby. Enhancement of the SIMPLE method for predicting incompressible fluid flows. *Numerical Heat Transfer*, 7:147, 1984.

[139] M. van Reeuwijk. *Direct simulation and regularization modeling of turbulent thermal convection*. PhD thesis, Delft University of Technology, 2007.

[140] M. van Reeuwijk, H.J.J. Jonker, and K. Hanjalic. Incompressibility of the Leray-alpha model for wall-bounded flows. *Physics of Fluids*, 18:018103, 2006.

[141] O.V. Vasilyev and D.E. Goldsteing. Local spectrum of commutation error in large eddy simulation. *Physics of Fluids*, 16(2):470–473, 2004.

[142] W.T. Vettering, W.H. Press, S.A. Teukolsky, and Flannery B.R. *Numerical Recipes in Fortran 90 - The art of scientific parallel computing*. Cambridge University Press, 1996.

[143] B. Vreman. Comment on 'Inapplicability of the dynamic Clark model to the large eddy simulation of incompressible turbulent channel flows'. *Physics of Fluids*, 16(2):L29, 2004.

[144] B. Vreman, B. Geurts, and H. Kuerten. Large-eddy simulation of the turbulent mixing layer. *Journal of Fluid Mechanics*, 339:357–390, 1997.

[145] B. Vreman, B.J. Geurts, and H. Kuerten. Large-eddy simulation of the temporal mixing layer using the Clark model. *Theoretical and Computational Fluid Dynamics*, 8:309–324, 1996.

[146] F. Waleffe. The nature of triad interactions in homogeneous turbulence. *Physics of Fluids A*, 4(2):350–363, 1992.

[147] D.J. Webb, B.A. de Cuvas, and C.S. Richmond. Improved advection schemes for ocean models. *Journal of Atmospheric and Oceanic Technology*, 15:1171–1187, 1988.

[148] G.B. Whitham. Two-timing, variational principles and waves. *Journal of Fluid Mechanics*, 44:373–395, 1970.

[149] G.S. Winckelmans, O. Wray, A.A. Vasilyev, and H. Jeanmart. Explicit-filtering large-eddy simulation using the tensor-diffusivity model supplemented by a dynamic Smagorinsky term. *Physics of Fluids*, 13(5):1385–1403, 2001.

[150] T.A. Zang. Numerical simulations of the dynamics of turbulent boundary layers: Perspectives of a transition simulator. *Philosophical Transactions of the Royal Society, A*, 336:95, 1991.

[151] Y. Zang, R.L. Street, and J.R. Koseff. A dynamic mixed subgrid-scale model and its application to turbulent recirculating flows. *Physics of Fluids A*, 5(12):3186–3196, 1993.

[152] H. Zhao and K. Mohseni. Anisotropic turbulent flow simulations using the Lagrangian-Averaged Navier-Stokes alpha equation. In *Proceedings of the 15th AIAA Fluid Dynamics conference and Exhibit*, June 2005.

[153] H. Zhao and K. Mohseni. A dynamic model for the Lagrangian Averaged Navier-Stokes α equations. *Physics of Fluids*, 17:075106, 2005.